Technische Universität München

Fakultät für Mathematik
Lehrstuhl M6 - Fachgebiet Mathematische Modellbildung (Prof. M. Brokate)

Mathematical Modeling and Pattern Formation for Bacterial Colonies

Aenne Christine Oelker, M.Sc.

Vollständiger Abdruck der von der Fakultät für Mathematik der Technischen Universität München zur Erlangung des akademischen Grades eines

Doktors der Naturwissenschaften (Dr. rer. nat.)

genehmigten Dissertation.

Vorsitzende: Prof. Dr. Silke Rolles

Prüfer der Dissertation:

1. Prof. Dr. Christina Kuttler
2. Prof. Fordyce A. Davidson, Ph.D., University of Dundee, Schottland/UK
3. Prof. Dr. Hermann J. Eberl, University of Guelph, Kanada

Die Dissertation wurde am 10.10.2017 bei der Technischen Universität München eingereicht und durch die Fakultät für Mathematik am 25.12.2017 angenommen.

Acknowledgement

First and foremost I would like to thank my advisor Prof. Dr. Christina Kuttler for introducing me to the exciting topic of bacterial pattern formation and for her invaluable support and guidance during the last years when I worked on this thesis. I am also very thankful for her continuous support in all aspects of writing this thesis and for always having an open door and making time for my questions despite her busy schedule.

I am very grateful to Prof. Fordyce A. Davidson, Ph.D. and to Prof. Dr. Hermann J. Eberl for taking the time to review my thesis and to participate in the examination committee. During my Ph.D. studies I was able to visit Prof. Davidson and his group at the University of Dundee in Scotland. I am very thankful to him for this opportunity and also to the Women for Math Science Entrepreneurial Program of TUM for the funding of this research stay. Furthermore, I would like to thank Prof. Dr. Silke Rolles for taking the chair of the examination committee.

The real data pictures in this thesis are the result of biological experiments performed at the Zentrum für Infektionsforschung of Julius-Maximilians-Universität Würzburg. I am very grateful to Dr. Daniel Lopez and Juan-Carlos Garcia-Betancur for their collaboration and for fruitful discussions.

During the time I have worked at TUM, I have greatly enjoyed the friendly and productive atmosphere at the chair for mathematical modeling (M6). My thanks for this go to Prof. Dr. Martin Brokate and all present and former colleagues at the chair. In addition, I would like to thank Dr. Hannes Petermeier for sharing his knowledge about teaching mathematics at the very beginning of my Ph.D. studies.

I am deeply grateful to Dr. Klaus-Dieter Reinsch and to Dr. Linus Wunderlich for thoroughly proofreading parts of this thesis and for their detailed feedback. Furthermore I am thankful to all those colleagues and friends who made the last years such a great experience.

I want to thank my parents Cornelia and Stephan for always encouraging me to independently choose my path in life and to put in my best effort and my "little" brothers David and Lukas for their understanding and for often visiting me in Munich when I did not have much time to travel. Finally, I want to thank my awesome boyfriend Thomas, who has been the best support I could hope for during the last years. I am also grateful to him for introducing me to the adequate use of "Pizza" and "Pommes" on ski and for always knowing exactly if it was time for some words of encouragement or for a series of jokes.

Publications by the author

- Oelker, A., Horger, T., Kuttler, C.,
  From Staphylococcus aureus gene regulation to its pattern formation, submitted, 2017, [110].

- Oelker, A., Horger, T., Kuttler, C.,
  A beautiful human pathogen: Staphylococcus aureus, submitted to The Beauty of Theoretical Biology, Springer, 2017, [109].

- Kaufmann, S., Horger, T., Oelker, A., Beck, S., Schulze, M., Nikolaou, K., Ketelsen, D., Horger, M.,
  Volume perfusion computed tomography (VPCT)-based evaluation of response to TACE using two different sized drug eluting beads in patients with nonresectable hepatocellular carcinoma: Impact on tumor and liver parenchymal vascularisation, European Journal of Radiology, Volume 84, pp. 2548–2554, 2015, [81].

- Kaufmann, S., Schulze, M., Horger, T., Oelker, A., Nikolaou, K., Horger, M.,
  Reproducibility of VPCT parameters in the normal pancreas: comparison of two different kinetic calculation models, Academic Radiology, Volume 22, pp. 1099–1105, 2015, [80].

- Kaufmann, S., Horger, T., Oelker, A., Kloth, C., Nikolaou, K., Schulze, M., Horger, M.,
  Characterization of hepatocellular carcinoma (HCC) lesions using a novel CT-based volume perfusion (VPCT) technique, European Journal of Radiology, Volume 84, pp. 1029–1035, 2015, [79].

- Horger, T., Oelker, A., Kuttler, C., Pérez-Velázquez, J.,
  Mathematical modeling of tumor-induced angiogenesis using porous medium diffusion, International Journal of Biomathematics and Biostatistics, Volume 2, pp. 145–165, 2013, [74].

Abstract

In this thesis, we study models for pattern formation in the Gram-positive bacterium *Staphylococcus aureus*. Starting from gene regulation mechanisms, we derive a reaction-diffusion model including quorum sensing and biofilm formation and demonstrate the potential of the model by finite element simulations. Furthermore we consider a front instability approach to determine the onset of pattern formation and investigate effects related to Darcy's law using level set simulations.

Zusammenfassung

In dieser Arbeit betrachten wir Modelle für Musterbildung im Gram-postiven Bakterium *Staphylococcus aureus*. Ausgehend von Genregulationsmechanismen leiten wir ein Reaktions-Diffusions-Modell mit Quorum Sensing und Biofilmbildung her und untersuchen es mit Finite Elemente Simulationen. Des Weiteren betrachten wir einen Front-Instabilitätsansatz, um zu bestimmen, wann Musterbildung einsetzt, und untersuchen mit Level Set Simulationen Effekte im Zusammenhang mit Darcy's Gesetz.

Contents

Part I.

Introduction

1. Motivation and outline

Bacteria are intriguing organisms, which show very diverse and intelligently coordinated behavior, often perfectly adapted to environmental conditions [72]. The bacterium *Staphylococcus aureus* (*S. aureus*) is an important human pathogen, which is of special interest since it is a main cause of hospital-acquired infections through biofilm formation in its methicillin resistant strains [68, 72, 78]. Furthermore, *S. aureus* is found in diverse biological settings, such as soil, human skin or public places like hospitals [68, 72]. It is relatively complex and has thus not yet been studied as profoundly as other bacteria, such as its close relative *Bacillus subtilis* (*B. subtilis*), e.g., [82, 127, 143]. The detailed study of *S. aureus* and its regulation systems by models and simulations in this thesis is aimed at a better understanding of the physical and biological mechanisms involved in its pattern formation. This knowledge may in the future be used to identify mutant types in a time- and cost-efficient way and may thus help to prevent or cure *S. aureus* infections.

Discrete and continuous patterns are observed in all areas of life and have been studied in a variety of biological settings. A famous example are animal coat patterns of diverse animals such as leopards, snakes or butterflies [106, 122] and also the skin [42, 131]. The same underlying mechanisms are found in phenomena such as chemical reactions and ecological interactions [106]. Further investigations have been carried out on patterns in chemotaxis [23, 28, 117], tumor growth [31, 83], general growing domains [27, 38] and neural models [106]. In many approaches, scale and domain growth considerations play a role. Furthermore, mathematical modeling approaches include not only Turing [106, 141] or Turing-Hopf [27] pattern formation, but also discrete models such as cellular automata [47, 51] and combined Turing-Hopf instability approaches for discrete models [48]. Pattern formation has also been investigated experimentally in the biological and physical context [23, 86, 132]. It is thus a natural phenomenon of great interest across several disciplines.

In a laboratory setting bacteria colonies show a variety of patterns. Several models have been developed to investigate this process using mostly reaction-diffusion

equations, e.g., [14, 98, 99, 102]. Furthermore, bacteria colony survival crucially depends on biofilm formation. This process has been studied in *S. aureus* and several related bacteria, e.g., [30, 35, 37, 100, 127]. Pattern formation is specific for different bacterial mutants, which have one or several disabled gene loci. Therefore the pattern formed by a bacterial colony is a characteristic feature which may help to determine the mutations of the bacteria [65]. Thus, in this thesis we investigate bacterial pattern formation of the Gram-positive bacterium *S. aureus* in the context of quorum sensing and biofilm formation.

To this end the thesis is divided into three parts, where Part I constitutes the introduction, Part II includes reaction-diffusion models and Part III deals with the effects of bacterial division. We introduce the necessary biological, physical and mathematical background, including the numerical simulation techniques, in Chapters 2 and 3 of Part I. Then in Chapter 4 of Part II, we derive a new model for the production of the *S. aureus* quorum sensing substance autoinducing peptide (AIP) and the principal biofilm component polysaccharide intercellular adhesin (PIA), starting from cell regulation mechanisms. Using finite element simulations, we show that changing the related parameter values in a system of five partial differential equations allows to obtain the qualitative phenotypes of *S. aureus* mutants as observed in the laboratory. We furthermore compare our results to the five morphologies of bacterial pattern formation introduced in [98]. In Chapter 5 we investigate a front instability approach for a reduced system of two partial differential equations, which includes nutrient-dependence in the bacterial diffusion term, and compare the obtained predictions to Turing instability parameters. Finally, in Part III, we investigate the effects of pressure on bacterial pattern formation. In this context we concentrate on effects induced by bacterial division, which all bacterial colonies experience and which are considered in Chapter 6. For the numerical simulations of Chapter 6 we employ a finite element based level set method.

The following introduction uses several biological abbreviations. A short overview of some important abbreviations can be found in Table 1.1 below.

Abbreviation	for	Abbreviation	for
TSS	toxic shock syndrome	MRSA strain	methicillin resistant *S. aureus* strain
AHL	acyl homoserine lactone	CSF	competence and sporulation factor
ATP	adenosine triphosphate	ABC transporter	ATP-binding cassette transporter
LHSC	lifting Hele-Shaw cell	EPS	exopolysaccharide
AIP	autoinducing peptide	PIA	polysaccharide intercellular adhesin

Table 1.1.: Abbreviations for biological terms used in the introduction.

2. Biological and physical background

In the following we give a short introduction to the biological setting which we model, namely pattern formation in the bacterium *S. aureus*, and to its special properties. This includes the process of quorum sensing in bacterial colonies. Furthermore, we introduce Darcy's law, which will be relevant in Part III.

2.1. The bacterium *Staphylococcus aureus*

Bacteria are very diverse prokaryotic microorganisms [72] that are about $0.1-700\,\mu m$ in length, but can show different morphologies [72]. After growing to a fixed size, bacteria reproduce asexually using the reproduction mechanism of binary fission [72]. Bacteria divide rapidly under optimal and nearly optimal conditions. If nutrients are sparse, some bacteria can sense the local population density and coordinate their behavior using quorum sensing. One distinguishes between Gram-positive and Gram-negative bacteria. This notation is due to the Gram straining method [72].

The bacterium *S. aureus* is a Gram-positive non-sporulating bacterium of the genus Staphylococcus, the class Bacilli and the order Bacillales. It is a close relative of the Gram-positive bacterium *B. subtilis*, which has the same class and order. Under the microscope *S. aureus* forms grape-like clusters [72] and large round golden or yellow colonies. This is the reason for the name of the bacterium: The Latin word "aureus" means "golden". The bacterium commonly occurs on the human skin and nasal passages and can cause a wide range of bacterial infections from very minor skin infections to fatal diseases such as pneumonia [72]. It is responsible for a large number of hospital-acquired infections since *S. aureus* bacteria can survive under harsh conditions, adhere to smooth surfaces and are well cultivated at a temperature of 37°C [72]. The methicillin resistant *S. aureus* (MRSA) strains show resistance against several antibiotics [72]. Furthermore, also resistances against disinfectants and against clearance by host defenses can be found [150]. Some strains produce

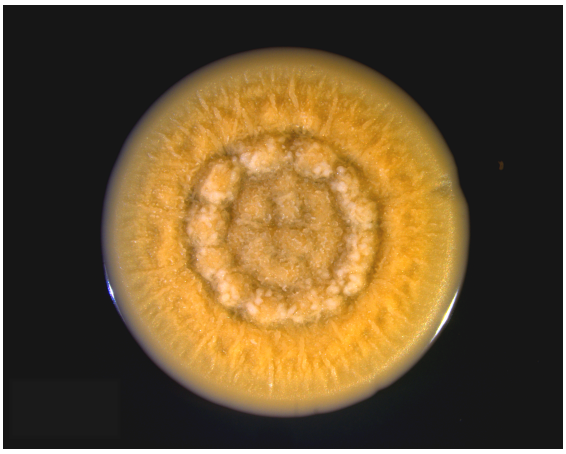

Figure 2.1.: *Staphylococcus aureus* pattern formation in the laboratory. Colony on 1.5% agar with standard nutrient concentration after five days [65].

toxins, which can lead to the toxic shock syndrome (TSS) [72]. *S. aureus* infections are persistent and difficult to treat. Together with the increasing awareness for the clinical relevance of bacterial biofilm formation [150], this leads to an increased interest in the study of this bacterium.

We investigate *S. aureus* mathematically in a laboratory setting, where the bacterium and its mutants are commonly grown in growth media with varying densities and nutrient concentrations. In this setting *S. aureus*, and also other bacteria such as *B. subtilis*, form distinct patterns on the agar surface as it can be seen in Figure 2.1. These patterns are characteristic of the bacterium and its mutants and thus strong candidates for the identification of particular mutants.

2.2. Quorum sensing in bacteria colonies

In general, bacteria live in large communities of cells. In order to coordinate the behavior of the population in a way that benefits the bacterial population as a whole, there is a need for communication and coordination of behavior within or between species. This is achieved by the use of signaling molecules such as autoinducers, that are excreted by the bacteria if they sense that the population density reaches certain threshold values.

Such a behavior was observed in the 1970's [55, 63, 108] for the bacteria *Vibrio fischeri* (*V. fischeri*) and *Vibrio harveyi*. The bacterium *V. fischeri* is found in the light organs of bony fishes and the squid at densities of $10^{10} - 10^{11}$ cells per

milliliter as well as in sea water, where it only reaches densities of less than 10^2 cells per milliliter. Due to this density difference, the bacteria can determine where they are using quorum sensing, and luminescence is only induced when the bacteria are associated to a host. With increasing cell density, the luminescence per cell increases up to its 100-fold value [77] and the bacteria provide light for the fish in a symbiotic process. The quorum sensing substance involved in the autoinduction of the bacterial luminescence is the autoinducer N-3-oxohexanoyl-l-homoserine lactone (3OC6-HSL) [6], a member of the acyl homoserine lactone (AHL) family [104] who is able to diffuse freely across the cell membrane [77]. At low cell densities the autoinducer can diffuse freely outside the cell, but at higher cell densities the molecules accumulate, which leads to quorum sensing activation.

In the DNA of *V. fischeri* two divergently transcribed units are responsible for the autoinducer synthesis: In the presence of autoinducer, the gene *luxR* encodes the LuxR protein which activates the *luxICDABEG* gene by binding at the corresponding binding site. The *luxI* gene then encodes the autoinducer synthase while the other genes play only mechanistic roles. The autoinducer synthase is responsible for producing the autoinducer molecule. This constitutes a positive feedback cycle as the level of the autoinducer has to reach a certain threshold for the cycle to start, which then further increases the autoinducer concentration [10].

The mechanism of quorum sensing can be found in many bacterial species, allowing the bacteria to accomplish a collective task. However the quorum sensing system itself differs for Gram-positive bacteria such as *S. aureus* or *B. subtilis*. *B. subtilis* monitors the concentration of competence and sporulation factor (CSF) in order to measure the cell density and determine the best time for its entry into sporulation [77]. In *S. aureus* bacteria the main quorum sensing system is the *agr* regulation system, which, depending on the environmental conditions, plays a role in the colony's biofilm formation.

There are two main characteristics of quorum sensing in Gram-positive bacteria in comparison to Gram-negative bacteria. The first is that Gram-positive bacteria employ secreted peptides as the autoinducers and the second is that they use two-component adaptive circuits for signal transduction. These consist of a family of homologous proteins, where the first component is a membrane-bound sensor kinase protein, which autophosphorylates to start the information transfer process, and the second component is a response regulator protein that controls gene transcription.

In this way, sensory information is relayed by cascades of (de-)phosphorylation and Gram-positive bacteria can adapt to a wide range of environmental conditions [10]. The peptide signaling substances are produced by cleaving a precursor protein, which is produced at the peptide signal precursor locus. The peptide signal is transported out of the cell by an ATP-binding cassette (ABC) transporter. The principle of the quorum sensing process in Gram-positive bacteria is depicted in Figure 2.2, which is adapted from [10].

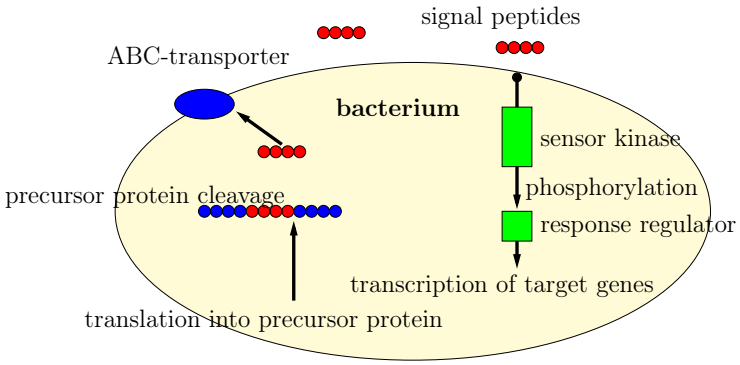

Figure 2.2.: The general principle of quorum sensing in a Gram-positive bacterium.

Deterministic, time-continuous models of quorum sensing can either consist of systems of ordinary differential equations if the spatial component is disregarded or of systems of partial differential equations if diffusion outside the cells is included into the model. In the case without diffusion, the exchange of molecules between the cytoplasm and the outside of the cell can be included as $\pm(d_1 u_\mathrm{e} - d_2 u_\mathrm{c})$, where u_c and u_e denote the concentrations of the signaling molecule in- and outside the cell and $d_1, d_2 \in \mathbb{R}_+$ denote the rates of diffusion into and out of the cell. When considering a setting in which diffusion takes place outside single cells, an integral formulation for the net inflow into the cell can be used and an appropriate condition has to be added for the evolution at the cell boundary [104].

The gene regulation processes inside the cell, and thus also the differences and similarities between the bacteria, influence the form of the quorum sensing substance production term $f(u_\mathrm{c})$. A general form for this term, which can be adapted to the degree of polymerization n, is introduced in [104] as

$$f(u_\mathrm{c}) := \alpha + \beta \frac{u_\mathrm{c}^n}{u_\mathrm{thresh} + u_\mathrm{c}^n} - \gamma_\mathrm{c} u_\mathrm{c}.$$

Here the parameter $\alpha \in \mathbb{R}_+$ denotes the basic production rate of the quorum sensing

substance and its increase due to a positive feedback is described by $\beta \in \mathbb{R}_+$. The parameter $u_{\text{thresh}} \in \mathbb{R}_+$ denotes the threshold between low and increased production levels and $\gamma_c \in \mathbb{R}_+$ is the abiotic degradation rate of the quorum sensing substance in the cytoplasm.

2.3. Darcy's law in Hele-Shaw cells

The setting of Hele-Shaw cells resembles the setting of bacterial growth in a laboratory. This is due to the fact that in both cases, displacements in a small layer of the respective substances are considered. The Hele-Shaw cell consists of two immiscible fluids between two parallel (glass) plates with the spacing $h \in \mathbb{R}_+$ between them. In the thin gap the more viscous fluid is displaced by the less viscous one or by air, which is considered as a non-viscous fluid. The point of investigating this scenario is that, while small-scale disturbances are stabilized by surface tension, interface instabilities can occur that lead to fingering patterns. In a lifting Hele-Shaw cell (LHSC) and also when a lower viscosity fluid is injected into the Hele-Shaw cell, these patterns closely resemble the branching patterns observed in bacterial colony growth [133, 134].

In this context, Darcy's law describes the dependence of the velocity $\mathbf{v}$ on the pressure gradient ∇p. The fluid dynamics in the thin gap of a Hele-Shaw cell can be derived from the three-dimensional Navier-Stokes equations via asymptotic analysis to the Darcy's law formulation given by [61, 132]:

$$\mathbf{v} = -\frac{h^2}{12\mu}\nabla p, \qquad \nabla \cdot \mathbf{v} = 0, \tag{2.1}$$

where the parameter $\mu \in \mathbb{R}_+$ denotes the viscosity. The evolution of the boundary depends on the surface tension's stabilizing effect according to the Young-Laplace boundary condition given by $[p] = -\gamma\kappa$, with the surface tension $\gamma \in \mathbb{R}_+$, the curvature of the boundary $\kappa \in \mathbb{R}$ and the pressure jump $[p]$ across the boundary in the direction of the outer normal vector.

2.4. Darcy's law in bacterial biofilm growth

Biofilms are found in many natural, industrial and medical settings. In medical settings, they can be responsible for chronic and possibly lethal infections. Biofilms consist of bacteria, their byproducts and also trapped particles. While laboratory

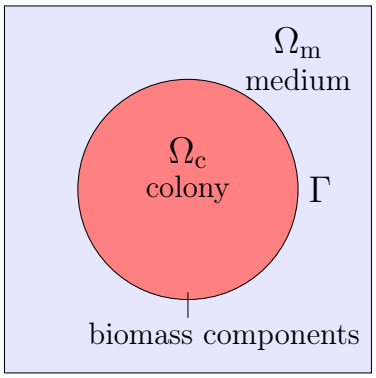

Figure 2.3.: Two-dimensional model setting for biomass growth modeling.

biofilms mostly consist of one single species, in nature several species may be involved, as well as fungi and algae or other microorganisms. The bacteria produce the exopolysaccharide (EPS) component of the extracellular matrix, which holds the colony together [152]. Depending on the biological situation under consideration, there are two main growth scenarios for a bacteria colony: In a liquid environment the bacteria in the biofilm obtain nutrients from all sides, which yields highly heterogeneous growth and possible detachment processes [2, 35, 36, 56, 64]. In a laboratory environment the colony feeds from the nutrient suspension, which leads to growth in height and planar expansion [127].

Bacterial colony growth in a surrounding medium depends on pressure build-up by dividing bacteria and on the surrounding medium density and nutrient concentration. The pressure induced by substrate-limited bacterial division results in the idea to introduce an equation for the pressure, from which the velocity is calculated using Darcy's law [49]. With the growth function of the biofilm denoted by g and Darcy's law given as $\mathbf{v} = -\lambda \nabla p$, in [49] the Poisson equation

$$-\lambda \Delta p = g$$

for the pressure is obtained. While the model in [49] is developed for the situation of biofilm growth into a static aqueous environment, the authors mention similarities to Hele-Shaw flow and bacterial colony pattern formation. Also in the situation of a circular colony as displayed in Figure 2.3, growth is driven by the availability of nutrients in the domain Ω_m outside the colony and biomass growth induces spreading of the population. The applicability of pressure-based models including Darcy's law in the situation of circular bacterial colony growth is further supported by [66, 67], where effects related to chemotaxis are considered.

Biologically the secretion of EPS is important in biofilm formation since the EPS induce osmotic pressure gradients [127]. The resulting biofilm growth, thickening and spreading leads to an increased relative fitness of those colonies which are able to secrete EPS. In the chronology of its evolution, a colony inoculated on an agar plate first thickens, and then starts expanding its base. In *B. subtilis* colonies, an approximately five-fold increase in radius is observed over 24 hours, with significantly slower expansion for EPS mutant colonies [127]. We note that also in multi-component biofilm models Darcy's law-like behavior is observed, for example in [127] for the relative motion of water with respect to the network component.

3. Mathematical background

In the following, we give a short introduction to several mathematical methods which are used in this thesis. We introduce time scale analysis and existing approaches for pattern formation, which are relevant in Part II. Furthermore, we define the necessary function spaces and introduce the appropriate techniques for the finite element simulations in this thesis and give a short introduction to level set methods, which are used in Part III.

3.1. Time scale analysis

Often the aim in biomathematical modeling is to describe several processes which happen on different timescales. A famous example for time scale analysis methods is Michaelis-Menten enzyme kinetics as established by Leonor Michaelis and Maud Menten in 1913 [101] and as described in [105]. Similar observations can be made in many living organisms and the corresponding dynamics differ from those of simple chemical reactions. In an enzyme kinetics process, a substrate is transformed into a product substance by the catalytic effects of enzymes, which form a complex with the substrate. The enzymes are not consumed in the process, but are again available for binding to the substrate after the process is completed. The entire process is often written in the form

$$\mathrm{E} + \mathrm{S} \underset{k_{-1}}{\overset{k_1}{\rightleftharpoons}} \mathrm{SE} \xrightarrow{k_2} E + P,$$

where arrows denote chemical reactions with the corresponding reaction rates indicated above or below. While a double arrow means that the reaction is reversible, this is not the case for a single arrow.

Using the law of mass action, a system of differential equations can be derived from the diagram of the chemical reactions, including differential equations for the enzyme (e), the substrate (s), the complex (c) and the product (p) concentrations. This system is simplified using that there is a constant amount of enzyme in the

system, i.e., $e(t) + c(t) = e_0$. Furthermore, the differential equation for the product concentration $p(t)$ can be omitted for now as it can be directly determined from the concentration of the complex and does not influence the other equations. Thus we obtain a system of two differential equations

$$\begin{aligned}\frac{ds}{dt} &= -k_1 e_0 s + (k_1 s + k_{-1})c,\\ \frac{dc}{dt} &= k_1 e_0 s - (k_1 s + k_{-1} + k_2)c,\end{aligned}$$

with the initial conditions $s(0) = s_0$ and $c(0) = 0$.

This system is then non-dimensionalized to include the relation between the initial values of enzymes and substrate $\varepsilon := \frac{e_0}{s_0}$. In the dimensionless system the new variables $u(\tau) := \frac{s(t)}{s_0}$ and $v(\tau) := \frac{c(t)}{e_0}$ are considered on the timescale $\tau := k_1 e_0 t$ and we obtain

$$\frac{du}{d\tau} = -u + (u + K - \lambda)v, \tag{3.1}$$

$$\frac{dv}{d\tau} = \frac{1}{\varepsilon}\left(u - (u + K)v\right), \tag{3.2}$$

with the initial conditions $u(0) = 1$ and $v(0) = 0$ as well as the constants $\lambda := \frac{k_2}{k_1 s_0}$ and $K := \frac{k_{-1}+k_2}{k_1 s_0}$. When we consider a system in which there is much less enzyme than substrate, we also obtain that $\varepsilon = \frac{e_0}{s_0} \ll 1$ and we can use this to consider the Equations (3.1) and (3.2) on two different timescales. The system as presented above is called the slow system, where Equation (3.1) represents the reference time scale and Equation (3.2) takes place on a much faster timescale since $\frac{1}{\varepsilon} \gg 1$.

When we use another timescale $\hat{\tau} := \frac{\tau}{\varepsilon}$ for the non-dimensionalization, we obtain the fast system

$$\frac{du}{d\hat{\tau}} = \varepsilon\left(-u + (u + K - \lambda)v\right), \tag{3.3}$$

$$\frac{dv}{d\hat{\tau}} = u - (u + K)v. \tag{3.4}$$

Now Equation (3.4) for the fast complex formation represents the reference time scale and the substrate conversion in Equation (3.3) is very slow in comparison.

The slow system in the limit $\varepsilon \to 0$ corresponds to a quasi-steady state assumption since we have that $\varepsilon\frac{dv}{d\tau} \approx 0$. From this we derive a fixed relation between the

concentrations of complexes and substrate $v = \frac{u}{u+K}$ and a differential equation for u of the form

$$\frac{du}{d\tau} = -u + (u + K - \lambda)\frac{u}{u+K} = -u + u - \frac{\lambda}{u+K}u = -\frac{\lambda u}{u+K}.$$

Thus the slow process of substrate to product conversion can now be described using only one single differential equation.

The fast complex formation takes place before the slow substrate conversion process. When considering the fast system in the limit $\varepsilon \to 0$, we obtain that $\frac{du}{d\hat{\tau}} = 0$, i.e., the value of u is constant. Equation (3.4) with the initial value $v(0) = v_0$ can then be solved as

$$v(\hat{\tau}) = v_0 \exp(-(u+K)\hat{\tau}) + \frac{u}{u+K}\left(1 - \exp(-(u+K)\hat{\tau})\right).$$

For $\hat{\tau} \to \infty$ we obtain the limit $\lim_{\hat{\tau}\to\infty} v(\hat{\tau}) = \frac{u}{u+K}$, which reminds us of the result for the relation between u and v obtained from the quasi-steady state assumption for the slow system. Thus we conclude that the fast system describes how the system settles on the slow manifold $v = \frac{u}{u+K}$, where its evolution then follows the slow system dynamics, as depicted in Figure 3.1.

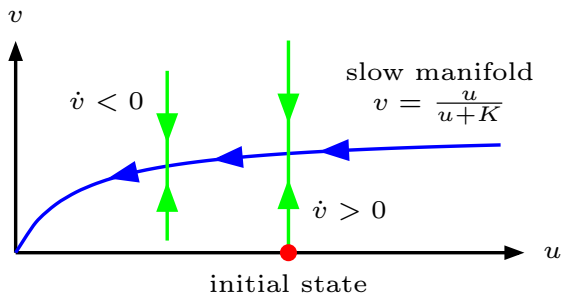

Figure 3.1.: Michaelis-Menten dynamics. Fast system makes the dynamics settle on the slow manifold, where slow system dynamics dominate.

Often one is interested only in the final result of such a process, in our case the rate of product formation $\frac{dp}{dt}$ on the original time scale. Due to the considerations above, it is now much easier to find a closed form expression for this rate. We use our results from the time scale analysis to obtain

$$\frac{dp}{dt} = k_2 c(t) = k_2 e_0 v(\tau) = k_2 e_0 \frac{u(\tau)}{u(\tau) + K} = \frac{k_2 e_0 s(t)}{s(t) + K_m},$$

where $K_m = s_0 K = \frac{k_{-1}+k_2}{k_1}$ is known as the Michaelis-Menten constant and we have obtained a saturated growth equation.

3.2. Pattern formation and bifurcations

Many biological mechanisms in nature generate spatial or temporal patterns. Among these are vital processes in embryology, animal coat pattern formation in zebras, snakes or alligators, as well as bacterial pattern formation. Apart from taking place in very different species, these processes also happen on different scales and serve different purposes. While in animal coat pattern formation, the pattern is formed on the coat of a single animal to protect it from predators or to facilitate hunting in a special environment, in bacterial pattern formation, an entire colony of bacteria participates in the formation of the pattern.

Despite these apparent differences, many biological mechanisms of pattern formation can be united through a similar description in terms of mathematics. The typical tool for this task are systems of reaction-diffusion equations, which describe the spatio-temporal evolution of the concentrations of the substances involved in the pattern formation process. Each of these equations typically includes a diffusion term, which may be standard Fickian diffusion, porous medium diffusion or also related diffusion mechanisms. The equations are then completed by their reaction components, which describe the interactions between the different substances.

In the case of Fickian diffusion, the system is of the form

$$\frac{\partial \mathbf{c}}{\partial t} = D\,\Delta \mathbf{c} + \mathbf{f}(\mathbf{c}),$$

where $\mathbf{c} = (c_1, \ldots, c_n)^T \in \mathbb{R}^n_+$ is the vector of the concentrations of the chemical substances and bifurcations rely on the behavior of the eigenvalues of the system.

Three principal types of instabilities in reaction-diffusion systems of this form are Turing, Hopf and wave instabilities. While Turing bifurcations yield patterns that are spatially periodic and stationary in time, Hopf bifurcations lead to spatially homogeneous patterns that are oscillatory in time and wave bifurcations produce patterns that are both spatially periodic and oscillatory in time [71, 149]. The most famous mechanism for the mathematical description of biological pattern formation in the case of constant diffusion coefficients is the Turing mechanism, which was

discovered by Turing in 1952 [141] and has been investigated since then in great detail, e.g., [88, 90, 92]. Furthermore, investigations of Turing pattern formation for inhomogeneities, e.g., [18, 91, 112, 113], and growing domains, e.g., [38, 39], have been performed. Here we follow the description of Turing pattern formation in [106].

In general, diffusion is considered to have a stabilizing effect on a system of differential equations. However, for the principle of Turing pattern formation the opposite is the case: Turing pattern formation takes place when a uniform steady state which is linearly stable in the absence of diffusion looses its spatial stability in the presence of diffusion. This process is called diffusion-driven instability and generates spatially inhomogeneous patterns. It has to involve at least two different substances with different diffusion constants $D_A \neq D_I$, where often the substance A is called the activator and the substance I is called the inhibitor. The corresponding nonlinear reaction terms are denoted by $F(A, I)$ and $G(A, I)$. Then the entire system reads

$$\begin{aligned} \frac{\partial A}{\partial t} &= D_A \Delta A + F(A, I), \\ \frac{\partial I}{\partial t} &= D_I \Delta I + G(A, I). \end{aligned}$$

For the diffusion-driven instability we take $d := \frac{D_I}{D_A} \in \mathbb{R}_+$ and consider the system of reaction-diffusion equations in its non-dimensional form

$$\frac{\partial u}{\partial t} = \Delta u + \gamma f(u, v), \tag{3.5}$$

$$\frac{\partial v}{\partial t} = d\,\Delta v + \gamma g(u, v), \tag{3.6}$$

where the parameter $\gamma \in \mathbb{R}_+$ results from the inclusion of a typical length scale in the non-dimensionalization of the original system and thus represents the size of the considered domain. These equations are accompanied by the homogeneous Neumann boundary condition

$$(\mathbf{n} \cdot \nabla) \begin{pmatrix} u \\ v \end{pmatrix} = 0 \qquad \text{on } \partial\Omega$$

with the outward unit normal vector $\mathbf{n}$ to the domain boundary $\partial\Omega$ and appropriate initial conditions $u(\mathbf{x}, 0)$ and $v(\mathbf{x}, 0)$.

The two-dimensional system without diffusion reads

$$\frac{du}{dt} = \gamma f(u,v), \qquad \frac{dv}{dt} = \gamma g(u,v),$$

and thus the spatially homogeneous steady state (u_0, v_0) can be determined as the positive solution to the condition $f(u,v) = g(u,v) = 0$. In order to investigate the stability, we linearize around the steady state (u_0, v_0) to obtain

$$\mathbf{w} = \begin{pmatrix} u - u_0 \\ v - v_0 \end{pmatrix}$$

and thus for $|\mathbf{w}|$ small, we have that

$$\mathbf{w}_t = \gamma A \mathbf{w}, \qquad \text{where} \qquad A = \begin{pmatrix} f_u & f_v \\ g_u & g_v \end{pmatrix}_{(u_0,v_0)}, \tag{3.7}$$

with the Jacobi matrix A. We look for solutions $\mathbf{w} \propto e^{\lambda t}$ in order to investigate how the spatial derivation from the equilibrium (u_0, v_0) evolves in time. Then the eigenvalues λ determine the stability behavior of the noise. Eigenvalues with $\Re(\lambda) < 0$ at the steady state $\mathbf{w} = 0$ mean that the steady state is linearly stable and the perturbations decay to zero as $t \to \infty$.

When we substitute the form of the solutions into Equation (3.7), we obtain from $\det(\gamma A - \lambda I) = 0$ that the characteristic equation reads

$$\lambda^2 - \gamma \underbrace{(f_u + g_v)}_{=\mathrm{tr}(A)} \lambda + \gamma^2 \underbrace{(f_u g_v - f_v g_u)}_{=\det(A)} = 0.$$

The eigenvalues λ_1 and λ_2 are calculated as

$$\lambda_{1/2} = \frac{1}{2}\gamma \left[\mathrm{tr}(A) \pm \left\{ \mathrm{tr}(A)^2 - 4\det(A) \right\}^{1/2} \right]$$

and $\Re(\lambda) < 0$ if

$$\mathrm{tr}(A) = f_u + g_v < 0 \qquad \text{and} \qquad \det(A) = f_u g_v - f_v g_u > 0, \tag{3.8}$$

which needs to be satisfied in order for the homogeneous stationary state without diffusion to be linearly stable. Therefore (3.8) imposes restrictions on the parameter range.

In the restricted parameter range we then analyze the full system of Equations (3.5)–(3.6) by linearizing about the steady state $\mathbf{w} = 0$, which gives

$$\mathbf{w}_t = D\,\Delta\mathbf{w} + \gamma A\mathbf{w}, \qquad \text{where} \qquad D = \begin{pmatrix} 1 & 0 \\ 0 & d \end{pmatrix}. \tag{3.9}$$

For the problem with diffusion we search for the roots λ of the characteristic polynomial

$$\det(\lambda I - \gamma A + Dk^2) = 0, \tag{3.10}$$

which depends on the wavenumber k. Furthermore, we define $\mathbf{W}(\mathbf{r})$ to be the time-independent solution of the spatial eigenvalue problem

$$\Delta\mathbf{W} + k^2\mathbf{W} = 0, \qquad (\mathbf{n}\cdot\nabla)\mathbf{W} = 0 \text{ on } \partial\Omega. \tag{3.11}$$

For example, if we consider a one-dimensional domain $\Omega = (0, p)$ where $p > 0$, with zero flux boundary conditions, then $\mathbf{W} \propto \cos\left(\frac{n\pi x}{p}\right)$, where n is an integer. With the wavenumber $k = \frac{n\pi}{p}$, we define the wavelength as $\omega = \frac{2\pi}{k} = \frac{2p}{n}$.

In a finite domain there is a discrete set of possible wavenumbers since n is an integer. Since the problem is linear, the solutions are of the form

$$\mathbf{w}(\mathbf{r}, t) = \sum_k c_k e^{\lambda t}\mathbf{W}_k(\mathbf{r}).$$

Here $\mathbf{W}_k(\mathbf{r})$ denotes the solution of (3.11) corresponding to k, λ denotes the eigenvalue for temporal growth and the coefficients c_k are determined by a Fourier expansion of the initial conditions in terms of $\mathbf{W}_k(\mathbf{r})$. Then Equation (3.10) follows by substituting $\mathbf{w}(\mathbf{r}, t)$ into Equation (3.9) and using (3.11).

From Equation (3.10) it follows that

$$\lambda^2 + \lambda\left[k^2(1+d) - \gamma(f_u + g_v)\right] + h(k^2) = 0, \tag{3.12}$$

where $h(k^2) := d\,k^4 - \gamma(d\,f_u + g_v)k^2 + \gamma^2\det(A)$. We now have to find λ such that $\Re(\lambda(k)) > 0$ for some $k = k_T \neq 0$ for the diffusion-driven instability. We calculate the dispersion relation $\lambda = \lambda(k)$ as

$$2\lambda = -\left[k^2(1+d) - \gamma(f_u + g_v)\right] \pm \sqrt{\left[k^2(1+d) - \gamma(f_u + g_v)\right]^2 - 4h(k^2)}. \tag{3.13}$$

Thus $\Re(\lambda(k)) > 0$ can be obtained if $h(k^2)$ or the coefficient of λ in Equation (3.12) are negative. However, due to the constraints in the case without diffusion, the coefficient of λ is greater than zero and thus we need $h(k^2) < 0$. Since from Equation (3.8) we know that $\det(A) > 0$, we find the additional condition

$$d\, f_u + g_v > 0 \Rightarrow d \neq 1. \tag{3.14}$$

Furthermore, in order to be able to achieve that $h(k^2) < 0$ for some nonzero k_T with $k_1^2 < k_T^2 < k_2^2$, we need the minimum $h_{\min} = \gamma^2 \left[\det(A) - \frac{(df_u+g_v)^2}{4d}\right]$ to be smaller than zero and therefore we obtain the condition

$$(df_u + g_v)^2 - 4d \det(A) > 0. \tag{3.15}$$

Thus we can state the following theorem [106]:

Theorem 3.2.1. *(Turing bifurcations)*
Let the matrix A satisfy $f_u + g_v < 0$ and $f_u g_v - f_v g_u > 0$. Let furthermore $d > 0$, $d \neq 1$ and $df_u + g_v > 0$. Then there are diagonal matrices D as introduced in (3.9), such that for certain k^2, the matrix $\gamma A - k^2 D$ has eigenvalues with positive real part if d satisfies

$$(d\, f_u + g_v)^2 > 4\, d \det(A).$$

Let us assume that $f_u > 0$ and $g_v < 0$. Then from the first condition in (3.8) and from (3.14), it follows that $d > 1$, which means that the inhibitor diffuses faster than the activator. The critical wavenumber, at which $h_{\min} = 0$, is determined from $k_c^2 = \gamma \left(\frac{\det(A)}{d_c}\right)^{1/2}$. For $d > d_c$ a band of unstable wavenumbers k appears, which represents a saddle-node bifurcation. Then the Turing solutions are of the form

$$\mathbf{w}(\mathbf{r}, t) \sim \sum_{k_1}^{k_2} c_k e^{\lambda(k^2)t} \mathbf{W}_k(\mathbf{r}) \qquad \text{for large } t,$$

since their behavior is determined by the eigenvalues with $\Re(\lambda(k)) > 0$. The conditions (3.8) and (3.14)–(3.15) evaluated at the spatially homogeneous stationary state (u_0, v_0) thus determine if a Turing pattern is formed. We can determine the relevant discrete wavenumbers k, and thus also the relevant eigenfunctions, on a finite domain, which tell us which spatial patterns are the ones that establish

(a) Pattern for $(n_s, D) = (1, 0.2)$. (b) No pattern for $(n_s, D) = (1, 3)$.

Figure 3.2.: Turing pattern simulations for Equations (5.1)–(5.2) with standard diffusion and parameters as in Figure 5.1. The initial nutrient concentration is $n_s = 1$ and D denotes the relation between the bacterial and nutrient diffusion coefficients.

themselves. The relevant band of unstable wavenumbers, in which the dispersion relation is positive, is given as

$$\begin{aligned} k_1^2 &= \frac{\gamma}{2d}\left[(d\,f_u + g_v) - ((d\,f_u + g_v)^2 - 4d\det(A))^{1/2}\right] < k^2 \\ &< \frac{\gamma}{2d}\left[(d\,f_u + g_v) + ((d\,f_u + g_v)^2 - 4d\det(A))^{1/2}\right] = k_2^2. \end{aligned}$$

Depending on the geometry of the domain, the eigenfunctions are determined analytically or numerically [106]. As seen above, Turing bifurcations happen when $h(k^2)$ becomes negative. For $h(k^2) = 0$ the linearization has a vanishing eigenvalue at the bifurcation point, i.e., $\Re(\lambda) = 0$ and $\Im(\lambda) = 0$, due to Equation (3.13). Bifurcation analysis can be performed for each system parameter found in one of the conditions (3.8), (3.14) and (3.15). As an example of such a bifurcation analysis, we perform a detailed Turing analysis in Chapter 5. This stability analysis is used to obtain the pattern formation results depicted in Figure 3.2, where standard diffusion simulations for two parameter sets are displayed on a rectangular domain.

3.3. Pattern formation for nutrient-dependent bacterial diffusion

In several papers on bacterial colony pattern formation such as [14, 98, 99, 102], computationally derived bifurcation diagrams are presented, but the conditions for instability are not derived in a formal way. The models in [98, 99, 102] consider the bacterium *B. subtilis*, where five main morphological patterns are observed: The diffusion-limited aggregation, the Eden, the concentric ring, the disk and the

dense branching morphology patterns. Some of these patterns, but not all of them at once, are achieved in the numerical simulations of the models. We will see in Part II that our detailed reaction-diffusion system is able to reproduce the whole spectrum of different pattern types at once. The corresponding simulation results are depicted in Figure 4.20 of Section 4.6.3.

The models in [82, 84, 98] vary in the number of equations considered. Apart from the concentrations of nutrients n and bacteria b, which are always included, sometimes also two separate bacteria concentrations of replicative and non-replicative bacteria are considered [98]. For the bacteria diffusion coefficient, both density-dependent terms of the form $\nabla\cdot(b\nabla b)$ [84] and terms of the mixed form $\nabla\cdot((1+\omega(\mathrm{x}))nb\nabla b)$ [82] are found. Further aspects are addressed in the papers by Ben-Jacob et al. [12, 13, 14], where it is assumed that the bacteria produce a wetting layer of fluid that leads to a diffusion term of the form $\nabla\cdot(l^{\gamma}\nabla b)$ with the exponent $\gamma\in\mathbb{R}_+$ [14]. Here l denotes the height of the lubrication layer in which the bacteria swim and the influence of chemotaxis on branching and chiral patterns is considered [13, 14]. In [12], a connection between bacterial pattern formation and Hele-Shaw cell modeling including surface tension is established.

Following the idea of [82], in this thesis we consider a bacterial diffusion coefficient which is dependent on both the nutrient and the bacteria densities. This form is due to the observation that bacterial movement is impeded if $b=0$ or $n=0$. Thus we have a diffusion term of the form $\nabla\cdot(\sigma nb\nabla b)$, which leads to a system related to the simple form

$$\frac{\partial b}{\partial t}=\nabla\cdot(\sigma nb\nabla b)+\varepsilon f(n,b), \tag{3.16}$$

$$\frac{\partial n}{\partial t}=\Delta n-f(n,b), \tag{3.17}$$

where possible approaches for $f(n,b)$ are a term of the form $f(n,b)=nb$ or a type II term of the form $f(n,b)=\frac{nb}{1+\gamma n}$.

Another possible approach [73] to determine when bacterial pattern formation takes place is to consider existence and uniqueness in the sense of weak solutions to a model with a bacterial diffusion term of the form $\nabla\cdot(d_b n^{\beta}b^{\alpha}\nabla b)$ with $d_b\in\mathbb{R}_+$ and the exponents $\alpha,\beta\in\mathbb{R}_+$ in the domain $\Omega\subset\mathbb{R}^2$ [73]. Here assumptions on the reaction terms as well as on the regularity of the initial data guarantee existence and uniqueness of the solutions in the weak sense. A crucial assumption is the

simplified subcritical growth assumption, which reads [73]

$$c+1 \leq \frac{2+\alpha}{1+\frac{\beta}{a}}$$

in the two-dimensional case for a reaction term of the form $f(n,b) = \frac{b^{c+1}n^{1+a}}{1+\gamma n^{1+a}}$ with $a \in \mathbb{R}_+$, $c \in \mathbb{R}_+^0$. Under several assumptions, which include the subcritical growth assumption, it is shown in [73] that the solutions exhibit no blowup in finite time, which means that they exist globally and are bounded in finite time. The corresponding numerical simulations show circular growth of the bacterial colony. If the condition is violated, finger-like patterns with and without blowups are observed.

However, for Equations (3.16)–(3.17) it holds that $\alpha = \beta = 1$. Furthermore, the type II reaction term introduced above corresponds to $a = c = 0$ and is not admissible. Another assumption in [73] is the assumption $\beta \geq 2$, which is not met here and thus the main theorem of the paper cannot be applied to the case $\nabla \cdot (\sigma n b \nabla b)$.

In the following, we look for a different way to analyze the onset of pattern formation, investigating closely the dependence of fingering patterns on the strength of the bacterial diffusion for the bacterial diffusion term $\nabla \cdot (\sigma n b \nabla b)$. We aim to take into account the special geometry of an initially circular bacterial colony, where the instability develops from the front between the bacteria and the agar solution in the domain [102, 103]. As we will see in Part II, the evolution of the instabilities from the moving front can be investigated analytically by a front instability approach.

3.4. Instabilities arising from front propagation

The principle of instabilities arising from front propagation is observed in several physical settings such as Hele-Shaw cells or solidification processes. In addition, several instabilities arise indirectly from the presence of interfaces such as the Rayleigh-Bénard convection instability, which develops in flat liquid layers heated from below and the Taylor-Couette instability, which is found where a viscous fluid moves between two rotating cylinders [138]. This motivates us to investigate models derived from the physical processes involved in colony growth in Part III.

The instability responsible for viscous fingering processes in a Hele-Shaw cell is the Saffman-Taylor instability [11, 121]. The higher the velocity and the lower the surface tension, the more unstable or chaotic behavior is observed at the

interface [16]. A measure that is used in experimental studies to determine if the flat interface is unstable is the parameter $\frac{1}{B}$ as defined below. The interface is considered unstable if

$$\frac{1}{B} := 12\frac{\mu V}{T}(\frac{w}{b})^2 > (2\pi)^2,$$

where V denotes the velocity of the interface, T the interfacial tension, μ the viscosity, w the width of the cell and b the plate spacing in the Hele-Shaw cell [137]. It is observed that fingers become unstable at large values of $1/B$ and small values yield a semicircular interface [137]. Some mechano-chemical models, which combine mechanical modeling with reaction-diffusion equations, have been introduced in [41, 42, 131] for skin morphogenesis.

3.5. Finite element methods

Finite element methods rely on the weak (or variational) formulation of a problem under investigation in appropriate function spaces [22]. In the weak formulation, well-behaved test functions are introduced and an integral formulation is considered, where derivatives can be shifted to the test functions by partial integration. For the discrete numerical procedure the problem is then solved on a finite-dimensional subspace of solutions. On the two-dimensional domain under investigation, a mesh of triangles or rectangles (quadrilaterals) is generated.

First let us introduce the necessary function spaces [22, 24, 60]. Let in the following $\Omega \subset \mathbb{R}^2$ denote the bounded Lipschitz domain under investigation with the boundary $\partial\Omega$. Then the Lebesgue spaces of integrable functions over Ω for $1 \leq p < \infty$ are defined as

$$L^p(\Omega) := \begin{cases} \left\{u\colon \Omega \to \mathbb{R} : \int_\Omega |u|^p \, d\mathbf{x} < \infty\right\}, & p < \infty \\ \left\{u\colon \Omega \to \mathbb{R} : \text{ess sup}\{|u(\mathbf{x})|, \mathbf{x} \in \Omega\} < \infty\right\}, & p = \infty \end{cases},$$

where $\text{ess sup}\{|u(\mathbf{x})|, \mathbf{x} \in \Omega\} = \inf_{A\subset\Omega, \mu(A)=0} \sup_{\mathbf{x}\in\Omega\setminus A} |u(\mathbf{x})|$ with the Lebesgue measure $\mu(A)$ of A. If a function is locally integrable, it belongs to the space

$$L^1_{\text{loc}} := \{u : u \in L^1(K),\, K \subset \Omega \text{ compact}\},$$

which is of special importance for the definition of the weak derivative of a function. In two dimensions, let α be a multiindex $\alpha = (\alpha_1, \alpha_2)$ of order $|\alpha| = \alpha_1 + \alpha_2 = k$.

Then for $\mathbf{x} = (x, y)^T$ we define the α-th partial derivative of a function as

$$D^\alpha u(\mathbf{x}) := \frac{\partial^{|\alpha|} u(\mathbf{x})}{\partial^{\alpha_1} x \, \partial^{\alpha_2} y}.$$

For $u, v \in L^1_{loc}$ we define the α-th weak derivative of u, i.e., $D^\alpha u = v$, as the function v that satisfies

$$\int_\Omega u D^\alpha \phi \, d\mathbf{x} = (-1)^{|\alpha|} \int_\Omega v\phi \, d\mathbf{x} \qquad \forall \phi \in C_c^\infty(\Omega),$$

where $C_c^\infty(\Omega)$ denotes the space of infinitely differentiable functions with compact support. If a function v is a derivative of u in the classical sense, it is also a weak derivative of u.

The spaces of the functions that are locally integrable and for which the weak derivatives for all multiindices up to order k exist and belong to $L^p(\Omega)$ are called Sobolev spaces

$$W^{k,p}(\Omega) := \{u \in L^1_{loc} : D^\alpha u \in L^p(\Omega), |\alpha| \leq k\}.$$

The case $p = 2$ stands out, as in this case the norm on the Sobolev space induces a natural inner product. The resulting spaces are the Hilbert spaces denoted by $H^k(\Omega) := W^{k,2}(\Omega)$.

Now we can introduce the variational formulation for a boundary value problem on $\Omega \subset \mathbb{R}^2$ given as

$$-\nabla \cdot (A(\mathbf{x})\nabla u) = f \text{ in } \Omega, \qquad u = 0 \text{ on } \partial\Omega,$$

for $A(\mathbf{x}) \in \mathbb{R}^{2\times 2}$ symmetric and uniformly positive definite, i.e., $A(\mathbf{x}) \geq \alpha_0 I$ for some $\alpha_0 \in \mathbb{R}_+$, and f sufficiently smooth. The continuous variational problem can then be restated in the weak form as:
Find the solution $u \in V := H^1(\Omega)$ such that

$$a(u, v) = l(v) \qquad \forall v \in V,$$

where v are the test functions and $a(u, v) := \int_\Omega A\nabla u \cdot \nabla v \, d\mathbf{x}$ and $l(v) := \int_\Omega fv \, d\mathbf{x}$ denote the bilinear form and the linear form, respectively.

The theorem of Lax-Milgram yields the existence and uniqueness of a solution to the problem in the weak form and reads [22, 24, 34]:

Theorem 3.5.1. *(Lax-Milgram)*
Let V be a Hilbert space, $a : V \times V \to \mathbb{R}$ a continuous coercive bilinear form with

$$|a(u,v)| \leq c_1||u||_V||v||_V \qquad \textit{and} \qquad |a(u,u)| \geq c_2||u||_V^2$$

for $u, v \in V$ and positive constants c_1, c_2 and l a continuous linear functional. Then it exists a unique $u \in V$ such that

$$a(u,v) = l(v) \qquad \forall v \in V.$$

For time-dependent problems, the derivative with respect to time has to be discretized using an adequate scheme. Such a scheme can be the explicit or the implicit Euler scheme or the Crank-Nicolson scheme.

We look for the solution in the standard finite element space of continuous piecewise polynomials of degree k called $V_h^k \subset V$, where

$$V_h^k := \{v_h \in H^1(\Omega) : v_h|_T \in \mathbb{P}_k(T),\, T \in \mathcal{T}_h\}.$$

Here $(\mathcal{T}_h)_{h>0}$ denotes the family of triangular meshes obtained through uniformly refining a conform triangulation of the domain Ω. The accuracy of the discrete solution u_h depends on the degree k of the piecewise polynomials contained in the approximation space as well as on the mesh size h. In the following, we use linear polynomials and denote $V_h := V_h^1$ for ease of notation.

In this case the discrete variational problem reads:
Find the solution $u_h \in V_h$ such that

$$a(u_h, v_h) = l(v_h) \qquad \forall v_h \in V_h.$$

If the set $\{\psi_1, \ldots, \psi_N\}$ describes a basis of V_h, we rewrite the above variational problem in terms of the basis of V_h and obtain the system of equations

$$\sum_{j=1}^{N} a(\psi_j, \psi_i) z_j = l(\psi_i), \qquad i = 1, \ldots, N,$$

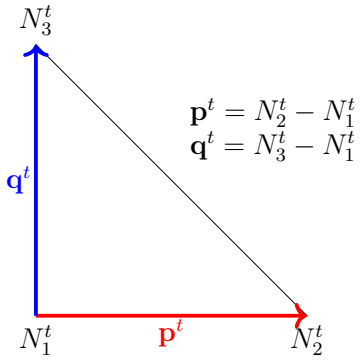

Figure 3.3.: Triangular finite element $T_t \in \mathcal{T}_h$ with three nodes N_i^t, $i = 1, 2, 3$.

using that $u_h = \sum_{j=1}^{N} z_j \psi_j$. This means that it is enough to consider the problem in terms of the basis functions. If the bilinear form is given as $a(u, v) = \int_\Omega \nabla u \cdot \nabla v \, d\mathbf{x}$ and the linear form is given as $l(v) = \int_\Omega f v \, d\mathbf{x}$, the corresponding system of equations can be written in matrix-vector form as $S\mathbf{z} = \mathbf{b}$. Here S denotes the stiffness matrix, which is given as $S = (\int_\Omega \nabla\psi_i(\mathbf{x})\nabla\psi_j(\mathbf{x}) \, d\mathbf{x})_{ij}$, and $\mathbf{b} = (\int_\Omega f\psi_i \, d\mathbf{x})_i$ denotes the right-hand side load vector. Then the integration for the weak problem is performed using routines for the expressions of the basis functions.

The size of these expressions depends on the number of nodes considered, as for linear polynomials each basis function can be chosen to correspond to one node [22]. For N nodes the matrix for a scalar problem has the size $N \times N$ and the load vector is of size $N \times 1$. Let us consider a single triangle T_t with the nodes $N_i^t = (x_i^t, y_i^t)$, $i = 1, 2, 3$ and the corresponding linear non-zero hat functions

$$\psi_i^t = \frac{1}{2|T_t|}(a_i^t + b_i^t x + c_i^t y), \qquad i = 1, 2, 3.$$

Then the weights a_i^t, b_i^t and c_i^t are chosen as

$$\begin{aligned}
a_1^t &= x_2^t y_3^t - x_3^t y_2^t, & b_1^t &= y_2^t - y_3^t, & c_1^t &= x_3^t - x_2^t, \\
a_2^t &= x_3^t y_1^t - x_1^t y_3^t, & b_2^t &= y_3^t - y_1^t, & c_2^t &= x_1^t - x_3^t, \\
a_3^t &= x_1^t y_2^t - x_2^t y_1^t, & b_3^t &= y_1^t - y_2^t, & c_3^t &= x_2^t - x_1^t,
\end{aligned}$$

such that we have $\psi_i^t(N_j^t) = \delta_{ij}$ for $i, j = 1, 2, 3$. This is due to the fact that the area of the triangle T_t can be described as

$$|T_t| = \frac{1}{2}\left|\det\begin{pmatrix} p_x^t & q_x^t \\ p_y^t & q_y^t \end{pmatrix}\right|$$

with the vectors $\mathbf{p}^t = (p_x^t, p_y^t)^T$ and $\mathbf{q}^t = (q_x^t, q_y^t)^T$ as depicted in Figure 3.3. For the gradients we obtain

$$\nabla \psi_i^t = \frac{1}{2|T_t|} \begin{pmatrix} b_i^t \\ c_i^t \end{pmatrix},$$

and thus, from the three non-zero hat functions, the triangle T_t contributes nine integral terms to the stiffness matrix S. Large calculations can be simplified when performed on a reference element, which is most often defined as the triangle with the vertices $(0,0)$, $(1,0)$ and $(0,1)$, where the linear basis functions are chosen as

$$\psi_1 := x, \qquad \psi_2 := y \qquad \text{and} \qquad \psi_3 := 1 - x - y.$$

Then an affine transformation is used to bijectively map the vertices of a triangle T_t onto those of the reference triangle.

3.6. Level set methods

Level set methods offer an elegant way to track the motion of an interface. In the following, we introduce the level set method in two dimensions following the approach as stated in [130] and shortly discuss the theoretical and computational advantages of the approach.

Let now the speed of propagation of a curve in normal direction be defined as $F = F(L, G, I)$, depending on the local (L), the global (G) and the independent (I) properties of the curve. Then we distinguish between the boundary value and the initial value level set formulations. The boundary value formulation is appropriate whenever the curve will not pass a point $\mathbf{x} \in \mathbb{R}^2$ twice, i.e., $F > 0$ always holds. In this approach, the position of the front can be characterized using the arrival time $T(\mathbf{x})$ at a point $\mathbf{x}$ as

$$|\nabla T| F = 1$$

since ∇T is orthogonal to the T level sets and its magnitude is inversely proportional to the speed T. It also holds that $T = 0$ on Γ, the initial location of the interface and the front Γ is in general given as $\Gamma(t) = \{\mathbf{x} : T(\mathbf{x}) = t\}$. The front motion can thus be described as a boundary value problem.

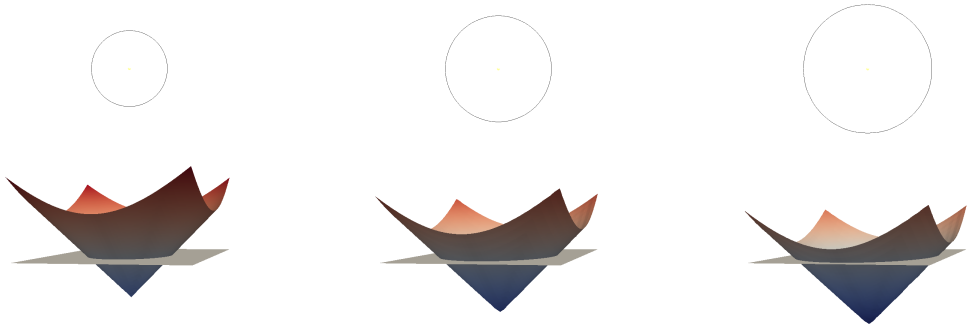

(a) $k = 0$. (b) $k = 200$. (c) $k = 350$.

Figure 3.4.: Three-dimensional level set cone simulation of the constant velocity expansion of a two-dimensional circle in time on a quadratic domain. Time step increasing from left to right.

If the speed F is not strictly positive or negative, we cannot use the boundary value formulation, but need to use the initial value formulation, which can be stated as follows:
We define the higher-dimensional function ϕ and define the front as the position of its zero level set

$$\phi(\mathbf{x}(t), t) = 0, \tag{3.18}$$

i.e., $\Gamma(t) = \{\mathbf{x} : \phi(\mathbf{x}, t) = 0\}$. Applying the chain rule to Equation (3.18) gives

$$\phi_t + \nabla\phi(\mathbf{x}(t), t) \cdot \mathbf{x}_t = 0,$$

which can be reformulated, using that $F = \mathbf{x}_t \cdot \mathbf{n}$ with $\mathbf{n} = \frac{\nabla\phi}{|\nabla\phi|}$, as

$$\phi_t + F|\nabla\phi| = 0,$$

when $\phi(\mathbf{x}, t = 0)$ is given.

A straight-forward example for the extension of the problem by one dimension is a circle, whose radius grows. As depicted in Figure 3.4, starting from a circle in the two-dimensional plane, as time progresses the growing circle forms a descending cone in $(\mathbf{x}, t)$ coordinates. At a fixed time we consider cross sections through this cone corresponding to the position of the circle in $\mathbf{x}$-coordinates at the fixed time. Numerically, level set methods are often considered in the context of finite difference methods, e.g., [130, 136], but also finite element approaches are available, e.g., [52,

69, 107]. Both presented schemes allow for explicit implementations, which can be made more efficient by the use of adaptive strategies. Furthermore, the normal direction of the moving front is easily calculated as

$$\mathbf{n} = \frac{\nabla T}{|\nabla T|} \qquad \text{or} \qquad \mathbf{n} = \frac{\nabla \phi}{|\nabla \phi|},$$

and the curvature as

$$\kappa = \nabla \cdot \frac{\nabla T}{|\nabla T|} \qquad \text{or} \qquad \kappa = \nabla \cdot \frac{\nabla \phi}{|\nabla \phi|},$$

respectively. While the initial value approach is suitable whenever the speed function F can be negative and positive, the boundary value approach is advantageous since it requires no time step and hence does not need to fulfill the Courant-Friedrichs-Lewy (CFL) stability conditions [130].

Part II.

Modeling with reaction-diffusion equations

4. Detailed system of reaction-diffusion equations for *Staphylococcus aureus*

Systems of reaction-diffusion equations, such as the ones introduced in [14, 82, 84, 99, 102], represent the standard approach for the study of bacterial pattern formation. While these models include partial differential equations for the nutrients as well as subgroups of the bacteria population, they do not take into account the roles of the bacterial biofilm and quorum sensing in pattern formation. Since biological evidence [37, 100, 127, 151] points towards an important role of these factors in bacterial colony growth, and consequently also in bacterial pattern formation, their roles are in the following considered more closely for the bacterium *S. aureus*.

This chapter contains results included in the submitted publication "A beautiful human pathogen: *Staphylococcus aureus*" [109] by the author with T. Horger and C. Kuttler and in the submitted publication "From *Staphylococcus aureus* gene regulation to its pattern formation" [110] by the author with T. Horger and C. Kuttler.

4.1. Model setting

In the following, we extend an existing modeling approach [65] for pattern formation in *S. aureus*, which is similar to the approaches in [98, 102]. We concentrate on the effects of gene regulation systems and derive terms for the development of the biofilm and quorum sensing substance concentrations, which are vital factors in bacterial colony growth [50, 65, 151] and thus in pattern formation. So far the system in [65] includes equations for the nutrient concentration, the replicative and the non-replicative bacteria densities and the concentration of the quorum sensing substance, which are denoted by the variables n for the nutrient concentration, the variables b and s for the densities of replicative and non-replicative bacteria and

the variable q for the quorum sensing substance, respectively. However, in [65] the evolution of the quorum sensing substance is considered in a generic way. The system in [65] is of the form

$$\frac{\partial n}{\partial t} = d_n \Delta n - G_1\, g_1(n,b)\, g_2(q), \tag{4.1}$$
$$\frac{\partial b}{\partial t} = \nabla \cdot (D_2(n,b)\nabla b) + G_2\, g_1(n,b)\, g_2(q) - a(n,b), \tag{4.2}$$
$$\frac{\partial s}{\partial t} = \nabla \cdot (D_3(b)\nabla s) + a(n,b),, \tag{4.3}$$
$$\frac{\partial q}{\partial t} = d_q \Delta q + f_2(b,q), \tag{4.4}$$

where the diffusion rates are given as

$$D_2(n,b) := \sigma n b \qquad \text{and} \qquad D_3(b) := \tau \frac{b}{b+b_s}$$

with the parameters $\sigma, \tau, b_s \in \mathbb{R}_+$. The term $D_3(b)$ represents the movement of the non-replicative bacteria, which is assumed to be a result of the non-replicative bacteria being pushed by the replicative ones. If the concentration of replicative bacteria $b(\mathbf{x},t)$ is zero, this diffusion coefficient is zero as well. The replicative bacteria growth term $g_1(n,b) := \frac{nb}{1+\gamma n}$ for $\gamma \in \mathbb{R}_+^0$ and the term

$$a(n,b) := \varepsilon \frac{b}{(1+\frac{b}{a_1})(1+\frac{n}{a_2})} \tag{4.5}$$

as well as the bacterial diffusion term $\nabla \cdot (\sigma n b \nabla b)$ in [65] are chosen according to [102], [98] and [82], respectively. Here and in the following, we assume all parameters to be non-negative as customary for the modeling of biological systems.

The complete replicative bacteria growth term $f_1(n,b,q)$ in [65] is of the form

$$f_1(n,b,q) := g_1(n,b)g_2(q) = \frac{nb}{1+\gamma n}\left(1 + \frac{1}{q_{\mathrm{m}} + \delta q}\right), \tag{4.6}$$

where $g_1(n,b) = \frac{nb}{1+\gamma n}$ as above and $g_2(q)$ is defined as $g_2(q) := 1 + \frac{1}{q_{\mathrm{m}}+\delta q}$. While the first factor $g_1(n,b)$ represents a Holling type II response term for the limited consumption of nutrients by the bacteria, the second factor $g_2(q)$ is chosen to account for the decrease of nutrient consumption with an increasing concentration of the quorum sensing substance concentration q. In [65] the quorum sensing substance concentration is modeled using standard diffusion, which is adequate due to the

small size of the molecules, and a generic quorum sensing term [59, 104] of the form

$$f_2(b,q) := \left(\alpha + \beta \frac{q^2}{q_{thr}^2 + q^2}\right) b - \mu_q q.$$

This term shows that there is always a basic production of the quorum sensing substance by the bacteria and that the production of the quorum sensing substance is subject to a positive feedback loop, where an increased quorum sensing concentration leads to a further increase of the production. Furthermore, the last term in $f_2(b,q)$ represents the decay rate of the substance.

Our aim for the modeling in the following sections is to obtain a quorum sensing reaction term, which is derived directly from the regulation processes in *S. aureus* bacteria and which is thus specific for this bacterium, instead of using a generic term. Furthermore, we include a new equation for the concentration of biofilm substance in the system, since biofilm is an important factor in bacteria colony growth. We also include the effects of biofilm and quorum sensing substance as we replace the diffusion coefficients d_n and $D_2(n,b)$ by newly derived coefficients $D_1(f)$ and $D_2(n,b,q)$. The spatial spread of biofilm and quorum sensing signaling molecules is assumed to be sufficiently well described by standard diffusion. For the reaction terms in the equations for the nutrient concentration, the replicative and the non-replicative bacteria densities, we use the terms introduced in [65]. Thus, the new extended system consists of five equations and is of the form

$$\frac{\partial n}{\partial t} = \nabla \cdot (D_1(f)\nabla n) - G_1\, f_1(n,b,q), \tag{4.7}$$

$$\frac{\partial b}{\partial t} = \nabla \cdot (D_2(n,b,q)\nabla b) + G_2\, f_1(n,b,q) - a(n,b), \tag{4.8}$$

$$\frac{\partial s}{\partial t} = \nabla \cdot (D_3(b)\nabla s) + a(n,b), \tag{4.9}$$

$$\frac{\partial q}{\partial t} = d_q \Delta q + f_2(b,q), \tag{4.10}$$

$$\frac{\partial f}{\partial t} = d_f \Delta f + f_3(n,b,q,f), \tag{4.11}$$

where the terms $f_2(b,q)$ and $f_3(n,b,q,f)$ and the coefficients $D_1(f)$ and $D_2(n,b,q)$ are derived in detail in the following sections.

Biofilm formation plays a crucial role for the development of an accurate and detailed model since the biofilm component constitutes the environment in which the bacterial colony grows and develops its characteristic features. Experimental

investigations of the role of biofilms in the growth of bacterial colonies extend to several types of bacteria [46, 100] and for our derivation of the additional equations in the pattern formation model, we take into account investigations of bacterial biofilms in the species *S. aureus* and *B. subtilis*. This is due to the fact that the Gram-positive bacterium *B. subtilis* is closely related to *S. aureus* and that its biofilm formation has been investigated in more detail in comparison to *S. aureus* biofilm formation, which is often considered with a focus on its role in MRSA strain infections [5]. The replicative bacteria are the only bacteria able to produce biofilm, such that a non-zero density of these bacteria is necessary for biofilm growth.

Furthermore, quorum sensing signaling molecules impede the attachment and development of a biofilm. Quorum sensing is mainly performed by the *agr* operon in *S. aureus*, a process which has been investigated in [21, 150, 151]. A mathematical model of the process was established in [76] and asymptotically analyzed on different time scales. Out of the timescales analyzed there, the time scale corresponding best to the processes considered in this modeling approach is the time scale of the approach to the steady state. On this timescale the reduced model consists of six ordinary differential equations, which describe the evolution of the concentrations of mRNA, cytoplasmic and transmembrane AgrB, AIP-bound receptor, phosphorylated AgrA and free AIP. The concentrations of transmembrane AgrC, anchored AgrD, cytoplasmic AgrA and up-regulated cells assume fixed values on this time scale. Then the development of the concentration $\bar{a}$ of the free quorum sensing signaling molecule AIP in time is described depending on the concentration S of anchored AgrD and the concentration R of transmembrane AgrC as [76]

$$\frac{d\bar{a}}{d\bar{\tau}} = \frac{\hat{\beta}\hat{\phi}}{\eta}\left(\frac{dR}{d\bar{\tau}} + \lambda R - \frac{dS}{d\bar{\tau}} - \lambda S\right) - \lambda_a \bar{a}. \tag{4.12}$$

Equation (4.12) indicates that there are many interdependencies. Thus this equation cannot be used without considering the evolution of the system in order to express the production of free AIP molecules. However, we aim to establish a form for the development of the concentration of AIP that can stand for itself, depending only on the AIP concentration and external factors like the nutrient or bacteria concentrations, while still taking into account the main processes involved. The equation for the AIP concentration then has an effect on the biofilm formation, since the repression of the *agr* system is necessary for the formation of biofilm [21].

The overall ability of bacteria to form biofilm is dependent on the particular carbon

source in the system as well as the laboratory strain used in the experiments. The biological experiments were performed using several mutants of the Newman strain of *S. aureus* on a tryptic soy broth (TSB) medium at 37°C. In this context a mutant is a bacterium in which one or several gene loci are disabled, e.g., an *agr* mutant is a bacterium which does not perform quorum sensing due to a disabled *agr* locus.

Biofilm is often produced by only a part of the bacterial population. If the bacterial population divides into a subpopulation of extracellular matrix (ECM) producers and a subpopulation of non-producers, the matrix producing bacteria are able to profit from the non-producing population by releasing antimicrobial agents against the non-producers and thriving on the molecules released by the lysed cells [94]. Constrained cell death in this situation leads to an accumulation of by-products, which makes the growth of the colony saturate and results in wrinkling on the colony surface [46]. Furthermore, the matrix-producing cells have a slightly higher division time [94]. Since this behavior is mainly observed in competitive situations with different strains, we do not include a differentiation into matrix producing and non-producing cells, but assume the production to be proportional to the number of reproductive bacteria. While the population, and with it the biofilm, grows, on top of the biofilm a thin film of liquid is formed. In the final stages of colony growth, water repellent hydrophobins can be found on top of the colony [148]. This facilitates nutrient transport in the bacterial colony.

4.2. Derivation of the system of equations

In the following, we consider the different regulation systems involved in the biofilm formation of *S. aureus* bacteria as depicted in Figure 4.1, first by themselves and then concerning the interactions between the systems.

S. aureus bacteria perform quorum sensing via the two regulation systems *agr* and *luxS*. While the *agr* system is only found in the *Staphylococcus* genus, the *luxS* system is found in many bacterial species. Quorum sensing systems regulate the behavior of the bacterial population in response to its own density by the help of signaling substances. The quorum sensing substance used in the *luxS* system is AI-2 and the corresponding substance for the *agr* system is AIP. These substances are produced with different aims. The goal of the *agr* system is to repress biofilm formation and determine the structure of the biofilm, mainly using the regulation factors PSM-α, PSM-β and δ-toxin. In *S. aureus*, the *luxS* system regulates the

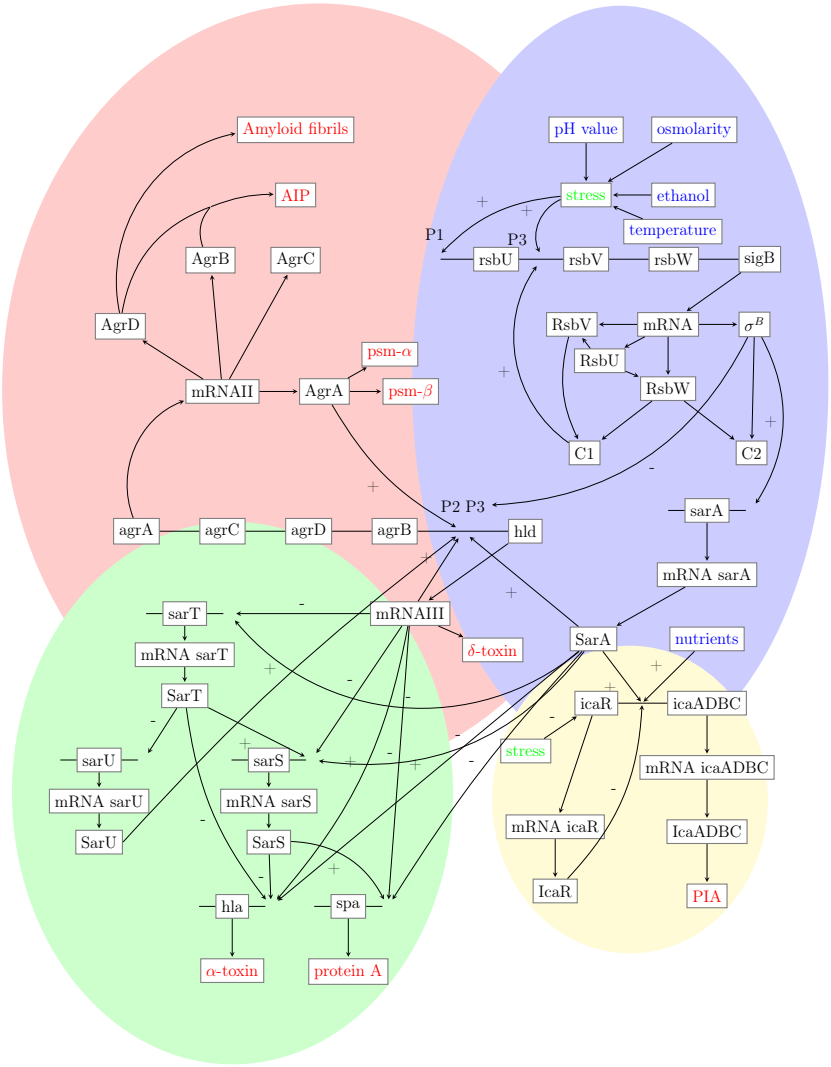

Figure 4.1.: Gene regulation in *S. aureus*. External influences written in blue, resulting variable stress written in green, output substances of a cell colony written in red. Red, blue, green and yellow areas indicate the *agr*, *sarA*, *sarA* homologue and *ica* regulation subsystems, respectively.

gene transcription of CP5, a capsular polysaccharide which is a cell wall component responsible for interaction with the host immune system during the invasive process [153]. Also according to [153], the *luxS* system is clearly involved only in the production of capsular polysaccharide. Since we consider bacterial growth in a laboratory setting, this pathway is not included into the model. Quorum sensing induced biofilm structuring is important under the aspect of pattern formation since it enhances the speed of nutrient transport in the biofilm [147].

The mediation of initial biofilm adhesion and aggregation into multicellular structures depends on a multitude of biophysical processes. Furthermore, initial adhesion

depends on the surface on which the biofilm grows: On biotic surfaces mediation takes place by Microbial Surface Components Recognizing Adhesive Matrix Molecules (MSCRAMM), while on abiotic surfaces Bap protein is an important regulator [43]. Due to the influence of physical factors, we do not consider initial adhesion in detail. Other surface molecules such as exopolysaccharides (EPS) and poly-N-acetylglucosamine (PNAG) homopolymer or polysaccharide intercellular adhesin (PIA) regulate biofilm aggregation. PIA controls the intercellular adhesion and is synthesized at the *ica* gene locus. There the *icaADBC* operon encodes the enzymatically active membrane proteins IcaA, IcaD and IcaC as well as the extracellular protein IcaB [44]. The protein IcaR is a transcriptional repressor of *ica* transcription, whose expression is regulated by the alternative sigma factor σ^B [44]. IcaR inhibits the expression of the *icaADBC* operon. The *agr* system is responsible for the formation of PSM-α and PSM-β molecules involved in biofilm structuring and dispersal [115]. The *sarA* homologues regulate the production of protein A as well as the transcription and translation of α-toxin.

In our numerical simulations in Section 4.6, we investigate the effects of mutations in the *ica*, *spa*, *psm-*α, *psm-*β and *agr* gene loci on bacterial pattern formation. Therefore in the following considerations of gene regulation mechanisms, we are especially interested in the quorum sensing substance AIP, the PSM, the biofilm component PIA and in the concentration of protein A and reduce the full system to account for these components.

For all concentrations of proteins and RNA, we consider concentrations of molecules per volume unit (in this case cm^3 or mm^3) in the dimensional model setting. Only the proportions of up-regulated cells are considered as non-dimensional values. The translation and transcription rates are measured in units translated/transcribed per second and the same applies for the uptake, degradation and dilution, separation, unbinding and (de)phosphorylation rates. If several molecules are required for a certain process to take place, we adjust for the additional units by taking appropriate units for the corresponding rate constants, e.g., the constant k in Equation (4.20) for the production of AIP from AgrD and AgrB has the unit $[k] = \frac{\mathrm{cm}^3}{\mathrm{molecules}\cdot\mathrm{second}}$.

4.2.1. The *agr* system

An approach to modeling the *S. aureus agr* quorum sensing system, which is depicted in the red area in Figure 4.1, can be found in [76]. The system of ordinary

differential equations is developed for the situation of a well-mixed environment with sufficient supply of ribosomes, such that at each pass the entire strand of mRNA is translated. These assumptions are reasonable also for our model. We start with an approach similar to [76] for modeling the *agr* system in the following, which is then adapted to our purpose of not only reducing the system, but finding single equations for some of the regulating factors, that include the effects of other regulatory systems in *S. aureus*. We consider the processes in a population of bacteria with a fixed number of cells, where a proportion of the cells is up-regulated for the activity of a regulatory system, such as the *agr* system, that uses phosphorylated AgrA for up-regulation.

Parameter	Rate constant for	Parameter	Rate constant for
$b_\cdot$	gene locus up-regulation	$u_\cdot$	gene locus down-regulation
$m_\cdot$	basal production of mRNA	$v_\cdot$	regulation-induced transcription
$\delta_\cdot$	degradation and dilution	$\kappa_\cdot$	translation

Table 4.1.: Recurring parameters in the regulation systems.

In the following, the basic binding speed at a gene locus is denoted by $b_\cdot$. It can be increased, depending on the binding of external substances to the promoters. In this process, the regulation of the binding speed depends on the amount of mRNA in the system, as well as on internal cross-regulation mechanisms with other regulatory subsystems. In the same way, down-regulation is proportional to the number of up-regulated cells and can be increased by the presence of certain substances. Furthermore, the degradation and dilution rate of a substance is always denoted by the parameter $\delta_\cdot$. For simplicity, the interaction terms in the model are chosen according to the law of mass action, without an explicit saturation term. Table 4.1 describes the meaning of typical recurring parameters and an overview of the *agr* regulation equations is depicted in Figure 4.2. Here the system influences are depicted in red, while the equations for the output variables, whose influence is considered in the following, are depicted in blue.

Let P_{agr} denote the proportion of up-regulated cells due to binding at the *agr* promoter with the binding speed b_{agr}. Let furthermore R_3 denote the amount of mRNAIII. Then in the basic model, in contrast to the approach in [76], we include multiple influences on the binding, resulting in the *agr* up-regulation activity, denoted by $[agr+] \geq 0$, and the *agr* down-regulation activity, denoted by $[agr-] \geq 0$. This allows the proportion of up-regulated bacteria to increase depending on the up-regulation factors as well as to decrease in proportion to the

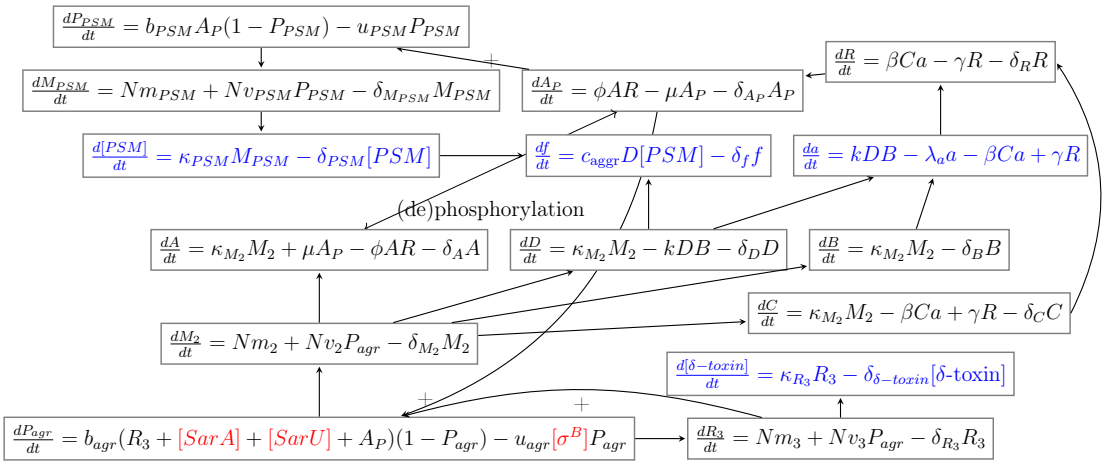

Figure 4.2.: Differential equations for gene regulation in the *S. aureus agr* subsystem. System influences in red, equations for output variables in blue.

down-regulation factors and the amount of up-regulated cells. The proportion of up-regulated cells is always between 0 and 1 since at $P_{agr} = 0$, the derivative is positive and negative at $P_{agr} = 1$. Thus, if the proportion of up-regulated bacteria is zero, no further down-regulation is possible and, if it is one, no further up-regulation is possible. In Figure 4.1, we see that activity at the *agr* operon is positively influenced by the amount of mRNAIII (R_3), phosphorylated AgrA (A_P), SarA ($[SarA]$) and SarU ($[SarU]$) [25] and negatively influenced by the concentration of σ^B ($[\sigma^B]$) [20]. Therefore we state our modeling approach as

$$[agr+] := R_3 + [SarA] + [SarU] + A_P, \qquad [agr-] := [\sigma^B], \tag{4.13}$$

$$\frac{dP_{agr}}{dt} = b_{agr}[agr+](1 - P_{agr}) - u_{agr}[agr-]P_{agr}, \tag{4.14}$$

$$\frac{dM_2}{dt} = Nm_2 + Nv_2P_{agr} - \delta_{M_2}M_2, \tag{4.15}$$

where N denotes the amount of bacteria per volume unit and m_2 denotes the basal production rate of mRNAII. The term $[agr+]$ is kept as simple as possible in that the influences of the substances are considered independently of each other. Equation (4.14) describes the increase of the proportion of up-regulated cells, which is proportional to $[agr+]$ and the amount of down-regulated cells $1 - P_{agr}$, and the decrease of this proportion, which is proportional to $[agr-]$ and the amount of up-regulated cells P_{agr}. The corresponding proportionality constants are denoted by b_{agr} and u_{agr}, respectively. In Equation (4.15) for the amount of mRNAII (M_2), the first term denotes the basal production and the parameter v_2 denotes the up-regulation velocity of this production by increased *agr* activity. Furthermore, the last term $-\delta_{M_2}M_2$ describes the degradation and dilution of mRNAII.

Variable	Concentration of	Variable	Concentration of
P_{agr}	*agr* up-regulated cells	M_2	mRNAII
B	AgrB	D	AgrD
C	AgrC	A	AgrA
a	AIP	R	AgrC-AIP complex
A_P	phosphorylated AgrA	R_3	RNAIII
P_{PSM}	PSM up-regulated cells	M_{PSM}	PSM mRNA
$[PSM]$	PSM	f	amyloid fibrils
[δ-toxin]	δ-toxin	$[SarA]$	SarA
$[SarU]$	SarU	$[\sigma^B]$	σ^B

Table 4.2.: Variables for the *agr* subsystem as described in Section 4.2.1.

As it can be seen in Table 4.2, in the following the concentrations of the proteins AgrB, AgrD, AgrC and AgrA are denoted by B, D, C and A, respectively. These proteins are produced by the P2 operon transcription and translation of mRNAII (M_2). While AgrB is a membrane protein, AgrA can be phosphorylated by AgrC (with bound AIP) and the quorum sensing substance AIP is produced from AgrD under the influence of AgrB, which is represented by the terms $\pm kDB$ in Equation (4.17) and Equation (4.20). Since we assume that the entire strand of mRNA is translated at each pass, we assume the translation rates to be of the same order κ_{M_2} and obtain

$$\frac{dB}{dt} = \kappa_{M_2} M_2 - \delta_B B, \tag{4.16}$$

$$\frac{dD}{dt} = \kappa_{M_2} M_2 - kDB - \delta_D D, \tag{4.17}$$

$$\frac{dC}{dt} = \kappa_{M_2} M_2 - \beta Ca + \gamma R - \delta_C C, \tag{4.18}$$

$$\frac{dA}{dt} = \kappa_{M_2} M_2 + \mu A_p - \phi AR - \delta_A A. \tag{4.19}$$

Here the variables a, A_P and R denote the concentrations of AIP, phosphorylated AgrA and AIP-bound AgrC, respectively. AIP is bound to AgrC ($\pm\beta Ca$) in a reversible ($\pm\gamma R$) binding and the phosphorylation and dephosphorylation of AgrA are modeled as $\pm\phi AR$ and $\pm\mu A_P$. For the concentrations of AIP, phosphorylated AgrA and AgrC-AIP complex we obtain

$$\frac{da}{dt} = kDB - \lambda_a a - \beta Ca + \gamma R, \tag{4.20}$$

$$\frac{dA_P}{dt} = \phi AR - \mu A_P - \delta_{A_P} A_P, \tag{4.21}$$

$$\frac{dR}{dt} = \beta Ca - \gamma R - \delta_R R, \tag{4.22}$$

where the constant λ_a denotes the degradation of AIP outside the cell.

We furthermore include the production of the biofilm-promoting phenol-soluble modulins (PSM) from AgrA, which are responsible for biofilm structuring and dispersal as well as the production of amyloid fibrils [116, 125]. The regulation of PSM is not directly dependent on the *agr* locus since the transcription is independent of the concentration of RNAIII [116]. We obtain

$$\frac{dP_{PSM}}{dt} = b_{PSM}A_P(1 - P_{PSM}) - u_{PSM}P_{PSM}, \tag{4.23}$$

$$\frac{dM_{PSM}}{dt} = Nm_{PSM} + Nv_{PSM}P_{PSM} - \delta_{M_{PSM}}M_{PSM}, \tag{4.24}$$

$$\frac{d[PSM]}{dt} = \kappa_{PSM}M_{PSM} - \delta_{PSM}[PSM], \tag{4.25}$$

$$\frac{df}{dt} = c_{\text{aggr}}D[PSM] - \delta_f f. \tag{4.26}$$

The *S. aureus agr* regulation of PSM genes occurs independently of RNAIII and is regulated by direct binding of the AgrA response regulator [119]. The PSM are expressed from several discrete loci in the *S. aureus* genome, which, due to their size, have only been discovered recently [125]. They stabilize the biofilm to the influence of mechanical stress and enzymatic degradation [125] and their production is positively influenced by *agr* activity. It was observed that PSM and the N-terminal amphipathic leader of the AgrD propeptide (N-AgrD) amino acid sequence aggregate to form amyloid fibrils, which are strongly resistant to degradation [126]. Due to the amphipathic α-helical structure of PSM, PSM can lyse eukaryotic cells, such as neutrophils, monocytes and erythrocytes, by non-specific destruction of biological membranes [54].

Apart from the P2 operon transcription considered above, we account for the P3 operon, which influences the production of protein A and α-toxin. The P3 operon is responsible for the formation of the untranslated RNAIII, which is an intracellular effector that up-regulates extracellular protein genes and down-regulates cell wall colonization factor genes [76]. RNAIII experiences transcription but not translation, which allows it to base pair with other mRNA strains in order to inhibit encoding of virulence factors [146]. Nevertheless δ-hemolysin (Hld)/δ-toxin is encoded by RNAIII by translation after a conformational change [15].

The transcription of δ-toxin and α-toxin is derepressed during the exponential

growth phase [93] and the inhibitor δ-toxin is one of the hydrophobic PSM [111]. The protein δ-toxin is encoded by the gene *hld* located within RNAIII (R_3), and we thus obtain the amount of δ-toxin by transcription from RNAIII. This gives the equations

$$\frac{dR_3}{dt} = Nm_3 + Nv_3P_{agr} - \delta_{R_3}R_3, \tag{4.27}$$

$$\frac{d[\delta\text{-toxin}]}{dt} = \kappa_{R_3}R_3 - \delta_{\delta\text{-toxin}}[\delta\text{-toxin}], \tag{4.28}$$

where the rate constants in Equation (4.27) are defined analogously to those in Equation (4.15) for the concentration of mRNAII.

4.2.2. The *sarA* system

In this section we investigate the *sarA* regulation subsystem as depicted in the blue area in Figure 4.1. *S. aureus* biofilm formation is essentially dependent on the staphylococcal accessory regulator *sarA*, while a minor role is also attributed to the σ^B-operon [142]. Furthermore, the production of biofilm in Staphylococci is a reaction of the bacterial population to environmental conditions, including the availability of salt and glucose, oxygen and iron and the pH environment [144]. In the following, we include the influence of environmental factors on the *sarA* system. To this end the formula

$$[str] := \alpha|\mathrm{T} - \mathrm{T_{ref}}| + \beta[\text{osmolarity}] + \gamma|\mathrm{pH} - \mathrm{pH_{ref}}| + \delta[\text{ethanol}]$$

is used to model the stress on the system. Here T denotes the temperature in degrees Celsius and for the temperature as well as for the pH level, we consider derivations from a reference equilibrium value. The dependencies are modeled using independent linear terms with the corresponding dimensional rate constants $\alpha, \beta, \gamma, \delta \in \mathbb{R}_+$. Note that, in contrast to salt concentration, osmolarity depends on the temperature of the medium. It is inversely proportional to temperature and high concentrations of NaCl can lead to salt stress. We do not set up a differential equation for $[str]$ since we assume that the included values are constant in a laboratory medium. Furthermore, we choose the parameters such that the values for $[str]$ are between 0 and 1.

Stress is a regulator of the production of the *rsbU* gene product, which together with the *rsbV* and *rsbW* gene products, influences the expression of the σ^B-operon,

Variable	Concentration of	Variable	Concentration of
$[str]$	stress in the system	$[C_1]$	RsbW-RsbV complex
$[C_2]$	RsbW-σ^B complex	P_{RsbU}	RsbU up-regulated cells
M_{RsbU}	RsbU mRNA	$[RsbU]$	RsbU
$[RsbV]$	RsbV	$[RsbW]$	RsbW
P_σ	sigma up-regulated cells	M_σ	sigma mRNA
P_{sarA}	*sarA* up-regulated cells	M_{sarA}	*sarA* mRNA

Table 4.3.: Variables for the *sarA* subsystem as described in Section 4.2.2.

responsible for the regulation of *sarA* transcription, in a competitively inhibitory process. The regulation of *rsbU* activity in *S. aureus* is different from that in *B. subtilis* [114] and thus investigated in detail in the following. An overview of the variables considered in the *sarA* subsystem can be found in Table 4.3 and the principal equations are depicted in Figure 4.3.

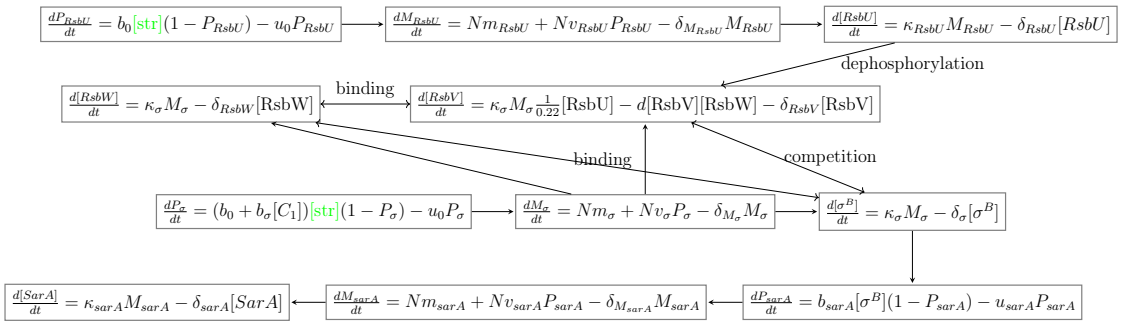

Figure 4.3.: Differential equations derived from gene regulation in the *S. aureus* *sarA* subsystem with σ^B. External influences in green.

The RNA polymerase (RNAP) core enzyme and the σ^B-factor can associate to form an RNAP holoenzyme [128], which recognizes promoter regions in the DNA, initiating transcription [46]. The regulatory protein RsbW binds to σ^B at the rate k_2 if the environmental stress on the system is low, keeping it from aggregating to the RNAP core enzyme. The corresponding complex is denoted by C_2. If the stress increases, RsbU dephosphorylates RsbV, such that RsbV can bind to RsbW. The complex C_1 is formed at rate k_1 and the activated σ^B factor is released, which then binds to the RNAP core enzyme, forming an RNAP holoenzyme [85]. Thus σ^B and RsbV compete for the binding with RsbW. All bindings as well as the dephosphorylation are assumed to be reversible. If the binding occurs at a certain rate k_i, $i \in \{1, 2\}$, then the rate for the reverse process is denoted by k_{-i}.

We set up differential equations for the complex formation processes. Similar to the

well-known Michaelis-Menten framework, we obtain

$$\frac{d[C_1]}{dt} = -k_{-1}[C_1] + k_1[RsbW][RsbV],$$
$$\frac{d[C_2]}{dt} = -k_{-2}[C_2] + k_2[RsbW][\sigma^B].$$

We assume that the rates of complex formation k_1 and k_2 depend on the stress level of the system. This means that the more stress, the higher the binding rate k_1 of RsbW and RsbV, and the lower the binding rate k_2 of RsbW and σ^B. We assume that the unbinding rates for both complexes are independent of the stress level and of the same order as the basic binding rates denoted by k_1^0 and k_2^0. Since the stress level $[str]$ is between 0 and 1, we model the binding rates as $k_1 = [str]k_1^0$ and $k_2 = (1 - [str])k_2^0$. The processes of binding and unbinding happen very fast and are thus assumed to be in equilibrium. It follows that the values $K_i := \frac{k_{-i}}{k_i}$ for $i \in \{1, 2\}$ are taken as

$$K_1 = \frac{[RsbW][RsbV]}{[C_1]}, \qquad K_2 = \frac{[RsbW][\sigma^B]}{[C_2]}. \tag{4.29}$$

This means that the equations for the complex formations do not have to be considered any further. The values K_i, which describe the relationships between binding and unbinding for the respective complexes, depend on $[str]$ as a consequence of the dependence of the k_i on $[str]$. Due to mass conservation for σ^B, $[RsbV]$ and $[RsbW]$ [101, 105], the following equations with the constant dimensional parameters σ_0, v_0 and r_0 hold:

$$[\sigma^B] + [C_2] = \sigma_0, \quad [RsbV] + [C_1] = v_0, \quad [RsbW] + [C_1] + [C_2] = r_0. \tag{4.30}$$

We thus express the amount of molecules of the complex $[C_1]$, composed of $[RsbW]$ and $[RsbV]$, in dependence on the concentrations of $[RsbV]$ and $[\sigma^B]$ molecules. The higher the concentration of $[C_1]$, the more transcription happens at the σ^B-operon. Using Equations (4.29)–(4.30) and multiplying by $\frac{r_0}{r_0} = 1$ we obtain the formula

$$[C_1] = r_0 \frac{[RsbV]/K_1}{1 + [RsbV]/K_1 + [\sigma^B]/K_2} = r_0 \frac{[RsbV][str]}{1 + [RsbV][str] + [\sigma^B](1 - [str])},$$

where the parameter r_0 carries the dimension of $[C_1]$. Here we set the basic binding and unbinding constants k_i^0 and k_{-i} from above to be equal, which results in the

fact that the constants

$$K_1 = \frac{1}{[str]} \qquad \text{and} \qquad K_2 = \frac{1}{1-[str]}$$

are inversely proportional to $[str]$ and $(1-[str])$, respectively. We model a system of competition, where the up-regulation of translation levels depends on the stress levels. We know that the amount of $[C_1]$ is in the interval $(0,1)$ if r_0 is chosen appropriately as $r_0 \in (0,1]$ and $[RsbV] \neq 0$. In order to consider the proportion of complexes in relation to the amount of biomass, we further set the value of r_0 to 1.

Additionally, we include the number of up-regulated cells P_σ. The σ^B-operon, consisting of *rsbU*, *rsbV*, *rsbW* and *sigB*, is controlled by two different promoters. The entire strand is transcribed from the σ^A-dependent promoter $sigB_{\mathrm{P1}}$, while part of it, i.e., *rsbV*, *rsbW* and *sigB*, is also transcribed from the σ^B-dependent promoter $sigB_{\mathrm{P3}}$. Both promoters show a rapid response to environmental stress [128].

In our system, the stress $[str]$ is a non-zero quantity. We thus model the increase in *sigB* transcription from the different promoters using different up-regulation mechanisms. While the binding rate constant for the up-regulation of RsbU production in Equation (4.31) is expressed as $b_0[str]$, the rate constant for RsbV, RsbW and σ^B in Equation (4.32) is of the form $(b_0 + b_\sigma[C_1])[str]$. This is due to the fact that transcription from the P3 promoter is increased because of the formation of the holoenzyme from σ^B and polymerase core enzyme. The corresponding amounts of mRNA are denoted by M_{RsbU} and M_σ. Here P_{RsbU} denotes the proportion of bacteria whose RsbU production is up-regulated and P_σ denotes the proportion of bacteria whose production of RsbV, RsbW and σ^B is up-regulated. We obtain the system

$$\frac{dP_{RsbU}}{dt} = b_0[str](1-P_{RsbU}) - u_0 P_{RsbU}, \tag{4.31}$$

$$\frac{dP_\sigma}{dt} = (b_0 + b_\sigma[C_1])[str](1-P_\sigma) - u_0 P_\sigma, \tag{4.32}$$

$$\frac{dM_{RsbU}}{dt} = Nm_{RsbU} + Nv_{RsbU}P_{RsbU} - \delta_{M_{RsbU}} M_{RsbU}, \tag{4.33}$$

$$\frac{dM_\sigma}{dt} = Nm_\sigma + Nv_\sigma P_\sigma - \delta_{M_\sigma} M_\sigma. \tag{4.34}$$

Environmental stress leads to a direct activation of the promoters. In *S. aureus*, overexpression of RsbU is sufficient to trigger an immediate and strong activation of σ^B [128]. This can be explained by a basal transcription of *rsbU* from the

σ^A-controlled P1 promoter at rate $\kappa_{RsbU} M_{RsbU}$. The protein RsbU then dephosphorylates RsbW to allow binding of RsbW to RsbV at rate $k_1[RsbV][RsbW]$. Then this enables the release of σ^B at rate $k_{-2}[C_2]$, which forms a holoenzyme at rate $k_2[\sigma^B][RsbW]$, which can induce transcription at the P3-promoter. Therefore, the amount of active σ^B increases with the concentration of RsbU, without any significant influence from the ratio RsbV/RsbV-P of standard and phosphorylated RsbV. The level of this basal activity is higher than the corresponding level for *B. subtilis*, which activates stress-induced σ^B-transcription due to a shift in the RsbV/RsbV-P ratio [114]. In addition, and in contrast to the case in *B. subtilis*, it was found that stress activates σ^B-dependent transcription, which takes place at the rate $\kappa_\sigma M_\sigma$, but is not accompanied by a strong accumulation of RsbV, RsbW, and σ^B [114]. The increase in σ^B- dependent transcription is modeled by the factor $[str]$ in Equation (4.32).

Only the dephosphorylated amount of RsbV is counted and we thus assume that the amount of RsbV is a direct consequence of the availability of RsbU, which dephosphorylates RsbV-P. We thus take the transcription term $\kappa_\sigma M_\sigma \frac{1}{0.22}[RsbU]$. If the cell is in an unstressed state, most of the RsbV is phosphorylated by RsbW [114] at the rate $d[RsbW][RsbV]$. In the unstressed as well as in the stressed cell, the RsbV/RsbV-P ratio is approximately 0.22 if RsbU is present. This ratio cannot be changed remarkably due to stress in *S. aureus*, only very high RsbU levels permit an increase up to 0.35, which was considered to not be significant [114]. Due to this fixed relationship, we do not model the amount of phosphorylated RsbV explicitly as it can be calculated from the amount of dephosphorylated RsbV at any time. Stress-induced binding of RsbV and RsbW is included using the rate $k_1[RsbV][RsbW]$ and the corresponding unbinding process has the rate $k_{-1}[C_1]$. Rate constants $\delta_\cdot$ denote the degradation rate constants of a substance. The Equations (4.36)–(4.38) for $[\sigma^B]$, $[RsbV]$ and $[RsbW]$ are simplified considerably by taking into account that $\frac{d[C_1]}{dt} = 0$ and $\frac{d[C_2]}{dt} = 0$. This yields

$$\frac{d[RsbU]}{dt} = \kappa_{RsbU} M_{RsbU} - \delta_{RsbU}[RsbU], \tag{4.35}$$

$$\begin{aligned} \frac{d[\sigma^B]}{dt} &= \kappa_\sigma M_\sigma - k_2[\sigma^B][RsbW] + k_{-2}[C_2] - \delta_\sigma[\sigma^B] \\ &= \kappa_\sigma M_\sigma - \delta_\sigma[\sigma^B], \end{aligned} \tag{4.36}$$

$$\begin{aligned} \frac{d[RsbV]}{dt} &= \kappa_\sigma M_\sigma \frac{1}{0.22}[RsbU] - (d + k_1)[RsbV][RsbW] + k_{-1}[C_1] - \delta_{RsbV}[RsbV] \\ &= \kappa_\sigma M_\sigma \frac{1}{0.22}[RsbU] - d[RsbV][RsbW] - \delta_{RsbV}[RsbV], \end{aligned} \tag{4.37}$$

$$\begin{aligned}\frac{d[RsbW]}{dt} &= \kappa_\sigma M_\sigma - (k_1[RsbV] + k_2[\sigma^B])[RsbW] + k_{-1}[C_1] + k_{-2}[C_2] \\ &\quad - \delta_{RsbW}[RsbW] \\ &= \kappa_\sigma M_\sigma - \delta_{RsbW}[RsbW]. \end{aligned} \tag{4.38}$$

The DNA binding protein SarA is transcribed via three overlapping transcripts at the *sarA* operon, denoted by P1, P2 and P3. While the P1 and P2 promoters are σ^A-dependent, the P3 promoter is positively regulated by σ^B [32]. Thus, the basic transcription is independent of the level of σ^B and additional transcription takes place at increased concentration levels. SarA also activates its own expression [25], but this is neglected here for the sake of model simplification. At the transition from exponential growth to late exponential and stationary growth, the *sarA* transcription shifts from the σ^A-dependent promoter to the σ^B-dependent promoter.
We obtain

$$\frac{dP_{sarA}}{dt} = b_{sarA}[\sigma^B](1 - P_{sarA}) - u_{sarA}P_{sarA}, \tag{4.39}$$

$$\frac{dM_{sarA}}{dt} = Nm_{sarA} + Nv_{sarA}P_{sarA} - \delta_{M_{sarA}}M_{sarA}, \tag{4.40}$$

$$\frac{d[SarA]}{dt} = \kappa_{sarA}M_{sarA} - \delta_{sarA}[SarA]. \tag{4.41}$$

The resulting equations are depicted in Figure 4.3. We have seen that SarA positively influences transcription at the *agr* locus. In the following section, we will see that the protein SarA also positively influences transcription at the *ica* locus and is thus a principal regulator of *S. aureus* biofilm formation.

4.2.3. The *ica* system

The intercellular adhesion (*ica*) locus depicted in the yellow area in Figure 4.1 is part of the accessory genes, which means that it cannot be found in every bacterial strain [7]. Nevertheless it is found in most *S. aureus* strains [44] and it is necessary for biofilm production [29]. In Figure 4.4 the principal equations for the *ica* system are depicted and an overview of the used variables can be found in Table 4.4.

The transcription at the *ica* locus is a direct consequence of the concentrations of σ^B and SarA. It is a requirement for the synthesis of the main extracellular polymeric substance component polysaccharide intercellular adhesin (PIA/PNAG). In the *ica* operon of *S. aureus* and *Staphylococcus epidermidis* (*S. epidermidis*), the *ica* genes *icaA*, *icaD*, *icaC* and *icaB* are transcribed divergently from the gene

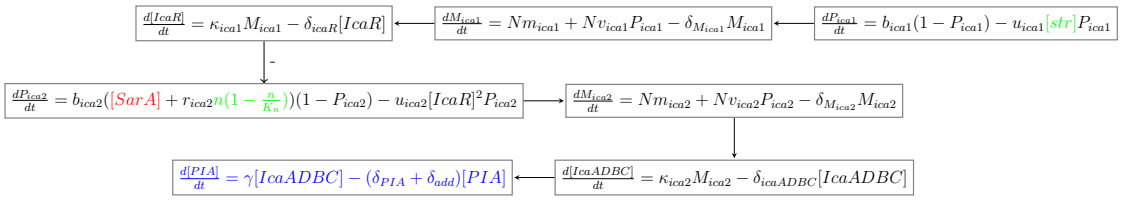

Figure 4.4.: Differential equations derived from gene regulation in the *S. aureus* *ica* subsystem. External influences in green, system influences in red, equations for output variables in blue.

icaR [44]. Many proteins directly and indirectly influence transcription at the *icaADBC* operon. Among the proteins included in our model, especially SarA has a direct influence through binding to the *icaADBC* promoter region and is thus included in Equation (4.42). Nevertheless, the transcription of *icaR* is unaffected by the deletion of *sarA* for both *S. epidermidis* and *S. aureus* [44]. The influence of σ^B may be considered indirect [44] since the *ica* locus does not have a corresponding binding site [29]. The IcaR dimers bind in cooperative pairs to the *icaADBC* operator, where they inhibit transcription [44]. Thus, we use the quadratic term $[IcaR]^2$ in Equation (4.42) for $[ica2-]$. In *S. epidermidis* the activity at the *icaR* locus is reduced by environmental stress, especially high levels of ethanol but remains unaffected by changed concentrations of NaCl and glucose. Furthermore, IcaR has no effect on the expression of its own gene in both *S. aureus* and *S. epidermidis*. In contrast, the concentration of glucose does have a small effect in *S. aureus* [44], where increasing levels of glucose lead to less repression by IcaR. In Equation (4.42) we model the positive influences of the SarA and nutrient concentrations on the gene locus with the weight r_{ica2}, since the nutrients do not bind at the promoter site. For the nutrient concentration n, we assume that the up-regulation due to nutrients can be described logistically.

Variable	Concentration of	Variable	Concentration of
n	nutrients	P_{ica1}	*icaR* up-regulated cells
M_{ica1}	icaR mRNA	$[IcaR]$	IcaR
P_{ica2}	*icaADBC* up-regulated cells	M_{ica2}	icaADBC mRNA
$[IcaADBC]$	IcaADBC	$[PIA]$	polysaccharide intercellular adhesin

Table 4.4.: Variables for the *ica* subsystem as described in Section 4.2.3.

The synthesis of PIA is achieved by a combination of all products of the *icaADBC* gene cluster. While the proteins IcaA and IcaD are necessary for the expolysaccharide synthesis, IcaC translocates the poly-N-acetylglucosamine polymer to the bacterial surface and IcaB deacetylates the molecule, enabling fixation to the bacte-

rial cell surface [44]. The *icaADBC* cluster genes are thus modeled together with the concentration $[IcaADBC]$ and we obtain the system of equations

$$[ica2+] := [SarA] + r_{ica2}n(1 - \frac{n}{K_n}), \qquad [ica2-] := [IcaR]^2, \tag{4.42}$$

$$\frac{dP_{ica1}}{dt} = b_{ica1}(1 - P_{ica1}) - u_{ica1}[str]P_{ica1}, \tag{4.43}$$

$$\frac{dP_{ica2}}{dt} = b_{ica2}[ica2+](1 - P_{ica2}) - u_{ica2}[ica2-]P_{ica2}, \tag{4.44}$$

$$\frac{dM_{ica1}}{dt} = Nm_{ica1} + Nv_{ica1}P_{ica1} - \delta_{M_{ica1}}M_{ica1}, \tag{4.45}$$

$$\frac{dM_{ica2}}{dt} = Nm_{ica2} + Nv_{ica2}P_{ica2} - \delta_{M_{ica2}}M_{ica2}, \tag{4.46}$$

$$\frac{d[IcaR]}{dt} = \kappa_{ica1}M_{ica1} - \delta_{icaR}[IcaR], \tag{4.47}$$

$$\frac{d[IcaADBC]}{dt} = \kappa_{ica2}M_{ica2} - \delta_{icaADBC}[IcaADBC], \tag{4.48}$$

$$\frac{d[PIA]}{dt} = \gamma[IcaADBC] - (\delta_{PIA} + \delta_{\text{add}}\frac{[\sigma^B]}{[SarA]})[PIA]. \tag{4.49}$$

The constants b_{ica1} and b_{ica2} denote the binding speeds at the *icaR* and *icaADBC* loci. A remarkable observation in some strains is that, while in combined *sarA* and σ^B mutants, the overall biofilm formation attributable to PIA is decreased following decreased *ica* activity, the decrease is strongest for *sarA* mutants. For mutants only in σ^B, the least decrease is observed. This may be explained by an intermediate substance that would either degrade the PIA product or repress the PIA synthesis, the production of the intermediate substance being up-regulated by $[\sigma^B]$ and down-regulated by $[SarA]$ [142]. We model this by an additional factor $\delta_{\text{add}}\frac{[\sigma^B]}{[SarA]}$ in the equation for the PIA production. This factor is close to δ_{add} if $[\sigma^B]$ and $[SarA]$ are present at similar levels and greater than δ_{add} if the level of σ^B is higher than that of $[SarA]$. If the concentration of $[\sigma^B]$ is smaller than that of $[SarA]$, the factor is less than δ_{add}. Since it is uncertain if this factor has a negative influence on the production of PIA or if it increases the degradation of the PIA already produced, both approaches are valid and for simplicity we choose to describe the influence as an additional degradation term. For our purpose, we can simplify even more by observing that the amount of $[SarA]$ is only up-regulated by the amount of $[\sigma^B]$. Thus we take $\lim_{t\to\infty}\frac{[\sigma^B]}{[SarA]} = \lim_{N\to\infty}\frac{[\sigma^B]}{[SarA]} = \text{const.}$ when the number of bacteria N increases with time. With the additional death δ_{add} we obtain the approximation

$$\frac{d[PIA]}{dt} \approx \gamma[IcaADBC] - (\delta_{PIA} + \delta_{\text{add}})[PIA].$$

4.2.4. The *sarA* homologue system

In this section we model the *sarA* homologues depicted in the green area in Figure 4.1. There are at least nine major *sarA* homologues, including *sarR*, *sarS*, *rot*, *sarT*, *sarU*, *sarV*, *mgrA*, *sarX* and *sarZ*. The gene loci *sarS* and *sarT* are adjacent, but transcribed divergently [95]. Furthermore, while no differences in expression among strains can be observed for the *sarA*, *sarT* and *sarU* genes [9], other homologues behave differently in different strains of *S. aureus*. We thus include the genes *sarT* and *sarU* into our model. The genes *mgrA*, *rot*, *sarZ*, *sarR* and *sarS* are expressed in all strains, but the level of expression varies from strain to strain [9]. As a representative of this group we include the *sarS* gene.

Variable	Concentration of	Variable	Concentration of
P_{sarT}	*sarT* up-regulated cells	M_{sarT}	sarT mRNA
$[SarT]$	SarT	P_{sarU}	*sarU* up-regulated cells
M_{sarU}	sarU mRNA	$[SarU]$	SarU
P_{sarS}	*sarS* up-regulated cells	M_{sarS}	sarS mRNA
$[SarS]$	SarS	P_{spa}	*spa* up-regulated cells
M_{spa}	spa mRNA	[protein A]	protein A
P_{hla}	*hla* up-regulated cells	M_{hla}	hla mRNA
[α-toxin]	α-toxin		

Table 4.5.: Variables for the *sarA* homologue subsystems as described in Section 4.2.4.

Very delicate interactions take place between the *sarA* homologues, which include interactions with the *agr* regulation system. They have an influence on the production of protein A (via *spa*) and α-toxin (via *hla*). The variables included into the model can be found in Table 4.5 and an overview of the regulation processes is depicted in Figure 4.5.

The *sarA*-*agr* network is responsible for the expression of cell-wall associated adhesins during exponential growth and the expression of secreted enzymes and toxins in the transition to post-exponential growth [124]. SarA directly regulates the expression of *sarS* and *sarT*. The transcription at *sarT* is further reduced by a high activity of the *agr* quorum sensing system. SarT binds to the *sarS* promoter, increasing its activity and SarS influences the transcription of *spa*. The transcription of *hla* depends on the level of SarT. This is expressed in the following system of equations

$$\frac{dP_{sarT}}{dt} = b_{sarT}(1 - P_{sarT}) - u_{sarT}([SarA] + R_3)P_{sarT}, \tag{4.50}$$

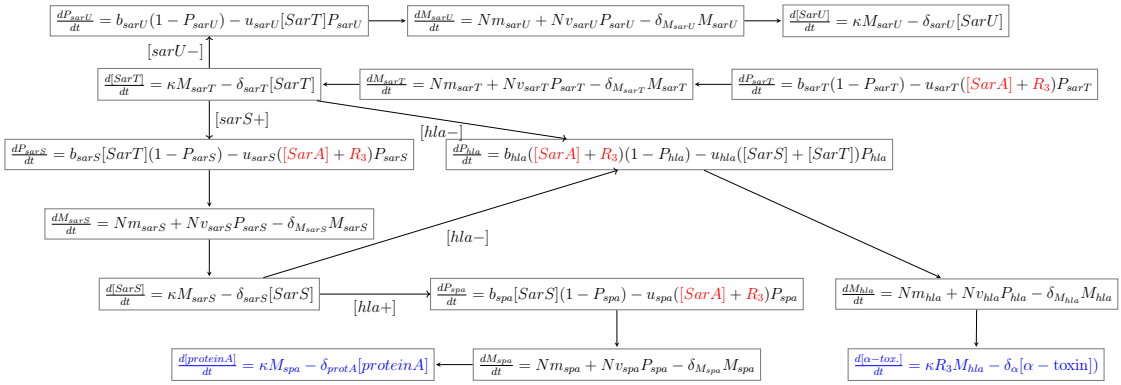

Figure 4.5.: Differential equations derived from gene regulation in the *S. aureus* sar homologue subsystems. System influences in red, equations for output variables in blue.

$$\frac{dM_{sarT}}{dt} = Nm_{sarT} + Nv_{sarT}P_{sarT} - \delta_{M_{sarT}}M_{sarT}, \tag{4.51}$$
$$\frac{d[SarT]}{dt} = \kappa M_{sarT} - \delta_{SarT}[SarT], \tag{4.52}$$
$$\frac{dP_{sarU}}{dt} = b_{sarU}(1 - P_{sarU}) - u_{sarU}[SarT]P_{sarU}, \tag{4.53}$$
$$\frac{dM_{sarU}}{dt} = Nm_{sarU} + Nv_{sarU}P_{sarU} - \delta_{M_{sarU}}M_{sarU}, \tag{4.54}$$
$$\frac{d[SarU]}{dt} = \kappa M_{sarU} - \delta_{SarU}[SarU], \tag{4.55}$$
$$\frac{dP_{sarS}}{dt} = b_{sarS}[SarT](1 - P_{sarS}) - u_{sarS}([SarA] + R_3)P_{sarS}, \tag{4.56}$$
$$\frac{dM_{sarS}}{dt} = Nm_{sarS} + Nv_{sarS}P_{sarS} - \delta_{M_{sarS}}M_{sarS}, \tag{4.57}$$
$$\frac{d[SarS]}{dt} = \kappa M_{sarS} - \delta_{SarS}[SarS]. \tag{4.58}$$

SarA has a further direct influence on its homologues since it binds to conserved regions termed Sar boxes within promoter regions of the genes encoding protein A and α-toxin [53] in the same way it binds to the promoter region for *agr*. Furthermore, mRNAIII regulates the transcription and translation of α-toxin [25]. We obtain the equations

$$[spa+] := [SarS], \qquad [spa-] := [SarA] + R_3, \tag{4.59}$$
$$\frac{dP_{spa}}{dt} = b_{spa}[spa+](1 - P_{spa}) - u_{spa}[spa-]P_{spa}, \tag{4.60}$$
$$\frac{dM_{spa}}{dt} = Nm_{spa} + Nv_{spa}P_{spa} - \delta_{M_{spa}}M_{spa}, \tag{4.61}$$
$$\frac{d[\text{protein A}]}{dt} = \kappa M_{spa} - \delta_{protA}[\text{protein A}], \tag{4.62}$$

$$[hla+] = [SarA] + R_3, \qquad [hla-] = [SarS] + [SarT], \tag{4.63}$$

$$\frac{dP_{hla}}{dt} = b_{hla}[hla+](1 - P_{hla}) - u_{hla}[hla-]P_{hla}, \tag{4.64}$$

$$\frac{dM_{hla}}{dt} = Nm_{hla} + Nv_{hla}P_{hla} - \delta_{M_{hla}}M_{hla}, \tag{4.65}$$

$$\frac{d[\alpha\text{-toxin}]}{dt} = \kappa R_3 M_{hla} - \delta_\alpha[\alpha\text{-toxin}]. \tag{4.66}$$

4.3. Non-dimensional equations

In this section we non-dimensionalize the dimensional model introduced in Section 4.2 in order to reduce the number of parameters in the system. It is important to choose an appropriate time scale, since we want to consider all subsystems on the same time scale. We further note that the processes in our model take place on very different time scales. In the following sections, we also consider the orders of the speeds of the different processes in order to justify time scale induced simplifications of the model.

An important assumption is that the new timescale is the same for all subsystems. Since often several proteins are translated from neighboring strangs of mRNA, we conclude that the mRNA are very similar and assume that the degradation rates of the mRNA needed for protein formation are the same in all subsystems. Thus, while we use different variables, such as $\delta_{M_{RsbU}}$ for the *sarA* subsystem or $\delta_{M_{ica1}}$ for the *ica* subsystem, in the following it is important to keep in mind that all these parameters are assumed to be equal to δ_{M_2}. Accordingly we choose the new timescale [76]

$$\tau := \delta_{M_2} t,$$

where $\delta_{M_2} = \delta_{R_3} = \delta_{M_{PSM}} = \delta_{M_{RsbU}} = \delta_{M_{ica1}} = \delta_{M_{sarT}}$. Time scale values for specific non-dimensional parameters of the model can be found in [70, 76].

4.3.1. The *agr* system

Following [76], for the *agr* subsystem we first determine the stationary states of the system in the case $k = 0$ and $P_{agr} = 0$ and then use these as the starting values of the system. We non-dimensionalize with respect to the starting values. Due to $k = 0$, the stationary values for a, R and A_P equal zero, i.e., $a(0) = R(0) = A_P(0) = 0$. We choose the non-dimensionalizations for these variables in order to simplify our system

as much as possible. Further the notation X' denotes the non-dimensionalized form of the original variable X. We find the following non-dimensional equations for the *agr* subsystem:

$$\frac{dP_{agr}}{d\tau} = b'_{agr}[agr+]'(1 - P_{agr}) - u'_{agr}[agr-]'P_{agr}, \tag{4.67}$$

$$\frac{dM'_2}{d\tau} = 1 + v'P_{agr} - M'_2, \tag{4.68}$$

$$\frac{dB'}{d\tau} = \lambda(M'_2 - B'), \tag{4.69}$$

$$\frac{dD'}{d\tau} = \lambda(M'_2 - D') - k'D'B', \tag{4.70}$$

$$\frac{dC'}{d\tau} = \lambda(M'_2 - C') - \frac{\beta'}{\eta}C'a' + \gamma'R', \tag{4.71}$$

$$\frac{dA'}{d\tau} = \lambda(M'_2 - A') + \mu'A'_P - \phi'A'R', \tag{4.72}$$

$$\frac{da'}{d\tau} = k'D'B' - \lambda'_a a' - \beta'C'a' + \gamma'\eta R', \tag{4.73}$$

$$\frac{dA'_P}{d\tau} = \phi'A'R' - \mu'A'_P - \lambda A'_P, \tag{4.74}$$

$$\frac{dR'}{d\tau} = \frac{\beta'}{\eta}C'a' - (\gamma' + \lambda)R'. \tag{4.75}$$

In these equations, as we use non-dimensional variables, we also employ new parameters, which are given as follows:

$$\lambda := \frac{\delta_A}{\delta_{M_2}} = \frac{\delta_B}{\delta_{M_2}} = \frac{\delta_C}{\delta_{M_2}} = \frac{\delta_D}{\delta_{M_2}} = \frac{\delta_{A_P}}{\delta_{M_2}} = \frac{\delta_R}{\delta_{M_2}}, \quad b'_{agr} := \frac{b_{agr}Nm_3}{\delta^2_{M_2}},$$

$$u'_{agr} := \frac{u_{agr}\kappa_\sigma Nm_\sigma}{\delta_{M_2}\delta_\sigma\delta_{M_\sigma}}, \quad v' := \frac{v_2}{m_2}, \quad k' := \frac{k\tilde{B}}{\delta_{M_2}} = \frac{kNm_2\kappa_{M_2}}{\delta^2_{M_2}\delta_B}, \quad \mu' := \frac{\mu}{\delta_{M_2}},$$

$$\lambda'_a := \frac{\lambda_a}{\delta_{M_2}}, \quad \gamma' := \frac{\gamma}{\delta_{M_2}}, \quad \beta' := \frac{\beta\tilde{C}}{\delta_{M_2}} = \frac{\beta Nm_2\kappa_{M_2}}{\delta^2_{M_2}\delta_C}, \quad \phi' := \frac{\phi\tilde{C}}{\delta_{M_2}} \quad \text{and} \quad \eta := \frac{\delta_D}{\delta_C}.$$

This means that also $\delta_A = \delta_B = \delta_C = \delta_D = \delta_{A_P} = \delta_R$ and $\eta = 1$, which is reasonable since the dominating factor is the dilution, which is the same for all substances. For the remaining reparametrizations we obtain

$$a' := \frac{\delta_{M_2}\delta_D}{Nm_2\kappa_{M_2}}a, \qquad A'_P := \frac{\delta_{M_2}\delta_A}{Nm_2\kappa_{M_2}}A_P, \qquad R' := \frac{\delta_{M_2}\delta_C}{Nm_2\kappa_{M_2}}R.$$

The resulting system is depicted in Figure 4.6. We furthermore reconsider the activation and deactivation factors as well, since the new timescale applies and the

variables are rescaled. Thus we obtain

$$[agr+]' := \frac{Nm_3}{\delta_{R_3}}(R_3' + \alpha([SarA]' + [SarU]' + A_P')) \quad \text{and} \quad [agr-]' := \frac{Nm_\sigma \kappa_\sigma}{\delta_\sigma \delta_{M_\sigma}}[\sigma^B]',$$

where the parameter α is defined as $\alpha := \frac{\kappa_X}{\delta_X}$ and assumed to be equal for all substances $X \in \{[SarA], [SarU], A_P\}$. This is detailed in Section 4.5.1.

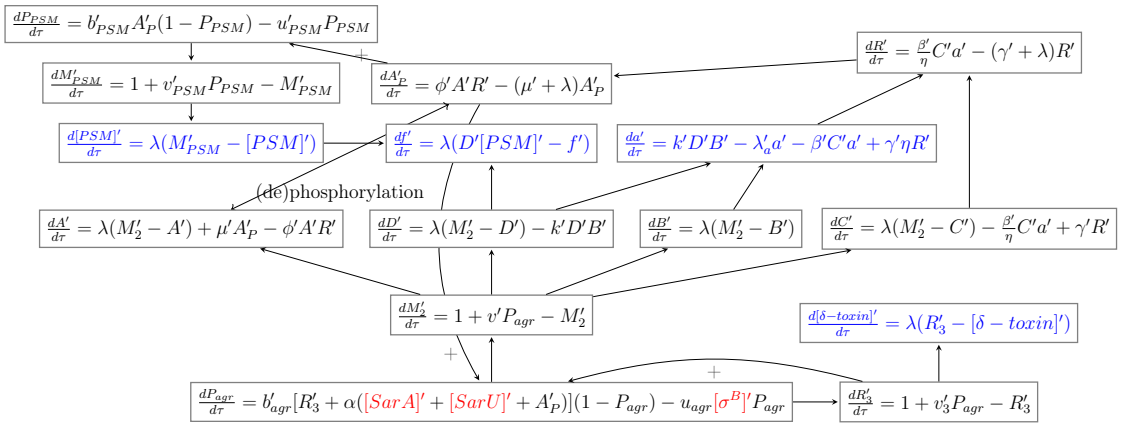

Figure 4.6.: Nondimensional differential equations derived from gene regulation in the *S. aureus agr* subsystem. System influences in red, equations for output variables in blue.

In the same way as above, we non-dimensionalize the equations for the PSM and for δ-toxin, where we also choose the new time scale $\tau = \delta_{M_2} t = \delta_{R_3} t = \delta_{M_{PSM}} t$. We non-dimensionalize using again the stationary points, this time assuming in addition that $P_{PSM} = 0$. The resulting equations are

$$\frac{dP_{PSM}}{d\tau} = b'_{PSM}A'_P(1 - P_{PSM}) - u'_{PSM}P_{PSM}, \tag{4.76}$$

$$\frac{dM'_{PSM}}{d\tau} = 1 + v'_{PSM}P_{PSM} - M'_{PSM}, \tag{4.77}$$

$$\frac{d[PSM]'}{d\tau} = \lambda(M'_{PSM} - [PSM]'), \tag{4.78}$$

$$\frac{df'}{d\tau} = \lambda(D'[PSM]' - f'), \tag{4.79}$$

$$\frac{dR'_3}{d\tau} = 1 + v'_3 P_{agr} - R'_3, \tag{4.80}$$

$$\frac{d[\delta\text{-toxin}]'}{d\tau} = \lambda(R'_3 - [\delta\text{-toxin}]'), \tag{4.81}$$

with the new parameters

$$\lambda := \frac{\delta_{PSM}}{\delta_{M_{PSM}}} = \frac{\delta_f}{\delta_{M_{PSM}}} = \frac{\delta_{\delta-toxin}}{\delta_{R_3}}, \quad b'_{PSM} := \frac{b_{PSM} N m_2 \kappa_{M_2}}{\delta_{R_3}\delta_{M_2}\delta_A}, \quad u'_{PSM} := \frac{u_{PSM}}{\delta_{R_3}},$$
$$v'_{PSM} := \frac{v_{PSM}}{m_{PSM}} \quad \text{and} \quad v'_3 := \frac{v_3}{m_3}.$$

Since in this case all stationary state components are greater zero, the reparametrizations are achieved from the stationary points. For the next system of equations we need the values of $[str]$ and the availability of nutrients. These quantities are already given as non-dimensional values.

4.3.2. The *sarA* system

The next subsystem to be non-dimensionalized is the *sarA* system of regulation with the competitive interaction between σ^B and RsbV for RsbW. The non-dimensional equations with the assumptions $P_{RsbU} = P_\sigma = P_{sarA} = 0$ and $d = b_0 = b_\sigma = b_{sarA} = 0$ and the new timescale $\tau = \delta_{M_2} t = \delta_{M_{RsbU}} t$ are of the form

$$\frac{dP_{RsbU}}{d\tau} = b'_0[str](1 - P_{RsbU}) - u'_0 P_{RsbU}, \tag{4.82}$$
$$\frac{dP_\sigma}{d\tau} = (b'_0 + b'_\sigma[C_1]')[str](1 - P_\sigma) - u'_0 P_\sigma, \tag{4.83}$$
$$\frac{dM'_{RsbU}}{d\tau} = 1 + v'_{RsbU} P_{RsbU} - M'_{RsbU}, \tag{4.84}$$
$$\frac{dM'_\sigma}{d\tau} = 1 + v'_\sigma P_\sigma - M'_\sigma, \tag{4.85}$$
$$\frac{d[RsbU]'}{d\tau} = \lambda(M'_{RsbU} - [RsbU]'), \tag{4.86}$$
$$\frac{d[\sigma^B]'}{d\tau} = \lambda(M'_\sigma - [\sigma^B]'), \tag{4.87}$$
$$\frac{d[RsbV]'}{d\tau} = \lambda(M'_\sigma[RsbU]' - [RsbV]') - d'[RsbV]'[RsbW]', \tag{4.88}$$
$$\frac{d[RsbW]'}{d\tau} = \lambda(M'_\sigma - [RsbW]'), \tag{4.89}$$
$$\frac{dP'_{sarA}}{d\tau} = b'_{sarA}[\sigma^B]'(1 - P_{sarA}) - u'_{sarA} P_{sarA}, \tag{4.90}$$
$$\frac{dM'_{sarA}}{d\tau} = 1 + v'_{sarA} P_{sarA} - M'_{sarA}, \tag{4.91}$$
$$\frac{d[SarA]'}{d\tau} = \lambda(M'_{sarA} - [SarA]'), \tag{4.92}$$

where we use the new parameters

$$b_0' := \frac{b_0}{\delta_{M_{RsbU}}}, \quad u_0' := \frac{u_0}{\delta_{M_{RsbU}}}, \quad b_\sigma' := \frac{b_\sigma}{\delta_{M_{RsbU}}}, \quad v_{RsbU}' := \frac{v_{RsbU}}{m_{RsbU}},$$
$$\lambda := \frac{\delta_{RsbU}}{\delta_{M_{RsbU}}} = \frac{\delta_\sigma}{\delta_{M_\sigma}} = \frac{\delta_{RsbV}}{\delta_{M_{RsbU}}} = \frac{\delta_{RsbW}}{\delta_{M_{RsbU}}} = \frac{\delta_{sarA}}{\delta_{M_{sarA}}}, \quad b_{sarA}' := \frac{b_{sarA} N m_\sigma \kappa_\sigma}{\delta_{M_{RsbU}} \delta_\sigma \delta_{M_\sigma}},$$
$$d' := \frac{d[\widetilde{RsbW}]}{\delta_{M_{RsbU}}} = \frac{d\kappa_\sigma N m_\sigma}{\delta_{M_{RsbU}} \delta_{RsbW} \delta_{M_\sigma}}, \quad u_{sarA}' := \frac{u_{sarA}}{\delta_{M_{RsbU}}} \quad \text{and} \quad v_{sarA}' := \frac{v_{sarA}}{m_{sarA}}.$$

4.3.3. The *ica* system

The *ica* regulation system is non-dimensionalized using the assumptions $P_{ica1} = P_{ica2} = 0$ and $b_{ica1} = b_{ica2} = 0$ and the new timescale $\tau = \delta_{M_2} t = \delta_{M_{ica1}} t$ to obtain the system

$$\frac{dP_{ica1}}{d\tau} = b_{ica1}'(1 - P_{ica1}) - u_{ica1}'[str]P_{ica1}, \tag{4.93}$$
$$\frac{dP_{ica2}}{d\tau} = b_{ica2}'[ica2+]'(1 - P_{ica2}) - u_{ica2}'[ica2-]'P_{ica2}, \tag{4.94}$$
$$\frac{dM_{ica1}'}{d\tau} = 1 + v_{ica1}'P_{ica1} - M_{ica1}', \tag{4.95}$$
$$\frac{dM_{ica2}'}{d\tau} = 1 + v_{ica2}'P_{ica2} - M_{ica2}', \tag{4.96}$$
$$\frac{d[IcaR]'}{d\tau} = \lambda(M_{ica1}' - [IcaR]'), \tag{4.97}$$
$$\frac{d[IcaADBC]'}{d\tau} = \lambda(M_{ica2}' - [IcaADBC]'), \tag{4.98}$$
$$\frac{d[PIA]'}{d\tau} = 2\lambda([IcaADBC]' - [PIA]'), \tag{4.99}$$

where we introduce the new parameters

$$b_{ica1}' := \frac{b_{ica1}}{\delta_{M_{ica1}}}, \quad b_{ica2}' := \frac{b_{ica2} N m_{sarA} \kappa_{sarA}}{\delta_{M_{ica2}} \delta_{M_{sarA}} \delta_{sarA}}, \quad u_{ica1}' := \frac{u_{ica1}}{\delta_{M_{ica1}}},$$
$$u_{ica2}' := \frac{u_{ica2} N^2 m_{ica1}^2 \kappa_{ica1}^2}{\delta_{M_{ica2}} \delta_{M_{ica1}}^2 \delta_{icaR}^2}, \quad v_{ica1}' := \frac{v_{ica1}}{m_{ica1}}, \quad v_{ica2}' := \frac{v_{ica2}}{m_{ica2}}$$
$$\text{and} \quad \lambda := \frac{\delta_{icaR}}{\delta_{M_{ica1}}} = \frac{\delta_{icaADBC}}{\delta_{M_{ica2}}} = \frac{\delta_{PIA}}{\delta_{M_{ica2}}} = \frac{\delta_{\text{add}}}{\delta_{M_{ica2}}}.$$

The non-dimensionalization for $[ica2+]$ is considered separately due to the dependence on the nutrient concentration n. From Equation (4.42) we know that

$[ica2+] = [SarA] + r_{ica2}n(1 - \frac{n}{K_n})$. The reparametrization yields

$$\begin{aligned} b_{ica2}[ica2+] &= b_{ica2}\left(\frac{\kappa_{sarA}Nm_{sarA}}{\delta_{sarA}\delta_{M_{sarA}}}[SarA]' + r_{ica2}n(1-\frac{n}{K_n})\right) \\ &= b'_{ica2}\left([SarA]' + r'_{ica2}n(1-\frac{n}{K_n})\right) = b'_{ica2}[ica2+]'. \end{aligned}$$

Inserting into the differential equation, we verify that the reparametrizations

$$b'_{ica2} := \frac{b_{ica2}\kappa_{sarA}Nm_{sarA}}{\delta_{sarA}\delta_{M_{sarA}}\delta_{M_{ica2}}} = \frac{b_{ica2}[S\widetilde{a}rA]}{\delta_{M_{ica2}}} \quad \text{and} \quad r'_{ica2} := \frac{r_{ica2}}{[S\widetilde{a}rA]}$$

are a good choice. Note that, in the partial differential equation model (4.7)–(4.11), the concentration of nutrients is also non-dimensional.

4.3.4. The *sarA* homologue system

For the *sarA* homologues *sarT*, *sarU* and *sarS*, the corresponding equations are non-dimensionalized with the assumptions $P_{sarT} = P_{sarU} = P_{sarS} = P_{spa} = P_{hla} = 0$ and $b_1 = b_2 = 0$ taking into account the new timescale $\tau = \delta_{M_2}t = \delta_{M_{sarT}}t$ as follows:

We assume that the degradation times for the *sarU* and *sarS* mRNAs are the same as the degradation time for the *sarT* mRNA and obtain the system of equations

$$\frac{dP_{sarT}}{d\tau} = b'_1(1 - P_{sarT}) - u'_2(\alpha[SarA]' + R'_3)P_{sarT}, \tag{4.100}$$
$$\frac{dM'_{sarT}}{d\tau} = 1 + v'_{sarT}P_{sarT} - M'_{sarT}, \tag{4.101}$$
$$\frac{d[SarT]'}{d\tau} = \lambda(M'_{sarT} - [SarT]'), \tag{4.102}$$
$$\frac{dP_{sarU}}{d\tau} = b'_1(1 - P_{sarU}) - u'_1[SarT]'P_{sarU}, \tag{4.103}$$
$$\frac{dM'_{sarU}}{d\tau} = 1 + v'_{sarU}P_{sarU} - M'_{sarU}, \tag{4.104}$$
$$\frac{d[SarU]'}{d\tau} = \lambda(M'_{sarU} - [SarU]'), \tag{4.105}$$
$$\frac{dP_{sarS}}{d\tau} = b'_2[SarT]'(1 - P_{sarS}) - u'_2(\alpha[SarA]' + R'_3)P_{sarS}, \tag{4.106}$$
$$\frac{dM'_{sarS}}{d\tau} = 1 + v'_{sarS}P_{sarS} - M'_{sarS}, \tag{4.107}$$
$$\frac{d[SarS]'}{d\tau} = \lambda(M'_{sarS} - [SarS]'), \tag{4.108}$$
$$\frac{dP_{spa}}{d\tau} = b'_2[SarS]'(1 - P_{spa}) - u'_2(\alpha[SarA]' + R'_3)P_{spa}, \tag{4.109}$$

$$\frac{dM'_{spa}}{d\tau} = 1 + v'_{spa}P_{spa} - M'_{spa}, \tag{4.110}$$

$$\frac{d[\text{protein A}]'}{d\tau} = \lambda(M'_{spa} - [\text{protein A}]'), \tag{4.111}$$

$$\frac{dP_{hla}}{d\tau} = b'_2(\alpha[SarA]' + R'_3)(1 - P_{hla}) - u'_1([SarS]' + [SarT]')P_{hla}, \tag{4.112}$$

$$\frac{dM'_{hla}}{d\tau} = 1 + v'_{hla}P_{hla} - M'_{hla}, \tag{4.113}$$

$$\frac{d[\alpha\text{-toxin}]'}{d\tau} = \lambda(M'_{hla} - [\alpha\text{-toxin}]'). \tag{4.114}$$

The relations between the parameters such as $\frac{b_{sarT}}{\delta_{M_{sarT}}}$ and $\frac{b_{sarU}}{\delta_{M_{sarU}}}$ are comparable and we thus simplify in the following by assuming that these and similar fractions take the same value. With the expressions $[S\widetilde{a}rT] = \frac{\kappa N m_{sarT}}{\delta_{M_{sarT}}\delta_{SarT}}$ and $[S\widetilde{a}rS] = \frac{\kappa N m_{sarS}}{\delta_{M_{sarS}}\delta_{SarS}}$, we obtain that in the above system the new parameters are calculated from the old ones as follows:

$$b'_1 := \frac{b_{sarT}}{\delta_{M_{sarT}}} = \frac{b_{sarU}}{\delta_{M_{sarU}}}, \quad b'_2 := \frac{b_{sarS}[S\widetilde{a}rT]}{\delta_{M_{sarS}}} = \frac{b_{spa}[S\widetilde{a}rS]}{\delta_{M_{spa}}} = \frac{b_{hla}[S\widetilde{a}rT]}{\delta_{M_{hla}}},$$

$$u'_1 := \frac{u_{hla}[S\widetilde{a}rT]}{\delta_{M_{hla}}} = \frac{u_{sarU}[S\widetilde{a}rT]}{\delta_{M_{sarU}}}, \quad u'_2 := \frac{u_{sarT}Nm_3}{\delta_{M_{sarT}}\delta_{R_3}} = \frac{u_{sarS}Nm_3}{\delta_{M_{sarS}}\delta_{R_3}} = \frac{u_{spa}Nm_3}{\delta_{M_{spa}}\delta_{R_3}},$$

$$\alpha := \frac{\kappa_{sarA}}{\delta_{sarA}}, \quad v'_{sarT} := \frac{v_{sarT}}{m_{sarT}}, \quad v'_{sarU} := \frac{v_{sarU}}{m_{sarU}}, \quad v'_{sarS} := \frac{v_{sarS}}{m_{sarS}}, \quad v'_{spa} := \frac{v_{spa}}{m_{spa}},$$

$$v'_{hla} := \frac{v_{hla}}{m_{hla}} \quad \text{and} \quad \lambda := \frac{\delta_{SarT}}{\delta_{M_{sarT}}} = \frac{\delta_{SarU}}{\delta_{M_{sarU}}} = \frac{\delta_{SarS}}{\delta_{M_{sarS}}} = \frac{\delta_{protA}}{\delta_{M_{spa}}} = \frac{\delta_{\alpha}}{\delta_{M_{hla}}}.$$

Note that in the following sections, we use the non-dimensional parameters and variables, while omitting the dashes on both the variables and the parameters for notational convenience.

4.4. Rescaled equations

As in Section 4.3 we keep the separation into subsystems and aim to reduce the submodels such that the remaining equations are those for the evolution of the concentrations of substances that influence another submodel.

For example the influences on the *agr*-system are the amount of bacteria and the amounts of the proteins SarA ($[SarA]$) and SarU ($[SarU]$). From this subsystem, we would like to keep the equations for the substances PSM ($[PSM]$), amyloid fibrils (f) and δ-toxin ($[\delta\text{-toxin}]$) as well as the equation for mRNAIII (R_3). Furthermore, the *sarA* system depends on the stress and nutrient levels and we are interested in

the concentration of SarA. The *ica* system uses the concentration of SarA and from this system the PIA concentration ($[PIA]$) is obtained. The *sarA* homologue system requires the concentrations of mRNAIII and SarA and yields the concentrations of protein A ([protein A]), α-toxin ([α-toxin]) and SarU. Our goal for the entire system is to achieve equations for the variables $[PSM]$, f, [δ-toxin], $[PIA]$, [protein A] and [α-toxin] dependent on the external stress ($[str]$), the concentration of nutrients (n) and the amount of replicative bacteria b in the full model.

First we determine the timescale, on which we consider the regulation processes. This timescale is the timescale of the slow system. Here the scale of interest is the scale in which the system up- and down-regulations happen. Thus the fast regulation processes are considered in relation to the regulations of P_{act} for the gene loci act $\in \{agr, PSM, RsbU, \sigma, sarA, ica1, ica2, sarT, sarU, sarS, spa, hla\}$ of interest. As an example, the changes in the concentration of AgrA, AgrB, AgrC and AgrD as well as those in the concentration of RNA have to be much faster than the reference time scale, since only many of those changes together can achieve a change in the proportion of up-regulated cells.

A recurring equation in the regulation processes is the equation

$$\frac{dP_{\text{act}}}{d\tau} = b_{\text{act}}[\text{act}+](1 - P_{\text{act}}) - u_{\text{act}}[\text{act}-]P_{\text{act}}.$$

Here we introduce the parameter $\hat{\varepsilon}$ since the parameters b_{act} and u_{act} are in fact of order $\hat{\varepsilon} \ll 1$, as this process is slow in comparison to the processes described in the recurring set of equations

$$\begin{aligned} \frac{dM_{\text{act}}}{d\tau} &= 1 + v_{\text{act}}P_{\text{act}} - M_{\text{act}}, \\ \frac{dX}{d\tau} &= \lambda(M_{\text{act}} - X), \end{aligned}$$

where X denotes a substance in the regulation system. We note that, in terms of notation, the *agr* system constitutes a special case, since here mRNAII (M_2) and RNAIII (R_3) have to be considered. For details we refer to Figure 4.6. Thus we rescale using the rescaled parameters, where we introduce $\hat{b}_{\text{act}}$ and $\hat{u}_{\text{act}}$ by the equations

$$b_{\text{act}} = \hat{\varepsilon}\hat{b}_{\text{act}} \qquad \text{and} \qquad u_{\text{act}} = \hat{\varepsilon}\hat{u}_{\text{act}}.$$

On the slow reference time scale $\hat{\tau} := \hat{\varepsilon}\tau$ of the changes in the proportions P_{act} of up-regulated cells, we then obtain the set of equations

$$\frac{dP_{\text{act}}}{d\hat{\tau}} = \hat{b}_{\text{act}}[\text{act}+](1 - P_{\text{act}}) - \hat{u}_{\text{act}}[\text{act}-]P_{\text{act}}, \tag{4.115}$$

$$\hat{\varepsilon}\frac{dM_{\text{act}}}{d\hat{\tau}} = 1 + v_{\text{act}}P_{\text{act}} - M_{\text{act}}, \tag{4.116}$$

$$\hat{\varepsilon}\frac{dX}{d\hat{\tau}} = \lambda(M_{\text{act}} - X). \tag{4.117}$$

Asymptotically, i.e., for $\hat{\varepsilon} \to 0$, the concentrations of the substances M_{act} and X depend on P_{act} in the form $X = M_{\text{act}} = 1 + v_{\text{act}}P_{\text{act}}$, where $v_{\text{act}} = \text{const.}$, which reduces the system [105]. The differential equation for the amount of X on the time scale $\hat{\tau}$ is a direct consequence of the evolution of P_{act} as

$$\frac{dX}{d\hat{\tau}} = v_{\text{act}}\frac{dP_{\text{act}}}{d\hat{\tau}} = v_{\text{act}}(\hat{b}_{\text{act}}[\text{act}+](1 - P_{\text{act}}) - \hat{u}_{\text{act}}[\text{act}-]P_{\text{act}}).$$

We can solve for P_{act} analytically, if [act+] and [act−] do not depend on P_{act} as described in Section 4.5. The connecting principle for all subsystems is that the evolution of the proportion of up-regulated cells is the slowest process. There are some differences between the speeds of the faster processes, some being even faster than others [76]. However, since we consider the processes on the slowest timescale, all the fast processes approach the quasi-steady state in the asymptotic limit. In the following, we use the regular variables b_{act} and u_{act} instead of the hatted ones for notational clarity.

In the processes described in the subsystems there are significant differences between certain rate constants, which are investigated here in order for the resulting description of biofilm formation to be accurate. In agreement with [76], we use the parameter $\varepsilon := \frac{m}{v} < 1$, which represents the relationship between the basal mRNA transcription rate and the regulation-induced transcription, valid for all subsystems. In order for quorum sensing to be effective, the quorum sensing induced regulation takes place faster than the regular effects. Some publications assume ε to be of order 10^{-3} [76]. This modeling assumption is due to the very analytic approach of the paper. Since our focus is directed towards including the results into a PDE model, we take rates similar to the ones introduced in [70]. Both models are consistent in magnitude, but in [70] it is assumed that the activation rates are the largest rates, being five times the degradation rates, about 100 times the rates of spontaneous separations and ten times the sizes of all remaining parameters.

The parameters to be considered for the *agr* system are the regulation speed (v), the binding rate of AIP to AgrC (β) and the activation rate of AgrA by AIP-bound AgrC (ϕ) as well as the dephosphorylation rate of AgrA (μ). The rate constant λ_a is the quotient of the degradation rate of AIP and the degradation and dilution rate of mRNAII. Since we consider the up-regulation process, we assume that the natural degradation outside the cell λ_a is very small [76]. We take most parameters to be close to 1 and choose $\varepsilon = 10^{-1}$. Then we introduce the $O(1)$ parameters $\tilde{v}, \tilde{\beta}, \tilde{\phi}, \tilde{\mu}, \tilde{\lambda}_a$ by

$$v = \frac{\tilde{v}}{\varepsilon}, \qquad \beta = \frac{\tilde{\beta}}{\varepsilon}, \qquad \phi = \frac{\tilde{\phi}}{\varepsilon}, \qquad \mu = \varepsilon\tilde{\mu}, \qquad \lambda_a = \varepsilon\tilde{\lambda}_a. \tag{4.118}$$

Thus in terms of magnitude the activation rates are about 100 times the spontaneous separation rates and 10 times the remaining parameters. These considerations of parameter orders of magnitude will be used in Section 4.5.6 to determine the magnitudes of the parameters in the full system.

4.4.1. The *agr* system

For the *agr* subsystem on the timescale $\hat{\tau}$, we find a subsystem similar to [76] with the concentration $X = B$ and can thus express the amount of AgrB in dependence of the amount of up-regulated cells. We find that only very few concentrations are needed in an explicit form since they provide the connections between the different subsystems. We investigate the *agr* subsystem asymptotically and obtain

$$\begin{aligned}
&M_2 = B = 1 + vP_{agr}, && D = \frac{\lambda M_2}{\lambda + kB} = \frac{\lambda(1 + vP_{agr})}{\lambda + k(1 + vP_{agr})}, && C = \frac{\lambda M_2 + \gamma R}{\lambda + \beta a},\\
&a = \frac{kDB + \gamma R}{\lambda_a + \beta C}, && A = \frac{\lambda M_2 + \mu A_P}{\lambda + \phi R}, && R = \frac{\beta C a}{(\gamma + \lambda)}\\
&\text{and} && A_P = \frac{\phi A R}{\mu + \lambda}.
\end{aligned} \tag{4.119}$$

Now we want to find an explicit form for the concentration of free AIP (a) and for the concentration of phosphorylated AgrA (A_P), which influences the *agr* activity term due to the positive feedback loop. In order to describe the concentration A_P explicitly, we need expressions for the concentrations of AgrA (A) and AIP-bound AgrC (R). A also depends on A_P and R, while R depends on the concentration of AgrC (C) and a. We thus want to find explicit expressions for all these variables in the steady state. We simplify the expression for a using that λ_a is very small, as stated in Equation (4.118). The term for the concentration of free AIP thus

simplifies to

$$a = \frac{kDB + \gamma R}{\lambda_a + \beta C} \overset{\lambda_a \approx 0}{\approx} \frac{kDB + \gamma R}{\beta C}.$$

The approximate expression for a is used to find that $Ca \approx \frac{kDB+\gamma R}{\beta}$ and to find a simpler expression for R given by

$$R = \frac{\beta C a}{\gamma + \lambda} = \frac{kDB + \gamma R}{\gamma + \lambda}.$$

We solve for R to obtain that

$$R = \frac{kDB}{\lambda}. \tag{4.120}$$

This is used to calculate

$$a \approx \frac{k(1+\frac{\gamma}{\lambda})}{\beta}\frac{DB}{C} = \frac{k(1+\frac{\gamma}{\lambda})}{\beta}\frac{DB(\lambda+\beta a)}{(\lambda M_2 + \gamma R)} = \frac{k(1+\frac{\gamma}{\lambda})}{\beta}\frac{\lambda+\beta a}{\frac{\lambda}{D}+\frac{\gamma k}{\lambda}}.$$

Since $B = M_2$ we can replace M_2 in the equation for D and thus find

$$\begin{aligned} a &\approx \frac{k(1+\frac{\gamma}{\lambda})}{\beta}\frac{\lambda}{\frac{\lambda}{D}+\frac{\gamma k}{\lambda}-k(1+\frac{\gamma}{\lambda})} = \frac{k(1+\frac{\gamma}{\lambda})}{\beta}\frac{\lambda}{\frac{\lambda}{D}-k} = \frac{k(1+\frac{\gamma}{\lambda})}{\beta}\frac{1}{\frac{1}{D}-\frac{k}{\lambda}} \\ &= \frac{k(1+\frac{\gamma}{\lambda})}{\beta}\frac{1}{\frac{\lambda+k(1+vP_{agr})}{\lambda(1+vP_{agr})}-\frac{k}{\lambda}} = \frac{k(1+\frac{\gamma}{\lambda})}{\beta}\frac{\lambda(1+vP_{agr})}{\lambda} \\ &= \frac{k(1+\frac{\gamma}{\lambda})}{\beta}(1+vP_{agr}). \end{aligned} \tag{4.121}$$

Inserting Equation (4.120) into the form for A from Equation (4.119) then gives $A = \frac{\lambda M_2 + \mu A_P}{\lambda + \frac{\phi k DB}{\lambda}}$, which is used to find the expression

$$A_P = \frac{\phi A R}{\mu + \lambda} = \frac{\phi(\lambda M_2 + \mu A_P)}{(\mu+\lambda)(\frac{\lambda^2}{kDB}+\phi)}. \tag{4.122}$$

Solving Equation (4.122) for the variable A_P yields

$$\begin{aligned} A_P &= \frac{\phi\lambda M_2}{(\mu+\lambda)(\frac{\lambda^2}{kDB}+\phi)(1-\frac{\phi\mu}{(\mu+\lambda)(\frac{\lambda^2}{kDB}+\phi)})} = \frac{\phi\lambda M_2}{(\mu+\lambda)(\frac{\lambda^2}{kDB}+\phi)-\phi\mu} \\ &= \frac{\phi\lambda(1+vP_{agr})}{(\mu+\lambda)\left[\frac{\lambda(\lambda+k(1+vP_{agr}))}{k(1+vP_{agr})^2}+\phi\right]-\phi\mu} = \frac{\phi\lambda(1+vP_{agr})}{(\mu+\lambda)\frac{\lambda(\lambda+k(1+vP_{agr}))}{k(1+vP_{agr})^2}+\lambda\phi} \end{aligned}$$

$$= \frac{(1+vP_{agr})}{(\mu+\lambda)\frac{\lambda+k(1+vP_{agr})}{k\phi(1+vP_{agr})^2}+1}, \tag{4.123}$$

where we use the known expressions for B and D from Equation (4.119). This equality and Equation (4.67) for P_{agr} form the reduced *agr* subsystem. Note that the velocity of up-regulation v is larger than other terms, and thus dominates the behavior. Other terms such as μ are very small.

Similarly, for the subsystem of PSM and δ-toxin we search expressions for the levels of $[PSM]$, f, [δ-toxin] and R_3. Thus we keep Equation (4.76) for P_{PSM} and, as a result, express the other variables as

$$\begin{aligned} M_{PSM} = [PSM] = 1 + v_{PSM}P_{PSM}, \qquad R_3 = [\delta\text{-toxin}] = 1 + v_3 P_{agr} \\ \text{and} \qquad f = D[PSM] = \frac{1+vP_{agr}}{1+\frac{k}{\lambda}(1+vP_{agr})}(1+v_{PSM}P_{PSM}). \end{aligned} \tag{4.124}$$

Again the velocities v_{PSM} and v_3 are the largest parameters.

4.4.2. The *sarA* system

For this system, we keep Equations (4.82)–(4.83) and Equation (4.90) for the proportions of up-regulated cells P_{RsbU}, P_σ and P_{sarA} on the timescale $\hat{\tau}$. Using these variables, we obtain for the other concentrations that it holds

$$\begin{aligned} M_{RsbU} = [RsbU] = 1 + v_{RsbU}P_{RsbU}, \qquad M_\sigma = [\sigma^B] = [RsbW] = 1 + v_\sigma P_\sigma, \\ [RsbV] = \frac{M_{RsbU}M_\sigma}{1+\frac{d}{\lambda}M_\sigma} = \frac{(1+v_{RsbU}P_{RsbU})(1+v_\sigma P_\sigma)}{1+\frac{d}{\lambda}(1+v_\sigma P_\sigma)} \qquad \text{and} \\ M_{sarA} = [SarA] = 1 + v_{sarA}P_{sarA}. \end{aligned} \tag{4.125}$$

The parameters v_{RsbU}, v_{sarA} and d are considered to be large and we are interested in the amount of SarA depending on the stress and the nutrient levels.

4.4.3. The *ica* system

Using the same principle as in the previous subsystems, we obtain the equations

$$\begin{aligned} M_{ica1} = [IcaR] = 1 + v_{ica1}P_{ica1}, \qquad M_{ica2} = [IcaADBC] = 1 + v_{ica2}P_{ica2} \\ \text{and} \qquad [PIA] = [IcaADBC] = 1 + v_{ica2}P_{ica2}. \end{aligned} \tag{4.126}$$

Furthermore, Equations (4.93) and (4.94) for P_{ica1} and P_{ica2} are included, where the parameters v_{ica1} and v_{ica2} represent the set of large parameters. In order to model the biofilm, we are interested in the resulting concentration of the substance PIA.

4.4.4. The *sarA* homologue system

For this system, we keep Equations (4.100), (4.103), (4.106), (4.109) and (4.112) for P_{SarT}, P_{SarU}, P_{SarS}, P_{spa} and P_{hla}, since we are interested in the quantities of protein A, α-toxin and SarU. In the usual way, we obtain that

$$\begin{aligned} M_{sarT} &= [SarT] = 1 + v_{sarT}P_{sarT}, \qquad M_{sarU} = [SarU] = 1 + v_{sarU}P_{sarU}, \\ M_{sarS} &= [SarS] = 1 + v_{sarS}P_{sarS}, \qquad M_{spa} = [\text{protein A}] = 1 + v_{spa}P_{spa} \\ &\text{and} \qquad M_{hla} = [\alpha\text{-toxin}] = 1 + v_{hla}P_{hla}. \end{aligned} \tag{4.127}$$

In this system the parameters v_{sarT}, v_{sarU}, v_{sarS}, v_{spa} and v_{hla} are considered to be large.

4.5. Modeling of biofilm formation

In the following, we consider in detail the necessary calculations to obtain the desired evolution equations from the reduced system of equations derived in Section 4.4.

4.5.1. Modeling the proportions of up-regulated cells

So far, we have derived a system of fewer evolution equations as well as explicit expressions for the amounts of the substances in direct dependence on the proportion of up-regulated cells. The general form for the development of the proportion of up-regulated cells is stated in Equation (4.115), with the general terms for the activation and inactivation of the up-regulation of a certain regulatory system denoted by [act+] and [act−]. In the following, we distinguish several levels of regulation. For the full system of partial differential equations, only the variables from Equations (4.128)–(4.134) are of interest. Thus, in these equations we assume that in order to have an effect on the regulation in another subsystem, a certain concentration of the substances must be reached. The concentration values calculated in Section 4.4 represent quasi-stationary solutions. This means that, while these variables are approximately stationary and can be calculated explicitly, other variables in the system may still change, for example due to the external input variables, and thus also change the quasi-stationary values. In the following, we

extend this quasi-stationary approach by assuming that also some of the proportions of up-regulated cells P_{act} are in an approximately stationary state. This assumption is taken for those variables P_{act}, which are not directly related to one of the output variables a, $[PSM]$, f, [δ-toxin], $[PIA]$, [protein A] and [α-toxin]. For the directly related P_{act} at the top level of the system we consider the full differential equation, in order to capture possible alterations by changing external concentrations.

For the general form of P_{act} we determine the explicit solution of Equation (4.115) as

$$\begin{aligned} P_{\text{act}}(\hat{\tau}) =& P_{\text{act}}(0)\exp(-(b_{\text{act}}[\text{act}+] + u_{\text{act}}[\text{act}-])\hat{\tau}) \\ &+ \frac{b_{\text{act}}[\text{act}+]}{b_{\text{act}}[\text{act}+] + u_{\text{act}}[\text{act}-]}\left(1 - \exp(-(b_{\text{act}}[\text{act}+] + u_{\text{act}}[\text{act}-])\hat{\tau})\right) \end{aligned}$$

with the initial condition $P_{\text{act}}(0) = 0$. Furthermore, we use an exponential relationship between the number of bacteria and time, i.e., $N = \exp(\frac{\hat{\tau}}{c}) \Leftrightarrow \hat{\tau} = c\ln(N)$, to obtain that

$$P_{\text{act}}(N) = \frac{b_{\text{act}}[\text{act}+]}{b_{\text{act}}[\text{act}+] + u_{\text{act}}[\text{act}-]}(1 - N^{-c(b_{\text{act}}[\text{act}+]+u_{\text{act}}[\text{act}-])}).$$

This allows to eliminate the explicit time dependency by a dependency on the number N of bacteria in the population. Exponential growth is a plausible simplification especially when the bacteria have sufficient supply of nutrients. Since the number of bacteria in the system is large and it holds that $b_{\text{act}}[\text{act}+]$, $u_{\text{act}}[\text{act}-]$ and $c > 0$, it is reasonable to consider the limit $N \to \infty$ as a further approximation. Figure 4.7 shows the fast convergence to $\frac{b_{\text{act}}[\text{act}+]}{b_{\text{act}}[\text{act}+]+u_{\text{act}}[\text{act}-]}$, even for relatively small numbers of bacteria such as $N = 100$. For $c = 1$ and $b_{\text{act}}[\text{act}+] + u_{\text{act}}[\text{act}-] = 1$ we calculate $1 - N^{-c(b_{\text{act}}[\text{act}+]+u_{\text{act}}[\text{act}-])} = 1 - 0.01 = 0.99$. Thus it holds that the relative approximation error $|\frac{P_{\text{act}}(N)-P_{\text{act}}}{P_{\text{act}}}| \leq 1\%$ already for $N \geq 100$, which is equivalent to $\hat{\tau} = \ln(100) \approx 4.61$. Note that for $b_{\text{act}}[\text{act}+] + u_{\text{act}}[\text{act}-] > 1$ the convergence is even faster. As a result we approximate the term $P_{\text{act}}(N)$ further to obtain that

$$P_{\text{act}} \approx \frac{b_{\text{act}}[\text{act}+]}{b_{\text{act}}[\text{act}+] + u_{\text{act}}[\text{act}-]},$$

where the dependence on N is also eliminated.

For the directly related P_{act} we assume that $\frac{dP_{\text{act}}}{d\hat{\tau}} \neq 0$. Thus for these equations in the full system we have $\frac{dX}{d\hat{\tau}} = \frac{dX}{dP_{\text{act}}}\frac{dP_{\text{act}}}{d\hat{\tau}} \neq 0$ and we obtain the following equations

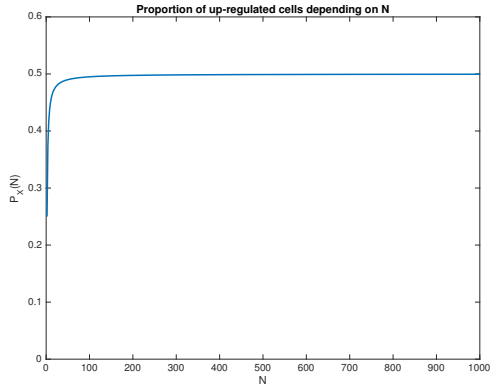

Figure 4.7.: Influence of N on $P_{\text{act}}(N)$ for the parameters $b_{\text{act}}[\text{act}+] = u_{\text{act}}[\text{act}-] = 0.5$, $c = 1$.

on the slow timescale

$$\frac{da}{d\hat{\tau}} = \frac{k(1+\frac{\gamma}{\lambda})}{\beta}\, v\, \frac{dP_{agr}}{d\hat{\tau}}, \tag{4.128}$$

$$\frac{d[PSM]}{d\hat{\tau}} = v_{PSM}\, \frac{dP_{PSM}}{d\hat{\tau}}, \tag{4.129}$$

$$\frac{df}{d\hat{\tau}} = \frac{v(1+v_{PSM}P_{PSM})}{(1+\frac{k}{\lambda}(1+vP_{agr}))^2}\, \frac{dP_{agr}}{d\hat{\tau}} + \frac{v_{PSM}(1+vP_{agr})}{1+\frac{k}{\lambda}(1+vP_{agr})}\, \frac{dP_{PSM}}{d\hat{\tau}}, \tag{4.130}$$

$$\frac{d[\delta\text{-toxin}]}{d\hat{\tau}} = v_3\, \frac{dP_{agr}}{d\hat{\tau}}, \tag{4.131}$$

$$\frac{d[PIA]}{d\hat{\tau}} = v_{ica2}\, \frac{dP_{ica2}}{d\hat{\tau}}, \tag{4.132}$$

$$\frac{d[\text{protein A}]}{d\hat{\tau}} = v_{spa}\, \frac{dP_{spa}}{d\hat{\tau}}, \tag{4.133}$$

$$\frac{d[\alpha\text{-toxin}]}{d\hat{\tau}} = v_{hla}\, \frac{dP_{hla}}{d\hat{\tau}}. \tag{4.134}$$

The next goal is to make the system dependent on the quantities that are involved in the exchange of information between the subsystems and finally derive an expression in terms of the external variables of the system, such as the concentration of AIP denoted by a. To this end we also non-dimensionalize the activation factors [act+]. In order to express these terms in terms of the non-dimensional variables, we insert the expressions found for the non-dimensional dashed variables. For example we see that in the new expression $[agr+]'$ the variables are multiplied by a factor. After sorting by orders of magnitude, we obtain

$$[agr+]' = \frac{Nm_3}{\delta_{R_3}} R_3' + \frac{\kappa_{sarA} N m_{sarA}}{\delta_{sarA}\delta_{M_{sarA}}}[SarA]' + \frac{\kappa_{sarU} N m_{sarU}}{\delta_{sarU}\delta_{M_{sarU}}}[SarU]' + \frac{Nm_2\kappa_{M_2}}{\delta_{M_2}\delta_A} A_P'$$

$$= \frac{Nm_3}{\delta_{R_3}} \left(R_3' + \frac{\kappa_{sarA}}{\delta_{sarA}}[SarA]' + \frac{\kappa_{sarU}}{\delta_{sarU}}[SarU]' + \frac{\kappa_{M_2}}{\delta_A} A_P' \right),$$

where we assume that $m_3 = m_{sarA} = m_{sarU} = m_2$ and $\delta_{R_3} = \delta_{M_{sarA}} = \delta_{M_{sarU}} = \delta_{M_2}$.

Consequently also the factors are assumed to be equal, i.e., $\alpha_{agr} := \frac{\kappa_{sarA}}{\delta_{sarA}} = \frac{\kappa_{sarU}}{\delta_{sarU}} = \frac{\kappa_{M_2}}{\delta_A}$ and thus they are also equal to the parameter $\alpha = \frac{\kappa_{sarA}}{\delta_{sarA}}$ from the *sarA* homologues subsystem in Section 4.3.4. The factor β_{agr} is incorporated into the factor b_{agr} in the differential equation as $b_{agr}' := b_{agr}\beta_{agr}$. This results in a simplified expression for $[agr+]'$, which is stated as

$$\begin{aligned}[agr+]' &= \frac{Nm_3}{\delta_{R_3}} \left(R_3' + \frac{\kappa_{sarA}}{\delta_{sarA}}([SarA]' + [SarU]' + A_P') \right) \\ &= \beta_{agr}(R_3' + \alpha([SarA]' + [SarU]' + A_P')). \end{aligned} \tag{4.135}$$

Again the prime is omitted in the following for notational clarity.

4.5.2. Modeling the concentration of AIP

Since we obtain that $a = \frac{k(1+\frac{\gamma}{\lambda})}{\beta}(1 + vP_{agr})$ from Equation (4.121), we calculate that

$$P_{agr} = \frac{1}{v}\left[\frac{\beta a}{k(1+\frac{\gamma}{\lambda})} - 1\right] = \frac{1}{v}\left[\frac{\beta\lambda a}{k(\lambda+\gamma)} - 1\right]. \tag{4.136}$$

Using Equation (4.124), this leads to

$$R_3 = 1 + v_3 P_{agr} = 1 + \frac{v_3}{v}\left[\frac{\beta\lambda a}{k(\lambda+\gamma)} - 1\right]. \tag{4.137}$$

We furthermore use that $P_{PSM} = \frac{[PSM]-1}{v_{PSM}}$, due to Equation (4.124), to obtain that

$$\frac{df}{d\hat{\tau}} = \frac{v[PSM]}{(1+\frac{a\beta}{\lambda+\gamma})^2}\frac{dP_{agr}}{d\hat{\tau}} + \frac{a\beta\lambda v_{PSM}}{k[(\lambda+\gamma)+\beta a]}\frac{dP_{PSM}}{d\hat{\tau}}.$$

We derive expressions for the derivatives of P_{agr}, P_{PSM} P_{ica2}, P_{spa} and P_{hla} and for $[PSM]$, that depend only on n, $[str]$ and a. To this end it is necessary to express A_P in terms of the external variable a using Equation (4.123) and the expression for P_{agr} from Equation (4.136). This is calculated as

$$A_P = \frac{1 + vP_{agr}}{(\mu+\lambda)\frac{\lambda+k(1+vP_{agr})}{k\phi(1+vP_{agr})^2} + 1} = \frac{\frac{\beta\lambda a}{k(\lambda+\gamma)}}{(\mu+\lambda)\frac{\lambda+k\frac{\beta\lambda a}{k(\lambda+\gamma)}}{k\phi(\frac{\beta\lambda a}{k(\lambda+\gamma)})^2} + 1}$$

$$
\begin{aligned}
&= \frac{k\phi(\frac{\beta\lambda a}{k(\lambda+\gamma)})^3}{(\mu+\lambda)(\lambda+k\frac{\beta\lambda a}{k(\lambda+\gamma)})+k\phi(\frac{\beta\lambda a}{k(\lambda+\gamma)})^2} \\
&= \frac{\phi(\beta\lambda a)^3}{(\mu+\lambda)(\lambda k^2(\lambda+\gamma)^3+k^2\beta\lambda a(\lambda+\gamma)^2)+k\phi(\beta\lambda a)^2(\lambda+\gamma)} \\
&= \frac{\phi(\beta\lambda a)^3}{(\mu+\lambda)\lambda k^2(\lambda+\gamma)^2(\lambda+\gamma+\beta a)+\phi k(\lambda+\gamma)(\beta\lambda a)^2} \\
&= \frac{a^3}{A_1+A_2a+A_3a^2}, \qquad (4.138)
\end{aligned}
$$

where we define

$$
A_1 := \frac{k^2(\mu+\lambda)(\lambda+\gamma)^3}{\phi\beta^3\lambda^2}, \quad A_2 := \frac{k^2(\mu+\lambda)(\lambda+\gamma)^2}{\phi\beta^2\lambda^2}, \quad A_3 := \frac{k(\lambda+\gamma)}{\beta\lambda}. \quad (4.139)
$$

We also replace the concentrations in the *agr* system activation term from Equation (4.135). The first factor that contributes to the regulation is the amount of SarA. Since $[SarA] = 1 + v_{sarA}P_{sarA}$, we consider Equation (4.90) for the proportion P_{sarA}. Then we determine P_σ from Equation (4.83) in order to use the expression $[\sigma^B] = 1 + v_\sigma P_\sigma$ from Equation (4.125). Furthermore, from Equation (4.125) we know that

$$
[RsbV] = \frac{M_{RsbU}M_\sigma}{1+\frac{d}{\lambda}M_\sigma} = \frac{(1+v_{RsbU}P_{RsbU})(1+v_\sigma P_\sigma)}{1+\frac{d}{\lambda}(1+v_\sigma P_\sigma)}.
$$

Since both *rsbV* and *sigB* are transcribed from the P3 operon and, in order to focus on the principal dependencies, we approximate by the assumption that $[RsbV] \approx [\sigma^B]$ in the equation

$$
[C_1] = r_0\frac{[RsbV][str]}{1+[RsbV][str]+[\sigma^B](1-[str])}.
$$

For $r_0 = 1$ this yields the expression

$$
[C_1] = \frac{[str]}{\frac{1}{[RsbV]}+[str]+(1-[str])} \approx [str].
$$

We can thus define

$$
g([str]) := (b_0 + b_\sigma[str])[str]
$$

and rewrite Equation (4.83) for the evolution of P_σ and determine its stationary

solution from the equation

$$\frac{dP_\sigma}{d\hat{\tau}} = g([str])(1 - P_\sigma) - u_\sigma P_\sigma \quad \text{as} \quad P_\sigma = \frac{g([str])}{g([str]) + u_\sigma} =: f([str]).$$

For the expression of $f([str])$, we obtain

$$\begin{aligned} f([str]) &= \frac{g([str])}{g([str]) + u_\sigma} = \frac{(b_0 + b_\sigma[str])[str]}{(b_0 + b_\sigma[str])[str] + u_\sigma} \\ &= \frac{B_1[str] + B_2[str]^2}{B_3 + B_1[str] + B_2[str]^2}, \end{aligned} \tag{4.140}$$

with $B_1 := b_0$, $B_2 := b_\sigma$ and $B_3 := u_\sigma$. Then we use this result to calculate $[\sigma^B]$, using Equation (4.125), as

$$[\sigma^B] = 1 + v_\sigma P_\sigma = 1 + v_\sigma f([str]).$$

Thus, in the following we turn to Equation (4.90) for P_{sarA} and obtain its solution as

$$P_{sarA} = \frac{b_{sarA}[\sigma^B]}{b_{sarA}[\sigma^B] + u_{sarA}}.$$

Using Equation (4.125), we calculate the expression

$$\begin{aligned} [SarA] &:= 1 + v_{sarA}\frac{b_{sarA}[\sigma^B]}{b_{sarA}[\sigma^B] + u_{sarA}} \\ &= 1 + v_{sarA}\frac{b_{sarA}(1 + v_\sigma f([str]))}{u_{sarA} + b_{sarA}(1 + v_\sigma f([str]))}. \end{aligned} \tag{4.141}$$

The evolution equations in the system of the *sarA* homologues are dependent of each other. Given the concentrations that can be calculated for this system, the concentration of SarU is needed as an input for the activation term of the *agr* system. The proportion of *sarU* up-regulated cells P_{sarU} is calculated from Equation (4.103) as

$$P_{sarU} = \frac{b_1}{b_1 + u_1[SarT]}$$

and thus using Equation (4.127) we obtain

$$[SarU] = 1 + v_{sarU}P_{sarU} = 1 + v_{sarU}\frac{b_1}{b_1 + u_1[SarT]}.$$

Therefore the concentration of SarU depends on the unknown concentration of SarT, which is determined in the following.

In order to determine the concentration of SarT, we consider the system of equations for the regulations of the gene loci *sarT*, *sarU* and *sarS*, which reads

$$\begin{aligned}
\frac{dP_{sarT}}{d\hat{\tau}} &= b_1(1 - P_{sarT}) - u_2(\alpha[SarA] + R_3)P_{sarT}, \\
\frac{dP_{sarU}}{d\hat{\tau}} &= b_1(1 - P_{sarU}) - u_1[SarT]P_{sarU}, \\
\frac{dP_{sarS}}{d\hat{\tau}} &= b_2[SarT](1 - P_{sarS}) - u_2(\alpha[SarA] + R_3)P_{sarS}.
\end{aligned}$$

They have the quasi-steady state solutions

$$\begin{aligned}
P_{sarT} &= \frac{b_1}{b_1 + u_2(\alpha[SarA] + R_3)}, \\
P_{sarU} &= \frac{b_1}{b_1 + u_1[SarT]}, \\
P_{sarS} &= \frac{b_2[SarT]}{b_2[SarT] + u_2(\alpha[SarA] + R_3)},
\end{aligned}$$

if the interdependence can be accounted for by the expression of the terms through the external variables such as the concentration of AIP (a) and the stress level ($[str]$). We thus start by determining P_{sarT}, which depends on the concentrations of SarA and mRNAIII, determined outside the subsystem for the *sarA* homologues. From the term for P_{sarT} we then calculate the concentration of SarT using Equation (4.127). Due to Equation (4.137), Equation (4.141) and the form of the solution P_{sarT}, we obtain the following result

$$\begin{aligned}
P_{sarT} &= \frac{b_1}{b_1 + u_2(\alpha[SarA] + R_3)} \\
&= b_1 \cdot \left[b_1 + u_2(\alpha + 1 - \frac{v_3}{v}) + \frac{u_2 v_3 \beta \lambda a}{vk(\lambda + \gamma)} + \frac{u_2 \alpha v_{sarA} b_{sarA}(1 + v_\sigma f([str]))}{b_{sarA}(1 + v_\sigma f([str])) + u_{sarA}} \right]^{-1}.
\end{aligned}$$

We then define A, B such that it holds that $P_{sarT} = b_1 \left[\frac{A}{B}\right]^{-1}$ and write A and B in the form

$$A = K_1 + K_2 a + (K_3 + K_4 a) f([str]) \quad \text{and} \quad B = b_{sarA} + u_{sarA} + b_{sarA} v_\sigma f([str]).$$

In these equations the constants K_i, $i \in \{1, \ldots, 4\}$ are defined as

$$\begin{aligned}
K_1 &:= u_2 \alpha v_{sarA} b_{sarA} + \left(b_1 + u_2(\alpha + 1 - \frac{v_3}{v})\right)(b_{sarA} + u_{sarA}),\\
K_2 &:= \frac{u_2 \beta \lambda v_3}{vk(\lambda + \gamma)}(b_{sarA} + u_{sarA}),\\
K_3 &:= \left[u_2 \alpha v_{sarA} + b_1 + u_2(\alpha + 1 - \frac{v_3}{v})\right] b_{sarA} v_\sigma \qquad \text{and}\\
K_4 &:= \frac{u_2 \beta \lambda v_3}{vk(\lambda + \gamma)} b_{sarA} v_\sigma.
\end{aligned}$$

Thus, we obtain from Equation (4.127) that for the concentration of SarT the following equation holds:

$$[SarT] = 1 + v_{sarT} b_1 \frac{B}{A} = 1 + v_{sarT} \frac{T_1 + T_2 f([str])}{K_1 + K_2 a + (K_3 + K_4 a) f([str])}. \tag{4.142}$$

In the above equation the parameters T_1 and T_2 are defined as

$$T_1 := b_1(b_{sarA} + u_{sarA}) \qquad \text{and} \qquad T_2 := b_1 b_{sarA} v_\sigma.$$

For the expression of the SarU concentration we again use Equation (4.127) to obtain

$$\begin{aligned}
[SarU] &= 1 + v_{sarU} P_{sarU} = 1 + v_{sarU} \frac{b_1}{b_1 + u_1 [SarT]}\\
&= 1 + v_{sarU} \frac{b_1 A}{(b_1 + u_1)A + u_1 v_{sarT} b_1 B}\\
&= 1 + v_{sarU}\, b_1 \frac{K_1 + K_2 a + (K_3 + K_4 a) f([str])}{K_5 + K_2 a + (K_6 + K_4 a) f([str])},
\end{aligned} \tag{4.143}$$

with the new parameters

$$\begin{aligned}
K_5 &:= (b_1 + u_1) K_1 + u_1 v_{sarT} b_1 (b_{sarA} + u_{sarA}),\\
K_6 &:= (b_1 + u_1) K_3 + u_1 v_{sarT} b_1 b_{sarA} v_\sigma.
\end{aligned}$$

The expression for SarS is calculated in the same way as those for SarT and SarA and is needed for the regulation of *spa* activity and thus the production of protein A. We use Equation (4.127) and calculate P_{sarS} to be

$$P_{sarS} = \frac{[SarT]}{[SarT] + \frac{u_2}{b_2}(\alpha [SarA] + R_3)}$$

$$
\begin{aligned}
&= \frac{1 + v_{sarT}\frac{b_1}{b_1+u_2(\alpha[SarA]+R_3)}}{1 + v_{sarT}\frac{b_1}{b_1+u_2(\alpha[SarA]+R_3)} + \frac{u_2}{b_2}(\alpha[SarA] + R_3)} \\
&= \frac{b_1(1 + v_{sarT}) + u_2(\alpha[SarA] + R_3)}{b_1(1 + v_{sarT}) + u_2\left(1 + \frac{b_1}{b_2}\right)(\alpha[SarA] + R_3) + \frac{u_2^2}{b_2}(\alpha[SarA] + R_3)^2} \\
&\approx \frac{b_1(1 + v_{sarT}) + u_2\left(\alpha\left(1 + v_{sarA}\frac{f([str])}{B_5+f([str])}\right) + 1 + \frac{v_3}{v}\left[\frac{\beta\lambda a}{k(\lambda+\gamma)} - 1\right]\right)}{b_1(1 + v_{sarT}) + u_2\left(1 + \frac{b_1}{b_2}\right)\left(\alpha\left(1 + v_{sarA}\frac{f([str])}{B_5+f([str])}\right) + 1 + \frac{v_3}{v}\left[\frac{\beta\lambda a}{k(\lambda+\gamma)} - 1\right]\right)} \\
&\qquad + \frac{u_2^2}{b_2}\left(\alpha\left(1 + v_{sarA}\frac{f([str])}{B_5+f([str])}\right) + 1 + \frac{v_3}{v}\left[\frac{\beta\lambda a}{k(\lambda+\gamma)} - 1\right]\right)^2 \\
&= \frac{b_1(1 + v_{sarT}) + u_2\left(1 + \alpha - \frac{v_3}{v}\right) + u_2\alpha v_{sarA}\frac{f([str])}{B_5+f([str])} + u_2\frac{v_3}{v}\frac{\beta\lambda a}{k(\lambda+\gamma)}}{b_1(1 + v_{sarT}) + u_2\left(1 + \frac{b_1}{b_2}\right)\left(1 + \alpha - \frac{v_3}{v}\right) + u_2\left(1 + \frac{b_1}{b_2}\right)\left[\alpha v_{sarA}\frac{f([str])}{B_5+f([str])}\right.} \\
&\qquad \left. + \frac{v_3}{v}\frac{\beta\lambda a}{k(\lambda+\gamma)}\right] + \frac{u_2^2}{b_2}\left[1 + \alpha - \frac{v_3}{v} + u_2\alpha v_{sarA}\frac{f([str])}{B_5+f([str])} + \frac{v_3}{v}\frac{\beta\lambda a}{k(\lambda+\gamma)}\right]^2 \\
&= \frac{S_1 + S_2\frac{f([str])}{B_5+f([str])} + S_3 a}{S_4 + S_5\frac{f([str])}{B_5+f([str])} + S_6 a + \left[S_7 + S_8\frac{f([str])}{B_5+f([str])} + S_9 a\right]^2}. \qquad (4.144)
\end{aligned}
$$

Here the new parameters S_i, $i \in \{1, \ldots, 9\}$ are defined as

$$
\begin{aligned}
&S_1 := b_1(1 + v_{sarT}) + u_2\left(1 + \alpha - \frac{v_3}{v}\right), \qquad S_2 := u_2\alpha v_{sarA}, \\
&S_3 := u_2\frac{v_3}{v}\frac{\beta\lambda}{k(\lambda+\gamma)}, \qquad S_4 := b_1\left(1 + v_{sarT}\right) + u_2\left(1 + \frac{b_1}{b_2}\right)\left(1 + \alpha - \frac{v_3}{v}\right), \\
&S_5 := \left(1 + \frac{b_1}{b_2}\right)S_2, \qquad S_6 := \left(1 + \frac{b_1}{b_2}\right)S_3, \qquad S_7 := \frac{u_2}{b_2^{1/2}}\left(1 + \alpha - \frac{v_3}{v}\right), \\
&S_8 := \frac{u_2}{b_2^{1/2}}S_2 \qquad \text{and} \qquad S_9 := \frac{1}{b_2^{1/2}}S_3.
\end{aligned}
$$

The expressions for the concentrations of mRNAIII (R_3) and phosphorylated AgrA (A_P) from Equation (4.137) and Equations (4.138)–(4.139) together with Equation (4.141) and Equation (4.143) for the concentrations of SarA and SarU are now used to rewrite Equation (4.135) and thus the evolution of P_{agr}.

Furthermore, we use that $P_{agr} = \frac{1}{v}\left[\frac{\beta\lambda a}{k(\lambda+\gamma)} - 1\right]$ according to Equation (4.136) and obtain

$$
\begin{aligned}
&\frac{dP_{agr}}{d\hat{\tau}} = b_{agr}[agr+](1 - P_{agr}) - u_{agr}[agr-]P_{agr} \\
&= b_{agr}[agr+]\left(1 + \frac{1}{v} - \frac{\beta\lambda a}{vk(\lambda+\gamma)}\right) - u_{agr}[agr-]\frac{1}{v}\left[\frac{\beta\lambda a}{k(\lambda+\gamma)} - 1\right]
\end{aligned}
$$

$$
\begin{aligned}
&= b_{agr}\left[R_3 + \alpha([SarA] + [SarU] + A_P)\right]\left(1 + \frac{1}{v} - \frac{\beta\lambda a}{vk(\lambda+\gamma)}\right) \\
&- u_{agr}[\sigma^B]\left[\frac{\beta\lambda a}{vk(\lambda+\gamma)} - \frac{1}{v}\right] \\
&= b_{agr}\left(1 + \frac{1}{v} - \frac{\beta\lambda a}{vk(\lambda+\gamma)}\right)\left[1 + 2\alpha - \frac{v_3}{v} + \frac{v_3}{v}\frac{\beta\lambda a}{k(\lambda+\gamma)}\right. \\
&+ \alpha v_{sarA}\frac{b_{sarA}(1+v_\sigma f([str]))}{u_{sarA} + b_{sarA}(1+v_\sigma f([str]))} + \alpha v_{sarU} b_1 \frac{K_1 + K_2 a + (K_3 + K_4 a) f([str])}{K_5 + K_2 a + (K_6 + K_4 a) f([str])} \\
&\left. + \alpha\frac{a^3}{A_1 + A_2 a + A_3 a^2}\right] - u_{agr}\left(1 + v_\sigma f([str])\right)\left[\frac{\beta\lambda a}{vk(\lambda+\gamma)} - \frac{1}{v}\right].
\end{aligned}
$$

This is equivalent to a general term of the form

$$
\begin{aligned}
\frac{dP_{agr}}{d\hat{\tau}} &= (C_1 - C_2 a)\left[C_3 + C_4 f([str]) + C_5 a + C_6\frac{1 + v_\sigma f([str])}{C_7 + 1 + v_\sigma f([str])}\right. \\
&\left. + C_8\frac{K_1 + K_2 a + (K_3 + K_4 a) f([str])}{K_5 + K_2 a + (K_6 + K_4 a) f([str])} + \frac{a^3}{A_1 + A_2 a + A_3 a^2}\right] - (C_9 + C_{10} f([str])),
\end{aligned} \tag{4.145}
$$

with $f([str])$ as defined in Equation (4.140) and the new parameters C_i, where $i \in \{1, \ldots, 10\}$, given by

$$
\begin{aligned}
C_1 &:= b_{agr}\left(1 + \frac{1}{v}\right), \qquad C_2 := b_{agr}\frac{\beta\lambda}{vk(\lambda+\gamma)}, \qquad C_3 := 1 + 2\alpha - \frac{v_3}{v} + \frac{u_{agr}}{b_{agr}}, \\
C_4 &:= \frac{u_{agr}}{b_{agr}} v_\sigma, \qquad C_5 := \frac{\beta\lambda}{vk(\lambda+\gamma)} v_3, \qquad C_6 := \alpha v_{sarA}, \qquad C_7 := \frac{u_{sarA}}{b_{sarA}}, \\
C_8 &:= \alpha v_{sarU} b_1, \qquad C_9 := u_{agr} \qquad \text{and} \qquad C_{10} := u_{agr} v_\sigma.
\end{aligned}
$$

We further reduce the expression for SarA from Equation (4.141) by using that $1 + v_\sigma f([str]) \approx v_\sigma f([str])$. Thus we obtain in Equation (4.145) that

$$
C_6\frac{1 + v_\sigma f([str])}{C_7 + 1 + v_\sigma f([str])} \approx C_6\frac{v_\sigma f([str])}{C_7 + v_\sigma f([str])} = C_6\frac{f([str])}{B_5 + f([str])} \tag{4.146}
$$

with $B_5 := \frac{C_7}{v_\sigma} = \frac{u_{sarA}}{b_{sarA} v_\sigma}$. Then Equation (4.145) reads

$$
\begin{aligned}
\frac{dP_{agr}}{d\hat{\tau}} &= (C_1 - C_2 a)\left[C_3 + C_4 f([str]) + C_5 a + C_6\frac{f([str])}{B_5 + f([str])}\right. \\
&\left. + C_8\frac{K_1 + K_2 a + (K_3 + K_4 a) f([str])}{K_5 + K_2 a + (K_6 + K_4 a) f([str])} + \frac{a^3}{A_1 + A_2 a + A_3 a^2}\right] - (C_9 + C_{10} f([str])).
\end{aligned} \tag{4.147}
$$

We see that *agr* up-regulation is dependent on the stress level and on the concentration of AIP. With the corresponding evolution for $\frac{dP_{agr}}{d\hat{\tau}}$ from Equation (4.147)

we obtain the differential equation for AIP that reads

$$\begin{aligned}\frac{da}{d\hat{\tau}} &= \frac{k(1+\frac{\gamma}{\eta})}{\beta}\, v\, \frac{dP_{agr}}{d\hat{\tau}} \\ &= C_{11}(C_1 - C_2 a)\Bigg[C_3 + C_4 f([str]) + C_5 a + C_6 \frac{f([str])}{B_5 + f([str])} \\ &+ C_8 \frac{K_1 + K_2 a + (K_3 + K_4 a) f([str])}{K_5 + K_2 a + (K_6 + K_4 a) f([str])} + \frac{a^3}{A_1 + A_2 a + A_3 a^2}\Bigg] - C_{11}(C_9 + C_{10} f([str])).\end{aligned} \tag{4.148}$$

with the new parameter C_{11} defined as $C_{11} := \frac{k(1+\frac{\gamma}{\eta})}{\beta} v$.

4.5.3. Modeling the concentrations of PSM, amyloid fibrils and δ-toxin

The next evolution equation to be investigated is Equation (4.76) for the evolution of P_{PSM}. PSM molecules enable the lysis of cells to gain nutrients. This equation constitutes a special case since here the regulation and the production of the regulator substance take place at the same level. We insert the term $A_P = \frac{a^3}{A_1 + A_2 a + A_3 a^2}$ from Equation (4.138) to obtain the equation

$$\frac{dP_{PSM}}{d\hat{\tau}} = b_{PSM} \frac{a^3}{A_1 + A_2 a + A_3 a^2}(1 - P_{PSM}) - u_{PSM} P_{PSM}.$$

This means that an increase in the PSM concentration is positively influenced by the concentration of free AIP, i.e., the presence of quorum sensing. Due to abundant nutrient supply in the medium and a homogeneous bacteria population, cell lysis only plays a minor role and the concentration of PSM is not included explicitly.

The evolution of the concentration of amyloid fibrils in Equation (4.130) is a direct result of the up-regulation mechanism for PSM production and of the *agr* activity. Since we do not include the evolution of P_{PSM} and since amyloid fibrils are most important in *in vivo* settings, Equation (4.130) is not investigated further here, but we note that the model can be extended accordingly if required and that we obtain important information for adapting the parameter values.

Equation (4.131) for δ-toxin only differs from Equation (4.147) for P_{agr} by the factor v_3 and can thus be derived without further calculation. This is in accordance with experimental results, as the amount of δ-toxin is directly related to *agr* activity. The substance δ-toxin inhibits spreading of the colony. Thus, it is used in the

spreading term of the active bacteria in the full model. Furthermore, δ-toxin, and thus *agr* activity, inhibits biofilm formation [111].

4.5.4. Modeling the concentrations of PIA, protein A and α-toxin

In order to investigate the concentration of PIA according to Equation (4.132), we consider regulation at the *ica* locus. From the evolution of P_{ica2} according to Equation (4.94), we find with Equation (4.42) that

$$\frac{dP_{ica2}}{d\hat{\tau}} = b_{ica2}\left([SarA] + r_{ica2}n\left(1 - \frac{n}{K_n}\right)\right)(1 - P_{ica2}) - u_{ica2}[IcaR]^2 P_{ica2}.$$

The terms in this equation are known since the concentration of SarA is calculated from Equation (4.141) and the concentration of nutrients (n) is explicitly included in the full model.

The evolution of P_{ica1} is described according to Equation (4.93), which has the stationary solution $P_{ica1} = \frac{b_{ica1}}{b_{ica1}+u_{ica1}[str]}$. This is then used to determine the concentration of IcaR from Equation (4.126) as

$$[IcaR] = 1 + v_{ica1}P_{ica1} = 1 + v_{ica1}\frac{b_{ica1}}{b_{ica1} + u_{ica1}[str]}.$$

Thus, with the expression for $[PIA]$ from Equation (4.126) and Equation (4.94) we calculate

$$\begin{aligned}
\frac{d[PIA]}{d\hat{\tau}} &= v_{ica2}\frac{dP_{ica2}}{d\hat{\tau}} \\
&= v_{ica2}\Bigg(b_{ica2}\left([SarA] + r_{ica2}n\left(1 - \frac{n}{K_n}\right)\right)(1 - P_{ica2}) \\
&\quad - u_{ica2}\left(1 + v_{ica1}\frac{b_{ica1}}{b_{ica1} + u_{ica1}[str]}\right)^2 P_{ica2}\Bigg) \\
&= v_{ica2}\Bigg(b_{ica2}\left([SarA] + r_{ica2}n\left(1 - \frac{n}{K_n}\right)\right)\left(1 - \frac{[PIA] - 1}{v_{ica2}}\right) \\
&\quad - u_{ica2}\left(1 + v_{ica1}\frac{b_{ica1}}{b_{ica1} + u_{ica1}[str]}\right)^2 \frac{[PIA] - 1}{v_{ica2}}\Bigg) \\
&= b_{ica2}\left([SarA] + r_{ica2}n\left(1 - \frac{n}{K_n}\right)\right)(1 + v_{ica2} - [PIA]) \\
&\quad - u_{ica2}\left(1 + v_{ica1}\frac{b_{ica1}}{b_{ica1} + u_{ica1}[str]}\right)^2 ([PIA] - 1),
\end{aligned}$$

where n denotes the nutrient concentration. With Equation (4.146), the above equation approximately reduces to the equation

$$\begin{aligned}\frac{d[PIA]}{d\hat{\tau}} &\approx b_{ica2}\left(1+v_{sarA}\frac{f([str])}{B_5+f([str])}+r_{ica2}n\left(1-\frac{n}{K_n}\right)\right)(v_{ica2}-[PIA])\\ &\quad-\frac{u_{ica2}b_{ica1}^2v_{ica1}^2}{(b_{ica1}+u_{ica1}[str])^2}([PIA]-1)\\ &=\left[P_1+P_2\frac{f([str])}{B_5+f([str])}+P_3n\left(1-\frac{n}{K_n}\right)\right](P_4-[PIA])\\ &\quad-\frac{P_5}{(P_6+[str])^2}([PIA]-1),\end{aligned}\tag{4.149}$$

with the new parameters

$$\begin{aligned}&P_1:=b_{ica2}, \qquad P_2:=b_{ica2}v_{sarA}, \qquad P_3:=b_{ica2}r_{ica2}, \qquad P_4:=v_{ica2},\\ &P_5:=\frac{u_{ica2}b_{ica1}^2v_{ica1}^2}{u_{ica1}^2} \qquad \text{and} \qquad P_6:=\frac{b_{ica1}}{u_{ica1}}.\end{aligned}$$

Thus, the evolution equation for PIA is written in dependence of the substance itself and the external variables n and $[str]$. PIA is considered to be a main biofilm indicator, thus from this equation the principal form of the biofilm evolution is obtained.

The concentrations of *spa* and *hla* up-regulated cells are called P_{spa} and P_{hla}, respectively, and evolve according to Equation (4.109) and Equation (4.112). Furthermore, we know the expressions for $[SarA]$, $[SarS]$ and R_3 from Equation (4.146), Equation (4.127) with Equation (4.144) and Equation (4.137).

Thus, we use the expression for protein A from Equation (4.127) to obtain that

$$\begin{aligned}&\frac{d[\text{prot A}]}{d\hat{\tau}}=v_{spa}\frac{dP_{spa}}{d\hat{\tau}}=v_{spa}\left[b_2[SarS](1-P_{spa})-u_2(\alpha[SarA]+R_3)P_{spa}\right]\\ &=v_{spa}\left[b_2[SarS]\left(1-\frac{[\text{prot A}]-1}{v_{spa}}\right)-u_2(\alpha[SarA]+R_3)\frac{[\text{prot A}]-1}{v_{spa}}\right]\\ &=b_2[SarS](1+v_{spa}-[\text{prot A}])-u_2(\alpha[SarA]+R_3)([\text{prot A}]-1)\\ &\approx\left(b_2+\frac{b_2\,v_{sarS}\left(S_1+S_2\frac{f([str])}{B_5+f([str])}+S_3a\right)}{S_4+S_5\frac{f([str])}{B_5+f([str])}+S_6a+\left[S_7+S_8\frac{f([str])}{B_5+f([str])}+S_9a\right]^2}\right)(1+v_{spa}-[\text{prot A}])\\ &\quad-u_2\left(\alpha\left(1+v_{sarA}\frac{f([str])}{B_5+f([str])}\right)+\left(1+\frac{v_3}{v}\left[\frac{\beta\lambda a}{k(\lambda+\gamma)}-1\right]\right)\right)([\text{prot A}]-1)\end{aligned}$$

$$
\begin{aligned}
&= \left(b_2 + \frac{b_2\, v_{sarS} \left(S_1 + S_2 \frac{f([str])}{B_5 + f([str])} + S_3 a \right)}{S_4 + S_5 \frac{f([str])}{B_5 + f([str])} + S_6 a + \left[S_7 + S_8 \frac{f([str])}{B_5 + f([str])} + S_9 a \right]^2} \right) (1 + v_{spa} - [\text{prot A}]) \\
&\quad - \left(u_2 \left(1 + \alpha - \frac{v_3}{v} \right) + S_2 \frac{f([str])}{B_5 + f([str])} + S_3 a \right) ([\text{prot A}] - 1) \\
&= \left(D_1 + D_2 \frac{S_1 + S_2 \frac{f([str])}{B_5 + f([str])} + S_3 a}{S_4 + S_5 \frac{f([str])}{B_5 + f([str])} + S_6 a + \left[S_7 + S_8 \frac{f([str])}{B_5 + f([str])} + S_9 a \right]^2} \right) (D_3 - [\text{prot A}]) \\
&\quad - \left(D_4 + S_2 \frac{f([str])}{B_5 + f([str])} + S_3 a \right) ([\text{prot A}] - 1),
\end{aligned}
$$

with the parameters

$$
D_1 := b_2, \quad D_2 := b_2 v_{sarS}, \quad D_3 := 1 + v_{spa} \quad \text{and} \quad D_4 := u_2 \left(1 + \alpha - \frac{v_3}{v} \right).
$$

The evolution equation for protein A has a form which depends on $[str]$, a and the concentration of protein A. We note that *agr* activity, represented by the concentration of AIP, is crucial for this equation.

Cell-to-cell interaction in biofilm formation is regulated by α-toxin. In addition to the evolution equations mentioned for the derivation of the equation for protein A, here we use that $[SarT]$ is given according to Equation (4.142). Analogously to the above derivation, we use that $[\alpha\text{-toxin}] = 1 + v_{hla} P_{hla}$ from Equation (4.127) to obtain that

$$
\begin{aligned}
&\frac{d[\alpha\text{-toxin}]}{d\hat{\tau}} = v_{hla} \frac{dP_{hla}}{d\hat{\tau}} \\
&= v_{hla} (b_2 (\alpha [SarA] + R_3)(1 - P_{hla}) - u_1 ([SarS] + [SarT]) P_{hla}) \\
&= v_{hla} \left(b_2 (\alpha [SarA] + R_3) \left(1 - \frac{[\alpha\text{-toxin}] - 1}{v_{hla}} \right) - u_1 ([SarS] + [SarT]) \frac{[\alpha\text{-toxin}] - 1}{v_{hla}} \right) \\
&= b_2 (\alpha [SarA] + R_3)(1 + v_{hla} - [\alpha\text{-toxin}]) - u_1 ([SarS] + [SarT])([\alpha\text{-toxin}] - 1) \\
&\approx b_2 \left(\alpha \left(1 + v_{sarA} \frac{f([str])}{B_5 + f([str])} \right) + \left(1 + \frac{v_3}{v} \left[\frac{\beta \lambda a}{k(\lambda + \gamma)} - 1 \right] \right) \right) (1 + v_{hla} - [\alpha\text{-toxin}]) \\
&\quad - u_1 \left(2 + v_{sarS} \frac{S_1 + S_2 \frac{f([str])}{B_5 + f([str])} + S_3 a}{S_4 + S_5 \frac{f([str])}{B_5 + f([str])} + S_6 a + \left[S_7 + S_8 \frac{f([str])}{B_5 + f([str])} + S_9 a \right]^2} \right. \\
&\quad \left. + v_{sarT} \frac{T_1 + T_2 f([str])}{K_1 + K_2 a + (K_3 + K_4 a) f([str])} \right) ([\alpha\text{-toxin}] - 1)
\end{aligned}
$$

$$
\begin{aligned}
&= b_2 \left(1 + \alpha - \frac{v_3}{v} + \alpha v_{sarA} \frac{f([str])}{B_5 + f([str])} + \frac{v_3}{v} \frac{\beta \lambda a}{k(\lambda + \gamma)}\right) (1 + v_{hla} - [\alpha\text{-toxin}]) \\
&\quad - u_1 \Bigg(2 + v_{sarS} \frac{S_1 + S_2 \frac{f([str])}{B_5 + f([str])} + S_3 a}{S_4 + S_5 \frac{f([str])}{B_5 + f([str])} + S_6 a + \left[S_7 + S_8 \frac{f([str])}{B_5 + f([str])} + S_9 a \right]^2} \\
&\quad + v_{sarT} \frac{T_1 + T_2 f([str])}{K_1 + K_2 a + (K_3 + K_4 a) f([str])} \Bigg) ([\alpha\text{-toxin}] - 1) \\
&= \left(E_1 + E_2 \frac{f([str])}{B_5 + f([str])} + E_3 a \right) (E_4 - [\alpha\text{-toxin}]) \\
&\quad - \Bigg(E_5 + E_6 \frac{S_1 + S_2 \frac{f([str])}{B_5 + f([str])} + S_3 a}{S_4 + S_5 \frac{f([str])}{B_5 + f([str])} + S_6 a + \left[S_7 + S_8 \frac{f([str])}{B_5 + f([str])} + S_9 a \right]^2} \\
&\quad + E_7 \frac{T_1 + T_2 f([str])}{K_1 + K_2 a + (K_3 + K_4 a) f([str])} \Bigg) ([\alpha\text{-toxin}] - 1),
\end{aligned}
$$

with the parameters

$$
\begin{aligned}
&E_1 := b_2 \left(1 + \alpha - \frac{v_3}{v}\right), \quad E_2 := b_2 \alpha v_{sarA}, \quad E_3 := b_2 \frac{v_3 \beta \lambda}{v k (\lambda + \gamma)}, \quad E_5 := 2u_1, \\
&E_4 := 1 + v_{hla}, \quad E_6 := u_1 v_{sarS} \qquad \text{and} \quad E_7 := u_1 v_{sarT}.
\end{aligned}
$$

Thus, also here we have found a form that depends on $[str]$, a and the concentration of α-toxin itself.

4.5.5. Derivation of the reaction and diffusion terms in the full model

In the previous Sections 4.5.2, 4.5.3 and 4.5.4, we have achieved a reduced system of equations, which allows to determine the evolution of the concentrations of the biofilm factors AIP, amyloid fibrils, PSM, protein A, δ-toxin (Hld), α-toxin (Hla) and PIA in time. The concentrations of these biofilm factors have very distinct effects on *S. aureus* biofilm formation, which are considered in detail in this section.

Although *S. aureus* bacteria do not have a flagella, they are able to spread on soft agar with a velocity of approximately $100 \frac{\mu \mathrm{m}}{\mathrm{min}}$. This spread is inhibited during the stationary growth phase by the secretion of inhibitors against colony-spreading [111]. The inhibitory activity can be measured for different *S. aureus* strains, taking one unit of colony-spreading inhibitory activity as the fraction that inhibits colony-spreading by 50%. An important inhibitor of colony-spreading is the protein δ-toxin.

Note that δ-toxin inhibits colony-spreading without having an effect on the growth rate of *S. aureus* [111]. The concentration of δ-toxin is therefore included into the replicative bacteria diffusion. From Equation (4.128) and Equation (4.131) we conclude that the development of the concentration of δ-toxin is proportional to that of the AIP concentration as

$$\frac{d[\delta\text{-toxin}]}{d\hat{\tau}} = \frac{v_3\beta}{vk(1+\frac{\gamma}{\eta})}\frac{da}{d\hat{\tau}}.$$

We define $\alpha_q := \frac{v_3\beta}{vk(1+\frac{\gamma}{\eta})}$ and observe that both concentrations are zero initially. Thus we assume that $[\delta\text{-toxin}] = \alpha_q a$ and divide by the factor $1+\alpha_q q$ in the diffusion of the replicative bacteria, where q denotes the concentration of the quorum sensing substance AIP in the full system.

Other PSM, like PSM-α and PSM-β, are stimulants of biofilm-spreading [33, 111]. They are able to lyse eukaryotic cells, especially in competitive settings with several bacteria types, due to their ability to destroy non-specific biological membranes [33]. The POPC vesicle lysing capacity is highest for PSM-β, a bit lower for PSM-α and lowest for δ-toxin [54]. We account for changes in the PSM concentrations by altering several parameter values accordingly. In *psm-α* and/or *psm-β* mutants, PSM-induced lysing is not available and thus the bacteria growth parameters G_1 and G_2 are smaller than in the wildtype bacterium. Furthermore, mutants lack biofilm structure and thus have decreased nutrient diffusion coefficients, while the diffusion coefficients for the biofilm itself and the replicative bacteria are increased. Note that, since PSM production depends on the availability of phosphorylated AgrA, also quorum sensing or *agr* mutants do not produce PSM. *In vivo*, *psm-α* and/or *psm-β* mutants produce thicker biofilms, show reduced channel formation and have a smoother surface than the wild-type [87].

Amyloid fibrils provide structural integrity to biofilms [120] and increase resistance to degradation [125]. This plays a role especially in *in vivo* settings, where bacterial colonies defend themselves against other bacterial strains or antibiotics. Since we investigate biofilm formation in a laboratory setting, we do not explicitly include amyloid fibrils into the full model, but note that their production depends on the *agr* locus, such that the presence or absence of amyloid fibrils plays a role in certain mutants. In terms of the parameters, due to the decreased structural integrity in quorum sensing or *agr* mutants, the diffusion coefficient σ of the replicative bacteria increases.

Colonies of bacteria lacking α-toxin are unable to adhere to plastic surfaces under static or flow conditions [26], since the substance α-toxin is necessary for cell-to-cell interaction during biofilm formation. Nevertheless α-toxin is no physical component of the biofilm and adhesion is not as important in our setting as it would be in a flow cell. Therefore the concentration of α-toxin is not explicitly included into the equation for the biofilm concentration.

Protein A is most important in the context of invasion of a biological host [45, 96]. Nevertheless, as protein A facilitates colony spreading in a biological host and has a positive effect on virulence, it also has an effect on laboratory colony growth. This effect is represented by an increase in the replicative bacteria growth parameter δ. In attachment or *spa* mutants the parameter δ is larger since *agr* and *sarA* activity negatively regulate *spa* activity, while *sarA* activity positively regulates *agr* activity. Therefore a decrease in *spa* activity goes hand-in-hand with an increase in quorum sensing effects. Furthermore, the decrease in cell wall anchoring of protein A in the *spa* mutant decreases the stability of the biofilm, which results in an increased nutrient diffusion coefficient.

Since the evolution of the factors described above can be calculated explicitly, as seen in Sections 4.5.3 and 4.5.4, our model for the laboratory setting may also be extended to include these factors explicitly if this is necessary for a biological setting. An example of a biological setting, in which these factors may be crucial, is the very important modeling of biofilm formation on medical implants, a possibly lethal process, including competition and host invasion.

Now we include the developments of the single substances into the full model. In the equation for the quorum sensing signaling molecule AIP, we include Equation (4.148) multiplied by the concentration of replicative bacteria as the growth and decay term for AIP. Denoting the AIP concentration in the full system by the variable q and the density of replicative bacteria by b, it is of the form

$$f_2(b, q) := b \frac{dq}{d\hat{\tau}}.$$

Furthermore, the diffusion of AIP is modeled with a constant diffusion coefficient d_q.

Initial microbial adhesion to surfaces is a complex process that involves bacterial

factors as well as physical interactions like Lifshitz-van der Waals forces, electrostatic forces, acid-base interactions and Brownian motion forces. Among the considered substances, PIA contributes to biofilm formation in *S. aureus* [29], and in the close *S. aureus* relative *S. epidermidis*, PIA is even considered a clear determinant of biofilm formation [30]. This indicates that it may be sufficient for our purposes to consider the amount of PIA for biofilm formation.

The production of PIA is not under the control of *agr* gene regulation [144]. Nevertheless the *agr* system must influence biofilm formation via other (unknown) mechanisms since repression of *agr* is necessary to form a biofilm and the reactivation of *agr* in established biofilms, through AIP addition or glucose depletion, triggers detachment [21]. We thus model decay of biofilm in *S. aureus* as being *agr*-mediated in a process that is different from the inter-cellular regulatory processes we have considered so far, since it depends on the extra-cellular presence of the quorum sensing signaling substance q. In addition to that, biofilm growth is assumed to be negatively affected by the presence of AIP. Here we use Equation (4.149) and denote the concentration of PIA by the full system variable f. Then the reaction term for the biofilm equation is of the form

$$f_3(n, b, q, f) := b \frac{df}{d\hat{\tau}} \frac{1}{1 + \beta_f q} - \mu_f f\, q.$$

Furthermore, the presence of biofilm facilitates diffusion and especially nutrient transport. Therefore the concentration of biofilm is included into the nutrient diffusion term by multiplication with the factor $1 + f \geq 1$. The slight increase or decrease in replicative bacteria diffusion due to the presence or absence of biofilm is represented by an appropriate change in the corresponding diffusion coefficient.

With the notation from Section 4.1 we denote the time scale of the full system by t and obtain the system of equations

$$\frac{\partial n}{\partial t} = \nabla \cdot (D_1(f)\nabla n) - G_1 f_1(n, b, q), \tag{4.150}$$

$$\frac{\partial b}{\partial t} = \nabla \cdot (D_2(n, b, q)\nabla b) + G_2 f_1(n, b, q) - a(n, b), \tag{4.151}$$

$$\frac{\partial s}{\partial t} = \nabla \cdot (D_3(b)\nabla s) + a(n, b), \tag{4.152}$$

$$\frac{\partial q}{\partial t} = d_q \Delta q + f_2(b, q), \tag{4.153}$$

$$\frac{\partial f}{\partial t} = d_f \Delta f + f_3(n, b, q, f). \tag{4.154}$$

Furthermore, we define the functions for the diffusion coefficients, which are given as

$$D_1(f) := d_n(1+f), \qquad D_2(n,b,q) := \frac{\sigma n b}{1+\alpha_q q}, \qquad D_3(b) := \tau \frac{b}{b+b_s}, \tag{4.155}$$

and which are used in the finite element discretization in Section 4.6.1.

4.5.6. Reparametrization of the reaction terms in the full model

In this section we summarize and simplify the terms in $f_2(b,q)$ and $f_3(n,b,q,f)$ further, where the reaction terms for the quorum sensing substance and the biofilm are as described in Equation (4.148) and Equation (4.149), respectively. For simplicity, we approximate the monotonically increasing function $f([str])$ by the variable $[str]$, since both $f([str])$ and $[str]$ are modeling assumptions. As both expressions take values in the interval $(0,1)$, this important characteristic is preserved. An example for the comparison of $f([str])$ as defined in Equation (4.140) and the function $f([str]) = [str]$ is depicted in Figure 4.8.

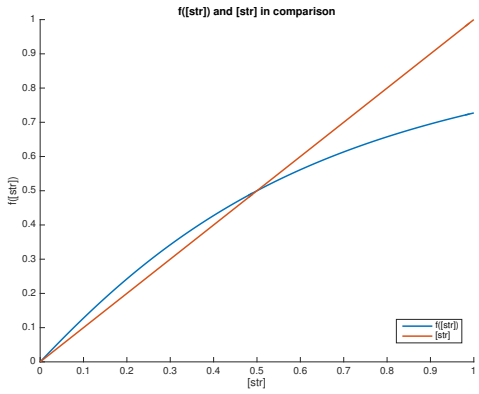

Figure 4.8.: Comparison of $f([str])$ and $[str]$ with the parameters $b_0 = b_\sigma = 1$ and $u_\sigma = 0.75$.

For $f_2(b,q)$ we obtain the equation

$$\begin{aligned} f_2(b,q) = b\, C_{11}\,(C_1 - C_2 q) \Bigg[& C_3 + C_4 f([str]) + C_5 q + C_6 \frac{f([str])}{B_5 + f([str])} \\ & + C_8 \frac{K_1 + K_2 q + (K_3 + K_4 q) f([str])}{K_5 + K_2 q + (K_6 + K_4 q) f([str])} + \frac{q^3}{A_1 + A_2 q + A_3 q^2} \Bigg] \\ & - C_{11}\,(C_9 + C_{10} f([str]))\, b \end{aligned} \tag{4.156}$$

Parameter	Formula	Magnitude
A_1	$\frac{k^2(\mu+\lambda)(\lambda+\gamma)^3}{\phi\beta^3\lambda^2}$	$\varepsilon^4\tilde{A}_1$
A_2	$\frac{k^2(\mu+\lambda)(\lambda+\gamma)^2}{\phi\beta^2\lambda^2}$	$\varepsilon^3\tilde{A}_2$
A_3	$\frac{k(\lambda+\gamma)}{\beta\lambda}$	$\varepsilon\tilde{A}_3$
B_5	$\frac{u_{sarA}}{b_{sarA}v_\sigma}$	$\varepsilon\tilde{B}_5$
C_1	$b_{agr}(1+\frac{1}{v})$	$\tilde{C}_1$
C_2	$b_{agr}\frac{\beta\lambda}{vk(\lambda+\gamma)}$	$\tilde{C}_2$
C_3	$1+2\alpha-\frac{v_3}{v}+\frac{u_{agr}}{b_{agr}}$	$\tilde{C}_3$
C_4	$\frac{u_{agr}}{b_{agr}}v_\sigma$	$\tilde{C}_4/\varepsilon$
C_5	$\frac{\beta\lambda}{vk(\lambda+\gamma)}v_3$	$\tilde{C}_5/\varepsilon$
C_6	αv_{sarA}	$\tilde{C}_6/\varepsilon$
C_8	$\alpha v_{sarU}b_1$	$\tilde{C}_8/\varepsilon$
C_9	u_{agr}	$\tilde{C}_9$
C_{10}	$u_{agr}v_\sigma$	$\tilde{C}_{10}/\varepsilon$
C_{11}	$\frac{k(1+\frac{\gamma}{\eta})}{\beta}v$	$\tilde{C}_{11}$
K_1	$u_2\alpha v_{sarA}b_{sarA}+(b_1+u_2(\alpha+1-\frac{v_3}{v}))(b_{sarA}+u_{sarA})$	$\tilde{K}_1/\varepsilon$
K_2	$\frac{u_2\beta\lambda v_3}{vk(\lambda+\gamma)}(b_{sarA}+u_{sarA})$	$\tilde{K}_2/\varepsilon$
K_3	$[u_2\alpha v_{sarA}+b_1+u_2(\alpha+1-\frac{v_3}{v})]b_{sarA}v_\sigma$	$\tilde{K}_3/\varepsilon^2$
K_4	$\frac{u_2\beta\lambda v_3}{vk(\lambda+\gamma)}b_{sarA}v_\sigma$	$\tilde{K}_4/\varepsilon^2$
K_5	$(b_1+u_1)K_1+u_1v_{sarT}b_1(b_{sarA}+u_{sarA})$	$\tilde{K}_5/\varepsilon$
K_6	$(b_1+u_1)K_3+u_1v_{sarT}b_1b_{sarA}v_\sigma$	$\tilde{K}_6/\varepsilon^2$
P_1	b_{ica2}	$\tilde{P}_1$
P_2	$b_{ica2}v_{sarA}$	$\tilde{P}_2/\varepsilon$
P_3	$b_{ica2}r_{ica2}$	$\tilde{P}_3$
P_4	v_{ica2}	$\tilde{P}_4/\varepsilon$
P_5	$\frac{u_{ica2}b_{ica1}^2v_{ica1}^2}{u_{ica1}^2}$	$\tilde{P}_5/\varepsilon^2$
P_6	$\frac{b_{ica1}}{u_{ica1}}$	$\tilde{P}_6$

Table 4.6.: Parameters from Sections 4.5.2–4.5.4 in terms of the non-dimensional model parameters with their corresponding magnitudes.

$$\begin{aligned}&\approx G_q\, b\,(1-\alpha q)\left[\beta_q\left(q+\alpha_3\frac{q^3}{1+c_1q+c_2q^2}\right)+\beta^\star_{str}\right.\\&\left.+\,\beta_{str,q}\,\frac{K_1+K_2q+(K_3+K_4q)[str]}{K_5+K_2q+(K_6+K_4q)[str]}\right]-\mu_{str}\,b,\end{aligned}$$

with the new parameters

$$G_q := C_1C_3C_{11},\qquad \alpha := \frac{C_2}{C_1},\qquad \beta_q := \frac{C_5}{C_3},\qquad \alpha_3 := \frac{1}{C_5A_1},\qquad c_1 := \frac{A_2}{A_1},$$
$$c_2 := \frac{A_3}{A_1},\qquad \beta^\star_{str} := 1+\frac{C_4}{C_3}[str]+\frac{C_6[str]}{C_3(B_5+[str])},\qquad \beta_{str,q} := \frac{C_8}{C_3}$$
$$\text{and}\qquad \mu_{str} := C_{11}(C_9+C_{10}[str]).$$

In the above definitions, we approximate the function $f([str])$ by the constant parameter $[str]$. Furthermore, the magnitudes of the above parameters are as

Parameter(s)	Formula	Magnitude
$[str]$	model assumption	$\in (0,1)$
d_q, d_f	model assumption	–
α_q	model assumption	–
β_f	model assumption	–
μ_f	model assumption	–
G_q	$C_1C_3C_{11}$	$\tilde{G}_q$
α	C_2/C_1	$\tilde{\alpha}$
β_q	C_5/C_3	$\tilde{\beta}_q/\varepsilon$
α_3	$(C_5A_1)^{-1}$	$\tilde{\alpha}_3/\varepsilon^3$
c_1	A_2/A_1	$\tilde{c}_1/\varepsilon$
c_2	A_3/A_1	$\tilde{c}_2/\varepsilon^3$
$\beta^\star_{str}$	$1+\frac{C_4}{C_3}[str]+\frac{C_6[str]}{C_3(B_5+[str])}$	$\tilde{\beta}^\star_{str}/\varepsilon$
$\beta_{str,q}$	C_8/C_3	$\tilde{\beta}_{str,q}/\varepsilon$
μ_{str}	$C_{11}(C_9+C_{10}[str])$	$\tilde{\mu}_{str}/\varepsilon$
G_f	P_1	$\tilde{G}_f$
$\gamma^\star_{str}$	$1+\frac{P_2[str]}{P_1(B_5+[str])}$	$\tilde{\gamma}^\star_{str}/\varepsilon$
γ_n	P_3/P_1	$\tilde{\gamma}_n$
K_f	P_4	$\tilde{K}_f/\varepsilon$
$\gamma^\star_{str,f}$	$\frac{P_5}{P_1(P_6+[str])^2}$	$\tilde{\gamma}^\star_{str,f}/\varepsilon^2$
K_n	model assumption	–

Table 4.7.: New parameters from Sections 4.5.5 and 4.5.6 in terms of the model parameters from Table 4.6 with their corresponding magnitudes.

described in Table 4.6 and Table 4.7. In our numerical simulations, we use the parameter magnitude results as indicators for the size relationships between the parameters in our derived equations, and adapt the overall parameter magnitudes to the parameters used in the nutrient and bacteria equations.

For the term $f_3(n,b,q,f)$ in the evolution equation of the biofilm, we obtain

$$\begin{aligned} f_3(n,b,q,f) &= b\left[\left(P_1+P_2\frac{f([str])}{B_5+f([str])}+P_3n\left(1-\frac{n}{K_n}\right)\right)(P_4-f)\right. \\ &\qquad \left.-\frac{P_5}{(P_6+[str])^2}(f-1)\right]\frac{1}{1+\beta_f q}-\mu_f\, f\, q \\ &\approx G_f\, b\left[\left(\gamma^\star_{str}+\gamma_n n\left(1-\frac{n}{K_n}\right)\right)(K_f-f)-\gamma^\star_{str,f}f\right]\frac{1}{1+\beta_f q}-\mu_f\, f\, q, \end{aligned} \tag{4.157}$$

with the new parameters

$$G_f := P_1, \qquad \gamma^\star_{str} := 1+\frac{P_2[str]}{P_1(B_5+[str])}, \qquad \gamma_n := \frac{P_3}{P_1}, \qquad K_f := P_4$$
$$\text{and} \qquad \gamma^\star_{str,f} = \frac{P_5}{P_1(P_6+[str])^2}.$$

The magnitudes of the parameters $\gamma^\star_{str}$, K_f and $\gamma^\star_{str,f}$ are also as described in

Table 4.7. Above we have approximated $(f-1)$ by f. Formulas for the equations are given in terms of the parameters in the non-dimensional model from Section 4.3 and we distinguish between the parameters introduced in Sections 4.5.2, 4.5.3 and 4.5.4 in Table 4.6 and those introduced in Sections 4.5.5 and 4.5.6 in Table 4.7.

4.5.7. Simulation of the system of regulation equations

In this section we simulate the non-dimensional system of ordinary differential equations introduced in Section 4.3 and given by the Equations (4.67)–(4.114). We investigate the behavior of these equations, with special attention to the system reduction, using an ordinary differential equation solver in MATLAB [97]. We take into account that the changes described in Equations (4.67)–(4.114) take place on different time scales, as seen in Section 4.4. Thus we simulate a system consisting of Equations (4.67), (4.76), (4.82), (4.83), (4.90), (4.93), (4.94), (4.100), (4.103), (4.106), (4.109) and (4.112), where the resulting concentrations of AIP and PIA are calculated using Equation (4.121) and Equation (4.126), respectively.

The concentrations resulting from this system are shown in Figure 4.9(a)–(c). The resulting concentrations of AIP and PIA in Figure 4.9(c) are then compared to those obtained directly from the reduced Equations (4.148) and (4.149) with the additional assumption $f([str]) \approx [str]$ in Figure 4.9(d).

In both cases, the concentrations of nutrients and the stress level are assumed to be constant at the levels $n = 5$ and $[str] = 0.5$. The parameters for the larger system are chosen as $n = 5$, $[str] = 0.5$, $b_{agr} = u_{agr} = \lambda = k = \gamma = \eta = b_{PSM} = u_{PSM} = b_0 = u_0 = b_\sigma = b_{sarA} = u_{sarA} = b_{ica1} = b_{ica2} = u_{ica1} = u_{ica2} = r_{ica2} = b_1 = u_2 = \alpha = u_1 = b_2 = 1$, $v = 3$, $v_3 = v_\sigma = v_{sarA} = v_{ica1} = v_{ica2} = v_{sarT} = v_{sarU} = v_{sarS} = 5$, $\mu = 0.1$ and $\phi = \beta = K_n = 10$ and the parameters for the reduced system are calculated from these parameters using the formulas from Table 4.6 and Table 4.7.

We see that both systems yield very similar concentrations of AIP and PIA, such that we can say that the reduction does not lead to a significant loss of accuracy. The peaks that arise in the concentrations of the larger system are due to the system taking longer to swing into its final stage. However, we see that these peaks do not alter the long-term behavior of the system significantly.

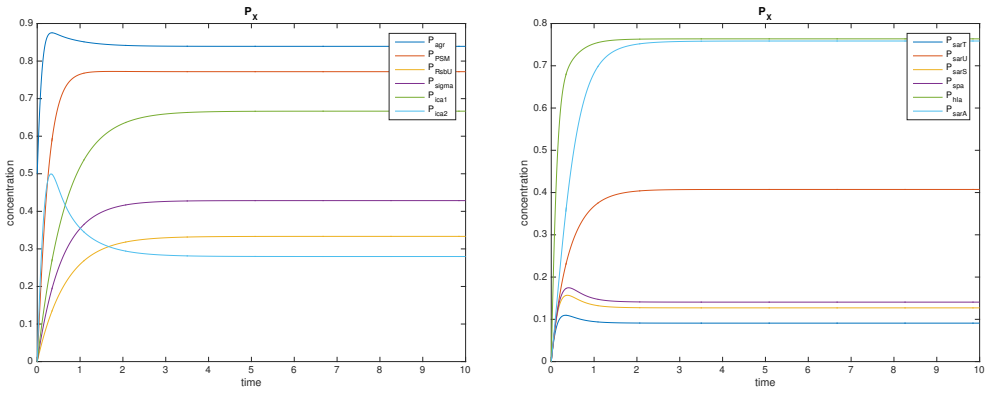

(a) Proportions of up-regulated cells from larger system.

(b) Proportions of up-regulated cells from larger system.

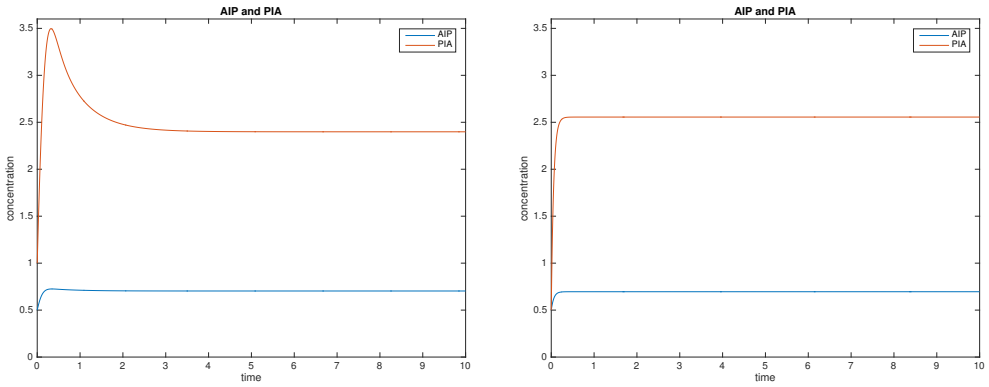

(c) Resulting concentrations of AIP and PIA from larger system.

(d) Concentrations of AIP and PIA from reduced system of two equations.

Figure 4.9.: Comparison of the concentrations of AIP and PIA from the larger rescaled system and the reduced system on the $\hat{\tau}$-timescale.

4.6. Simulation of the full system

In this section the finite element discretization of our system is presented and we simulate the full system of partial differential equations derived in Section 4.5 using a time-adaptive finite element method in two spatial dimensions which is implemented in MATLAB. For further details on finite element methods, we refer to Section 3.5 and the references [22, 24]. Note that the model uses a random diffusion component from a triangular distribution as introduced in [82], in order to reflect the stochastic fluctuation of the random movement of bacteria. This means that the diffusion parameter σ has the form $\sigma = \sigma_0(1 + \Delta)$, where Δ is taken from a triangular distribution supported by $[-1, 1]$. Furthermore, as in [82], the initial distribution of cells is chosen as a normal distribution of the form $b_0(\mathbf{x}) = b_{\mathrm{M}} \exp(-(x^2 + y^2)/6.25)$, where we take $b_{\mathrm{M}} = 0.71$.

4.6.1. Finite element discretization

We use a finite element method to simulate the model given by the Equations (4.150)–(4.154) with the functions $f_1(n,b,q)$, $a(n,b)$, $f_2(b,q)$, $f_3(n,b,q,f)$ and the diffusion coefficients given by Equations (4.5)–(4.6) and (4.155)–(4.157). We recall that our resulting system is of the form

$$\begin{aligned}
\frac{\partial n}{\partial t} &= \nabla \cdot (D_1(f)\nabla n) - G_1 f_1(n,b,q),\\
\frac{\partial b}{\partial t} &= \nabla \cdot (D_2(n,b,q)\nabla b) + G_2 f_1(n,b,q) - a(n,b),\\
\frac{\partial s}{\partial t} &= \nabla \cdot (D_3(b)\nabla s) + a(n,b),\\
\frac{\partial q}{\partial t} &= d_q \Delta q + f_2(b,q),\\
\frac{\partial f}{\partial t} &= d_f \Delta f + f_3(n,b,q,f).
\end{aligned}$$

For the finite element method we need the weak form of the equations and use the implicit Euler method for the time derivatives. For the simple case of an ODE problem of the form $\frac{dy}{dt} = f(t,y)$, $y(0) = y_0$, the implicit Euler approximation is of the form $y_{k+1} = y_k + \delta t\, f(t_{k+1}, y_{k+1})$ with the time step δt. In the following, this method is applied to the weak formulation of the time-dependent PDE problem in order to obtain a variational formulation.

Since we assume homogeneous Neumann boundary conditions, this results in a variational problem of the form

$$\begin{aligned}
&F((n,b,s,q,f),(u,v,w,m,p)) =\\
&\quad\int_\Omega \Big[\frac{n-n_k}{\delta t}\,u + D_1(f)\,\nabla n\cdot\nabla u + G_1 f_1(n,b,q)\,u\\
&\qquad + \frac{b-b_k}{\delta t}\,v + D_2(n,b,q)\,\nabla b\cdot\nabla v - G_2\,f_1(n,b,q)\,v + a(n,b)\,v\\
&\qquad + \frac{s-s_k}{\delta t}\,w + D_3(b)\,\nabla s\cdot\nabla w - a(n,b)\,w\\
&\qquad + \frac{q-q_k}{\delta t}\,m + d_q\,\nabla q\cdot\nabla m - f_2(b,q)\,m\\
&\qquad + \frac{f-f_k}{\delta t}\,p + d_f\,\nabla f\cdot\nabla p - f_3(n,b,q,f)\,p\Big]\,d\mathbf{x} \;=\; 0.
\end{aligned}$$

Here the terms n_k, b_k, s_k, q_k and f_k denote the approximations of the respective concentrations in the previous time step k. This means that in fact we have taken $(n,b,s,q,f) := (n_{k+1}, b_{k+1}, s_{k+1}, q_{k+1}, f_{k+1})$. Our goal is to determine the tuple

(n, b, s, q, f) such that

$$F((n, b, s, q, f), (u, v, w, m, p)) = 0$$

for all $(u, v, w, m, p) \in (H^1(\Omega))^5$. This is achieved numerically by linearizing the functional F at $(\hat{n}, \hat{b}, \hat{s}, \hat{q}, \hat{f})$ in the direction $(\delta n, \delta b, \delta s, \delta q, \delta f)$ for the fixed tuple of test functions (u, v, w, m, p). The linear problem to be solved for each iteration then becomes:
Find $(\delta n, \delta b, \delta s, \delta q, \delta f) \in (H^1(\Omega))^5$ such that

$$\hat{F}((\hat{n} + \delta n, \hat{b} + \delta b, \hat{s} + \delta s, \hat{q} + \delta q, \hat{f} + \delta f), (u, v, w, m, p)) = 0 \tag{4.158}$$

for all test functions $(u, v, w, m, p) \in (H^1(\Omega))^5$. To compute the solution of the linearized problem in each step, we employ a Newton method. Note that the starting point for the Newton iteration is always the solution calculated in the last time step. Then the solution of (4.158) is computed and the new approximation is taken to be the solution from the last time step plus the calculated solution. This procedure is repeated until the given error tolerance is reached.

In order to set up the linearized Equation (4.158) appropriately, we simplify our notation and define

$$\hat{\mathbf{x}} := (\hat{n}, \hat{b}, \hat{s}, \hat{q}, \hat{f}), \qquad \mathbf{y} := (u, v, w, m, p) \qquad \text{and} \qquad \delta\mathbf{x} := (\delta n, \delta b, \delta s, \delta q, \delta f).$$

Then we sort the terms in the resulting expression by their dependency on the vector $\delta\mathbf{x}$ to achieve a problem of the form

$$\hat{F}(\hat{\mathbf{x}} + \delta\mathbf{x}, \mathbf{y}) = \mathfrak{a}(\delta\mathbf{x}, \mathbf{y}) - \mathfrak{f}(\mathbf{y}) = 0, \tag{4.159}$$

to be solved for $\delta\mathbf{x}$. Here the residual $-\mathfrak{f}(\mathbf{y})$ is defined as

$$\begin{aligned}
-\mathfrak{f}(\mathbf{y}) = \int_\Omega \Big[& \frac{1}{\delta t}(\hat{n}u - n_k u) + D_1(\hat{f})\,\nabla\hat{n}\cdot\nabla u + G_1\, f_1(\hat{n}, \hat{b}, \hat{q})\, u \\
& + \frac{1}{\delta t}(\hat{b}v - b_k v) + D_2(\hat{n}, \hat{b}, \hat{q})\,\nabla\hat{b}\cdot\nabla v - G_2\, f_1(\hat{n}, \hat{b}, \hat{q})\, v + a(\hat{n}, \hat{b})\, v \\
& + \frac{1}{\delta t}(\hat{s}w - s_k w) + D_3(\hat{b})\,\nabla\hat{s}\cdot\nabla w - a(\hat{n}, \hat{b})\, w \\
& + \frac{1}{\delta t}(\hat{q}m - q_k m) + d_q\,\nabla\hat{q}\cdot\nabla m - f_2(\hat{b}, \hat{q})\, m \\
& + \frac{1}{\delta t}(\hat{f}p - f_k p) + d_f\,\nabla\hat{f}\cdot\nabla p - f_3(\hat{n}, \hat{b}, \hat{q}, \hat{f})\, p \Big]\, d\mathbf{x},
\end{aligned}$$

and the matrix $\mathfrak{a}(\delta\mathbf{x}, \mathbf{y})$ is of the form

$$\begin{aligned}
\mathfrak{a}(\delta\mathbf{x}, \mathbf{y}) = \int_\Omega \Big[& \frac{1}{\delta t}\delta n\, u + D_{1f}(\hat{f})\, \delta f\, \nabla\hat{n}\cdot\nabla u + D_1(\hat{f})\, \nabla\delta n\cdot\nabla u \\
& + G_1 f_{1n}(\hat{n},\hat{b},\hat{q})\, \delta n\, u + G_1 f_{1b}(\hat{n},\hat{b},\hat{q})\, \delta b\, u + G_1 f_{1q}(\hat{n},\hat{b},\hat{q})\, \delta q\, u \\
& + \frac{1}{\delta t}\, \delta b\, v + D_{2n}(\hat{n},\hat{b},\hat{q})\, \delta n\, \nabla\hat{b}\cdot\nabla v + D_{2b}(\hat{n},\hat{b},\hat{q})\, \delta b\, \nabla\hat{b}\cdot\nabla v \\
& + D_{2q}(\hat{n},\hat{b},\hat{q})\, \delta q\, \nabla\hat{b}\cdot\nabla v + D_2(\hat{n},\hat{b},\hat{q})\, \nabla\delta b\cdot\nabla v - G_2 f_{1n}(\hat{n},\hat{b},\hat{q})\, \delta n\, v \\
& - G_2 f_{1b}(\hat{n},\hat{b},\hat{q})\, \delta b\, v - G_2 f_{1q}(\hat{n},\hat{b},\hat{q})\, \delta q\, v + a_n(\hat{n},\hat{b})\, \delta n\, v + a_b(\hat{n},\hat{b})\, \delta b\, v \\
& + \frac{1}{\delta t}\, \delta s\, w + D_{3b}(\hat{b})\, \delta b\, \nabla\hat{s}\cdot\nabla w + D_3(\hat{b})\, \nabla\delta s\cdot\nabla w - a_n(\hat{n},\hat{b})\, \delta n\, w \\
& - a_b(\hat{n},\hat{b})\, \delta b\, w \\
& + \frac{1}{\delta t}\, \delta q\, m + d_q\, \nabla\delta q\cdot\nabla m - f_{2b}(\hat{b},\hat{q})\, \delta b\, m - f_{2q}(\hat{b},\hat{q})\, \delta q\, m \\
& + \frac{1}{\delta t}\, \delta f\, p + d_f\, \nabla\delta f\cdot\nabla p - f_{3n}(\hat{n},\hat{b},\hat{q},\hat{f})\, \delta n\, p - f_{3b}(\hat{n},\hat{b},\hat{q},\hat{f})\, \delta b\, p \\
& - f_{3q}(\hat{n},\hat{b},\hat{q},\hat{f})\, \delta q\, p - f_{3f}(\hat{n},\hat{b},\hat{q},\hat{f})\, \delta f\, p \Big]\, d\mathbf{x}.
\end{aligned}$$

Since we consider a system of five differential equations, we distinguish several cases in the numerical assemblation of the matrix and the residual. There are five cases, one for each model variable $u_{\text{test}} \in \{u, v, w, m, p\}$, for assembling the residual $\mathfrak{f}(\mathbf{y})$ and 25 cases, one for each pair $(c_{\text{sol}}, u_{\text{test}})$ with $c_{\text{sol}} \in \{\delta n, \delta b, \delta s, \delta q, \delta f\}$, for assembling the system matrix $\mathfrak{a}(\delta\mathbf{x}, \mathbf{y})$. Furthermore, in the equations for $\mathfrak{f}(\mathbf{y})$ and $\mathfrak{a}(\delta\mathbf{x}, \mathbf{y})$ above, several terms of the same form can be found. In the equations for $\mathfrak{f}(\mathbf{y})$ and $\mathfrak{a}(\delta\mathbf{x}, \mathbf{y})$, terms of the same form can be treated in the same way numerically and therefore we distinguish different routines, which assemble the residual terms of the form

$$\int_\Omega f\, u_{\text{test}}\, d\mathbf{x} \qquad \text{and} \qquad \int_\Omega f\, \nabla g\cdot\nabla u_{\text{test}}\, d\mathbf{x}$$

and the matrix terms of the form

$$\begin{aligned}
M &= \int_\Omega f\, c_{\text{sol}}\, u_{\text{test}}\, d\mathbf{x}, \qquad S = \int_\Omega f\, \nabla c_{\text{sol}}\cdot\nabla u_{\text{test}}\, d\mathbf{x} \qquad \text{and} \\
R &= \int_\Omega f\, c_{\text{sol}}\, \nabla g\cdot\nabla u_{\text{test}}\, d\mathbf{x},
\end{aligned}$$

where f and g denote the coefficient functions.

We solve the variational problem over the space $(V_h)^5$, where V_h denotes the finite

element space of continuous piecewise linear polynomials given as

$$V_h := \{v_h \in H^1(\Omega) : v_h|_T \in \mathbb{P}_1(T), T \in \mathcal{T}_h\},$$

introduced in Section 3.5. We introduce the basis $\{\psi_j\}_{j\in[5N]}$, where N denotes the number of ansatz functions, in order to rewrite the variational problem. Note that since the problem has five equations, the basis components are in fact vectors of the form $\psi_j = (\phi_j, 0, 0, 0, 0)$ for $j \in [N]$, $\psi_j = (0, \phi_{j-N}, 0, 0, 0)$ for $j \in [2N]\backslash[N]$, $\psi_j = (0, 0, \phi_{j-2N}, 0, 0)$ for $j \in [3N]\backslash[2N]$, $\psi_j = (0, 0, 0, \phi_{j-3N}, 0)$ for $j \in [4N]\backslash[3N]$ and $\psi_j = (0, 0, 0, 0, \phi_{j-4N})$ for $j \in [5N]\backslash[4N]$, where $\{\phi_j\}_{j\in[N]}$ is a Lagrange or nodal basis of the space V_h.

Then the variational problem from Equation (4.159) in discrete form reads:
Find $\mathbf{v}_h \in (V_h)^5$ such that

$$\mathfrak{a}(\mathbf{v}_h, \psi_i) = \mathfrak{f}(\psi_i) \qquad \forall \psi_i \in (V_h)^5.$$

Since $\mathbf{v}_h = \sum_{j=1}^{5N} z_j\psi_j$, this is equivalent to $\sum_{j=1}^{5N} \mathfrak{a}(\psi_j, \psi_i)z_j = \mathfrak{f}(\psi_i)$ for $i = 1, \ldots, 5N$. In matrix notation the problem thus takes the form $A\mathbf{z} = \mathbf{b}$, where we write the matrix $A(i, j) = \mathfrak{a}(\psi_j, \psi_i) \in \mathbb{R}^{5N\times5N}$, with the components $M(i, j), S(i, j), R(i, j) \in \mathbb{R}^{5N\times5N}$, and the vector $\mathbf{b}(i) = \mathfrak{f}(\psi_i) \in \mathbb{R}^{5N}$ with the components described above, in terms of the basis functions.

4.6.2. Time adaptivity

We distinguish between time and space adaptivity. While the latter involves changing the finite element mesh and consequently requires appropriate error estimation, time adaptivity only changes the time step in the simulation of a parabolic problem. For our parabolic boundary value problem, we use a separate time discretization and can thus consider time adaptivity as a separate process. We control the time step based on the number of Newton steps required to obtain the spatial solution. The underlying idea is to assume that a fast numerical convergence of the Newton method implies that the solution is uncritical and that it has a good quality. Thus, the four parameters

$$\text{newton}_{\text{min}} < \text{newton}_{\text{nearlymin}} < \text{newton}_{\text{nearlymax}} < \text{newton}_{\text{max}}$$

and two constant time factors $\alpha_1, \alpha_2 \in (0,1)$ with $\alpha_1 \leq \alpha_2$ are defined. The time step is forced to be larger than a minimal value in order to stop the algorithm if convergence cannot be reached. If the number of Newton steps needed is larger than $\text{newton}_{\text{max}}$ or if the solution did not converge, the step size is reduced by multiplication with the smaller factor α_1. For a number of Newton steps that is between $\text{newton}_{\text{nearlymax}}$ and $\text{newton}_{\text{max}}$, the step size is only reduced by multiplication with the larger factor α_2. If the number of Newton steps needed is too small, i.e., less than or equal $\text{newton}_{\text{nearlymin}}$, or the update norm is too small, the time step is increased by division by the factor α_2.

4.6.3. Comparison of the numerical results to real data

This section is divided into two parts: In the first part we perform simulations of bacteria colony growth in the wildtype and in several mutants of the bacterium *S. aureus* "Newman". We then compare our results to real data in the form of biological observations of bacteria colonies grown in the laboratory. The biological real data observations have in part been published in [65] and are reprinted under the terms of the Creative Commons Attribution License. This is indicated by the reference [65] in the captions of the corresponding figures. Further biological observations result from experiments performed at the University of Würzburg, also as indicated in the figure captions. In the second part we compare our results to the five morphologies of bacterial colonies introduced in [82, 98].

Parameter	Value	Parameter	Value	Parameter	Value	Parameter	Value
G_1	7	G_2	7	σ	0.5	G_f	0.1
G_q	0.1	μ_q	0.1	δ	1	d_n	1
d_f	2	d_q	1	ε	10	γ	1
q_m	0.3	z	1	τ	0.25	b_s	2
$1/a_1$	2400	$1/a_2$	120	ρ	1	α_q	1
α	0.1	β_q	1	α_3	100	c_1	1
c_2	100	$\beta^\star_{str}$	1	$\beta_{str,q}$	1	$K_1 = K_2$	1
K_3	10	K_4	10	K_5	1	K_6	10
$[str]$	0.5	$\gamma^\star_{str}$	1	γ_n	0.5	$\gamma^\star_{str,f}$	10
β_f	1	μ_f	0	K_f	10	K_n	10

Table 4.8.: Parameter values for the simulation of the wildtype *S. aureus* bacteria colony.

For the wildtype bacterium we choose moderate parameter values since all regulation subsystems are active and contribute to the growth of the colony. These parameter values are described in Table 4.8 and the corresponding simulation results are depicted in Figures 4.10–4.12. In order to display the colony structure, we

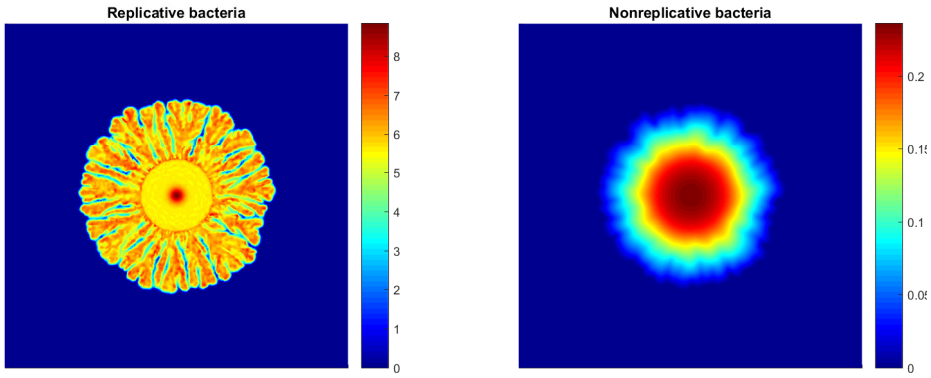

(a) Replicative bacteria.

(b) Nonreplicative bacteria.

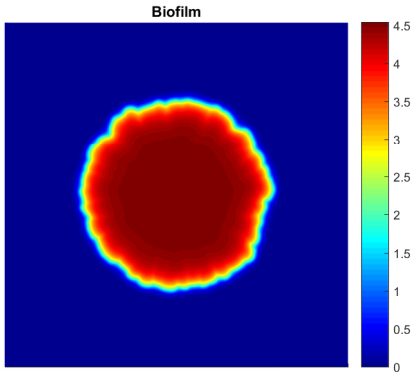

(c) Biofilm concentration.

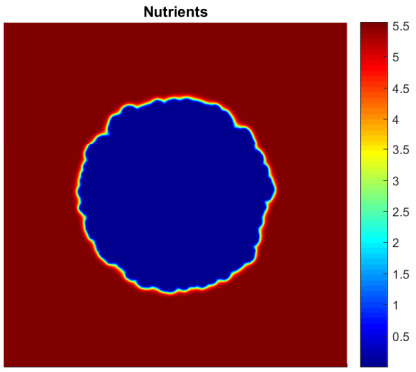

(d) Nutrient concentration.

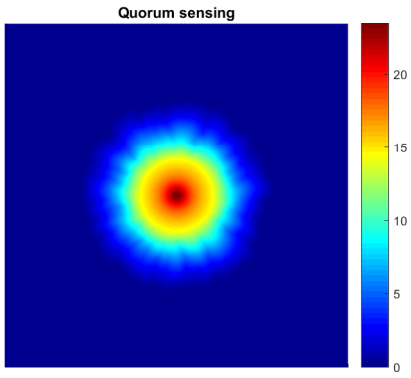

(e) Quorum sensing substance.

Figure 4.10.: *S. aureus* wildtype single concentrations as obtained from simulation with the parameters indicated in Table 4.8.

add up the concentrations of replicative and non-replicative bacteria as well as the concentration of biofilm as depicted in Figure 4.10(a)–(c) to obtain the colony depicted in Figure 4.12(b). Since the dimensionless concentration of biofilm is in the range of 0 to 4.5, these values are indicated by a light blue color and the larger

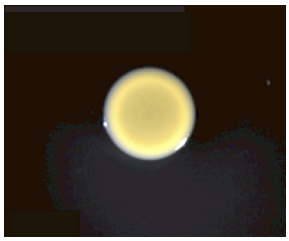

(a) First day.

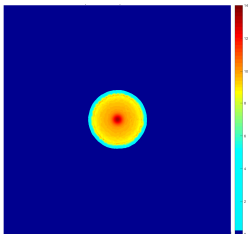

(b) Simulation at $t = 2.28$.

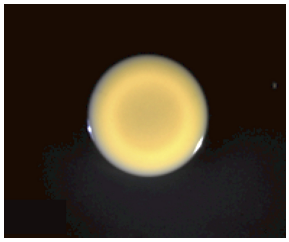

(c) Second day.

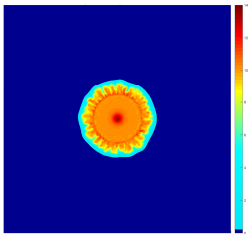

(d) Simulation at $t = 4.57$.

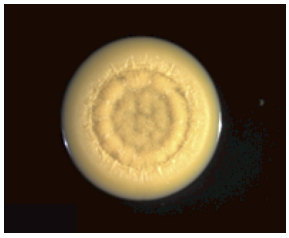

(e) Third day.

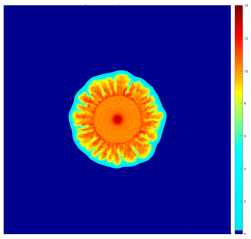

(f) Simulation at $t = 6.85$.

(g) Fourth day.

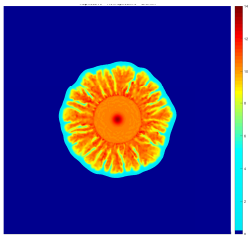

(h) Simulation at $t = 9.20$.

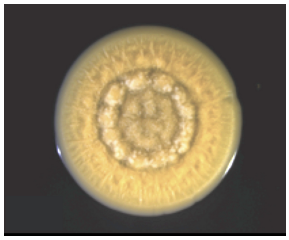

(i) Fifth day.

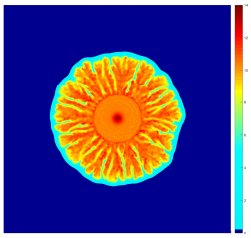

(j) Simulation at $t = 11.55$.

Figure 4.11.: *S. aureus* wildtype colony evolution in time observed in the laboratory [65] in comparison to the evolution as obtained from simulation with the parameters indicated in Table 4.8. Simulations take values in the interval $[0, 14]$.

concentration values, which range up to 14 in areas where bacteria are present, are indicated by shades of yellow and red. The concentrations of nutrients and

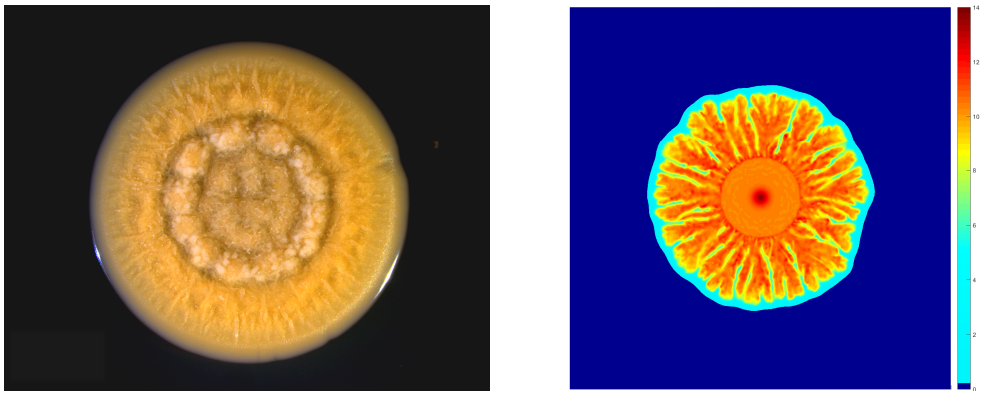

(a) *S. aureus* wildtype colony evolution. (b) *S. aureus* wildtype simulation result.

Figure 4.12.: *S. aureus* wildtype bacteria colony as obtained from simulation with the parameters indicated in Table 4.8 in (b) in comparison to biological real data [65] in (a).

quorum sensing molecules are not added since these molecules are very small and thus cannot be seen in the real data. The single component concentrations are depicted in Figure 4.10 and Figure 4.11 shows the evolution of the wildtype bacteria colony in time. In the biological real data in Figure 4.12(a) we observe that the wildtype bacterium shows a quite distinct structure with concentric rings of bacteria and a narrow fingering or wrinkling structure towards the outer area of the colony. The colony is mostly round with only few shallow dents. Furthermore, we observe a thin layer of biofilm surrounding the bacteria in the real data. These features are reproduced in the simulation result depicted in Figure 4.12(b), where a distinct ring structure is observed, the colony fingers are close and a thin layer of biofilm surrounds the colony. Thus in this case a good agreement is reached between the real data and the simulation result.

The real data for the extracellular matrix or *ica* mutant as depicted in Figure 4.13(a) shows a less pronounced colony structure, especially in the inner area where the ring structure is weaker than in the wildtype colony. The colony is round and very narrow wrinkles are observed in the outer parts. Furthermore, the colony does not have a surrounding biofilm layer. In this case we set $G_f = \mu_f = 0$ since the *ica* locus of the bacteria is deactivated. The lack of biofilm leads to a slower availability of nutrients for colony growth, such that the growth rates G_1 and G_2 are decreased to $G_1 = G_2 = 5$. In addition, we take $\sigma = 1$ in the replicative bacteria diffusion since, without the added structure of the biofilm, the bacteria move faster. In the simulation results depicted in Figure 4.13(b) we observe that a good agreement is reached as the ring structure is less pronounced and the branches are very close.

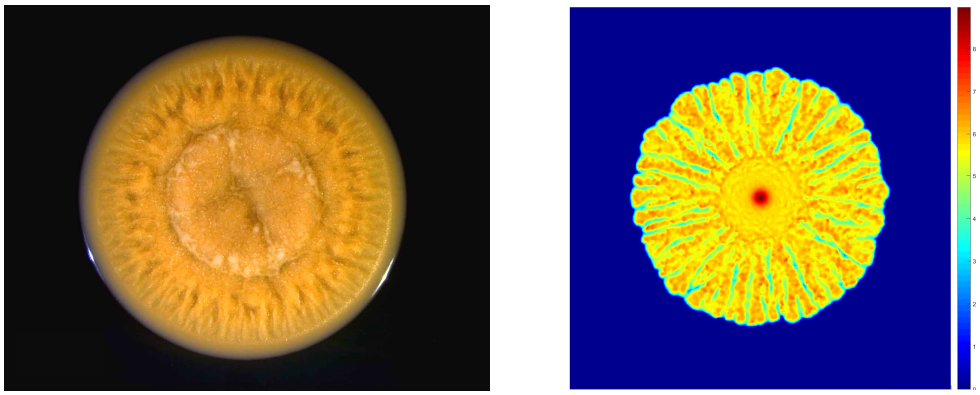

(a) *Ica* mutant colony evolution. (b) *Ica* mutant simulation result.

Figure 4.13.: *S. aureus ica* mutant bacteria colony as obtained from simulation with the described parameter changes in (b) and biological real data [65] in (a).

For the interested reader, the single concentrations of the five components, as shown above for the wildtype colony, are depicted in Figure A1.1 in the appendix.

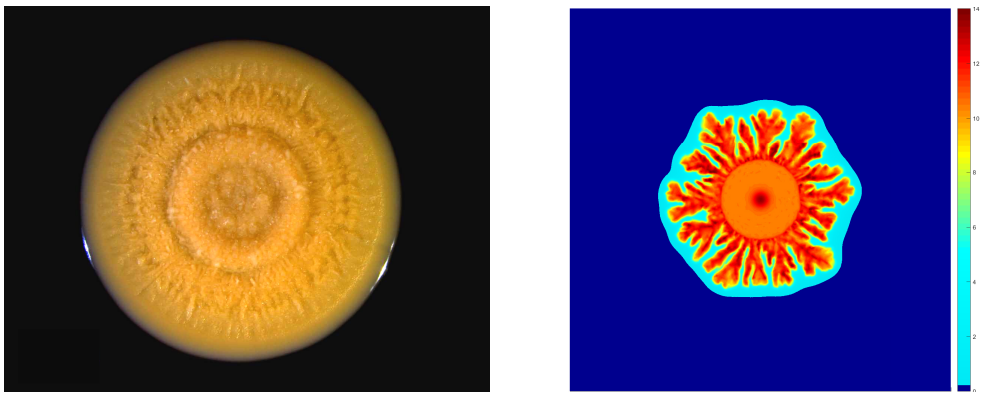

(a) *Spa* mutant colony evolution. (b) *Spa* mutant simulation result.

Figure 4.14.: *S. aureus spa* mutant bacteria colony as obtained from simulation with the described parameter changes in (b) and biological real data [65] in (a).

In Figure 4.14(a) we see the real data for the attachment mutant, in which the *spa* locus is disabled. As in the wildtype, the ring structure can be observed, but it is even more pronounced. An important difference to the wildtype is that the spaces between the wrinkles in the outer part of the colony are larger in the *spa* mutant. The bacteria colony is surrounded by a biofilm layer. Since a decrease in the concentration of protein A is linked to an increase in the AIP concentration, we obtain the effects of the *spa* mutation by increasing the effects of the quorum sensing substance on colony growth, thus increasing the parameter δ from $\delta = 1$ to $\delta = 5$. In

addition, protein A binds to the cell wall envelope [45, 96], thus providing stability to the biofilm. In the attachment mutant bacterium, the biofilm is still present, but less stable, leading to the slightly increased nutrient diffusion coefficient $d_n = 1.5$. In the simulation result depicted in Figure 4.14(b) we observe a good agreement of the simulations as the distances between the fingers are increased, while a very distinct ring structure is observed. For the interested reader, Figure A1.2 in the appendix depicts the single concentrations for the *spa* mutant.

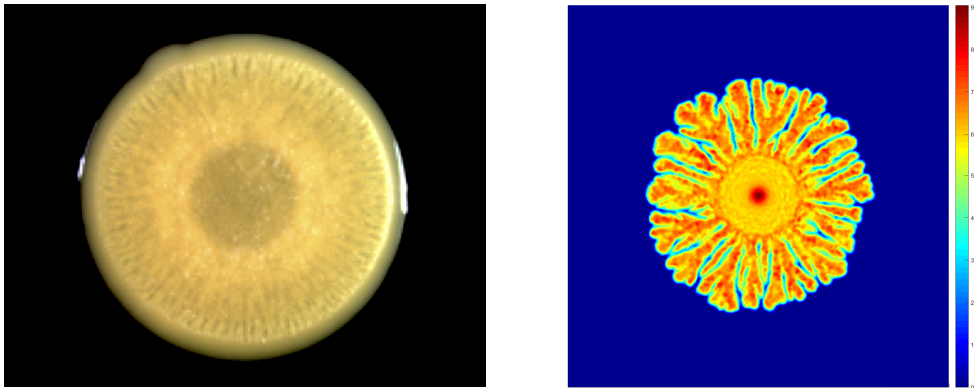

(a) *Ica* and *spa* mutant colony evolution. (b) *Ica* and *spa* mutant simulation result.

Figure 4.15.: *S. aureus ica* and *spa* mutant bacteria colony as obtained from simulation with the described parameter changes in (b) and biological real data [65] in (a).

The combined *spa* and *ica* mutant real data is depicted in Figure 4.15(a) and shows features from both mutations. Here the concentric ring structure is more pronounced than in the *ica* mutant and the outer areas of the colony show wider gaps between the wrinkles in the colony structure. As above, there is no biofilm formation due to the *ica* locus mutation. We combine the parameters $G_1 = G_2 = 5$, $\sigma = 1$ from the *ica* mutant with the parameters $\delta = 5$, $d_n = 1.5$ from the *spa* mutant to obtain the simulation result depicted in Figure 4.15(b). In comparison to the *ica* mutant simulation result, it shows a stronger ring structure and wider gaps between the fingers, and thus a good agreement of the real data and the simulation. In addition, the single concentrations are depicted in Figure A1.3 in the appendix.

The amyloid type 1 or *psm-α* mutant biological observation depicted in Figure 4.16(a) has a rather pronounced ring structure and narrow wrinkling in the outer areas of the round colony, which means that the wrinkles in the outer part are close to each other. In the real data as well as in the simulation result, depicted in Figure 4.16(b), we observe a layer of biofilm, which surrounds the bacteria colony

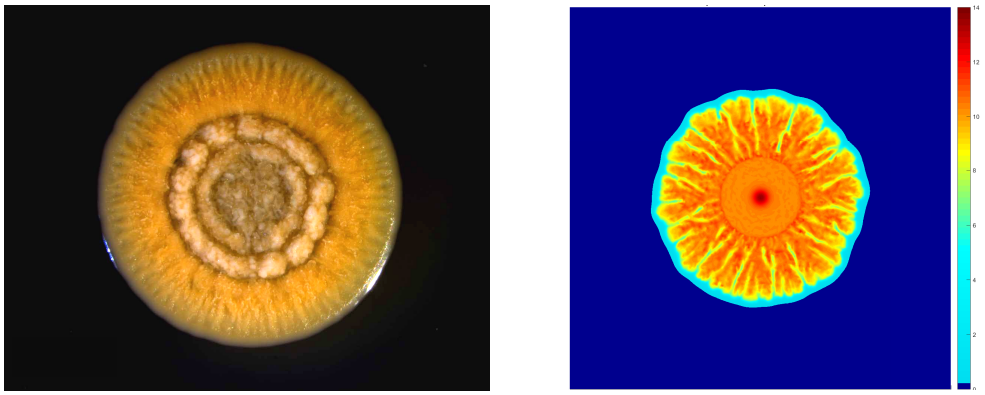

(a) *Psm-α* mutant colony evolution. (b) *Psm-α* mutant simulation result.

Figure 4.16.: *S. aureus psm-α* mutant bacteria colony as obtained from simulation with the described parameter changes in (b) and biological real data [65] in (a).

and which is larger than the corresponding layer in the wildtype colony. Concerning the regulation mechanisms, the effect of a lack of PSM is mainly the decreased POPC vesicle lysing capacity. Since this capacity is smaller for PSM-α than for PSM-β, also the decrease is smaller and thus we obtain the growth parameters $G_1 = G_2 = 6$. Due to the structuring effect of PSM, we decrease the parameter d_n to $d_n = 0.7$ in the mutant. Since the *psm-α* mutation has much slighter effects than the *psm-β* mutation on biofilm diffusion, we do not change the parameter d_f here. The interested reader can find the single concentrations for the *psm-α* mutant in Figure A1.4 in the appendix.

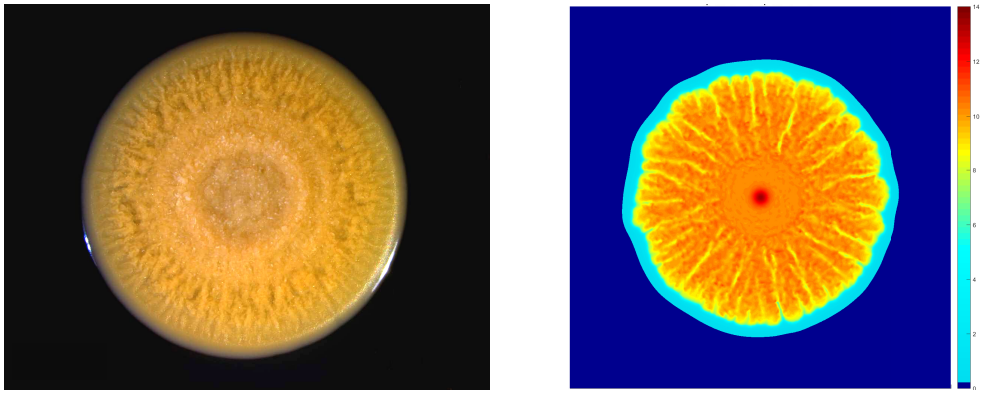

(a) *Psm-β* mutant colony evolution. (b) *Psm-β* mutant simulation result.

Figure 4.17.: *S. aureus psm-β* mutant bacteria colony as obtained from simulation with the described parameter changes in (b) and biological real data [65] in (a).

Similar choices are taken for the amyloid type 2 or *psm-β* mutant real data de-

picted in Figure 4.17(a), where the growth parameters are decreased to the values $G_1 = G_2 = 4$. Since the *psm-β* mutation has a much stronger effect than the *psm-α* mutation, here we also slightly increase the replicative bacteria diffusion parameter to $\sigma = 0.65$. This reflects the fact that the lack of biofilm structure makes it easier for the bacteria to move. Due to the structuring effect of PSM, the parameter d_n is changed to the value $d_n = 0.4$. Furthermore, since PSM positively influences biofilm dispersal [87], we increase the mutant biofilm diffusion coefficient to $d_f = 3$. The further decrease in G_1 and G_2 is due to the higher lysing capacity of PSM-β. The colony of this mutant shows very little structure and very little wrinkling in a round colony shape in both the real data and the simulation results depicted in Figure 4.17(b). Additionally the single concentrations for the *psm-β* mutant can be found in Figure A1.5 in the appendix.

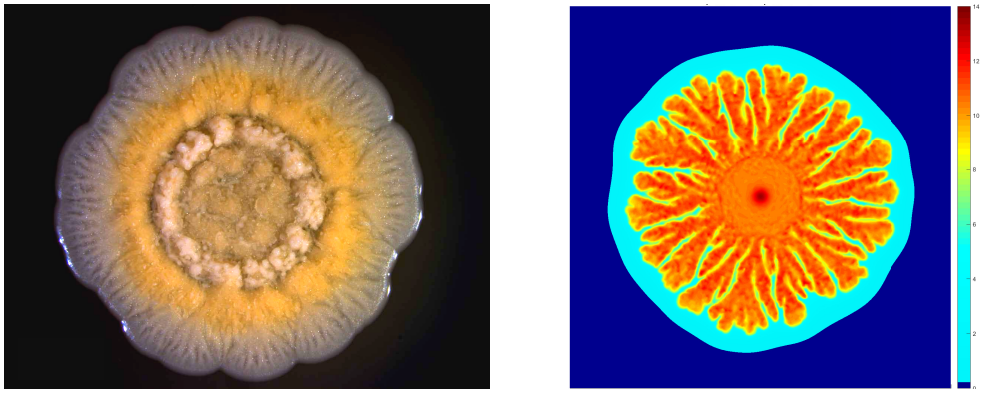

(a) *Psm-α* and *psm-β* mutant colony evolution.

(b) *Psm-α* and *psm-β* mutant simulation result.

Figure 4.18.: *S. aureus psm-α* and *psm-β* mutant bacteria colony as obtained from simulation with the described parameter changes in (b) and biological real data [89] in (a).

The biological observation for the mutant in both amyloid type 1 and type 2 is depicted in Figure 4.18(a). We observe a colony that shows a ring structure like the amyloid type 1 mutant and an outer area with very few wrinkles like the type 2 mutant. Furthermore, the colony shape is no longer round, but has pronounced dents resulting in a flower-like colony shape. It is observed that the biofilm-enhancing effect in *psm-α* and *psm-β* mutants is not additive. A possible reason for this is the absence of the benefits on biofilm structuring and maturation induced by low concentrations of PSM-β, as it is the case in *S. epidermidis* [87, 145], a close relative of *S. aureus*. Thus we cannot simply add the effects from the type 1 and type 2 mutants. We take the nutrient consumption parameters $G_1 = G_2 = 2.5$, which are

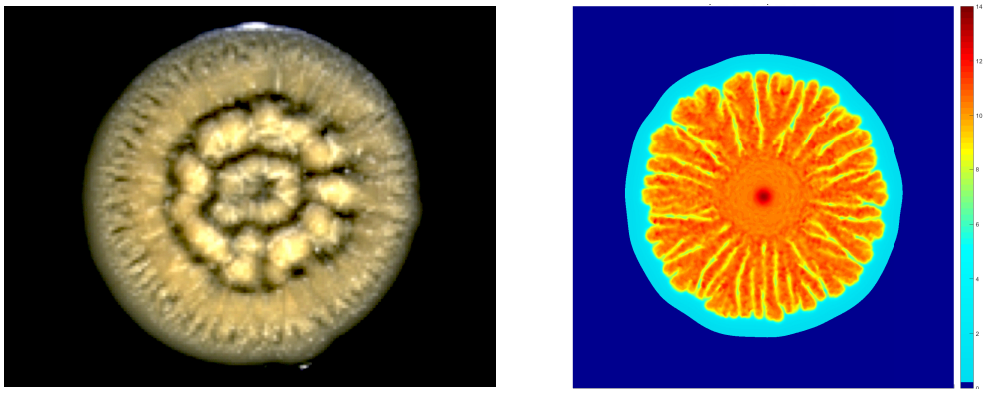

(a) *Agr* mutant colony evolution. (b) *Agr* mutant simulation result.

Figure 4.19.: *S. aureus agr* mutant bacteria colony as obtained from simulation with the described parameter changes in (b) and biological real data [65] in (a).

smaller than the corresponding parameters in the single mutants. Furthermore, we set the bacteria diffusion parameter to $\sigma = 0.6$, which represents a value in between the values chosen for the *psm-α* and *psm-β* mutants. This is also the case for the nutrient diffusion coefficient, which is chosen to be $d_n = 0.5$ and the biofilm diffusion coefficient $d_f = 2.5$. In the simulation results depicted in Figure 4.18(b), a good agreement of the simulation results is observed as the flower-like shape as well as the predicted changes in wrinkling and ring structure are reproduced. Again the interested reader can find the single concentration simulation results in Figure A1.6 in the appendix.

The quorum sensing or *agr* mutant real data as displayed in Figure 4.19(a) shows a very clear structure in the middle of the colony, while towards the outer areas, the colony flattens and shows more pronounced dents. The colony is surrounded by a biofilm layer, which is slightly uneven, but not as uneven as in the case of the *psm-α* and *psm-β* mutant colony. Since there is no quorum sensing, the parameters G_q and μ_q are set to zero. No *agr* activity also means that there are no PSM, which lyse cells to gain nutrients and help in biofilm structuring and dispersal. Thus the growth parameters are decreased, i.e., $G_1 = G_2 = 2.5$ as in the *psm-α* and *psm-β* mutant colony. Furthermore, since the biofilm is less structured without PSM, the diffusion coefficient of the replicative bacteria is again increased to $\sigma = 0.6$. Analogously to the *psm-α* and *psm-β* mutant, the diffusion parameters for the nutrients and for the biofilm are chosen as $d_n = 0.5$ and $d_f = 2.5$, respectively. We observe a good agreement of the simulation result depicted in Figure 4.19(b), where the structure in the middle of the colony as well as the slightly uneven biofilm layer

Mutant	$G_1 = G_2$	σ	G_f	G_q	μ_q	δ	d_n	d_f
Wildtype	7	0.5	0.1	0.1	0.1	1	1	2
Ica	5	1	0	0.1	0.1	1	1	2
Spa	7	0.5	0.1	0.1	0.1	5	1.5	2
Ica and *spa*	5	1	0	0.1	0.1	5	1.5	2
Psm-α	6	0.5	0.1	0.1	0.1	1	0.7	2
Psm-β	4	0.65	0.1	0.1	0.1	1	0.4	3
Psm-α and *-*β	2.5	0.6	0.1	0.1	0.1	1	0.5	2.5
Agr	2.5	0.6	0.1	0	0	1	0.5	2.5

Table 4.9.: Changed parameter values for the simulation of the *S. aureus* mutant bacteria colonies in comparison to the parameters for the wildtype.

are reproduced. In addition, the single concentrations are depicted in Figure A1.7 in the appendix. A summary of the changes in the parameter values for the mutants considered above is found in Table 4.9.

In Figure 4.20 the results for the five bacterial morphologies as introduced in [98] are displayed. As in [98], the type of pattern is investigated depending on the initial nutrient concentration n_0 and the concentration of the growth medium or the bacterial diffusion coefficient σ, respectively. We distinguish five different morphologies: The diffusion-limited aggregation (DLA) denoted by A, the Eden-like morphology denoted by B, the concentric ring-like morphology denoted by C, the disk-like morphology denoted by D and the dense branching morphology (DBM) denoted by E in Figure 4.20. Diffusion-limited aggregation colonies show a star-like structure with only few branches, which have larger gaps in between them, and are observed for low values of both n_0 and σ. In the Eden-like morphology, the bacteria colony has a flower-like shape and the branches are close. In comparison to the parameters in the DLA case, here the initial nutrient concentration is significantly larger. The concentric ring-like morphology shows a rather round shape, in which concentric structures are observed and is found for large values of n_0 and rather large values of σ. The disk-like morphology has a surface with very little structure and a round colony shape, which is mainly caused by large diffusion coefficients. In the DBM, the branches are dense but can be clearly distinguished and the shape of the colony is mostly round. This is the case for medium to large diffusion coefficients in combination with a medium to small initial nutrient concentration.

To obtain the morphologies displayed in Figure 4.20, we use the wildtype parameter values as described in Table 4.8 and alter the parameters n_0 and σ, and in one case also the parameter α_q, as indicated by the axes of the diagram. Varying only these three parameters yields a wide range of colony morphologies. The wildtype

colony represents a dense branching morphology phenotype at $(\sigma, n_0) = (0.5, 1.11)$. Another DBM is found at $(0.5, 0.7)$, thus at the same nutrient level as the DLA representative, which is found at $(0.2, 0.7)$. The Eden-like morphology is observed at a larger initial nutrient concentration at $(0.1, 2.0)$ and disk-like patterns are obtained at $(1.0, 2.0)$ and $(0.5, 3.0)$. For the concentric ring-like morphology we obtain the result displayed at $(0.2, 4.0)$, where a ring structure is observed in the inner part of the colony while the outer part of the colony shows a pattern which resembles the beginning of branching, such that two different levels are observed. Thus, the arrangement of the different colony types in the (σ, n_0) plane qualitatively replicates the classification scheme displayed in [98].

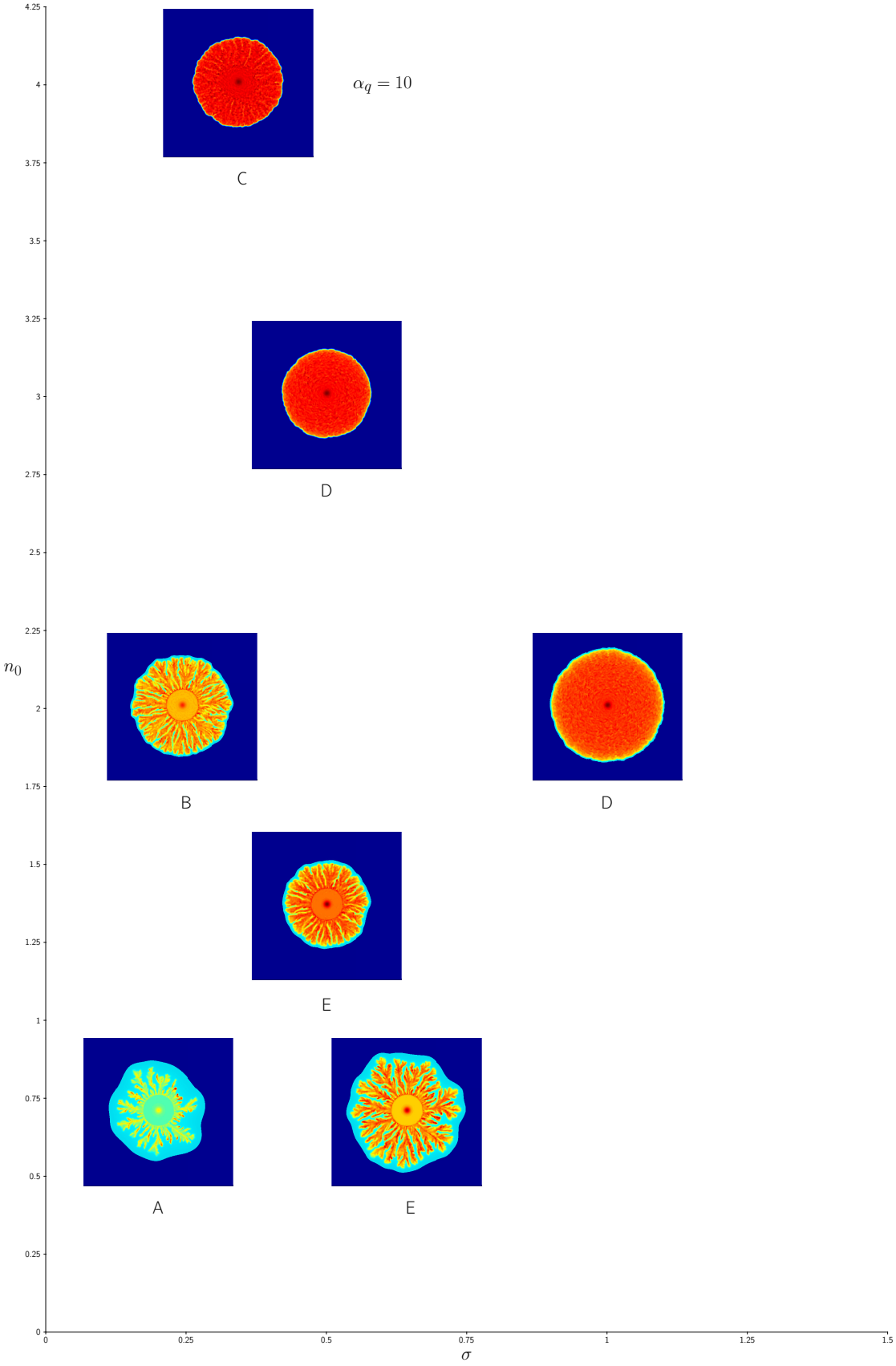

Figure 4.20.: The five morphologies as obtained from simulations of the five equation model. Dependence of pattern formation on levels of σ and n_0.

5. Analysis of pattern formation

In this chapter we investigate methods to analyze pattern formation in the simplified situation of a reduced system consisting of two partial differential equations. Starting from standard Turing approaches as described in Part I, Section 3.2 for the investigation of a system such as Equations (4.1)–(4.2), we later consider a front instability approach in order to determine the onset of fingering for the mixed bacterial diffusion term.

5.1. Turing pattern formation analysis

Turing pattern formation analysis as introduced in Section 3.2 represents a well-known approach for the investigation of pattern formation in systems of reaction-diffusion equations. However, we keep in mind that there are two main challenges for our situation of bacterial pattern formation. The first one is the initially circular geometry of the biological setting, which does not represent a spatially homogeneous stationary state as required for Turing pattern formation, and the second one is the inhomogeneous bacteria diffusion coefficient. Our aim in the following is to investigate the mechanisms behind the pattern formation in our particular model setting. We start by investigating which role Turing pattern mechanisms could play. To this end, we derive the corresponding Turing parameters and investigate simulation results around these parameters.

For a system of equations similar to Equations (4.1)–(4.2), a spatially homogeneous stationary state is not readily obtained. As we consider only the equations for the nutrient concentration n and the replicative bacteria density b, we obtain that the steady state concentrations $(\bar{n}, \bar{b})$ have to satisfy the equation

$$\frac{\partial \bar{n}}{\partial t} = -G_1 g_1(\bar{n}, \bar{b}) = 0,$$

where we recall that $g_1(\bar{n}, \bar{b}) = \frac{\bar{n}\bar{b}}{1+\gamma\bar{n}}$. This is only possible if either $\bar{n} = 0$ or $\bar{b} = 0$.

In order to obtain

$$\frac{\partial \bar{b}}{\partial t} = G_2 g_1(\bar{n}, \bar{b}) - a(\bar{n}, \bar{b}) = 0,$$

also $a(\bar{n}, \bar{b}) = \varepsilon \frac{\bar{b}}{(1+\frac{\bar{b}}{a_1})(1+\frac{\bar{n}}{a_2})}$ has to vanish. This leads to the two possible types of steady states $(\bar{n}, \bar{b}) = (0, 0)$ and $(\bar{n}, 0)$ with $\bar{b} = 0$ and $\bar{n} > 0$. In both cases, one of the steady state concentrations is zero. Thus, in the following, we consider a simple modified system of equations of the form

$$\frac{\partial n}{\partial t} = d_n \Delta n - G_1 \frac{nb}{1+\gamma n} + \varepsilon_0, \tag{5.1}$$

$$\frac{\partial b}{\partial t} = \nabla \cdot (\sigma n b \nabla b) + G_2 \frac{nb}{1+\gamma n} - \mu b, \tag{5.2}$$

in the domain Ω. Here the parameter ε_0 denotes a small positive inflow of nutrients into the system and is necessary for a positive spatially homogeneous state of the system. The spatially homogeneous stationary state of such a system is

$$(\bar{n}, \bar{b}) = (\frac{\mu}{G_2 - \gamma\mu}, \frac{G_2 \varepsilon_0}{G_1 \mu}). \tag{5.3}$$

Then, the required positivity of the stationary state gives the first restriction on the parameters $d_n, \sigma, G_1, G_2, \gamma, \varepsilon_0, \mu \in \mathbb{R}_+$ as

$$G_2 - \gamma\mu > 0. \tag{5.4}$$

With the transformations $n \to \bar{n} + n_1$ and $b \to \bar{b} + b_1$, the bacteria diffusion term is linearized as

$$\nabla \cdot (nb\nabla b) = \underbrace{\bar{n}\bar{b}}_{=:\rho/\sigma} \Delta b_1 + \underbrace{\nabla \cdot (n_1 b_1 \nabla b_1) + \bar{b}\nabla \cdot (n_1 \nabla b_1) + \bar{n}\nabla \cdot (b_1 \nabla b_1)}_{=:g(n_1,b_1)/\sigma}.$$

Using the diffusion coefficient reparametrization $D := \frac{\sigma}{d_n}$, the resulting linearized system is of the form

$$\frac{\partial n_1}{\partial t} = \Delta n_1 + j_{11} n_1 + j_{12} b_1, \tag{5.5}$$

$$\frac{\partial b_1}{\partial t} = D\bar{n}\bar{b}\Delta b_1 + j_{21} n_1 + j_{22} b_1 + g(n_1, b_1). \tag{5.6}$$

The entries of the Jacobian $J = (j_{kl})_{k,l=1,2}$ in $(\bar{n}, \bar{b})$ are

$$j_{11} = -\frac{G_2\varepsilon_0(\gamma\mu - G_2)^2(9\gamma^2\mu^2 + 4G_2\gamma\mu + G_2^2)}{\mu(G_2 + \gamma\mu)^4},\ j_{12} = -\frac{G_1\mu(4\gamma^2\mu^2 + 3G_2\gamma\mu + G_2^2)}{(G_2 + \gamma\mu)^3},$$
$$j_{21} = \frac{G_2^2\varepsilon_0(\gamma\mu - G_2)^2(9\gamma^2\mu^2 + 4G_2\gamma\mu + G_2^2)}{G_1\mu(G_2 + \gamma\mu)^4} \quad \text{and} \quad j_{22} = -\frac{\gamma^2\mu^3(\gamma\mu - G_2)}{(G_2 + \gamma\mu)^3}.$$

Furthermore, the linearized system matrix $L_\lambda := J - B_\lambda$, where $-B_\lambda\mathbf{u}$ is defined as $-B_\lambda\mathbf{u} := \begin{pmatrix}\Delta n_1 & \frac{\rho}{d_n}\Delta b_1\end{pmatrix}^T$, constitutes a mapping $L_\lambda : X^2 \to (H^2(\Omega))^2$ from the space $X^2 := \{\mathbf{u} \in (H^2(\Omega))^2 : \frac{\partial \mathbf{u}}{\partial \mathbf{n}} = 0 \text{ on } \partial\Omega\}$.

With the above results we perform the Turing stability analysis according to Theorem 3.2.1 in Section 3.2. Following (3.8), the stability of the equilibrium without diffusion translates to the Turing conditions

$$\operatorname{tr}(J) = j_{11} + j_{22} < 0 \qquad \text{and} \qquad \det(J) = j_{11}j_{22} - j_{12}j_{21} > 0. \tag{5.7}$$

The remaining Turing conditions for the diffusion-driven instability read

$$j_{22} + D\bar{n}\bar{b}j_{11} > 0 \qquad \text{and} \qquad (j_{22} + D\bar{n}\bar{b}j_{11})^2 > 4D\bar{n}\bar{b}(j_{11}j_{22} - j_{12}j_{21}), \tag{5.8}$$

as in (3.14)–(3.15). Then the first condition from (5.7) is fulfilled if the condition

$$\begin{aligned} j_{11} + j_{22} < 0 \qquad &\iff \qquad \varepsilon_0 > \frac{\gamma^2\mu^4(G_2 + \gamma\mu)}{G_2(G_2 - \gamma\mu)(9\gamma^2\mu^2 + 4G_2\gamma\mu + G_2^2)} \\ &\iff \qquad \bar{n} = \frac{\mu}{G_2 - \gamma\mu} < \frac{\varepsilon_0 G_2(9\gamma^2\mu^2 + 4G_2\gamma\mu + G_2^2)}{\gamma^2\mu^3(G_2 + \gamma\mu)} \end{aligned}$$

holds. Furthermore, due to (5.4), we know that the right-hand side, and thus also ε_0, are greater than zero.

We verify that the second condition from (5.7) always holds by inserting the terms for $j_{11}j_{22} < 0$ and $j_{12}j_{21} < 0$. We obtain the condition

$$\begin{aligned} & j_{11}j_{22} - j_{12}j_{21} > 0 \\ \iff & \left(-\frac{G_2\varepsilon_0(\gamma\mu - G_2)^2(9\gamma^2\mu^2 + 4G_2\gamma\mu + G_2^2)}{\mu(G_2 + \gamma\mu)^4}\right)\left(-\frac{\gamma^2\mu^3(\gamma\mu - G_2)}{(G_2 + \gamma\mu)^3}\right) - \\ & \left(-\frac{G_1\mu(4\gamma^2\mu^2 + 3G_2\gamma\mu + G_2^2)}{(G_2 + \gamma\mu)^3}\right)\left(\frac{G_2^2\varepsilon_0(\gamma\mu - G_2)^2(9\gamma^2\mu^2 + 4G_2\gamma\mu + G_2^2)}{G_1\mu(G_2 + \gamma\mu)^4}\right) > 0 \\ \iff & \left(\frac{G_2\varepsilon_0(\gamma\mu - G_2)^2(9\gamma^2\mu^2 + 4G_2\gamma\mu + G_2^2)}{\mu(G_2 + \gamma\mu)^4}\right). \end{aligned}$$

$$\left[\frac{\gamma^2\mu^3(\gamma\mu - G_2) + G_2\mu(4\gamma^2\mu^2 + 3G_2\gamma\mu + G_2^2)}{(G_2+\gamma\mu)^3}\right] > 0$$

$$\iff \left[\gamma^3\mu^4 \underbrace{-G_2\gamma^2\mu^3 + 4G_2\gamma^2\mu^3}_{=3G_2\gamma^2\mu^3} + 3G_2^2\gamma\mu^2 + G_2^3\mu\right] > 0,$$

which is fulfilled since the parameters are positive by definition.

The first condition in (5.8) yields the inequality

$$\begin{aligned}
&D\bar{n}\bar{b}j_{11} + j_{22} > 0\\
\iff &D\bar{n}\bar{b}\left(-\frac{G_2\varepsilon_0(\gamma\mu - G_2)^2(9\gamma^2\mu^2 + 4G_2\gamma\mu + G_2^2)}{\mu(G_2+\gamma\mu)^4}\right) + \left(-\frac{\gamma^2\mu^3(\gamma\mu - G_2)}{(G_2+\gamma\mu)^3}\right) > 0\\
\iff &- D\bar{n}\bar{b}G_2\varepsilon_0(G_2 - \gamma\mu)^2(9\gamma^2\mu^2 + 4G_2\gamma\mu + G_2^2) + \gamma^2\mu^4(G_2 - \gamma\mu)(G_2+\gamma\mu) > 0\\
\iff &D < \frac{\gamma^2\mu^3(G_2+\gamma\mu)}{\bar{b}G_2\varepsilon_0(9\gamma^2\mu^2 + 4G_2\gamma\mu + G_2^2)}.
\end{aligned}$$

Furthermore, we note that again the right-hand side is greater than zero.

For the second condition in (5.8) we find the following inequality to be fulfilled by the diffusion parameter D:

$$\begin{aligned}
&(j_{22} + D\bar{n}\bar{b}j_{11})^2 > 4D\bar{n}\bar{b}(j_{11}j_{22} - j_{12}j_{21})\\
\iff &j_{22}^2 - 2D\bar{n}\bar{b}j_{11}j_{22} + D^2\bar{n}^2\bar{b}^2j_{11}^2 > -4D\bar{n}\bar{b}j_{12}j_{21}\\
\iff &\frac{\gamma^4\mu^6(\gamma\mu - G_2)^2}{(G_2+\gamma\mu)^6} - \frac{2D\bar{n}\bar{b}G_2\varepsilon_0(\gamma\mu - G_2)^3(9\gamma^2\mu^2 + 4G_2\gamma\mu + G_2^2)\gamma^2\mu^2}{(G_2+\gamma\mu)^7}\\
&+ \frac{D^2\bar{n}^2\bar{b}^2G_2^2\varepsilon_0^2(\gamma\mu - G_2)^4(9\gamma^2\mu^2 + 4G_2\gamma\mu + G_2^2)^2}{\mu^2(\gamma\mu + G_2)^8} >\\
&\frac{4D\bar{n}\bar{b}(4\gamma^2\mu^2 + 3G_2\gamma\mu + G_2^2)G_2^2\varepsilon_0(\gamma\mu - G_2)^2(9\gamma^2\mu^2 + 4G_2\gamma\mu + G_2^2)}{(\gamma\mu + G_2)^7}\\
\iff &D^2\bar{n}^2\bar{b}^2G_2^2\varepsilon_0^2(G_2 - \gamma\mu)^2(9\gamma^2\mu^2 + 4G_2\gamma\mu + G_2^2)^2 + \gamma^4\mu^8(G_2+\gamma\mu)^2 >\\
&2D\bar{n}\bar{b}G_2\varepsilon_0\mu^2(9\gamma^2\mu^2 + 4G_2\gamma\mu + G_2^2)(G_2+\gamma\mu)[\gamma^3\mu^3 + 7G_2\gamma^2\mu^2 + 6G_2^2\gamma\mu + 2G_2^3]\\
\iff &D^2\bar{b}^2G_2^2\varepsilon_0^2(9\gamma^2\mu^2 + 4G_2\gamma\mu + G_2^2)^2 + \gamma^4\mu^6(G_2+\gamma\mu)^2 >\\
&2D\bar{n}\bar{b}G_2\varepsilon_0(9\gamma^2\mu^2 + 4G_2\gamma\mu + G_2^2)(G_2+\gamma\mu)[\gamma^3\mu^3 + 7G_2\gamma^2\mu^2 + 6G_2^2\gamma\mu + 2G_2^3].
\end{aligned}$$

For the Turing bifurcations we are especially interested in the relationship between the diffusion coefficients and the initial values. For the chosen parameter values $G_1 = \gamma = 1$, $G_2 = 0.2$, $\varepsilon_0 = 0.01$ and $\mu = 0.1$, we calculate that the spatially

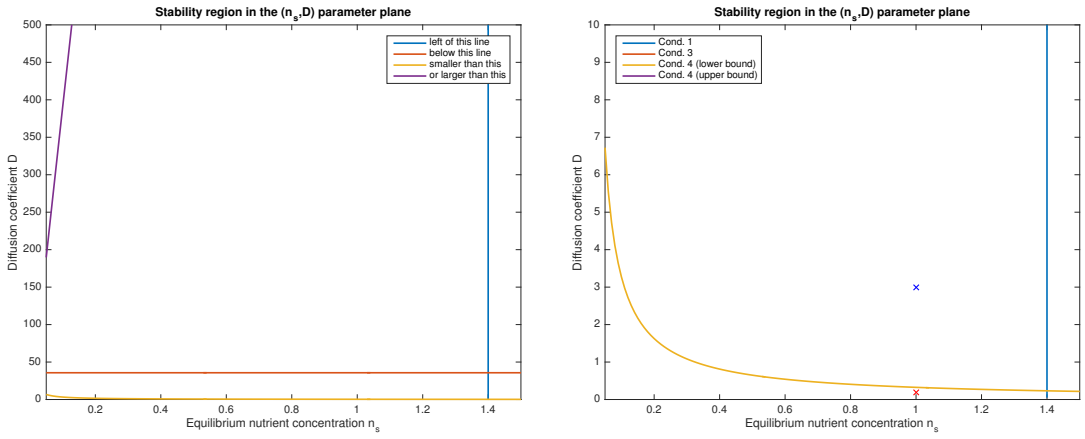

(a) Conditions on the parameters. (b) Zoom into admissible area.

Figure 5.1.: Turing bifurcation diagram for Equations (5.5), (5.6). Parameters $G_1 = \gamma = 1$, $\mu = 0.1$, $G_2 = 0.2$, $\varepsilon_0 = 0.01$. Parameter sets $(n_s, D) = (1, 0.2)$ and $(n_s, D) = (1, 3)$ for simulations indicated by red and blue cross.

homogeneous stationary state is $(\bar{n}, \bar{b}) = (1, 0.02)$.

Thus it follows that $\bar{n}\bar{b} = 0.02$ and the Turing bifurcation takes place at $D_{\text{crit}} = \frac{\sigma_{\text{crit}}}{d_{n_{\text{crit}}}} = 0.3247$. We observe that in this fraction the nutrient diffusion $d_{n_{\text{crit}}}$ is high in comparison to the bacteria diffusion σ_{crit}, even more so when we consider the relationship between $d_{n_{\text{crit}}}$ and the effective diffusion value $\rho_{\text{crit}} := \sigma_{\text{crit}}\bar{n}\bar{b}$. From $\frac{\rho_{\text{crit}}}{d_{n_{\text{crit}}}} = D_{\text{crit}}\bar{n}\bar{b}$ we calculate $d_{n_{\text{crit}}} = \frac{\rho_{\text{crit}}}{0.3247 \cdot 0.02} \approx 154\rho_{\text{crit}}$, which is unrealistic in a biological scenario.

The bifurcation diagram for the chosen parameter values is displayed in Figure 5.1, where a set of parameter values for which we expect Turing pattern formation is indicated by a red cross and another set of parameter values, where we do not expect a Turing pattern, is indicated by a blue cross. Using these parameter values and standard diffusion with the coefficient $D\bar{n}\bar{b}$ for initially homogeneous concentrations with a random disturbance, we obtain the simulation results depicted in Figure 3.2 in Section 3.2. With the same sets of parameter values for the bacterial colony simulations of Equations (5.1)–(5.2), we obtain the results later displayed in Figure 5.5 in Section 5.3.

An approach which seems promising for bacterial colony pattern formation is Turing pattern analysis using an inhomogeneity approach. Inhomogeneity approaches as introduced in [112, 113] and [17, 18, 19, 91] are appealing since they allow for

inhomogeneity in either the diffusion coefficient or in one of the remaining parameters of a system of model equations. This idea appears promising to represent some aspects of the special geometry of our model. Due to the circular geometry of the bacterial colony, polar coordinates in the two-dimensional domain Ω are of interest to investigate pattern formation along the one-dimensional radius of the colony. However, while the colony, and thus also the radius, grow in time, a fixed radius is required to divide the domain into two subdomains. Furthermore, a single inhomogeneous parameter approach is not fully tailored to represent the inhomogeneities in colony growth, as there are several differences in- and outside the colony and thus step functions are needed for several parameters. Thus we do not consider Turing inhomogeneity approaches in detail, but in the following section concentrate on a front instability approach, which is based on traveling wave solutions.

5.2. Front instability approach

In [123], global existence of traveling wave solutions of the system of equations describing bacterial pattern formation introduced in [82], which is similar to our system, is investigated. With the assumption $d_n = 0$ in the equation for the nutrient density, the existence of sharp type traveling wave solutions is shown and a minimum wave speed is derived. In [62], the existence of a finite traveling wave solution for the degenerate mixed diffusion equation is investigated also in the case $d_n \neq 0$. This approach opens another path to investigate bacterial pattern formation in the special geometry of a growing bacterial colony. In order to determine when branching is observed, we consider traveling wave solutions along the one-dimensional radial direction. If diffusion is large enough, perturbations are smoothed out, otherwise they develop to a pattern. Traveling wave approaches such as [57, 75, 103, 140] can help to determine the critical diffusion coefficient for the onset of pattern formation in our mixed diffusion model. In the following, we consider a numerical traveling wave approach as introduced in [103].

For the planar front instability ansatz we do not need to modify our two-equation system by adding a constant ε_0 as in Equations (5.1)–(5.2) in order to obtain a positive spatially homogeneous steady state. However, we want to ensure mass conservation and reduce the number of parameters. For proof of principle we therefore do not include a bacterial death term $-\mu b$ and take $G_1 = G_2 = 1$. We

consider the system of equations

$$\frac{\partial n}{\partial t} = d_n \Delta n - \frac{nb}{1+\gamma n}, \tag{5.9}$$

$$\frac{\partial b}{\partial t} = \nabla \cdot (\sigma n b \nabla b) + \frac{nb}{1+\gamma n}. \tag{5.10}$$

Note that we extend the non-linear diffusion term in the form

$$\nabla \cdot (\sigma n b \nabla b) = \sigma (nb\Delta b + [b\nabla n + n\nabla b] \cdot \nabla b).$$

In the following, we rescale using $D := \frac{\sigma}{d_n}$. The system of Equations (5.9)–(5.10) has the two trivial homogeneous solutions $(n^\star, b^\star) = (c_n, 0)$ and $(0, c_b)$. Of these homogeneous solutions, the first one is unstable since any small population of bacteria can invade and due to the ample nutrient supply the population will grow. The second solution is stable since any small amount of nutrients is eaten by the bacteria, leading back to the stationary state. The propagation of the bacteria field into the nutrient field corresponds to a propagation of the stable stationary state into the unstable stationary state.

The problem stated in Equations (5.9)–(5.10) is well-posed, but the solutions may not be classical due to the nutrient dependent diffusion [73, 123]. Following [123], we can assume that for suitable initial and boundary conditions there exists a unique pair of solutions (n, b) for all positive times. Furthermore, as in [123], we deduce that the traveling wave solutions are the only long time solutions supported by Equations (5.9)–(5.10). This is further supported by the results in [62], where an existence and uniqueness proof is conducted for traveling wave solutions to a system with mixed diffusion for the bacteria and reaction terms of the form $n^q b^l$ with $q, l > 1$.

We consider a one-dimensional traveling wave approach in the radial direction $(x, y) = (x, 0)$ with the variable $\xi := x - v_0 t$, which yields the equations

$$Dnb\frac{d^2 b}{d\xi^2} + D\left[b\frac{dn}{d\xi} + n\frac{db}{d\xi}\right]\frac{db}{d\xi} + v_0\frac{db}{d\xi} + \frac{nb}{1+\gamma n} = 0, \tag{5.11}$$

$$\frac{d^2 n}{d\xi^2} + v_0\frac{dn}{d\xi} - \frac{nb}{1+\gamma n} = 0, \tag{5.12}$$

in the co-moving frame. In the following, we adapt the approach from [103] for the case of bacteria density dependent diffusion to our bacteria density and nutrient concentration dependent diffusion model. For large negative values of ξ, n ap-

proaches 0 and the term $\frac{d}{d\xi}\left[nb\frac{db}{d\xi}\right]$ represents a smaller effective diffusion coefficient than the bacteria density dependent term $\frac{d}{d\xi}\left[b\frac{db}{d\xi}\right]$. Thus, the changes in the concentrations towards $\xi \to -\infty$ are slower than in the bacteria density dependent case.

The boundary conditions at $\xi \to \pm\infty$ are given by the homogeneous steady states. Thus for $\xi \to -\infty$ we obtain

$$\begin{aligned} b(\xi \to -\infty) &= c_b, \qquad & d_\xi b(\xi \to -\infty) &= 0, \\ n(\xi \to -\infty) &= 0, \qquad & d_\xi n(\xi \to -\infty) &= 0, \end{aligned}$$

and for $\xi \to \infty$ we obtain

$$\begin{aligned} b(\xi \to \infty) &= 0, \qquad & d_\xi b(\xi \to \infty) &= 0, \\ n(\xi \to \infty) &= c_n, \qquad & d_\xi n(\xi \to \infty) &= 0. \end{aligned}$$

The stable state $(c_b, 0)$ at $\xi \to -\infty$ invades the unstable state $(0, c_n)$ at $\xi \to \infty$. We choose ξ such that the region outside the colony in which $b(\xi) = 0$ corresponds to the region in which $\xi > 0$. Thus, in this region the system of linear equations [103]

$$b(\xi) = 0, \qquad \frac{d^2n}{d\xi^2} + v_0\frac{dn}{d\xi} = 0$$

is valid. It is solved explicitly to yield $n(\xi) = c_n - c_0\exp(-v_0\xi)$, where $c_0 \in \mathbb{R}_+$ is a constant. At the boundary $\xi = 0$ the boundary conditions

$$n(0) = c_n - c_0 > 0, \qquad \frac{dn}{d\xi}|_{\xi=0} = v_0c_0, \tag{5.13}$$

have to be fulfilled. We consider the area near $\xi = 0$, where for $\xi \to 0$ we assume that the concentration b shows a behavior of the form $b(\xi) \sim A(-\xi)^\alpha$ according to [62, 103]. Inserting this form into Equation (5.11) for the traveling wave yields

$$\begin{aligned} &DnA(-\xi)^\alpha\alpha(\alpha-1)A(-\xi)^{\alpha-2} + D\left[A(-\xi)^\alpha\frac{dn}{d\xi} - n\alpha A(-\xi)^{\alpha-1}\right]\cdot \\ &\qquad (-\alpha A(-\xi)^{\alpha-1}) - v_0\alpha A(-\xi)^{\alpha-1} + \frac{nA(-\xi)^\alpha}{1+\gamma n} = 0 \\ \Longleftrightarrow\; &Dn\alpha(\alpha-1)A^2(-\xi)^{2\alpha-2} - D\alpha A^2\frac{dn}{d\xi}(-\xi)^{2\alpha-1} + Dn\alpha^2A^2(-\xi)^{2\alpha-2} \\ &\qquad - v_0\alpha A(-\xi)^{\alpha-1} + \frac{nA(-\xi)^\alpha}{1+\gamma n} = 0. \end{aligned}$$

Since the dominant terms in ξ have to cancel out at $\xi = 0$, it holds that

$$Dn(0)\alpha(\alpha-1)A^2(-\xi)^{2\alpha-2} + Dn(0)\alpha^2A^2(-\xi)^{2\alpha-2} - v_0\alpha A(-\xi)^{\alpha-1} = 0.$$

It follows that for the above equation to be fulfilled it has to hold that

$$\alpha = 1 \qquad \text{and} \qquad A = \frac{v_0}{Dn(0)}. \tag{5.14}$$

Since we have chosen reaction terms that fulfill conservation of mass, we can reduce the order of the system. Adding Equations (5.11) and (5.12) yields the system

$$\begin{aligned} D\frac{d}{d\xi}\left(nb\frac{db}{d\xi}\right) + v_0\frac{db}{d\xi} + \frac{nb}{1+\gamma n} &= 0, \\ \frac{d^2n}{d\xi^2} + D\frac{d}{d\xi}\left(nb\frac{db}{d\xi}\right) + v_0\frac{dn}{d\xi} + v_0\frac{db}{d\xi} &= 0, \end{aligned}$$

and by integration from $-\infty$ to ξ in the second equation, we obtain the system

$$\begin{aligned} D\frac{d}{d\xi}\left(nb\frac{db}{d\xi}\right) + v_0\frac{db}{d\xi} + \frac{nb}{1+\gamma n} &= 0, \\ \frac{dn}{d\xi} + Dnb\frac{db}{d\xi} + v_0(n + b - c_b) &= 0. \end{aligned}$$

Since the derivatives vanish at $\xi \to \pm\infty$, it holds that $c_b = c_n = 1$. Any other choice of c_b, c_n can be transformed to this case using a renormalized diffusion coefficient D_R as described in [103].

Following the approaches described in [58, 103, 118], we consider a heteroclinic orbit in the $(b, d_\xi b, n)$ phase space and shoot to a fitting point in order to determine the planar velocity v_0. Since the values for $\xi > 0$ are determined analytically, we do not need to use a shooting method on the positive line. Instead, at $\xi = 0$, we compare the analytically obtained concentrations to those from the shooting method on $\xi < 0$ and choose v_0 as the value for which the boundary conditions are fulfilled. For the computation of the front profiles, the initial concentrations $(n_{\text{init}}, b_{\text{init}}) = (0.001, 0.999)$ are chosen for computational reasons and the point $\xi = 0$ is set such that $b(0) = 0$. In Figure 5.2 the obtained values of v_0 for several values of D are displayed. As expected, in comparison to the bacteria density dependent case with $k = 1$ [103], we observe that smaller values of v_0 are chosen. Furthermore, the behavior for small values of D differs as we observe very small and also similar values of v_0 for small D. This reflects the fact that the effective diffusion is further

reduced by the dependence on the small nutrient concentration.

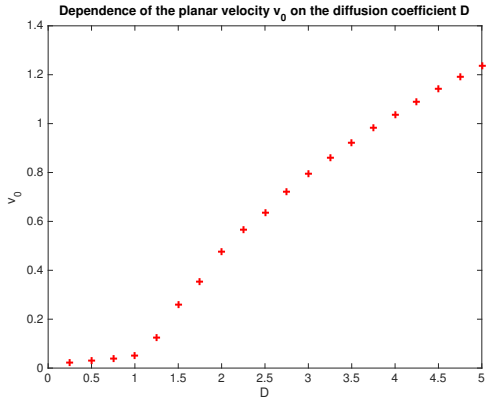

Figure 5.2.: Planar front velocities v_0 in dependence of the diffusion coefficient $D \in [0.25, 5.00]$.

In the following Sections 5.2.1 and 5.2.2, two different approaches to investigate stability are presented. Since these approaches yield very similar results in the bacteria density dependent case [103], we only perform one of these approaches for the stability analysis, namely the investigation of the critical line as described in Section 5.2.2.

5.2.1. Linear stability analysis investigating the dispersion relation

In the following, we introduce a perturbation of the front in order to study its linear stability. This approach is relevant for both stability investigations mentioned above. The perturbations are not only perturbations in b and n, but also in the shape of the line. As in [103], for $(x, y) \in \mathbb{R}^2$, we focus on perturbations of the form $h(y,t) := \varepsilon \exp(iqy + \omega t)$ and switch to the locally co-moving frame

$$\zeta := x - v_0 t + h(y,t) = \xi + h(y,t).$$

This yields the expressions

$$b(\zeta, y, t) = b_0(\zeta) + \varepsilon b_1(\zeta) \exp(iqy + \omega t) \qquad \text{and} \tag{5.15}$$

$$n(\zeta, y, t) = n_0(\zeta) + \varepsilon n_1(\zeta) \exp(iqy + \omega t), \tag{5.16}$$

where (b_0, n_0) is the planar front solution determined above. Furthermore, ε denotes the amplitude, q is the wave number and b_1, n_1 are twice continuously differentiable

functions away from 0 with $\frac{b_1}{b_0}$, $\frac{n_1}{n_0}$ bounded.

Linearization of Equations (5.9)–(5.10) about the uniformly translating solution with $\varepsilon = 0$ gives the matrix formulation

$$\mathcal{L}\begin{pmatrix} b_1 \\ n_1 \end{pmatrix} = \begin{pmatrix} \omega + Dn_0 b_0 q^2 & 0 \\ 0 & \omega + q^2 \end{pmatrix} \begin{pmatrix} b_1 + \frac{\partial b_0}{\partial \zeta} \\ n_1 + \frac{\partial n_0}{\partial \zeta} \end{pmatrix}, \tag{5.17}$$

where the matrix operator $\mathcal{L}$ has the components

$$\mathcal{L}_{11} = Dn_0 b_0 \frac{\partial^2}{\partial \zeta^2} + Dn_0 \frac{\partial^2 b_0}{\partial \zeta^2} + 2Dn_0 \frac{\partial b_0}{\partial \zeta}\frac{\partial}{\partial \zeta} + D\frac{\partial n_0}{\partial \zeta} \underbrace{\frac{\partial}{\partial \zeta}(b_0 \cdot)}_{=\frac{\partial b_0}{\partial \zeta} + b_0 \frac{\partial}{\partial \zeta}} + v_0 \frac{\partial}{\partial \zeta} + \frac{n_0}{1+\gamma n_0},$$

$$\mathcal{L}_{12} = Db_0 \frac{\partial^2 b_0}{\partial \zeta^2} + D(\frac{\partial b_0}{\partial \zeta})^2 + \underbrace{\frac{D}{2}\frac{\partial b_0^2}{\partial \zeta}\frac{\partial}{\partial \zeta}}_{=Db_0 \frac{\partial b_0}{\partial \zeta}\frac{\partial}{\partial \zeta}} + \frac{b_0}{(1+\gamma n_0)^2},$$

$$\mathcal{L}_{21} = -\frac{n_0}{1+\gamma n_0} \qquad \text{and}$$

$$\mathcal{L}_{22} = \frac{\partial^2}{\partial \zeta^2} + v_0 \frac{\partial}{\partial \zeta} - \frac{b_0}{(1+\gamma n_0)^2}.$$

A main difference to the results in [103] are the non-diagonal derivative terms in $\mathcal{L}$, which are due to the mixed bacterial diffusion coefficient. Furthermore, the form of the terms $\mathcal{L}_{11}$ and $\mathcal{L}_{12}$ is due to the expansion

$$\begin{aligned} \frac{\partial}{\partial \zeta}\left(nb\frac{\partial b}{\partial \zeta}\right) &= nb\frac{\partial^2 b}{\partial \zeta^2} + \left[b\frac{\partial n}{\partial \zeta} + n\frac{\partial b}{\partial \zeta}\right]\frac{\partial b}{\partial \zeta} = nb\frac{\partial^2 b}{\partial \zeta^2} + b\frac{\partial b}{\partial \zeta}\frac{\partial n}{\partial \zeta} + n\left(\frac{\partial b}{\partial \zeta}\right)^2 \\ &= nb\frac{\partial^2 b}{\partial \zeta^2} + \frac{1}{2}\frac{\partial b^2}{\partial \zeta}\frac{\partial n}{\partial \zeta} + n\left(\frac{\partial b}{\partial \zeta}\right)^2. \end{aligned}$$

The planar front looses stability when ω becomes positive for spatial modes in $(0, q_{\max})$. Thus, the onset of lateral instability happens when the derivative $\frac{d\omega}{d(q^2)}$ at $q = 0$ becomes positive due to the variation of a model parameter. Since it holds that

$$\mathcal{L}\begin{pmatrix} \frac{\partial b_0}{\partial \zeta} \\ \frac{\partial n_0}{\partial \zeta} \end{pmatrix} = 0, \tag{5.18}$$

we introduce the variables $\bar{b}_1 := b_1 + \frac{\partial b_0}{\partial \zeta}$ and $\bar{n}_1 := n_1 + \frac{\partial n_0}{\partial \zeta}$ and write the system (5.17)

as

$$\mathcal{L}\begin{pmatrix}\bar{b}_1\\ \bar{n}_1\end{pmatrix} = \begin{pmatrix}\omega + Dn_0b_0q^2 & 0\\ 0 & \omega + q^2\end{pmatrix}\begin{pmatrix}\bar{b}_1\\ \bar{n}_1\end{pmatrix}. \tag{5.19}$$

Again, two different domains meet at $\zeta = 0$ and are considered separately. On the positive line $b_0 = 0$ and also for $\zeta > 0$, it holds that $b_1(\zeta) = 0$. Thus we solve for $b_1(\zeta)$ and $n_1(\zeta)$ in the system of equations, which is given as

$$\begin{aligned} b_1 &= 0,\\ \frac{\partial^2 n_1}{\partial\zeta^2} + v_0\frac{\partial n_1}{\partial\zeta} - (\omega + q^2)n_1 &= (\omega + q^2)\frac{\partial n_0}{\partial\zeta}, \end{aligned}$$

and obtained from Equation (5.19).

With $\frac{\partial n_0}{\partial\zeta}$ as defined above, the solution for $n_1(\zeta)$ in this system is calculated explicitly as

$$n_1(\zeta) = -c_0v_0\exp(-v_0\zeta) + d_0\exp(-\lambda\zeta),$$

where $\lambda := \frac{v_0 - \sqrt{v_0^2 + 4(\omega+q^2)}}{2}$ and d_0 is a constant. We furthermore investigate the behavior of n_1 and b_1 as $\zeta \to 0$ from the left. Since n_1 and its derivative are continuous across $\zeta = 0$, for n_1 and $\partial_\zeta n_1$ at $\zeta = 0$ we obtain

$$n_1(0) = -c_0v_0 + d_0 \qquad \text{and} \tag{5.20}$$

$$\partial_\zeta n_1(0) = c_0v_0^2 - d_0\lambda. \tag{5.21}$$

The expression $\frac{b_1}{b_0}$ has to remain bounded, such that perturbations are arbitrarily small when $\varepsilon \to 0$. Therefore we consider $b_1 \sim B(-\zeta)^\beta$. Inserting this form into Equation (5.17) yields

$$\begin{aligned} &Dn_0b_0\frac{\partial^2 b_1}{\partial\zeta^2} + Dn_0\frac{\partial^2 b_0}{\partial\zeta^2}b_1 + v_0\frac{\partial b_1}{\partial\zeta} + \frac{n_0b_1}{1+\gamma n_0} + 2Dn_0\frac{\partial b_0}{\partial\zeta}\frac{\partial b_1}{\partial\zeta} + D\frac{\partial n_0}{\partial\zeta}\frac{\partial}{\partial\zeta}(b_0b_1)\\ &+ \frac{b_0n_1}{(1+\gamma n_0)^2} + Db_0\frac{\partial^2 b_0}{\partial\zeta^2}n_1 + D\left(\frac{\partial b_0}{\partial\zeta}\right)^2 n_1 + Db_0\frac{\partial b_0}{\partial\zeta}\frac{\partial n_1}{\partial\zeta}\\ &= (\omega + Dn_0b_0q^2)\left(b_1 + \frac{\partial b_0}{\partial\zeta}\right). \end{aligned}$$

We insert the expressions $b_0 = A(-\zeta)$ and $\frac{\partial b_0}{\partial \zeta} = -A$ and obtain the equation

$$\begin{aligned}
&Dn_0 A(-\zeta)^{\beta-1}\beta(\beta-1)B + 0 - v_0\beta B(-\zeta)^{\beta-1} + \frac{n_0 B(-\zeta)^\beta}{1+\gamma n_0} + 2Dn_0 A\beta B(-\zeta)^{\beta-1} \\
&- D\frac{\partial n_0}{\partial \zeta}AB(\beta+1)(-\zeta)^\beta + \frac{A(-\zeta)n_1}{(1+\gamma n_0)^2} + 0 + DA^2 n_1 - DA^2(-\zeta)\frac{\partial n_1}{\partial \zeta} \\
&= \omega B(-\zeta)^\beta - \omega A + Dn_0 A(-\zeta)^{\beta+1}q^2 B - ADn_0 B(-\zeta)^\beta q^2.
\end{aligned}$$

When we consider only the dominant terms and assume that they have to cancel for the equation to be fulfilled at $\zeta = 0$, we obtain $\beta = 1$ and

$$\begin{aligned}
&Dn_0(0)A\beta(\beta-1)B - v_0\beta B + 2Dn_0(0)A\beta B + DA^2 n_1(0) + \omega A = 0 \\
\iff &B[Dn_0(0)A\beta(\beta+1) - v_0\beta] + DA^2 n_1(0) + \omega A = 0 \\
\overset{\beta=1}{\iff} &B = -\frac{DA^2 n_1(0) + \omega A}{2Dn_0(0)A - v_0} \overset{(5.14)}{=} -\left(\frac{v_0 n_1(0)}{Dn_0(0)^2} + \frac{\omega}{Dn_0(0)}\right) = -A\left(\frac{n_1(0)}{n_0(0)} + \frac{\omega}{v_0}\right).
\end{aligned}$$

This means that the quotient $\frac{b_1}{b_0} = -(\frac{n_1(0)}{n_0(0)} + \frac{\omega}{v_0})$ remains finite as the quotient $\frac{n_1(0)}{n_0(0)}$ also remains finite. At $\zeta \to -\infty$ all perturbations vanish, which yields that for $\zeta \to -\infty$ we obtain

$$\begin{aligned}
b_1(\zeta) &\to 0, \qquad \partial_\zeta b_1(\zeta) \to 0, \\
n_1(\zeta) &\to 0, \qquad \partial_\zeta n_1(\zeta) \to 0.
\end{aligned}$$

Due to Equation (5.15) and Equation (5.16), this means that $b_0(\zeta)$ and $n_0(\zeta)$ show the same behavior as $b(\zeta, y, t)$ and $n(\zeta, y, t)$ as $\zeta \to -\infty$. This allows to calculate the functions $b_0(\zeta)$, $n_0(\zeta)$ as well as their derivatives $\partial_\zeta b_0(\zeta)$ and $\partial_\zeta n_0(\zeta)$ from Equation (5.18) as an ordinary differential equation initial value problem. The resulting profiles of b_0 and n_0 for the parameter values $\gamma = 0.1$, $D = 3.5$ and $v_0 = 0.9231$ are depicted in Figure 5.3.

Using a shooting method on Equation (5.17) for different values of q, which starts at $\zeta \to -\infty$ and ends at $\zeta = 0$, in [103] a dependence of the form $\omega = \omega(D, q, k)$ for the wavelength is found. Here k denotes the exponent in the bacteria density dependent diffusion coefficient as used in [103]. Then the numerical linear dispersion relation is obtained by performing the shooting method for several values of D and k. However this approach is not performed here.

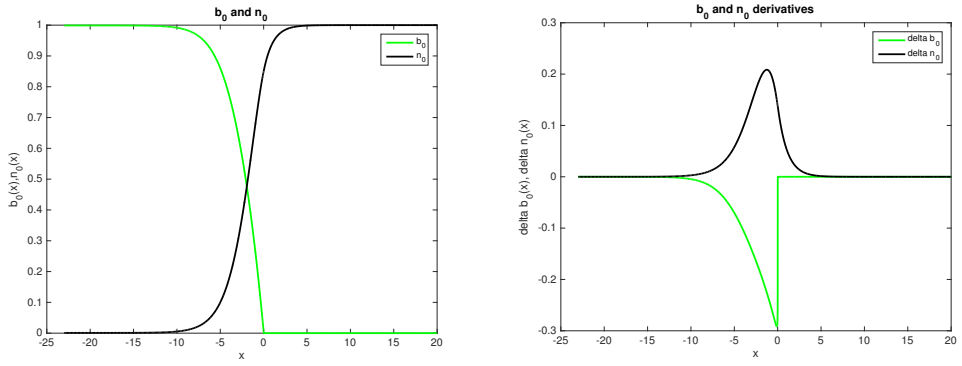

(a) Profiles of n_0 and b_0.

(b) Profiles of $\frac{\partial n_0}{\partial \zeta}$ and $\frac{\partial b_0}{\partial \zeta}$.

Figure 5.3.: Profiles for the parameters $\gamma = 0.1$, $D = 3.5$ and $v_0 = 0.9231$.

5.2.2. Linear stability analysis investigating the ω-q^2 curve

For the onset of instability we are interested in the critical diffusion coefficient D_c, such that for all $D < D_c$ a long-wavelength $q = 0$ instability is found while all modes are stable for $D > D_c$. The critical line is defined [103] as the line where it holds that

$$\frac{d\omega}{d(q^2)}|_{q=0} = 0.$$

The $q = 0$ mode is called the translational mode and it is the eigenmode of $\mathcal{L}$ from Equation (5.17) to the eigenvalue $\omega = 0$ [103]. Here ω is small and of order q^2 when q is small. Furthermore for $q = 0$ also $n_1 = b_1 = 0$ and thus for small q these terms are of order q^2 as well.

Thus, in Equation (5.17) the right-hand side terms involving n_1 and b_1 are of order q^4 and we obtain the following equation of order q^2

$$\mathcal{L}\begin{pmatrix} b_1 \\ n_1 \end{pmatrix} = \begin{pmatrix} \omega + Dn_0 b_0 q^2 & 0 \\ 0 & \omega + q^2 \end{pmatrix} \begin{pmatrix} \frac{\partial b_0}{\partial \zeta} \\ \frac{\partial n_0}{\partial \zeta} \end{pmatrix}.$$

Here the operator $\mathcal{L}$ is as introduced in Equation (5.17) and has a zero eigenvalue. We use the solvability condition for the left zero mode $\Psi = (\Psi_1, \Psi_2)^T$, which, following [103], reads

$$\int_{-\infty}^{\infty} d\zeta \begin{pmatrix} \Psi_1 \\ \Psi_2 \end{pmatrix}^T \begin{pmatrix} \omega + Dn_0 b_0 q^2 & 0 \\ 0 & \omega + q^2 \end{pmatrix} \begin{pmatrix} \frac{\partial b_0}{\partial \zeta} \\ \frac{\partial n_0}{\partial \zeta} \end{pmatrix} = 0.$$

This equation is rewritten as

$$\omega \int_{-\infty}^{\infty} d\zeta \left(\Psi_1 \frac{\partial b_0}{\partial \zeta} + \Psi_2 \frac{\partial n_0}{\partial \zeta} \right) = -q^2 \int_{-\infty}^{\infty} d\zeta \left(D\Psi_1 n_0 b_0 \frac{\partial b_0}{\partial \zeta} + \Psi_2 \frac{\partial n_0}{\partial \zeta} \right)$$

and, following [103], for $q^2 \to 0$ we find the equation

$$\frac{d\omega}{d(q^2)}|_{q=0} = -\frac{\int_{-\infty}^{\infty} d\zeta \left(D\Psi_1 n_0 b_0 \frac{\partial b_0}{\partial \zeta} + \Psi_2 \frac{\partial n_0}{\partial \zeta} \right)}{\int_{-\infty}^{\infty} d\zeta \left(\Psi_1 \frac{\partial b_0}{\partial \zeta} + \Psi_2 \frac{\partial n_0}{\partial \zeta} \right)}. \tag{5.22}$$

Thus, our task is to find the point at which the integral in the numerator changes sign. In order to calculate the integral, we determine the adjoint matrix operator of $\mathcal{L}$ and determine the zero mode solution numerically using a shooting method.

5.2.2.1. The adjoint eigenmodes

The left eigenvector of the matrix operator $\mathcal{L}$ is the same as the right eigenvector of the adjoint matrix operator $\mathcal{L}^\star$ given by

$$\mathcal{L}^\star = \begin{pmatrix} Dn_0 b_0 \frac{\partial^2}{\partial \zeta^2} + (Db_0 \frac{\partial n_0}{\partial \zeta} - v_0) \frac{\partial}{\partial \zeta} + \frac{n_0}{1+\gamma n_0} & -\frac{n_0}{1+\gamma n_0} \\ \frac{b_0}{(1+\gamma n_0)^2} - Db_0 \frac{\partial b_0}{\partial \zeta} \frac{\partial}{\partial \zeta} & \frac{\partial^2}{\partial \zeta^2} - v_0 \frac{\partial}{\partial \zeta} - \frac{b_0}{(1+\gamma n_0)^2} \end{pmatrix}. \tag{5.23}$$

This adjoint matrix operator $\mathcal{L}^\star$ is obtained by partial integration from the operator $\mathcal{L}$. In general, we obtain boundary terms. Here the requirement that the boundary terms vanish yields the boundary conditions on the adjoint functions, which have to stay bounded [103].

As in [103] for $\zeta > 0$ we have $b_0 = 0$ and thus it holds that

$$\mathcal{L}^\star = \begin{pmatrix} -v_0 \frac{\partial}{\partial \zeta} + \frac{n_0}{1+\gamma n_0} & -\frac{n_0}{1+\gamma n_0} \\ 0 & \frac{\partial^2}{\partial \zeta^2} - v_0 \frac{\partial}{\partial \zeta} \end{pmatrix}.$$

Therefore the component Ψ_2 in Equation (5.22) has to fulfill the homogeneous ordinary differential equation

$$\frac{\partial^2 \Psi_2}{\partial \zeta^2} - v_0 \frac{\partial \Psi_2}{\partial \zeta} = 0,$$

which can have an exponential or a constant solution. Since, due to the boundary condition, the solution has to remain bounded, we have $\Psi_2 = \psi_0 = \text{const.}$ for $\zeta > 0$.

This yields the boundary conditions at $\zeta = 0$, which read

$$\Psi_2(\zeta = 0) = \psi_0, \qquad \frac{\partial \Psi_2}{\partial \zeta}|_{\zeta=0} = 0. \tag{5.24}$$

Furthermore, b_0 vanishes for positive ζ and thus Ψ_1 is only needed for $\zeta < 0$. For $\zeta < 0$, we determine Ψ_1 and Ψ_2 using a shooting method, as described in the following section.

5.2.2.2. A shooting method for the adjoint eigenmodes

The zero mode solution Ψ is determined using a shooting method [118, 135]. Shooting methods can be used to approximate the solution of a second order ordinary differential equation boundary value problem of the form

$$y''(t) = f(t, y(t), y'(t)), \qquad y(t_0) = y_0, \qquad y(t_1) = y_1$$

on the time interval $[t_0, t_1]$ by the solution $y(t; a)$ of the initial value problem

$$y''(t) = f(t, y(t), y'(t)), \qquad y(t_0) = y_0, \qquad y'(t_0) = a.$$

The resulting error is measured by the function $F(a) := y(t_1, a) - y_1$. If the function $F(a)$ has a root $a^\star$, then $y(t, a^\star)$ solves the boundary value problem.

For the mode Ψ with $\Psi = (\Psi_1, \Psi_2)^T$ we obtain the two-dimensional system of equations

$$\begin{aligned} Dn_0 b_0 \frac{\partial^2 \Psi_1}{\partial \zeta^2} + \left(Db_0 \frac{\partial n_0}{\partial \zeta} - v_0 \right) \frac{\partial \Psi_1}{\partial \zeta} + \frac{n_0}{1 + \gamma n_0} (\Psi_1 - \Psi_2) = 0, \\ \frac{\partial^2 \Psi_2}{\partial \zeta^2} - v_0 \frac{\partial \Psi_2}{\partial \zeta} - Db_0 \frac{\partial b_0}{\partial \zeta} \frac{\partial \Psi_1}{\partial \zeta} + \frac{b_0}{(1 + \gamma n_0)^2} (\Psi_1 - \Psi_2) = 0, \end{aligned}$$

from Equation (5.23).

This set is then translated to a four-dimensional system in order to avoid the second derivatives and we obtain the system

$$\begin{aligned} \frac{\partial \Psi_1}{\partial \zeta} &= Z_1, \\ \frac{\partial Z_1}{\partial \zeta} &= \frac{1}{Dn_0 b_0} \left(\left(v_0 - Db_0 \frac{\partial n_0}{\partial \zeta} \right) Z_1 + \frac{n_0}{1 + \gamma n_0} [\Psi_2 - \Psi_1] \right), \end{aligned}$$

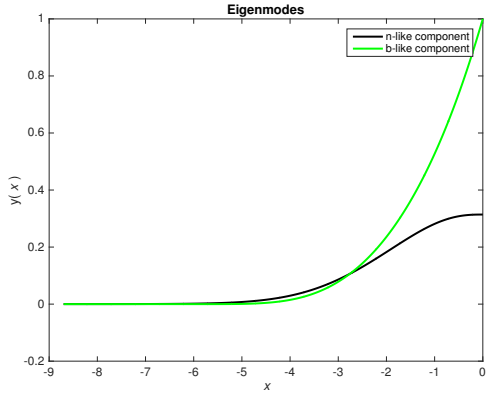

Figure 5.4.: Components of the zero right eigenvector of the adjoint operator for $\gamma = 0.1$, $D = 3.5$ and $v_0 = 0.9231$.

$$\frac{\partial \Psi_2}{\partial \zeta} = Z_2,$$
$$\frac{\partial Z_2}{\partial \zeta} = v_0 Z_2 + D b_0 \frac{\partial b_0}{\partial \zeta} Z_1 + \frac{b_0}{(1+\gamma n_0)^2}[\Psi_2 - \Psi_1].$$

The component Ψ_2 is related to n and defined on $(-\infty, \infty)$. Since the positive solution is determined as $\Psi_2 = \psi_0$, the boundary conditions for Ψ_2 at $\{-\infty, 0\}$ are

$$\Psi_2(-\infty) = 0, \qquad \Psi_2(0) = \psi_0,$$

such that the modes can be continuously extended into the domain ahead of the front. For the components related to b defined on $(-\infty, 0]$, there is no right boundary condition, as long as the solution does not diverge. On the left boundary $-\infty$ we have $\Psi_1(-\infty) = 0$. Furthermore, the solutions have to satisfy

$$\frac{\partial \Psi_2}{\partial \zeta}|_{\zeta=0} = 0$$

according to Equation (5.24). The resulting modes Ψ_1 and Ψ_2 obtained from the numerical simulations are depicted in Figure 5.4. The shooting method for the calculation of the modes uses a fourth-order Runge-Kutta method.

Using n_0, b_0 as well as their derivatives with respect to ζ and the solution Ψ, the constant D_c is calculated as the value at which the numerator in Equation (5.22) changes sign. In this calculation the translational mode $(\partial_\zeta b_0, \partial_\zeta n_0)$ is calculated as the right zero eigenmode of $\mathcal{L}$, as described above. We approximate by integrating

over the interval $\zeta \in [-a_{\text{int}}, b_{\text{int}}]$ as

$$\int_{-\infty}^{\infty} d\zeta \left(D\Psi_1 n_0 b_0 \frac{db_0}{d\zeta} + \Psi_2 \frac{\partial n_0}{\partial \zeta} \right) \approx \int_{-a_{\text{int}}}^{0} d\zeta \left(D\Psi_1 n_0 b_0 \frac{\partial b_0}{\partial \zeta} + \Psi_2 \frac{\partial n_0}{\partial \zeta} \right) + \int_{0}^{b_{\text{int}}} d\zeta \left(\psi_0 \frac{\partial n_0}{\partial \zeta} \right)$$

since $b_0 = 0$ for $\zeta > 0$. Furthermore, ψ_0 denotes the constant value of Ψ_2 for $\zeta > 0$.

This approximation is admissible since at larger absolute values of ζ only small changes are induced. For small negative ζ, only small values of n_0 and $\frac{\partial n_0}{\partial \zeta}$ are observed and for large positive ζ the expression $\frac{\partial n_0}{\partial \zeta}$ is small as well. The integration is performed in MATLAB using trapezoidal numerical integration. In comparison to the bacteria density dependent case, the factor n_0 lowers the effective diffusion coefficient for $\zeta < 0$. Therefore we expect to obtain a larger critical diffusion coefficient D_c for the long-wavelength instability than in the bacteria density dependent case. In fact for our example of $\gamma = 0.1$, we obtain the critical diffusion coefficient $D_{\text{c}} \approx 3.95$ in comparison to the critical diffusion coefficient $D_{\text{c}} \approx 1.5$ for the case $k = 1$ in [103].

A diffusion coefficient $D > D_{\text{c}}$ means that all modes are stable. Thus, in this case we can exclude an instability. However, whether an instability is observed for $D < D_{\text{c}}$ also depends on the size of the domain and on the total simulation time, and we investigate simulations on large domains in the following.

5.3. Comparison of the stability results using numerical simulations

The numerical simulations of the systems (5.1)–(5.2) and (5.9)–(5.10) in this section are performed using the numerical finite element methods described in Section 4.6, adapted to the considered systems of equations.

In order to obtain the simulation results depicted in Figure 3.2 in Section 3.2, we use the classical Turing pattern formation setting of randomly disturbed spatially homogeneous initial concentrations. In this case, Turing patterns are obtained as expected from the evaluation of the Turing conditions. In contrast, bacterial colony growth does not represent a classical setting as we do not have spatially homogeneous initial conditions and since there is a mixed diffusion term in the

equation for the bacteria density. However, we would like to obtain an impression of how the bacteria colony simulations change around the Turing instability parameters derived in Section 5.1.

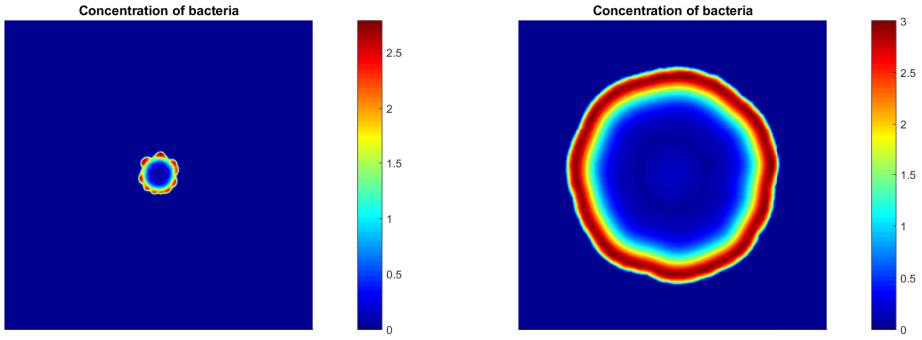

(a) Colony for $D = 0.2$ at $t = 241.92$. (b) Colony for $D = 3$ at $t = 241.92$.

Figure 5.5.: Simulation of Equations (5.1)–(5.2) with parameters $d_n = G_1 = \gamma = 1.0$, $G_2 = 0.2$, $\varepsilon_0 = 0.01$, $\mu = 0.1$ on a domain of size 240×240 with varying parameter $D = \frac{\sigma}{d_n}$.

Thus a comparison of two different bacteria colonies for (in)stability parameters as predicted by the Turing pattern formation analysis is displayed in Figure 5.5. In this figure, we observe a similar behavior in both cases, with a rounder colony shape for the higher diffusion coefficient $D = 3$. Furthermore, due to the relationship between the growth rates, where many nutrients are needed for only little bacteria colony growth, the highest concentration of bacteria is found at the colony border. As expected, the diffusion coefficient $D = 3$, which is increased far from the bifurcation value $D_{\text{crit}} = 0.3247$, leads to a considerably faster growth of the bacteria colony. In both cases, a very low concentration of bacteria is observed in the middle of the colony due to a combination of slow growth due to lack of nutrients and diffusion. In contrast to the case $D = 3$, for $D = 0.2$, the start of fingering behavior can be observed in Figure 5.5. However a similar fingering behavior is also observed in the case $D = 1$, which lies outside the Turing pattern domain. We note that obtaining parameters which fit the Turing instability regime was rather difficult and that we also concluded before that these parameters represent a biologically less relevant case, which can also be observed in the simulation results. Thus, we conclude that the observed pattern formation in bacterial colony growth is not directly related to a Turing mechanism.

An analogous comparison for the front instability approach from Section 5.2 is

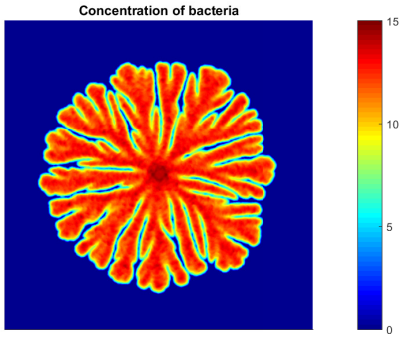

(a) Colony for $D = 1$ at $t = 279.92$.

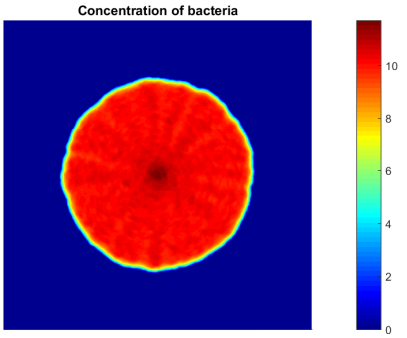

(b) Colony for $D = 3$ at $t = 84.92$.

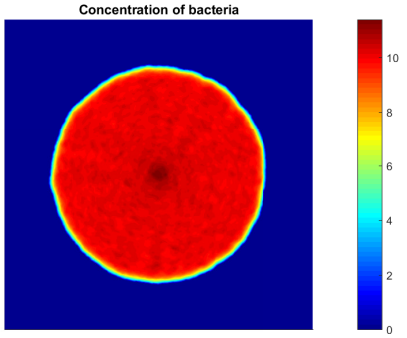

(c) Colony for $D = 3.5$ at $t = 84.92$.

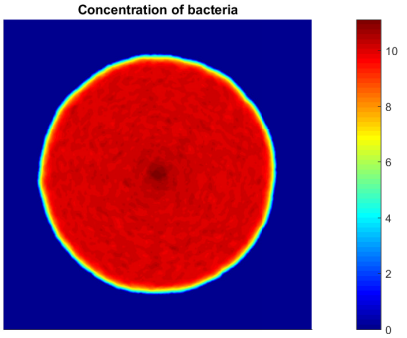

(d) Colony for $D = 4$ at $t = 84.92$.

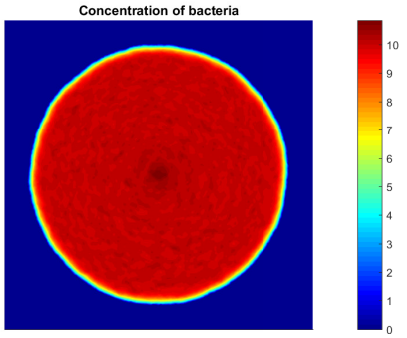

(e) Colony for $D = 4.5$ at $t = 84.92$.

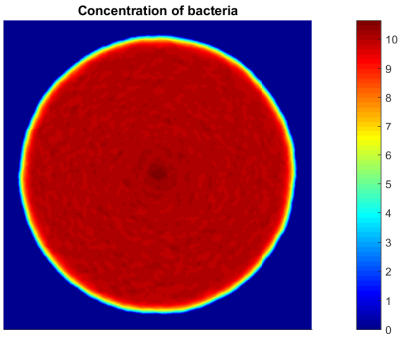

(f) Colony for $D = 5$ at $t = 84.92$.

Figure 5.6.: Simulation of Equations (5.9)–(5.10) with parameters $d_n = 1$, $\gamma = 0.1$ on a domain of size 240×240 with varying $D = \frac{\sigma}{d_n}$. Change in the stability regime at $D = 3.95$ predicted by front instability approach.

depicted in Figure 5.6 and Figure 5.7. These figures display simulation results for parameter values $D \in \{1.0, 3.0, 3.5, 4.0, 4.5, 5.0\}$, such that we cover values of D close to the predicted critical diffusion coefficient $D_c \approx 3.95$. We recall that we expect all modes to be stable for $D > D_c$, with a colony expanding in a round shape without instabilities. This behavior is observed in Figure 5.6, where for $D \geq 4$ the colonies are round and without structure. For decreasing values of $D < 4$

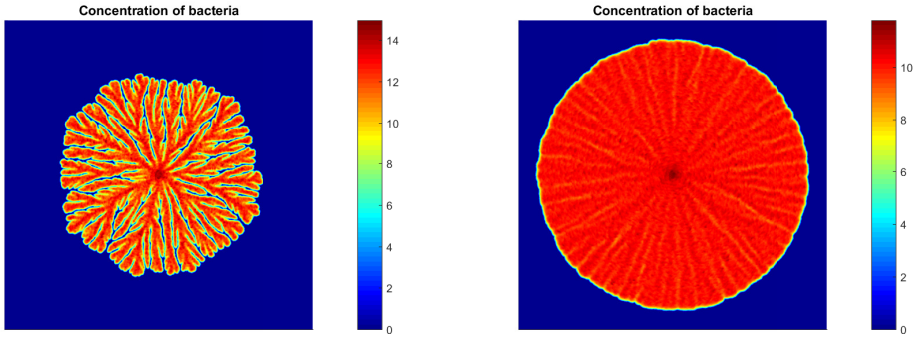

(a) Colony for $D = 1$ at $t = 488.92$. (b) Colony for $D = 3$ at $t = 249.92$.

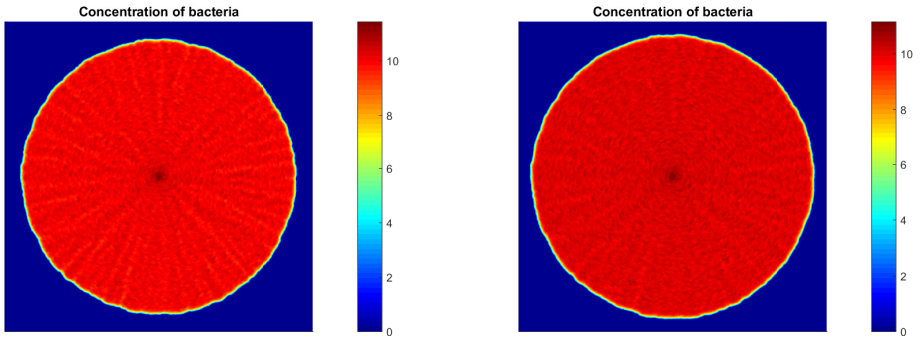

(c) Colony for $D = 3.5$ at $t = 224.92$. (d) Colony for $D = 4$ at $t = 209.92$.

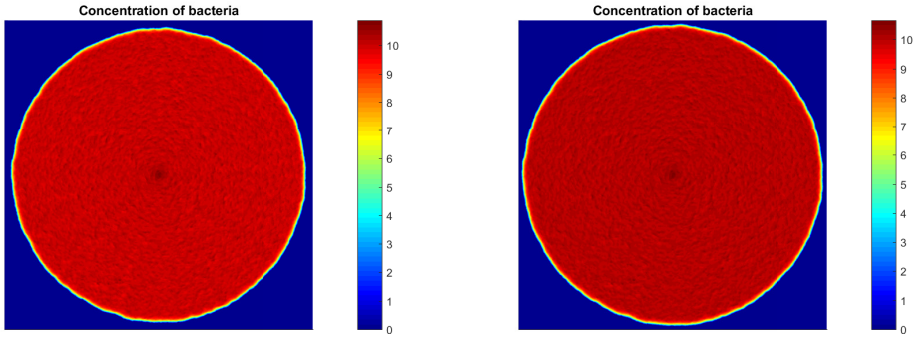

(e) Colony for $D = 4.5$ at $t = 199.92$. (f) Colony for $D = 5$ at $t = 189.92$.

Figure 5.7.: Simulation of Equations (5.9)–(5.10) with parameters $d_n = 1$, $\gamma = 0.1$ on a domain of size 500×500 with varying $D = \frac{\sigma}{d_n}$. Change in the stability regime at $D = 3.95$ predicted by front instability approach.

such as $D = 3.5$ or $D = 3$, the colonies start to show small indentations and a structure develops inside the colonies. Simulations are performed on a domain of size 240×240. As an example of full fingering behavior, we include the case $D = 1$. Since the observed patterning behavior agrees well with the prediction of the front instability approach, the approach seems appropriate.

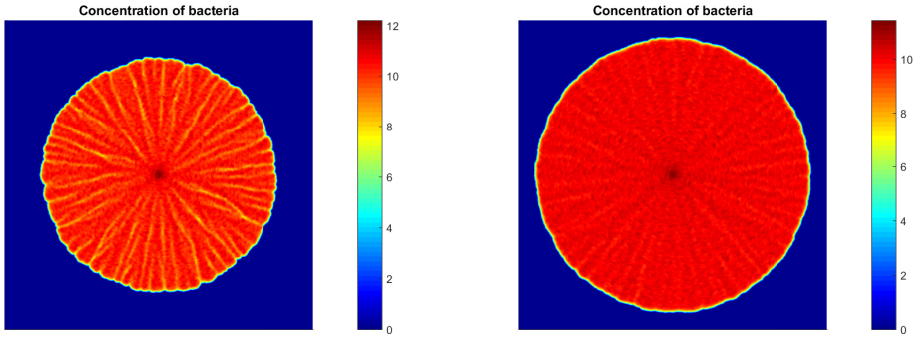

(a) Colony for $D = 2.5$ at $t = 249.92$. (b) Colony for $D = 3.5$ at $t = 224.92$.

Figure 5.8.: Simulation of Equations (5.9)–(5.10) with parameters $d_n = 1$, $\gamma = 0.1$, $D \in \{2.5, 3.5\}$ on a domain of size 500×500.

According to [103], stability behavior depends on the system size and simulation time since long-wavelength instabilities only develop if the corresponding unstable modes are able to enter the domain. Thus, in Figure 5.7 we display simulation results for the larger domain size 500×500 and longer simulation times. For both domains, the mesh sizes of the finite elements are similar. We observe that the round colony structure for $D \geq 4$ is preserved and that for decreasing D a structure is observed inside the colony. In Figure 5.8(b), the colony for $D = 3.5$ is depicted. If the parameter D is decreased further away from the critical value, we obtain the simulation result displayed in Figure 5.8(a) for $D = 2.5$. In this simulation we observe a further step in the transition to full fingering behavior as in the case $D = 1$, as we see that the colony structure and small indentations at the colony boundary start to develop into fingers.

D	r_{surr}	r_{dom}	$\frac{r_{\text{surr}} - r_{\text{dom}}}{r_{\text{surr}}}$	D	r_{surr}	r_{dom}	$\frac{r_{\text{surr}} - r_{\text{dom}}}{r_{\text{surr}}}$
1	177	172.87	0.0234	3	237.5	235.68	0.0077
3.5	240.5	239.02	0.0062	4	247.5	246.41	0.0044
4.5	256.5	255.32	0.0046	5	262	260.84	0.0044

Table 5.1.: Comparison of the radius of a colony with the same area to the colony surrounding radius.

To also quantify the results, we extract a black-and-white representation of the colonies in Figure 5.7 in MATLAB and compare the radius that would correspond to a circular domain of the same area to the radius of the smallest circle surrounding the colony. This yields the relative results displayed in Table 5.1. We observe that for $D \geq 4$, the relative radial difference remains below 0.5%, where a completely circular domain is never reached due to the random bacterial diffusion component.

Furthermore, we note that even a perfect circle is never completely round on a discrete numerical grid.

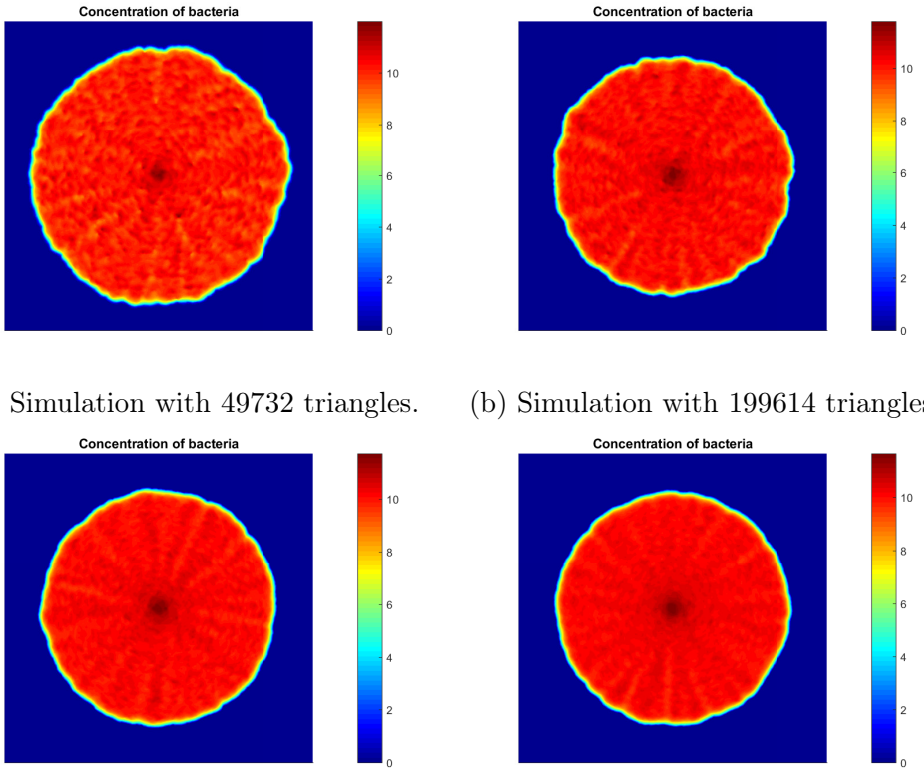

(a) Simulation with 49732 triangles. (b) Simulation with 199614 triangles.

(c) Simulation with 448814 triangles. (d) Simulation with 795874 triangles.

Figure 5.9.: Simulation of Equations (5.9)–(5.10) with parameters $D = 3$ on a domain of size 240×240 with varying degrees of refinement.

The simulations in Figure 5.6 are performed on a rectangular domain with side length 240 and 448814 triangles. At this point we note that the choice of a sufficient degree of refinement is important as it assures numerical convergence of the method. This convergence can be observed in Figure 5.9, where simulation results of the colony with $D = 3$ at time 104.92 are displayed for several degrees of refinement. Convergence is observed in the colony size, which decreases when a finer mesh is chosen until, for our chosen mesh size and the simulation result depicted in Figure 5.9(c), even in comparison to the considerably finer mesh with 795874 triangles and the simulation result depicted in Figure 5.9(d), only small non-qualitative changes are observed.

Part III.

Modeling with pressure

6. Modeling the effects of pressure due to bacterial division

The approaches considered so far have emphasized bacterial regulation processes in the cell and between cells, which are described using systems of reaction-diffusion equations. Physical effects such as pressure induced by the division of bacteria have so far been considered indirectly in the different forms of diffusion, which aim at evening out concentration differences. However these processes play an important role in colony growth. In the following, we concentrate on pressure effects induced by bacterial division, a process which is relevant for all bacteria colonies.

In laboratory experiments it is observed that the colony shape of *S. aureus* bacteria does not only depend on the mutant, but also in a very general way on the environmental conditions. In Figure 6.1 the shapes of *S. aureus* wildtype bacteria colonies for varying concentrations of the agar medium are depicted. We observe very different morphologies, where at the lowest agar concentration the colony seems to almost flow out and at the highest agar concentration colony growth is restricted to a small circular area. Furthermore, in Figure 6.2 colony shapes after 5 days for different nutrient concentrations in the medium are depicted. We observe that a higher nutrient concentration in the medium leads to a rounder shape of the colony and less fingering behavior and that an increasing agar concentration leads to a significantly slower growth of the bacterial colony. In order to describe these processes, models for the expansion of a colony due to cell division as in [49] or models for the swelling of gel-like substances from the physical literature as in [37, 127] are of great interest. In all cases, the formation of biofilm, which encompasses all components, is important for the physical processes.

Using a pressure model, we investigate in the following, which effects of *S. aureus* pattern formation can be explained by the physics of biomass growth alone. The

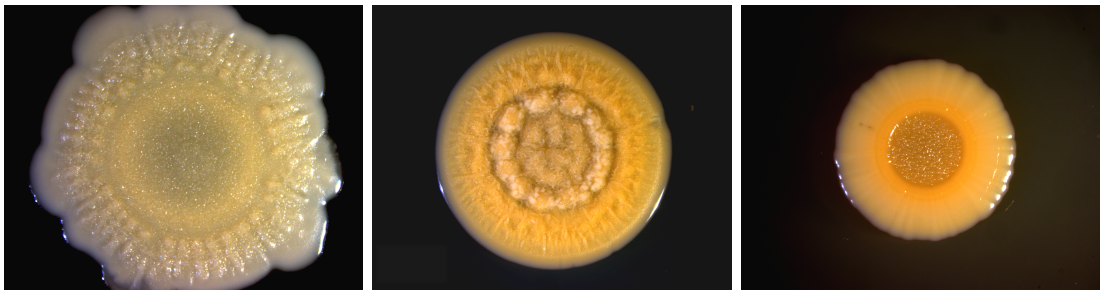

(a) Colony after 5 days at agar concentration 0.5%. (b) Colony after 5 days at agar concentration 1.5%. (c) Colony after 5 days at agar concentration 3.0%.

Figure 6.1.: Influence of the agar concentration on *S. aureus* pattern formation in the laboratory [65, 89]. Nutrient concentration at standard level.

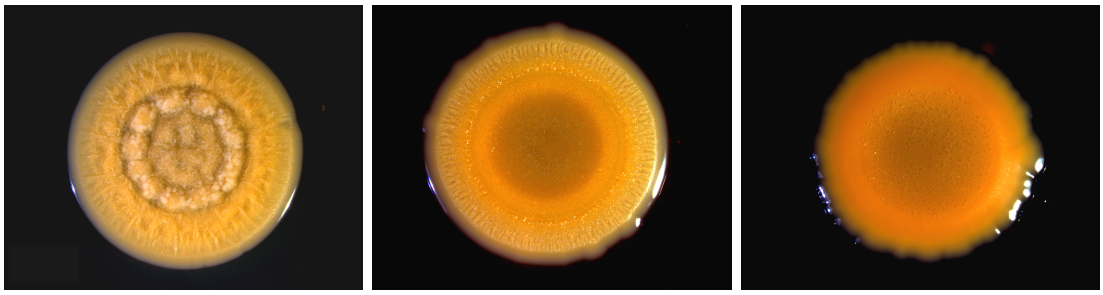

(a) Colony after 5 days at standard nutrient concentration. (b) Colony after 5 days at double nutrient concentration. (c) Colony after 5 days at five fold nutrient concentration.

Figure 6.2.: Influence of the nutrient concentration on *S. aureus* pattern formation in the laboratory [65, 89]. Agar concentration at 1.5% (standard level).

starting point for our modeling is Darcy's law in Hele-Shaw cells as introduced in Equation (2.1) in Section 2.3. Then, in order to consider the evolution of a growth limiting nutrient substance, a reaction-diffusion equation for the concentration n is introduced, which drives biomass expansion described by a nutrient-dependent Poisson equation.

6.1. Mathematical modeling

Bacteria colony expansion due to an increase of pressure from bacteria division is similar in different bacteria species, such as *B. subtilis* and *S. aureus* and is a process which can also be observed in similar form for other phenomena. While for colony expansion with biofilm formation as described in [127], osmotic stresses seem to be an important factor, all species experience pressure effects due to bacterial division. Furthermore, species who do not secrete the exopolysaccharide (EPS) component of

the extracellular matrix or EPS mutants of species that usually secrete EPS show slower expansion [127]. This is due to the fact that this expansion is mainly led by cell-cell interactions, which we study in this chapter.

In a first modeling approach, we concentrate on the horizontal bacteria colony expansion in the domain $\bar{\Omega} = \bar{\Omega}_a \cup \bar{\Omega}_b \subset \mathbb{R}^2$, divided into the colony subdomain Ω_b and the subdomain Ω_a. The boundary between the subdomains is defined as $\Gamma := \bar{\Omega}_a \cap \bar{\Omega}_b$ and the boundary of the whole domain is denoted by $\partial\Omega$. For the modeling we adapt the approaches from [49, 67], which model situations similar to the situation in a Hele-Shaw cell. In [67] the influence of chemotactic motility on bacteria colony expansion is considered in an equation of the form

$$\frac{\partial \rho}{\partial t} + \nabla \cdot (\rho \mathbf{v}) = \nabla \cdot m,$$

where $m = \chi \rho \nabla n$ denotes the chemotactic coefficient. Then with the assumption of constant bacterial density ρ and Darcy's law $\mathbf{v} = -K\nabla p$, a Poisson equation of the form

$$\nabla^2 p = -\frac{\chi}{K}\nabla^2 n$$

for the colony area is obtained. In contrast, in [49] biofilm growth is limited by substrate availability and a Poisson equation of the form

$$-\lambda \nabla^2 p = g(u(S))$$

is obtained, where $g(u(S)) = u_{max}\frac{S}{S+K_S}$ denotes the use of the substrate S. While for the model presented in [67] moving boundary simulations of a circular bacteria colony are available, the model from [49], which includes the growth function, is considered in the setting of biofilm growth in height. Our model is based on the model from [49]. However, we consider time-dependence in the nutrient equation for colony growth and investigate the situation of circular growth of the entire bacteria colony instead of investigating the growth of biofilm layers.

For our model, as in both of the above references, we consider the density of biomass b, which includes biofilm and bacteria in the case of a wildtype colony, and the concentration of nutrients n and assume that the nutrients are only consumed in the colony subdomain. We assume the evolution to take place according to

Equation (5.9) in Section 5.2 with the consumption rate α, which is stated as

$$\frac{\partial n}{\partial t} = d_n \Delta n - \alpha \frac{nb}{1+\gamma n}. \tag{6.1}$$

Since $b = 0$ outside the colony subdomain Ω_b, consumption automatically takes place only in the area where $b \neq 0$. As stated in [49], diffusion constants can be different in- and outside the colony subdomain, but this case is not considered here.

For the biomass, Darcy's law $\mathbf{v} = -K\nabla p$ holds for the two-dimensional velocity vector $\mathbf{v} = (v_x, v_y)^T$. This means that the propagation velocity of the colony is proportional to the pressure gradient, with the proportionality constant $K := k/\mu$ depending on the permeabilty tensor k and the kinematic viscosity μ. In the colony subdomain, the mass conservation law

$$\frac{\partial b}{\partial t} + \nabla \cdot (b\mathbf{v}) = \beta \frac{nb}{1+\gamma n} \tag{6.2}$$

holds, where b denotes the density of the biomass and $\beta \in \mathbb{R}_+$ describes the speed of the conversion of nutrients to biomass. If we assume constant density in the colony subdomain, Equation (6.2) simplifies to the equation

$$\nabla \cdot \mathbf{v} = \beta \frac{n}{1+\gamma n}.$$

Then we use Darcy's law to obtain a Poisson equation for the pressure of the form

$$-K\nabla^2 p = \beta \frac{n}{1+\gamma n}. \tag{6.3}$$

We assume that there is a constant non-zero concentration of biomass b in the colony area and no biomass, i.e., $b = 0$, outside this area.

In contrast to the paper [67], where a moving boundary approach is used, we employ a level set approach as described in Section 3.6. Starting from appropriate initial conditions, we calculate the concentration of nutrients using Equation (6.1) and from this the pressure distribution on the entire domain using Equation (6.3) for the colony subdomain and a Laplace equation on Ω_a. The pressure distribution yields the pressure gradients and thus also the velocity field using Darcy's law. Then, the level set signed distance function is updated using Equation (6.5) and the biomass density for the next iteration is determined from the position of the level set.

This allows to determine the evolution of the colony without considering separate subdomains, which are only connected at the boundary Γ. Especially for the concentration of nutrients, diffusion should take place across the boundary. Then continuity of the nutrient concentration and of the flux

$$[n]|_\Gamma = 0, \qquad \nabla n^+ \cdot \mathbf{n}|_\Gamma = \nabla n^- \cdot \mathbf{n}|_\Gamma, \tag{6.4}$$

as described in [67], are automatically satisfied. Here $\mathbf{n}$ denotes the outward normal vector of the colony domain. Furthermore, following [49], we do not include surface tension effects. The stability analysis in [66, 67] heavily relies on the used separation of domains and performs coupling at the radius of the colony at time t. Since our approach does not provide this separation of domains, we do not perform a similar stability analysis here.

6.2. Numerical simulations

For the numerical simulations we combine a finite element simulation of the Poisson equation given in Equation (6.3) and the reaction-diffusion equation given in Equation (6.1) for the nutrient concentration with a finite element based level set formulation for the position of the interface as in [2, 3, 52, 136].

6.2.1. Level set modeling approach

The level set modeling approach is appropriate for a system of this form since we track the motion of an interface using the distance of the points in the domain to the interface. We consider the evolution of a two-dimensional colony with uniform density on the planar domain $\Omega \subset \mathbb{R}^2$ with homogeneous Neumann boundary. The two different subdomains are the colony area Ω_b and the area Ω_a containing the agar medium surrounding the colony. Note that, as mentioned in the introduction, the boundary between the domains is defined as $\Gamma(t) := \{\mathbf{x} : \phi(\mathbf{x}(t), t) = 0\}$.

Then the level set formulation for the motion of this interface is constructed as follows: Let $\mathbf{x}(0) \in \Omega$ denote the initial position of a particle in Ω and $\mathbf{x}(t)$ denote the trace of this particle over time $t \geq 0$. If a particle starts on the interface, it remains on it for the entire calculation, which means that its signed distance level set function $\phi(\mathbf{x}(t), t)$ is zero, i.e., $\phi(\mathbf{x}(t), t) = 0$ for all $t \geq 0$. We recall that

differentiation then yields that

$$\phi_t + \nabla\phi(\mathbf{x}, t) \cdot \mathbf{x}_t = 0, \tag{6.5}$$

where $\mathbf{x}_t$ denotes the time derivative of the trace of the particle. This displacement is described using the velocity field $\mathbf{v} = -K\nabla p$ obtained from Darcy's law.

When calculating the evolution of the level set using Equation (6.5), the signed distance function property of the level set function $\phi(\mathbf{x}(t), t)$ may be lost as the level sets adjacent to the zero level set may move with different velocities than the zero level set. This makes the advection of the level set less accurate. In order to reestablish the signed distance property, different approaches to reinitialize the level set function have been developed, e.g., [40, 107, 130, 136]. These aim at fulfilling two main requirements: The zero-level set position should be preserved and the norm of the level set function gradient should satisfy $||\nabla\phi|| \approx 1$. We distinguish partial differential equation approaches and geometric approaches.

Partial differential equation approaches use a pseudo time-stepping scheme. To this end, we introduce the pseudo timescale τ, which is not related to the physical time t. On this scale an equation of the form

$$\frac{\partial d}{\partial \tau} = S_h(\phi)(1 - ||\nabla d||), \tag{6.6}$$

$$d(\mathbf{x}, 0) = \phi(\mathbf{x}, t), \tag{6.7}$$

is introduced, where $d(\mathbf{x}, \tau)$ corresponds to the level set function on the pseudo timescale. When this equation is solved to equilibrium, it holds that $||\nabla d|| = 1$, since convergence occurs when the right hand side is zero. Thus the steady solutions are distance functions. Furthermore, $S_h(\phi)$ denotes a smoothed sign function depending on the initial condition for the pseudo timescale equation, which can for example be of the form $S_h(\phi) = \frac{\phi}{\sqrt{\phi^2+h^2}}$ as in [136] or $S_h(\phi) = \frac{\phi}{\sqrt{\phi^2+|\nabla\phi|^2h^2}}$ as in [40] and where $0 < h \ll 1$. However, solving Equations (6.6)–(6.7) to equilibrium may require many steps and may thus slightly move the zero level set. A strategy to overcome this shortfall is introduced in [136] for the finite difference method, and extended to the finite element case in [107]. The idea is to apply a constraint which ensures that the volume occupied by the colony and the agar components remains constant during the reinitialization.

Therefore at the pseudo time step τ_k, we consider the volume V^k in each element as an integral over the element area Ω_e given as

$$V^k = \int_{\Omega_e} H(d^k)\, d\Omega_e,$$

where d^k is the distance field at the k-th iteration of the pseudo time redistancing and $H(\phi)$ denotes the Heaviside function

$$H(\phi) = \begin{cases} 0, & \text{if } \phi < 0 \\ \frac{1}{2}, & \text{if } |\phi| = 0 \\ 1, & \text{if } \phi > 0 \end{cases}.$$

Since the volume should not change, we require that $V^k = V^0$. Thus we can write

$$V^k - V^0 \approx (\tau^k - \tau^0) \int_{\Omega_e} \frac{dH'_\varepsilon(d^0)}{d\tau}\, d\Omega_e \approx \int_{\Omega_e} H'_\varepsilon(d^0)(d^k - d^0)\, d\Omega_e = 0, \tag{6.8}$$

where we take $H'_\varepsilon(d)$ of the form

$$H'_\varepsilon(d) = \begin{cases} 0, & \text{if } |d| > \varepsilon \\ \frac{1}{2}\left[\frac{1}{\varepsilon} + \frac{1}{\varepsilon}\cos(\frac{\pi d}{\varepsilon})\right], & \text{if } |d| \leq \varepsilon \end{cases}.$$

By a projection of the current level set values $\tilde{d}^k$ to values d^k, which satisfy Equation (6.8), according to [107], we assume that the new distance field can be calculated as

$$d^k = \tilde{d}^k + \lambda_{\Omega_e}(\tau^k - \tau^0) H'_\varepsilon(d^0), \quad \text{where} \quad \lambda_{\Omega_e} = \frac{-\int_{\Omega_e} H'_\varepsilon(d^0)\left(\frac{\tilde{d}^k - d^0}{\tau^k - \tau^0}\right) d\Omega_e}{\int_{\Omega_e} (H'_\varepsilon(d^0))^2\, d\Omega_e}$$

and λ_{Ω_e} is constant in Ω_e. However, we observe that, while it preserves the zero level set for few pseudo time steps, this method also induces a slight change in the zero level set for many steps. Furthermore, several parameters have to be chosen, making the calculations difficult to control.

An alternative reparametrization method is geometric reparametrization via the fast marching method [129, 130], which aims at solving the eikonal equation $||\nabla\phi|| = 1$ directly. For our simulations, we use a finite element based version of this method, similar to the one introduced in [69].

In the initialization of the method in [69], the set $\mathcal{I}$ denotes the collection of triangles which contain the discrete interface. Then the set of vertices corresponding to $\mathcal{I}$ is defined as

$$\mathcal{F} := \{v \in V(T) : T \in \mathcal{I}\} \subset \mathcal{V},$$

where $V(T)$ denotes the set of vertices of a triangle T and $\mathcal{V}$ denotes the collection of all vertices. For each vertex v belonging to the set $\mathcal{F}$, the discrete approximation $d(v)$ of the distance function is calculated. This approximation relies on orthogonal projections and the calculated distance function is assumed to be good enough, such that $\mathcal{F}$ represents the set of accepted vertices.

The active set of vertices $\mathcal{A}$ is defined as the set of the vertices which are not in $\mathcal{F}$ themselves, but have a neighboring vertex in $\mathcal{F}$, i.e., we take

$$\mathcal{A} := \{v \in \mathcal{V}\backslash\mathcal{F} : N(v) \cap \mathcal{F} \neq \emptyset\},$$

where $N(v)$ denotes the collection of all neighboring vertices of v. For these vertices the distance function is approximated similarly, but in relation to the distances already known for $\mathcal{F}$. Then the vertex $v_{\min} \in \mathcal{A}$ with the minimal distance function is chosen and moved to the set $\mathcal{F}$ and those of its neighbors which are not in $\mathcal{F}$ are added to the set $\mathcal{A}$, i.e., we obtain $\mathcal{F}_{\text{new}} = \mathcal{F} \cup \{v_{\min}\}$ and $\mathcal{A}_{\text{new}} = (\mathcal{A} \cup \mathcal{N})\backslash\{v_{\min}\}$ with $\mathcal{N} := N(v_{\min})\backslash\mathcal{F}$. The distances of the neighbors are calculated and the procedure is repeated until $|\mathcal{A}| = 0$. The zero level set function is uniquely determined by the calculated distance function and can now be determined with only very minor changes to the zero level set before the reinitialization.

Our variant of the reinitialization method is similar to the fast marching method described above. An example for the use of our method is depicted in Figure 6.3. In a first step, we determine the set of elements, which are intersected by the zero level set. This set of elements is colored in green in the example. In each of these triangular elements, we determine the points on the edges where the zero level set intersects. For the example element in Figure 6.3, these are the points P_0 and P_1. The discrete approximation of the circular zero level set, depicted in blue in the example, consists of line segments, which connect the intersection points.

For the calculation of the approximate distance function $d(v)$, we enrich the set $\{P_0, P_1\}$ of vertices on the zero level set by several additional points on the line

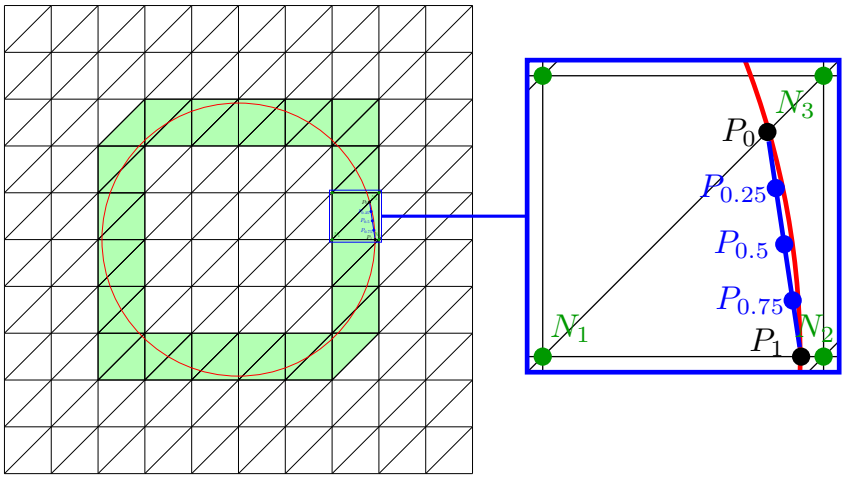

Figure 6.3.: Fast marching reinitialization method on a coarse example finite element grid with the circular zero level set in red and its discrete approximation in blue. The green area describes the set $\mathcal{I}$ of triangles which are intersected by the zero level set.

between the two intersection points. Thus, in the example P_0 and P_1 as well as the points $P_{0.25}$, $P_{0.5}$ and $P_{0.75}$ form a set $\{P_0, P_{0.25}, P_{0.5}, P_{0.75}, P_1\}$ which approximates the zero level set $\{\mathbf{x} : \phi(\mathbf{x}(t), t) = 0\}$. The approximate distance functions for the vertices $v(T)$ belonging to triangles T in the set of intersected elements $\mathcal{I}$ are calculated as the minimal distances to the set of points on the zero level set, which is similar to the projection in [69]. In the example this means that the approximation for the distance function $d(v)$ for $v \in \{N_1, N_2, N_3\}$ is calculated as the minimal distance to the set $\{P_0, P_{0.25}, P_{0.5}, P_{0.75}, P_1\}$ of points on the zero level set. Note that in the implementation the set of points on the zero level set is calculated for all triangles in $\mathcal{I}$ at once, such that cases where the minimal distance is achieved for a point belonging to another triangle is treated accordingly. The calculated distance function is assumed to be good enough, such that the set $\mathcal{F}$ of the vertices belonging to triangles from the set $\mathcal{I}$ represents the set of accepted vertices. For the example in Figure 6.3, the set $\{N_1, N_2, N_3\}$ is a subset of the set $\mathcal{F}$. Then the remaining distances are calculated in relation to this set. In order to ensure convergence, the level set simulations of bacterial colony growth have been performed on grids with different refinement levels and an appropriate refinement level has been chosen for our following simulations.

6.2.2. Comparison of the numerical results to real data

The following simulations are performed in FEniCS [139] and the simulation results are visualized in Paraview [1]. Using the parameter values in Table 6.1 on a circular

Parameter	Value	Parameter	Value	Parameter	Value	Parameter	Value
d_n	0.01	γ	1.0	K	0.01	$\alpha = \beta$	100
n_0	1.0	r_0	0.05	R	0.5	$\varepsilon_{\text{dist}}$	0.001

Table 6.1.: Parameter and initial values for the level set simulation of colony growth due to bacterial division.

domain of radius $R = 0.5$, we obtain the simulation results depicted in Figure 6.4, which represent the shape of the zero level set function at different time points.

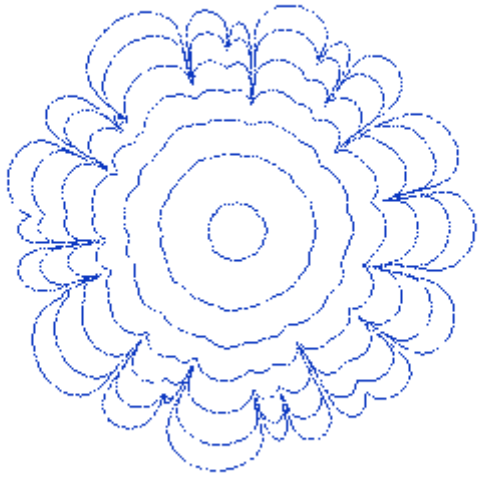

Figure 6.4.: Level set simulation of Equations (6.1),(6.3) and (6.5) with Darcy's law for parameter values as indicated in Table 6.1 at times $t = 0, 0.25, \ldots, 1.25, 1.45$.

The corresponding level sets in three dimensions at selected time points are depicted in Figure 6.5. Here the signed distance property of the level set resulting from the fast marching method reinitialization can be observed. The initial level set function is slightly perturbed so that the initial zero level set has the radius

$$r = r_0 + \varepsilon_{\text{dist}}(\cos(3\theta) + \sin(7\theta) + \cos(15\theta) + \sin(25\theta)),$$

which changes with the polar coordinate angle θ of a point in $\Omega \subset \mathbb{R}^2$ [132]. This represents the fact that the shape of the initial bacteria colony is not perfectly circular. The chosen circular domain has a radius of $R = 0.5$, where the initial radius of the colony is chosen as $r_0 = 0.05$. Furthermore, the mesh for the level set function is refined twice around the zero level set. This refinement is adapted as the level set moves.

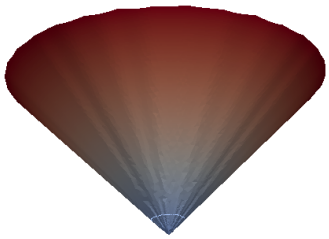

(a) Level set from the side at $t = 0.0$.

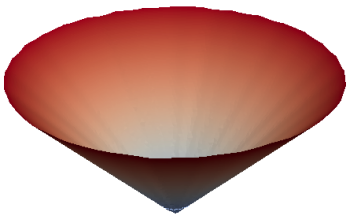

(b) Level set from above at $t = 0.0$.

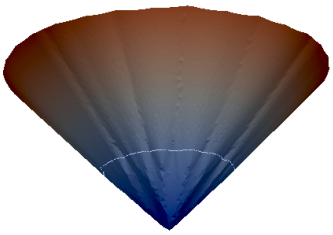

(c) Level set from the side at $t = 0.5$.

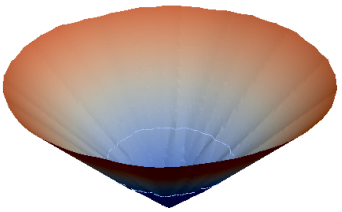

(d) Level set from above at $t = 0.5$.

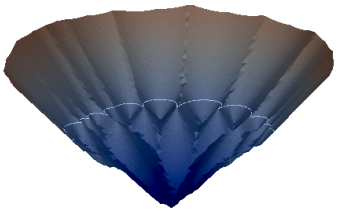

(e) Level set from the side at $t = 1.0$.

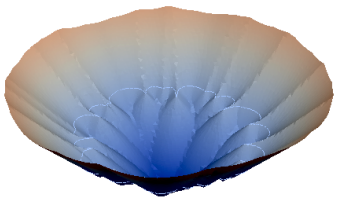

(f) Level set from above at $t = 1.0$.

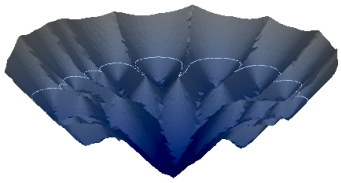

(g) Level set from the side at $t = 1.45$.

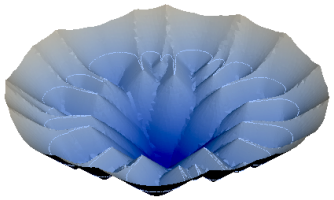

(h) Level set from above at $t = 1.45$.

Figure 6.5.: Three-dimensional views of the level set function $\phi(\mathbf{x}, t)$ corresponding to selected timesteps of the colony level sets in Figure 6.4.

Changing a total of only three model parameters, we investigate the model's reaction to changing environmental conditions. Note that the colonies grow at very different

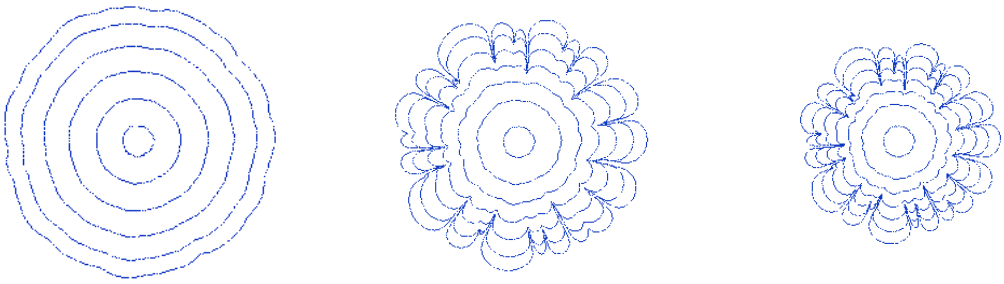

(a) Simulation for $d_n = 0.05$, $K = 0.05$, $t = 0, 0.15, \ldots, 0.9$.

(b) Simulation for $d_n = 0.01$, $K = 0.01$, $t = 0, 0.25, \ldots, 1.25, 1.45$.

(c) Simulation for $d_n = 0.005$, $K = 0.005$, $t = 0, 0.25, \ldots, 1.5$.

Figure 6.6.: Simulations for the influence of the agar concentration on *S. aureus* pattern formation.

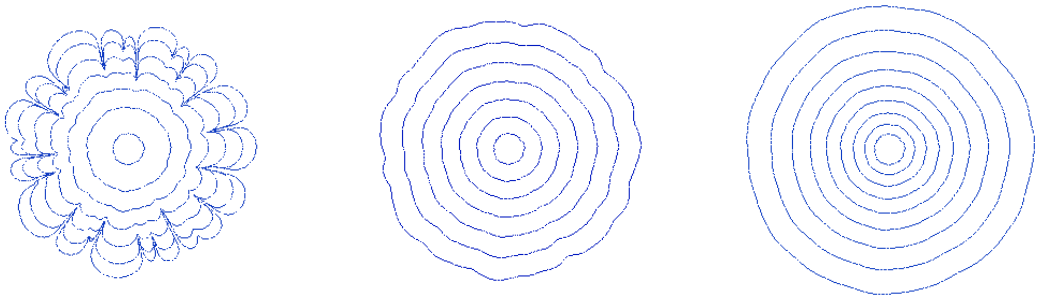

(a) Simulation for $n_0 = 1$ $t = 0, 0.25, \ldots, 1.25, 1.45$.

(b) Simulation for $n_0 = 1.5$, $t = 0, 0.1, \ldots, 0.6$.

(c) Simulation for $n_0 = 2$, $t = 0, 0.05, \ldots, 0.4$.

Figure 6.7.: Simulations for the influence of the initial nutrient concentration on *S. aureus* pattern formation.

speeds, such that in Figure 6.6 and Figure 6.7 different ranges of time steps are depicted. We model the varying agar concentrations as depicted in Figure 6.1 by simultaneously increasing or decreasing the parameter K in Darcy's law and the parameter d_n for the nutrient diffusion, where an increase in these values corresponds to a decreased agar concentration and a decrease corresponds to an increased agar concentration. As expected the colony grows faster for the case corresponding to a decreased agar concentration depicted in Figure 6.6(a) and slower growth is observed for an increased agar concentration in Figure 6.6(c). However, for the decreased parameters the colony shape is similar to the reference case, whereas the real data in Figure 6.1 shows a round colony shape. This corresponds well to the first time steps of colony growth, but not to the later ones, where the simulated

colony in Figure 6.6(c) shows fingering. However, also the biological observation in Figure 6.1(c) shows a compressed fingering structure inside the round colony. Varying the initial value of the nutrients, we obtain results that replicate the biological data as depicted in Figure 6.7. In the numerical simulations, we observe that for an increasing initial nutrient concentration, the colonies grow faster, needing less time steps to reach the domain boundary. Also for increasing n_0 the colony shape becomes rounder as expected from the real data. Thus we obtain a good qualitative agreement with the real data depicted in Figure 6.2.

In [127] a distinct effect of agar concentration on EPS-mediated spreading is observed. As the *S. aureus* wildtype strains considered in the experiments are able to secrete EPS, including osmotic pressure effects into the modeling should be the next step in the investigation of the dependence of colony evolution on agar concentration. The mathematical modeling of *S. aureus* colony expansion due to biofilm osmotic pressure effects is similar to that of *B. subtilis* as described in [127]. While *B. subtilis* bacteria loose their ability to move using their flagella at the secretion of the biofilm component EPS, the bacterium *S. aureus* is also able to secrete EPS, but does not have a flagella at all. Thus, the slow expansion process of the biofilm driven by osmotic pressure must be comparable in both species and similar models should apply. As in the case of *B. subtilis*, this is not appropriate for the EPS mutant, which shows slower expansion caused mainly by cell-cell interactions instead of osmotic effects, as described in this chapter.

While the model in [127] considers bacterial biofilm growth in height, models such as [35, 36] are available, which model biofilm growth in a similar way to two-dimensional multi-component tumor growth [4, 8]. Thus, a possible approach would be to consider the biofilm as a biological gel composed of the main biomass components EPS and water as in [37], where the polymer-producing bacteria are enmeshed in the EPS. Then the EPS experiences swelling and contraction induced by the osmotic pressure gradient and the forces acting in this situation are physical forces resulting from the deformation of the matrix as well as chemical forces from osmotic processes. From mass and momentum balance equations, a model could then be derived for the evolution of the colony.

However, the crucial features of such a model are the different concentrations of the colony components at different points in space, such that a level set approach, which relies on the assumption that the concentrations of the components are constant

inside the domain, is no longer adequate. Instead the evolution of the colony could be described using transport equations for the single components resulting from mass balance considerations.

Part IV.

Conclusion and outlook

Conclusion and outlook

In this thesis we have considered several aspects of pattern formation processes in bacterial colonies under laboratory conditions. We have focused on two different modeling approaches, namely reaction-diffusion equations with nutrient-dependent bacterial diffusion and pressure-based approaches.

We have first introduced the biological, physical and mathematical background and the numerical simulation techniques in Chapters 2 and 3 of Part I.

In Part II we have considered classical reaction-diffusion equation models. Thus, in Chapter 4, starting from a detailed consideration of the gene regulation processes in *Staphylococcus aureus*, we have derived ordinary differential equations to describe the temporal evolution of the concentrations of the quorum sensing substance AIP and of the biofilm. These were then incorporated into a partial differential equation model consisting of evolution equations for the concentrations of replicative and non-replicative bacteria, nutrients, quorum sensing substance and biofilm. We have performed the corresponding numerical simulations using a time-adaptive finite element method and demonstrated that the mutation-dependent pattern formation of *S. aureus* bacteria in the laboratory can be obtained from the newly developed system by a variation of the parameters associated to the mutated gene loci. We have also demonstrated the reproduction of the five qualitative morphologies of bacteria pattern formation with our model. Furthermore, in Chapter 5 we have briefly considered Turing pattern formation approaches. We have observed that these approaches do not yield a sufficient explanation for the fingering behavior observed in bacterial colonies. However, we have derived a critical diffusion parameter for the onset of long-wavelength instabilities in a reduced system of two partial differential equations with mixed diffusion by adapting a front instability approach.

In Part III, we have investigated a very general model for the effects of pressure induced by biomass growth on pattern formation in the bacterial colony. We have concentrated on the effects induced by bacterial division in Chapter 6. For the

numerical simulations we have again employed a finite element method, which was coupled to a level set method with a fast marching reinitialization.

The investigations in this thesis help to better understand *S. aureus* gene regulation processes related to pattern formation as well as pressure-induced effects in general bacterial pattern formation. Pattern formation is of special interest not only due to the patterns themselves, but also due to the differences in pattern formation for mutant colonies of a bacterium. In case of a pathological *S. aureus* infection, determining which kind of bacterium is responsible for the infection is an important part of finding the right treatment. In this context time is crucial. Growing bacterial colonies in a laboratory and analyzing the obtained patterns may allow to determine the mutant type in a time- and cost-efficient way. The results from this thesis may be used to help develop a methodology for this, which is able to isolate and recognize typical graphical patterns which can be attributed to a certain mutant. In terms of future work, it seems promising to investigate further pressure-related influences on colony growth such as osmotic pressure effects as described at the end of Chapter 6. The related model approaches can become very complex and, in comparison with experimental real data, further effects in pattern formation can be isolated and studied in detail. Future work could also include investigating a possible combination of these general models with specific models for quorum sensing or considering pattern formation of mixed bacterial colonies.

Appendix

A1. Simulation results for the mutant colonies

On the following pages, the single concentration simulation results for the *ica*, *spa*, *ica*/*spa*, *psm*-α, *psm*-β, *psm*-α/*psm*-β and *agr* mutant colonies discussed in Section 4.6.3 are displayed.

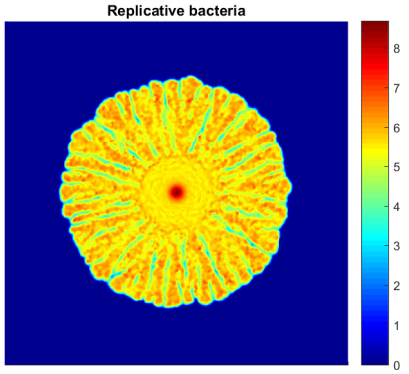

(a) Replicative bacteria.

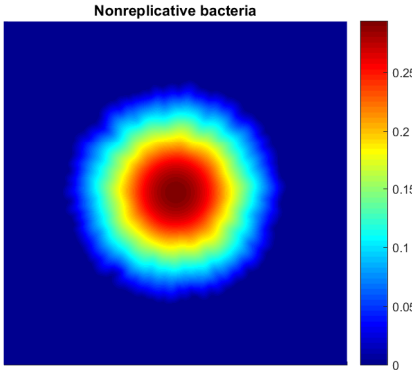

(b) Nonreplicative bacteria.

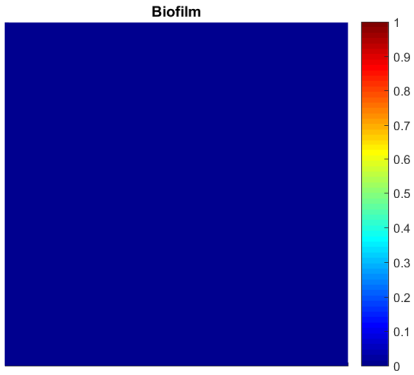

(c) Biofilm concentration.

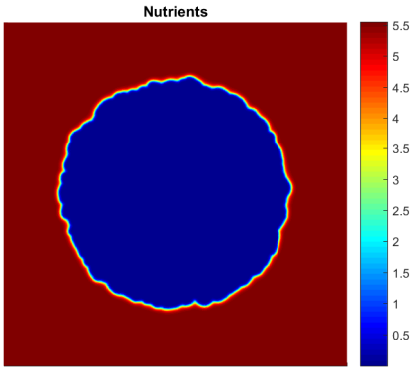

(d) Nutrient concentration.

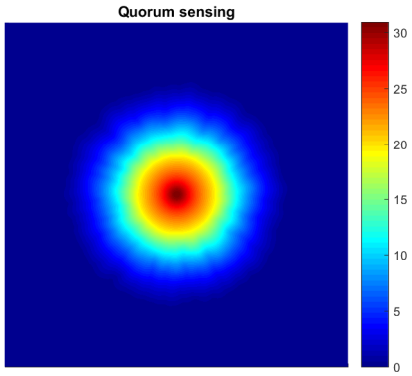

(e) Quorum sensing substance.

Figure A1.1.: Single concentrations for the *S. aureus ica* mutant as obtained from simulation with the parameters indicated in Section 4.6.3.

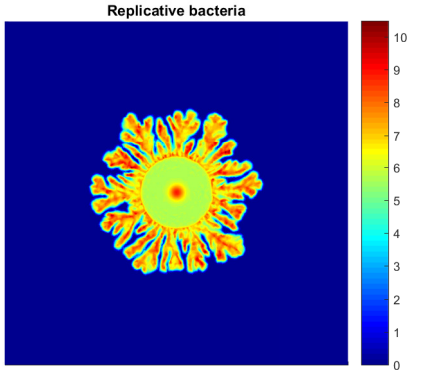

(a) Replicative bacteria.

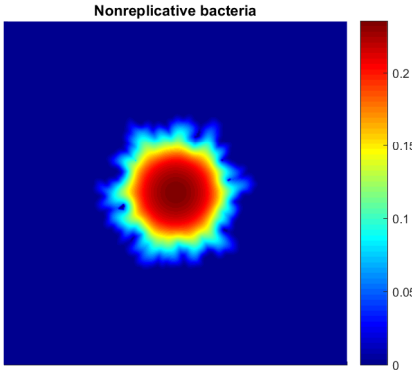

(b) Nonreplicative bacteria.

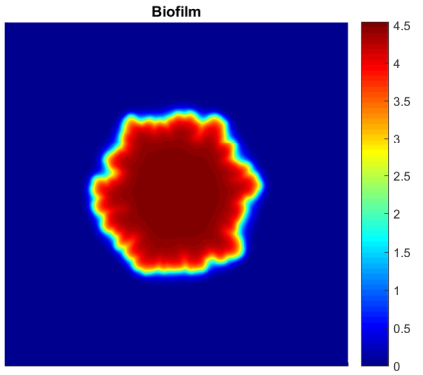

(c) Biofilm concentration.

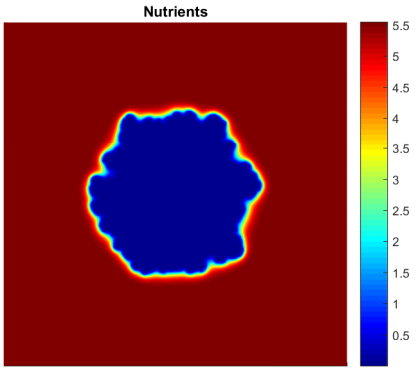

(d) Nutrient concentration.

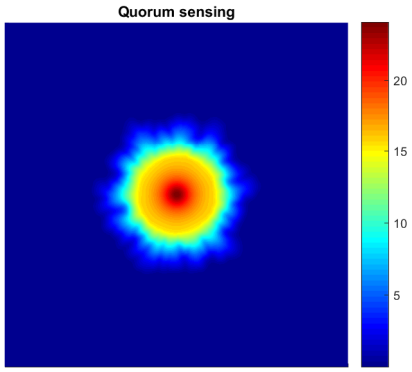

(e) Quorum sensing substance.

Figure A1.2.: Single concentrations for the *S. aureus spa* mutant as obtained from simulation with the parameters indicated in Section 4.6.3.

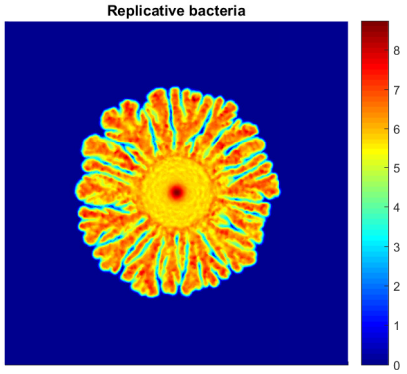

(a) Replicative bacteria.

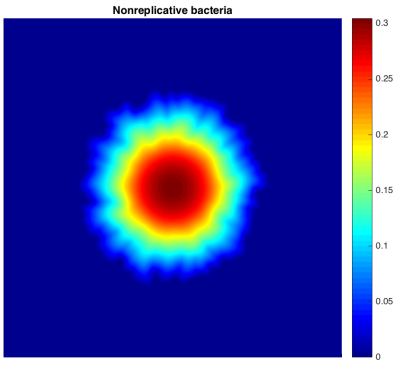

(b) Nonreplicative bacteria.

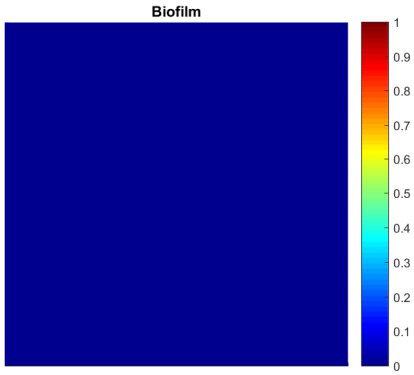

(c) Biofilm concentration.

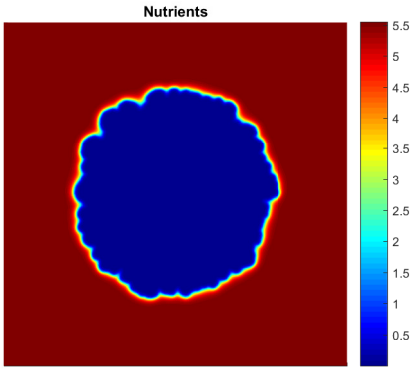

(d) Nutrient concentration.

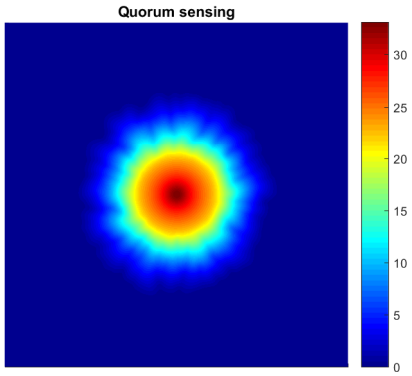

(e) Quorum sensing substance.

Figure A1.3.: Single concentrations for the *S. aureus ica* and *spa* mutant obtained by simulation with the parameters from Section 4.6.3.

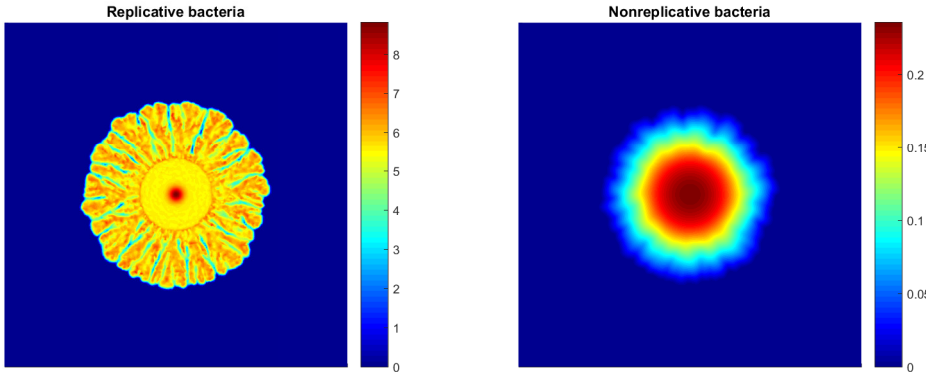

(a) Replicative bacteria.

(b) Nonreplicative bacteria.

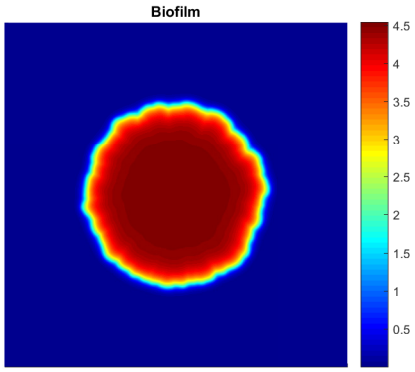

(c) Biofilm concentration.

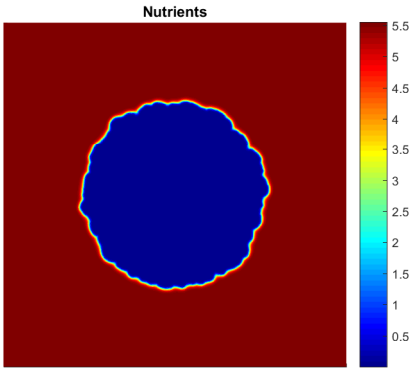

(d) Nutrient concentration.

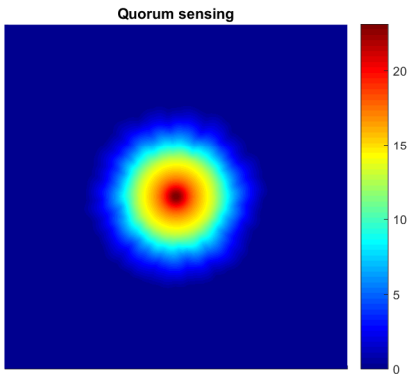

(e) Quorum sensing substance.

Figure A1.4.: Single concentrations for the *S. aureus psm-α* mutant as obtained from simulation with the parameters indicated in Section 4.6.3.

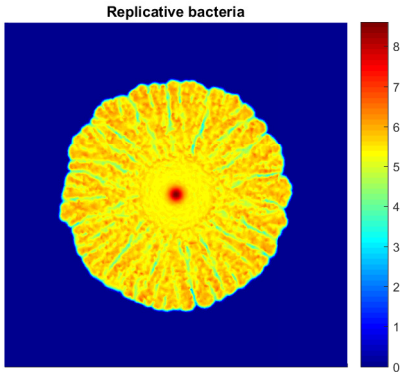

(a) Replicative bacteria.

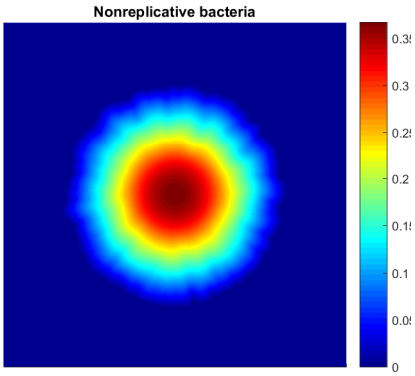

(b) Nonreplicative bacteria.

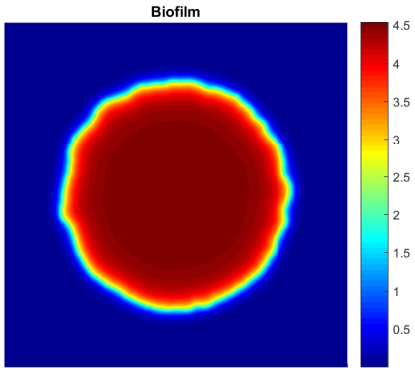

(c) Biofilm concentration.

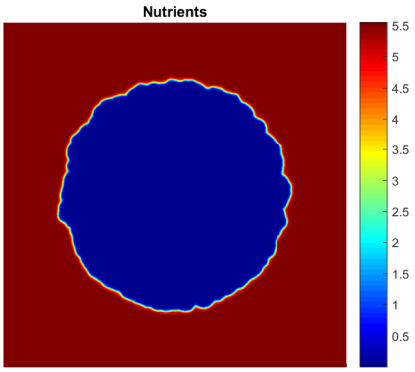

(d) Nutrient concentration.

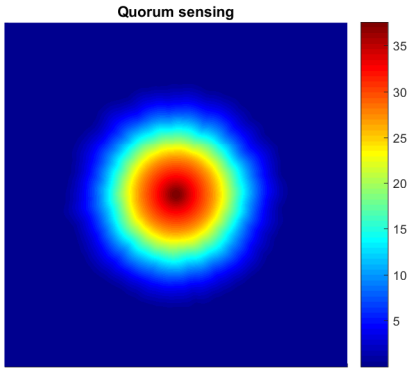

(e) Quorum sensing substance.

Figure A1.5.: Single concentrations for the *S. aureus psm-β* mutant as obtained from simulation with the parameters indicated in Section 4.6.3.

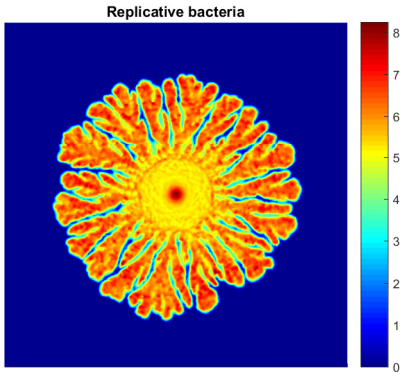

(a) Replicative bacteria.

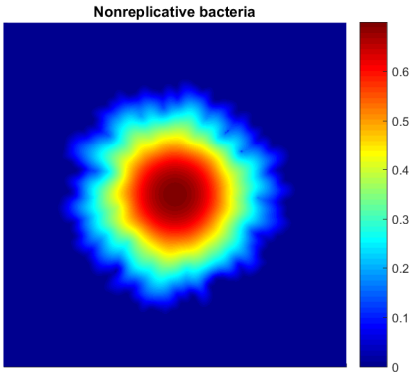

(b) Nonreplicative bacteria.

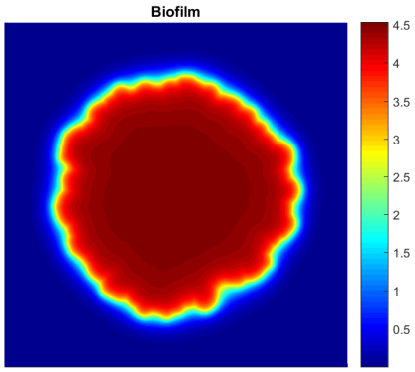

(c) Biofilm concentration.

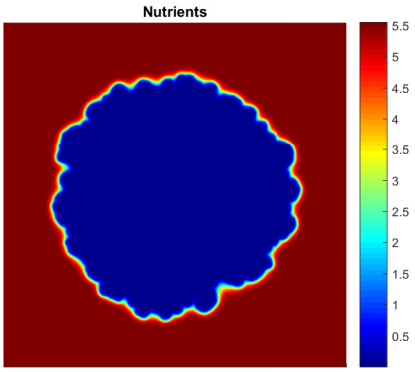

(d) Nutrient concentration.

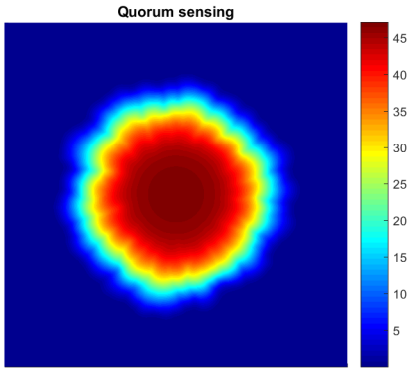

(e) Quorum sensing substance.

Figure A1.6.: Single concentrations for the *S. aureus psm-α* and *psm-β* mutant obtained by simulation with the parameters from Section 4.6.3.

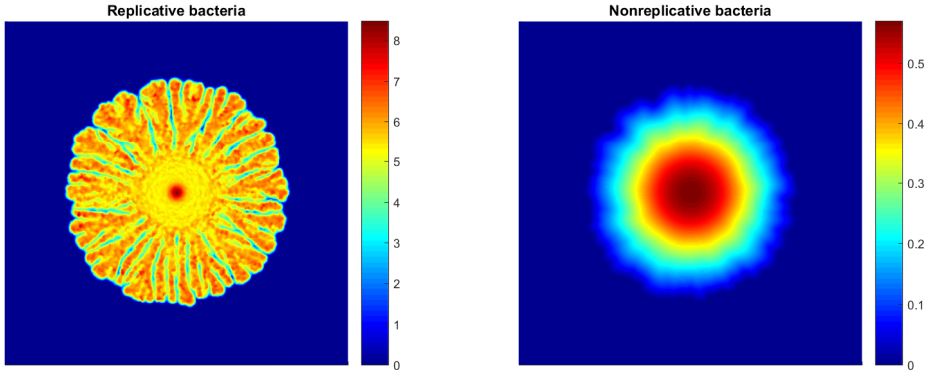

(a) Replicative bacteria.

(b) Nonreplicative bacteria.

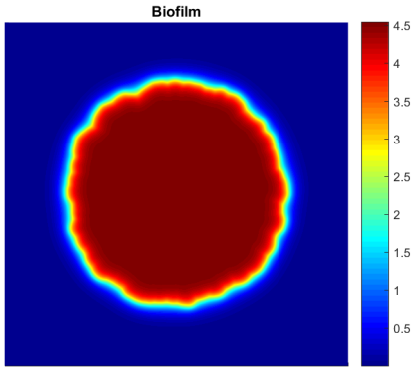

(c) Biofilm concentration.

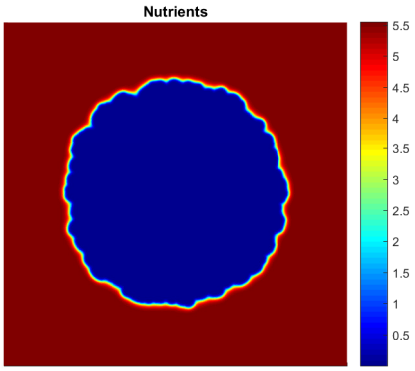

(d) Nutrient concentration.

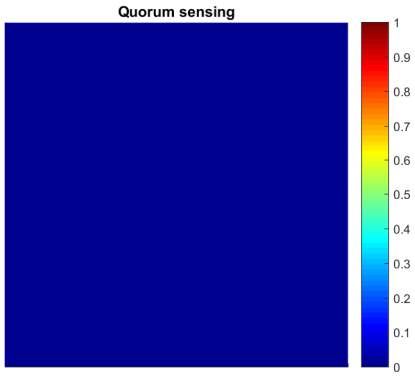

(e) Quorum sensing substance.

Figure A1.7.: Single concentrations for the *S. aureus agr* mutant as obtained from simulation with the parameters indicated in Section 4.6.3.

List of figures

List of tables

Bibliography

[1] J. Ahrens, B. Geveci, and C. Law. *ParaView: An end-user tool for large data visualization. Visualization handbook*. Elsevier, 2005.

[2] E. Alpkvist and I. Klapper. "A multidimensional multispecies continuum model for heterogeneous biofilm development". In: *Bulletin of Mathematical Biology* 69 (2007), pp. 765–789.

[3] E. Alpkvist et al. "A new mathematical model for chemotactic bacterial colony growth". In: *Water Science and Technology* 49.11–12 (2004), pp. 187–192.

[4] D. Ambrosi and L. Preziosi. "Cell adhesion mechanisms and stress relaxation in the mechanics of tumours". In: *Biomechanics and Modeling in Mechanobiology* 8.5 (2009), pp. 397–413.

[5] E. Ando et al. "Biofilm formation among methicillin-resistant *Staphylococcus aureus* isolates from patients with urinary tract infection". In: *Acta Medica Okayama* 58.4 (2004), pp. 207–214.

[6] L.C.M. Antunes et al. "A mutational analysis defines *Vibrio fischeri* LuxR binding sites". In: *Journal of Bacteriology* 190.13 (2008), pp. 4392–4397.

[7] C.R. Arciola et al. "Polysaccharide intercellular adhesin in biofilm: Structural and regulatory aspects". In: *Frontiers in Cellular and Infection Microbiology* 5 (2015).

[8] S. Astanin and L. Preziosi. "Multiphase models of tumor growth". In: *Selected Topics in Cancer Modeling*. Modeling and simulation in science, engineering and technology. Birkhäuser Boston, 2008, pp. 1–31.

[9] A. Ballal and A.C. Manna. "Expression of the sarA family of genes in different strains of *Staphylococcus aureus*". In: *Microbiology* 155 (2009), pp. 2342–2352.

[10] B.L. Bassler and M.B. Miller. "The Prokaryotes Volume 2: Ecophysiology and Biochemistry". In: ed. by M. Dworkin et al. Springer, 2006. Chap. Quorum sensing, pp. 336–353.

[11] M. Ben Amar and E.C. Poiré. "Pushing a non-Newtonian fluid in a Hele-Shaw cell: From fingers to needles". In: *Physics of Fluids* 11.7 (1999), pp. 1757–1767.

[12] E. Ben-Jacob. "From snowflake formation to growth of bacterial colonies I: Diffusive patterning in azoic systems". In: *Contemporary Physics* 34.5 (1993), pp. 247–273.

[13] E. Ben-Jacob. "From snowflake formation to growth of bacterial colonies II: Cooperative formation of complex colonial patterns". In: *Contemporary Physics* 38.3 (1997), pp. 205–241.

[14] E. Ben-Jacob et al. "Mathematical models for biological pattern formation". In: ed. by P.K. Maini and H.G. Othmer. Springer, 2001. Chap. Modelling branching and chiral colonial patterning of lubricating bacteria, pp. 211–253.

[15] Y. Benito et al. "*Staphylococcus aureus* agr regulatory RNA, and identification of the RNA domain involved in repression of protein A expression". In: *RNA* 6 (2000), pp. 668–679.

[16] D. Bensimon et al. "Viscous flows in two dimensions". In: *Reviews of Modern Physics* 58.4 (1986).

[17] D.L. Benson, P.K. Maini, and J.A. Sherratt. "Analysis of pattern formation in reaction diffusion models with spatially inhomogeneous diffusion coefficients". In: *Mathematical and Computer Modelling* 17.12 (1993), pp. 29–34.

[18] D.L. Benson, P.K. Maini, and J.A. Sherratt. "Unravelling the Turing bifurcation using spatially varying diffusion coefficients". In: *Journal of Mathematical Biology* 37 (1998), pp. 381–417.

[19] D.L. Benson, J.A. Sherratt, and P.K. Maini. "Diffusion driven instability in an inhomogeneous domain". In: *Bulletin of Mathematical Biology* 55.2 (1993), pp. 265–384.

[20] M. Bischoff, J.M. Entenza, and P. Giachino. "Influence of a functional *sigB* operon on the global regulators *sar* and *agr* in *Staphylococcus aureus*". In: *Journal of Bacteriology* 183.17 (2001), pp. 5171–5179.

[21] B.R. Boles and A.R. Horswill. "Agr-mediated dispersal of *Staphylococcus aureus* biofilms". In: *PLoS Pathogens* 4.4 (2008).

[22] D. Braess. *Finite Elemente: Theorie, schnelle Löser und Anwendungen in der Elastizitätstheorie*. 3rd edition. Springer, 2003.

[23] M.P. Brenner, L.S. Levitov, and E.O. Budrene. "Physical mechanisms for chemotactic pattern formation by bacteria". In: *Biophysical Journal* 74 (1998), pp. 1677–1693.

[24] S. Brenner and R. Scott. *The mathematical theory of finite element methods*. 3rd edition. Springer, 2008.

[25] S. Bronner, H. Monteil, and G. Prevost. "Regulation of virulence determinants in *Staphylococcus aureus*: Complexity and applications". In: *FEMS Microbiology Reviews* 28 (2004), pp. 183–200.

[26] N.C. Caiazza and G.A. O'Toole. "Alpha-toxin is required for biofilm formation by *Staphylococcus aureus*". In: *Journal of Bacteriology* 185.10 (2003), pp. 3214–3217.

[27] J.A. Castillo, F. Sanchez-Garduno, and P. Padilla. "A Turing-Hopf bifurcation scenario for pattern formation on growing domains". In: *Bulletin of Mathematical Biology* 78.7 (2016), pp. 1410–1449.

[28] F. Centler and M. Thullner. "Chemotactic preferences govern competition and pattern formation in simulated two-strain microbial communities". In: *Frontiers in Microbiology* 6.40 (2015).

[29] N. Cerca, J.L. Brooks, and K.K. Jefferson. "Regulation of the intercellular adhesin locus regulator (icaR) by SarA, sigmaB, and IcaR in *Staphylococcus aureus*". In: *Journal of Bacteriology* 190.19 (2008), pp. 6530–6533.

[30] N. Cerca et al. "Quantitative analysis of adhesion and biofilm formation on hydrophilic and hydrophobic surfaces of clinical isolates of *Staphylococcus epidermidis*". In: *Research in Microbiology* 156.4 (2005), pp. 506–514.

[31] M.A. Chaplain, M. Ganesh, and I.G. Graham. "Spatio-temporal pattern formation on spherical surfaces: Numerical simulation and application to solid tumour growth". In: *Journal of Mathematical Biology* 42.5 (2001), pp. 387–423.

[32] A.L. Cheung and A.C. Manna. "Role of the distal sarA promoters in SarA expression in *Staphylococcus aureus*". In: *Infection and Immunity* 73.7 (2005), pp. 4391–4394.

[33] G.Y.C. Cheung et al. "Phenol-soluble modulins – critical determinants of staphylococcal virulence". In: *FEMS Microbiology Reviews* 38.4 (2014), pp. 698–719.

[34] P.G. Ciarlet. *The finite element method for elliptic problems*. Classics in Applied Mathematics. SIAM Philadelphia, 2002.

[35] F. Clarelli et al. "A fluid dynamics model of the growth of phototropic biofilms". In: *Journal of Mathematical Biology* 66.7 (2013), pp. 1387–1408.

[36] F. Clarelli et al. "A fluid dynamics multidimensional model of biofilm growth: Stability, influence of environment and sensitivity". In: *Mathematical Medicine and Biology* 33.4 (2016), pp. 371–395.

[37] N.G. Cogan and J.P. Keener. "The role of the biofilm matrix in structural development". In: *Mathematical Medicine and Biology* 21 (2004), pp. 147–166.

[38] E.J. Crampin, E.A. Gaffney, and P.K. Maini. "Reaction and diffusion on growing domains: Scenarios for robust pattern formation". In: *Bulletin of Mathematical Biology* 61 (1999), pp. 1093–1120.

[39] E.J. Crampin, W.W. Hackborn, and P.K. Maini. "Pattern formation in reaction-diffusion models with nonuniform domain growth". In: *Bulletin of Mathematical Biology* 64 (2002), pp. 747–769.

[40] R. Croce, M. Griebel, and M.A. Schweitzer. "Numerical simulation of bubble and droplet deformation by a level set approach with surface tension in three dimensions". In: *Numerical Methods in Fluids* 62.9 (2010), pp. 963–993.

[41] G.C. Cruywagen, P.K. Maini, and J.D. Murray. "Biological pattern formation on two-dimensional spatial domains: A nonlinear bifurcation analysis". In: *SIAM Journal on Applied Mathematics* 57.6 (1997), pp. 1485–1509.

[42] G.C. Cruywagen, P.K. Maini, and J.D. Murray. "Sequential pattern formation in a model of skin morphogenesis". In: *IMA Journal of Mathematics Applied in Medicine and Biology* 9 (1992), pp. 227–248.

[43] C. Cucarella et al. "Bap, a *Staphylococcus aureus* surface protein involved in biofilm formation". In: *Journal of Bacteriology* 183.9 (2001), pp. 2888–2896.

[44] D. Cue, M.G. Lei, and C.Y. Lee. "Genetic regulation of the intercellular adhesion locus in Staphylococci". In: *Frontiers in Cellular and Infection Microbiology* 2.38 (2012).

[45] A.C. DeDent, M. McAdow, and O. Schneewind. "Distribution of protein A on the surface of *Staphylococcus aureus*". In: *Journal of Bacteriology* 189.12 (2007), pp. 4473–4484.

[46] J. Dervaux, J.C. Magniez, and A. Libchaber. "On growth and form of *Bacillus subtilis* biofilms". In: *Interface Focus* 4.6 (2014).

[47] A. Deutsch. "Towards analyzing complex swarming patterns in biological systems with the help of lattice-gas cellular automata". In: *Journal of Biological Systems* 3 (1995), pp. 947–955.

[48] L.A. Diaz Rodrigues, D.C. Mistro, and S. Petrovskii. "Pattern formation, long-term transients, and the Turing-Hopf bifurcation in a space- and time-discrete predator-prey system". In: *Bulletin of Mathematical Biology* 73.8 (2011), pp. 1812–1840.

[49] J. Dockery and I. Klapper. "Finger formation in biofilm layers". In: *SIAM Journal on Applied Mathematics* 62.3 (2001), pp. 853–869.

[50] J.D. Dockery and J.P. Keener. "A mathematical model for quorum sensing in *Pseudomonas aeruginosa*". In: *Bulletin of Mathematical Biology* 63 (2001), pp. 95–116.

[51] S. Dormann, A. Deutsch, and A.T. Lawniczak. "Fourier analysis of Turing-like pattern formation in cellular automaton models". In: *Future Generation Computer Systems* 17.7 (2001), pp. 901–909.

[52] R. Duddu et al. "A combined extended finite element and level set method for biofilm growth". In: *International Journal for Numerical Methods in Engineering* 2 (2006), pp. 1–33.

[53] P.M. Dunman et al. "Transcription profiling-based identification of *Staphylococcus aureus* genes regulated by the *agr* and/or *sarA* loci". In: *Journal of Bacteriology* 183.24 (2001), pp. 7341–7353.

[54] A.C. Duong, G.Y.C. Cheung, and M. Otto. "Interaction of phenol-soluble modulins with phosphatidylcholine vesicles". In: *Pathogens* 1 (2012), pp. 3–11.

[55] A. Eberhard. "Inhibition and activation of bacterial luciferase synthesis". In: *Journal of Bacteriology* 109.3 (1972), pp. 1101–1105.

[56] H.J. Eberl, D.F. Parker, and M.C.M. van Loosdrecht. "A new deterministic spatio-temporal continuum model for biofilm development". In: *Journal of Theoretical Medicine* 3 (2001), pp. 161–175.

[57] U. Ebert and W. van Saarloos. "Universal algebraic relaxation of fronts propagating into an unstable state and implications for moving boundary approximations". In: *Physical Review Letters* 80.8 (1998), pp. 1650–1653.

[58] U. Ebert, W. van Saarloos, and C. Caroli. "Propagation and structure of planar streamer fronts". In: *Physical Review E* 55.2 (1997), pp. 1530–1549.

[59] B.O. Emerenini et al. “A mathematical model of quorum sensing induced biofilm detachment”. In: *PLOS ONE* 10.7 (2015).

[60] L.C. Evans. *Partial differential equations*. 2nd. American Mathematical Society, 2010.

[61] P. Fast and M.J. Shelley. “Moore’s law and the Saffman–Taylor instability”. In: *Journal of Computational Physics* 212 (2006), pp. 1–5.

[62] P. Feng and Z. Zhou. “Finite traveling wave solutions in a degenerate cross-diffusion model for bacterial colony”. In: *Communications on pure and applied analysis* 6.4 (2007), pp. 1145–1165.

[63] W.C. Fuqua, S.C. Winans, and E.P. Greenberg. “Quorum sensing in bacteria: The LuxR-LuxI family of cell density-responsive transcriptional regulators”. In: *Journal of Bacteriology* 176.2 (1994), pp. 269–275.

[64] C.A. Fux, S. Wilson, and P. Stoodley. “Detachment characteristics and oxacillin resistance of Staphyloccocus aureus biofilm emboli in an in vitro catheter infection model”. In: *Journal of Bacteriology* 186.14 (2004), pp. 4486–4491.

[65] J.C. Garcia-Betancur et al. “Cell differentiation defines acute and chronic infection cell types in *Staphylococcus aureus*”. In: *eLife* (2017). URL: `https://elifesciences.org/articles/28023`.

[66] C. Giverso, M. Verani, and P. Ciarletta. “Branching instability in expanding bacterial colonies”. In: *MOX-Report No. 57* (2014).

[67] C. Giverso, M. Verani, and P. Ciarletta. “Branching instability in expanding bacterial colonies”. In: *Journal of The Royal Society Interface* 12.90 (2014).

[68] R.J. Gordon and F.D. Lowy. “Pathogenesis of methicillin-resistant *Staphylococcus aureus* infection”. In: *Clinical Infectious Diseases* 46.5 (2008), pp. 350–359.

[69] S. Groß, V. Reichelt, and A. Reusken. “A finite element based level set method for two-phase incompressible flows”. In: *Computing and Visualization in Science* 9.4 (2006), pp. 239–257.

[70] E. Gustafsson et al. “Characterizing the dynamics of the quorum-sensing system in *Staphylococcus aureus*”. In: *Journal of Molecular Microbiology and Biotechnology* 8.4 (2004), pp. 232–242.

[71] S. Hata, H. Nakao, and A. Mikhailov. "Sufficient conditions for wave instability in three-component reaction-diffusion systems". In: *Progress of Theoretical and Experimental Physics* (2014).

[72] H. Hof and R. Dörries. *Medizinische Mikrobiologie*. 5th edition. Thieme, 2000.

[73] T. Horger et al. "Analysis of a bacterial model with nutrient-dependent degenerate diffusion". In: *Mathematical Methods in the Applied Sciences* 38.17 (2015), pp. 3851–3865.

[74] T. Horger et al. "Mathematical modeling of tumor-induced angiogenesis using porous medium diffusion". In: *International Journal of Biomathematics and Biostatistics* 2 (2013), pp. 145–165.

[75] D. Horvath et al. "Instabilities in propagating reaction-diffusion fronts". In: *Journal of Chemical Physics* 98.8 (1993), pp. 6332–6343.

[76] S. Jabbari et al. "Mathematical modelling of the agr operon in *Staphylococcus aureus*". In: *Journal of Mathematical Biology* 61 (2010), pp. 17–54.

[77] D. Kaiser and R. Losick. "How and why bacteria talk to each other". In: *Cell* 73 (1993), pp. 873–885.

[78] T. Kantyka, L.N. Shaw, and J. Potempa. "Cysteine Proteases of Pathogenic Organisms". In: Advances in Experimental Medicine and Biology. Springer. Chap. Papain-like proteases of *Staphylococcus aureus*, pp. 1–14.

[79] S. Kaufmann et al. "Characterization of hepatocellular carcinoma (HCC) lesions using a novel CT-based volume perfusion (VPCT) technique". In: *European Journal of Radiology* 84 (2015), pp. 1029–1035.

[80] S. Kaufmann et al. "Reproducibility of VPCT parameters in the normal pancreas: Comparison of two different kinetic calculation models". In: *Academic Radiology* 22 (2015), pp. 1099–1105.

[81] S. Kaufmann et al. "Volume perfusion computed tomography (VPCT)-based evaluation of response to TACE using two different sized drug eluting beads in patients with nonresectable hepatocellular carcinoma: Impact on tumor and liver parenchymal vascularisation". In: *European Journal of Radiology* 84 (2015), pp. 2548–2554.

[82] K. Kawasaki et al. "Modeling spatio-temporal patterns generated by *Bacillus subtilis*". In: *Journal of Theoretical Biology* 188.2 (1997), pp. 177–185.

[83] E. Khain and L.M. Sander. "Dynamics and pattern formation in invasive tumor growth". In: *Physical Review Letters* 96.18 (2006).

[84] S. Kitsunezaki. "Interface dynamics for bacterial colony formation". In: *Journal of the Physical Society of Japan* 66 (1997), pp. 1544–1550.

[85] J.K.-M. Knobloch et al. "RsbU-dependent regulation of *Staphylococcus epidermidis* biofilm formation is mediated via the alternative sigma factor sigmaB by repression of the negative regulator gene icaR". In: *Infection and Immunity* 72.7 (2004), pp. 3838–3848.

[86] A.J. Koch and H. Meinhardt. "Biological pattern formation: From basic mechanisms to complex structures". In: *Reviews of Modern Physics* 66.4 (1994), pp. 1481–1507.

[87] K.Y. Le et al. "Molecular determinants of staphylococcal biofilm dispersal and structuring". In: *Frontiers in Cellular and Infection Microbiology* 4.167 (2014).

[88] R.-T. Liu, S.-S. Liaw, and P.K. Maini. "Oscillatory Turing patterns in a simple reaction-diffusion system". In: *Journal of the Korean Physical Society* 50.1 (2007), pp. 234–238.

[89] D. Lopez and J.C. Garcia-Betancur. *S. aureus* laboratory results, displayed with permission.

[90] P.K. Maini. "Spatial and spatiotemporal pattern formation in generalised Turing systems". In: *Mathematical and Computer Modelling* 32.11 (1996), pp. 71–77.

[91] P.K. Maini, D.L. Benson, and J.A. Sherratt. "Pattern formation in reaction-diffusion models with spatially inhomogeneous diffusion coefficients". In: *IMA Journal of Mathematics Applied in Medicine and Biology* 9 (1992), pp. 197–213.

[92] P.K. Maini et al. "Turing's model for biological pattern formation and the robustness problem". In: *Interface Focus* 2 (2012), pp. 487–496.

[93] C.D. Majerczyk et al. "Staphylococcus aureus CodY negatively regulates virulence gene expression". In: *Journal of Bacteriology* 190.7 (2008), pp. 2257–2265.

[94] E.E. Mann et al. "Modulation of eDNA release and degradation affects *Staphylococcus aureus* biofilm maturation". In: *PLoS ONE* 4.6 (2009).

[95] A.C. Manna and A.L. Cheung. "SarU, a sarA homolog, is repressed by SarT and regulates virulence genes in *Staphylococcus aureus*". In: *Infection and Immunity* 71.1 (2003), pp. 343–353.

[96] L.A. Marraffini, A.C. DeDent, and O. Schneewind. "Sortases and the art of anchoring proteins to the envelopes of gram-positive bacteria". In: *Microbiology and Molecular Biology Reviews* 70.1 (2006), pp. 192–221.

[97] *MATLAB Release 2016a, The MathWorks, Inc., Natick, Massachusetts, United States.*

[98] M. Matsushita et al. "Formation of colony patterns by a bacterial cell population". In: *Physica A* (1999), pp. 190–199.

[99] M. Matsushita et al. "Interface growth and pattern formation in bacterial colonies". In: *Physica A* (1998), pp. 517–524.

[100] E. Mhatre, R. Gallegos Monterrosa, and A.T. Kovács. "From environmental signals to regulators: Modulation of biofilm development in Gram-positive bacteria". In: *Journal of Basic Microbiology* 54 (2014), pp. 1–17.

[101] L. Michaelis and M.L. Menten. "Die Kinetik der Invertinwirkung". In: *Biochemische Zeitschrift* 49 (1913), pp. 335–369.

[102] M. Mimura, H. Sakaguchi, and M. Matsushita. "Reaction-diffusion modelling of bacterial colony patterns". In: *Physica A* (2000), pp. 283–303.

[103] J. Müller and W. van Saarloos. "Morphological instability and dynamics of fronts in bacterial growth models with nonlinear diffusion". In: *Physical Review E* 65.6 (2002).

[104] J. Müller et al. "Cell-cell communication by quorum sensing and dimension-reduction". In: *Journal of Mathematical Biology* 53 (2006), pp. 672–702.

[105] J.D. Murray. *Mathematical biology: I. An introduction.* 3rd edition. Springer Berlin Heidelberg, 2002.

[106] J.D. Murray. *Mathematical biology: II. Spatial models and biomedical applications.* 3rd edition. Springer Berlin Heidelberg, 2003.

[107] S. Nagrath, K.E. Jansen, and R.T. Lahey Jr. "Computation of incompressible bubble dynamics with a stabilized finite element level set method". In: *Computer Methods in Applied Mechanics and Engineering* 194 (2005), pp. 4565–4587.

[108] K.H. Nealson, T. Platt, and J.W. Hastings. "Cellular control of the synthesis and activity of the bacterial luminescent system". In: *Journal of Bacteriology* 104.1 (1970), pp. 313–322.

[109] A. Oelker, T. Horger, and C. Kuttler. "A beautiful human pathogen: *Staphylococcus aureus*". Submitted to The Beauty of Theoretical Biology. 2017.

[110] A. Oelker, T. Horger, and C. Kuttler. "From *Staphylococcus aureus* gene regulation to its pattern formation". Submitted. 2017.

[111] Y. Omae, K. Sekimizu, and C. Kaito. "Inhibition of colony-spreading activity of *Staphylococcus aureus* by secretion of delta-hemolysin". In: *The Journal of Biological Chemistry* 287.19 (2012), pp. 15570–15579.

[112] K.M. Page, P.K. Maini, and N.A.M. Monk. "Complex pattern formation in reaction-diffusion systems with spatially varying parameters". In: *Physica D* 202 (2005), pp. 95–115.

[113] K.M. Page, P.K. Maini, and N.A.M. Monk. "Pattern formation in spatially heterogeneous Turing reaction-diffusion models". In: *Physica D* 181 (2003), pp. 80–101.

[114] J. Pane-Farre et al. "Role of RsbU in controlling SigB activity in *Staphylococcus aureus* following alkaline stress". In: *Journal of Bacteriology* 191.8 (2009), pp. 2561–2573.

[115] S. Periasamy et al. "How *Staphylococcus aureus* biofilms develop their characteristic structure". In: *PNAS* 109.4 (2012), pp. 1281–1286.

[116] A. Peschel and M. Otto. "Phenol-soluble modulins and staphylococcal infection". In: *Nature Reviews Microbiology* 11 (2013), pp. 667–673.

[117] A.A. Polezhaev et al. "Spatial patterns formed by chemotactic bacteria *Escherichia coli*". In: *The International Journal of Developmental Biology* 50 (2006), pp. 309–314.

[118] W.H. Press et al. *Numerical recipes: The art of scientific computing*. Cambridge University Press, New York, 1986.

[119] S.Y. Queck et al. "RNAIII-independent target gene control by the agr quorum- sensing system: Insight into the evolution of virulence regulation in *Staphylococcus aureus*". In: *Molecular Cell* 32.1 (2008), pp. 150–158.

[120] D. Romero et al. "Amyloid fibers provide structural integrity to *Bacillus subtilis* biofilms". In: *PNAS* 107.5 (2010), pp. 2230–2234.

[121] P.G. Saffman and G. Taylor. "The penetration of a fluid into a porous medium or Hele-Shaw cell containing a more viscous liquid". In: *Proceedings of the Royal Society A: Mathematical, Physical and Engineering Sciences* 245.1242 (1958), pp. 312–329.

[122] E. Sander and T. Wanner. "Pattern formation in a nonlinear model for animal coats". In: *Journal of Differential Equations* 191 (2003), pp. 143–174.

[123] R.A. Satnoianu et al. "Travelling waves in a nonlinear degenerate diffusion model for bacterial pattern formation". In: *Discrete and Continuous Dynamical Systems - Series B* 1.3 (2001), pp. 339–362.

[124] K.A. Schmidt, A.C. Manna, and A.L. Cheung. "SarT influences sarS expression in *Staphylococcus aureus*". In: *Infection and Immunity* 71.9 (2003), pp. 5139–5148.

[125] K. Schwartz et al. "Functional amyloids composed of phenol soluble modulins stabilize *Staphylococcus aureus* biofilms". In: *PLoS Pathogens* 8.6 (2012).

[126] K. Schwartz et al. "The AgrD N-terminal leader peptide of *Staphylococcus aureus* has cytolytic and amyloidogenic properties". In: *Infection and Immunity* 82.9 (2014), pp. 3837–3844.

[127] A. Seminara et al. "Osmotic spreading of *Bacillus subtilis* biofilms driven by an extracellular matrix". In: *PNAS* 109.4 (2012), pp. 1116–1121.

[128] M.M. Senn et al. "Molecular analysis and organization of the sigmaB operon in *Staphylococcus aureus*". In: *Journal of Bacteriology* 187.23 (2005), pp. 8006–8019.

[129] J.A. Sethian. "A fast marching level set method for monotonically advancing fronts". In: *Proceedings of the National Academy of Sciences of the United States of America* 93.4 (1996), pp. 1591–1595.

[130] J.A. Sethian. *Level set methods and fast marching methods*. 2nd edition. Cambridge University Press, 1999.

[131] L.J. Shaw and J.D. Murray. "Analysis of a model for complex skin patterns". In: *SIAM Journal on Applied Mathematics* 50.2 (1990), pp. 628–648.

[132] M.J. Shelley, F.-R. Tian, and K. Wlodarski. "Hele-Shaw flow and pattern formation in a time-dependent gap". In: *Nonlinearity* (1997), pp. 1471–1495.

[133] S. Sinha, T. Dutta, and S. Tarafdar. "Adhesion and fingering in the lifting Hele-Shaw cell: Role of the substrate". In: *The European Physical Journal E* 25 (2008), pp. 267–275.

[134] S. Sinha et al. "Radially interrupted viscous fingers in a lifting Hele-Shaw cell". In: *The European Physical Journal E* 36 (2003), pp. 297–300.

[135] J. Stoer and R. Bulirsch. *Einführung in die Numerische Mathematik II*. Heidelberger Taschenbuch, Springer, 1973.

[136] M. Sussman, P. Smereka, and S. Osher. "A level set approach for computing solutions to incompressible two-phase flow". In: *Journal of Computational Physics* 114 (1994), pp. 146–159.

[137] P. Tabeling, G. Zocchi, and A. Libchaber. "An experimental study of the Saffman-Taylor instability". In: *Journal of Fluid Mechanics* 177 (1987), pp. 67–82.

[138] G.I. Taylor. "Stability of a viscous liquid contained between two rotating cylinders". In: *Philosophical Transactions of the Royal Society of London, Series A* 223 (1923), pp. 289–343.

[139] *The FEniCS Project. Version 1.6.*

[140] A. Toth, D. Horvath, and W. van Saarloos. "Lateral instabilities of cubic autocatalysis reaction fronts in a constant electric field". In: *Journal of Chemical Physics* 111.24 (1999), pp. 10964–10968.

[141] A.M. Turing. "The chemical basis of morphogenesis". In: *Philosophical Transactions of the Royal Society of London B: Biological Sciences* 237.641 (1952), pp. 37–72.

[142] J. Valle et al. "SarA and not sigmaB is essential for biofilm development by *Staphylococcus aureus*". In: *Molecular Microbiology* 48.4 (2003), pp. 1075–1087.

[143] H. Vlamakis et al. "Sticking together: Building a biofilm the *Bacillus subtilis way*". In: *Nature Reviews Microbiology* 11.3 (2013), pp. 157–168.

[144] C. Vuong et al. "*Staphylococcus epidermidis* polysaccharide intercellular adhesin production significantly increases during tricarboxylic acid cycle stress". In: *Journal of Bacteriology* 187.9 (2005), pp. 2967–2973.

[145] R. Wang et al. "*Staphylococcus epidermidis* surfactant peptides promote biofilm maturation and dissemination of biofilm-associated infection in mice". In: *The Journal of Clinical Investigation* 121.1 (2011), pp. 238–248.

[146] L.S. Waters and G. Storz. "Regulatory RNAs in bacteria". In: *Cell* 136.4 (2009), pp. 615–628.

[147] J.N. Wilking et al. "Liquid transport facilitated by channels in *Bacillus subtilis* biofilms". In: *Proceedings of the National Academy of Sciences* 110 (2013), pp. 848–852.

[148] J.M. Wood. "Osmosensing by bacteria: Signals and membrane-based sensors". In: *Microbiology and Molecular Biology Reviews* 63.1 (1999), pp. 230–262.

[149] L. Yang et al. "Pattern formation arising from interactions between Turing and wave instabilities". In: *Journal of Chemical Physics* 117.15 (2002).

[150] J.M. Yarwood and P.M. Schlievert. "Quorum sensing in Staphylococcus infections". In: *The Journal of Clinical Investigation* 112.11 (2003), pp. 1620–1625.

[151] J.M. Yarwood et al. "Quorum sensing in *Staphylococcus aureus* biofilms". In: *Journal of Bacteriology* 186.6 (2004), pp. 1838–1850.

[152] T. Zhang, N.G. Cogan, and Q. Wang. "Phase-field models for biofilms. I. Theory and 1-D simulations". In: *SIAM Journal on Applied Mathematics* 69.3 (2008), pp. 641–669.

[153] L. Zhao et al. "*Staphylococcus aureus* AI-2 quorum sensing associates with the KdpDE two-component system to regulate capsular polysaccharide synthesis and virulence". In: *Infection and Immunity* (2010), pp. 3506–3515.